UNIVERSITÀ DEGLI STUDI DI UDINE

Dipartimento di Ingegneria Elettrica, Gestionale e Meccanica

Corso di Dottorato in Ingegneria Industriale e dell'Informazione
Ciclo XXVIII

Tesi di Dottorato di Ricerca

CHARACTERIZATION AND MODELING OF POWER LINE COMMUNICATION CHANNELS

Dottorando:
ALBERTO PITTOLO

Relatore:
Prof. ANDREA M. TONELLO

8 Aprile 2016

ANNO ACCADEMICO
2015/2016

Contents

List of Tables

List of Figures

List of Acronyms

4D	four-dimensional
AC	alternating current
ACG	average channel gain
ADSL	asymmetric DSL
AO	alternating optimization
ARIB	Association of Radio Industries and Businesses
ASIC	application-specific integrated circuit
AWGN	additive white Gaussian noise
BB	broad-band
BB-FS	broadband frequency spectrum
BB-PLC	broadband PLC
C-CDF	complementary cumulative distribution function
C-PSD	cross-PSD
CAN	controller area network
CB	coherence bandwidth
CC	conventional car
CDF	cumulative distribution function
CENELEC	European Committee for Electrotechnical Standardization
CFR	channel frequency response

CIR channel impulse response

CLT central limit theorem

CM common mode

CP cyclic prefix

CSI channel state information

CSMA carrier-sense multiple access

CTF channel transfer function

DAF deterministic auto-correlation function

DB distribution board

DC direct current

DES Data Encryption Standard

DSL digital subscriber line

DSO digital storage oscilloscope

DSP digital signal processing

DWMT discrete wavelet multitone

E protective earth

EC electric car

EMC electromagnetic compatibility

EMI electromagnetic interference

EN European Norm

ERDF Électricité Réseau Distribution France

ESP Spain

ETSI European Telecommunications Standards Institute

FCC Federal Communications Commission

FDMA frequency-division multiple access

FEC forward error correction

FFT fast Fourier transform

FM frequency modulation

FPL front position light

FSK frequency-shift keying

HD-PLC High-Definition Power Line Communication Alliance

HDR high data-rate

HP HomePlug Powerline Alliance

HPAV HomePlug AV

HV high voltage

i.i.d. independent and identically distributed

IDFT inverse discrete Fourier transform

IEC International Electrotechnical Commission

IEEE Institute of Electrical and Electronics Engineers

ISO International Organization for Standardization

ISO/OSI Open Systems Interconnection

ISP inter-system protocol

ITA Italy

ITU International Telecommunication Union

KKT Karush–Kuhn–Tucker

LDPC low-density parity check

LIN local interconnect network

LV low voltage

MAC media access control

MIMO multiple-input multiple-output

MU multiple user

MV medium voltage

N	neutral
NB	narrow-band
NB-FS	narrowband frequency spectrum
NB-PLC	narrowband PLC
NEC	National Electric Code
OFDM	orthogonal frequency division multiplexing
OPERA	Open PLC European Research Alliance
pdf	probability density function
P	phase
PDP	power delay profile
PHY	physical layer
PL	path loss
PLC	power line communication
PLS	physical layer security
PRIME	Power Line Intelligent Metering Evolution Alliance
PSD	power spectral density
q-q	quantile-quantile
QoS	quality of service
RF	radio frequency
RMS	root-mean-square
RMS-DS	root-mean-square delay spread
RP	room service panel
RS	Reed-Solomon
RSA	Rivest-Shamir-Adleman
RSE	Ricerca Sistema Energetico
RV	random variable

SAF statistical auto-correlation function

SCR silicon controlled rectifiers

SDO standards-developing organization

SIC successive interference cancellation

SIMO single-input multiple-output

SISO single-input single-output

SNR signal-to-noise ratio

SS substation switchboard

STF special task force

SVD singular value decomposition

TDMA time-division multiple access

TEM transverse electro-magnetic

TIA Telecommunications Industry Association

TL transmission line

UNB ultra narrow band

UPA Universal Powerline Alliance

USA United States

VNA vector network analyzer

w.r.t. with respect to

ZF zero forcing

List of Symbols

Table 1: List of the most commonly used symbols.

Symbol	Unit	Definition
$\{\cdot\}^*$	-	Complex conjugate operator
$\{\cdot\}^+$	-	Pseudo inverse operator
$\{\cdot\}^\dagger$	-	Hermitian operator
$\{\cdot\}^\top$	-	Transpose operator
$\overline{\{\cdot\}}$	-	Average value
$\alpha_{\mathcal{E}}$	-	Coefficient for CIR tails cutting
$\alpha_{\ell,p}$	-	Noise cross-correlation coefficient among modes ℓ and p
$\mathbf{a}_m$	V	Vector of transmitted MIMO symbols at m-th frequency
A	-	Amplitude of the CFR
A_{dB}	dB	Logarithmic version of the CFR squared amplitude
β_M	-	Main channel power gain
β_W	-	Eavesdropper channel power gain
B	Hz	Positive transmission bandwidth
$\mathbf{B}_m$	-	MIMO precoding matrix at m-th frequency
$\mathcal{B}_C^{(\xi)}$	Hz	Deterministic coherence bandwidth at level ξ
$\hat{\mathcal{B}}_C^{(\xi)}$	Hz	Statistical coherence bandwidth at level ξ
$\overline{\mathcal{B}}_C^{(\xi)}$	Hz	Average value of $\mathcal{B}_C^{(\xi)}$ among the considered database
$\chi_{\ell,p}$	-	Normalized spatial covariance for MIMO transmission
$\mathcal{C}$	bps	Maximum achievable rate, i.e. capacity
$\mathcal{C}_S$	bps	Maximum achievable secrecy rate, i.e. secrecy capacity
Δf	Hz	Frequency resolution
Δ_{tx}	-	MIMO Δ-style transmitting modes $tx \in \{1, \ldots, 3\}$
Δt	s	Temporal (time) resolution
d_i	-	Singular values of $\mathbf{H}$ on the diagonal of $\mathbf{D}$
D	s	Channel impulse response duration

(continue on the next page)

(continued from the previous page)

Symbol	Unit	Definition
$\mathbf{D}$	-	Rectangular diagonal matrix of the SVD of $\mathbf{H}(f)$
$\hat{\mathbf{D}}_m$	-	Same as $\mathbf{D}$ for $\hat{\mathbf{H}}_m$ at m-th frequency
$\mathcal{D}$	m	Geometrical distance
η	-	Variable for the QoS
$\mathbf{E}_m$	-	MIMO equalizing matrix at m-th frequency
$E[\cdot]$	-	Expectation operator
$\mathcal{E}$	V^2	Total channel energy
$\mathcal{E}_C$	V^2	Discrete time normalized cumulative pulse energy
φ	rad	Phase of the CFR
$\phi_{\ell,p}$	-	Time-domain correlation coefficient among ℓ and p
Φ	-	Statistical auto-correlation function
$\overline{\Phi}$	Hz	Average value of Φ
f	Hz	Continuous frequency
f_1	Hz	Start signaling frequency
f_2	Hz	Stop signaling frequency
f_x	-	Probability density function of the channel input x
$\mathcal{F}$	-	Set of all the possible pdfs of the channel input x
$\mathcal{G}$	dB	Average channel gain
$\overline{\mathcal{G}}$	dB	Average value of $\mathcal{G}$ among the considered database
$\mathcal{G}_{s_{rx},\Delta_{tx}}$	dB	MIMO ACG among Δ_{tx} and s_{rx} modes
$h(n)$	-	Channel impulse response at time $t = nT$
h_x	-	Gain coefficient of the channel x
H	-	SISO channel frequency response
$\mathbf{H}$	-	MIMO channel frequency response matrix
$\widetilde{\mathbf{H}}$	-	Reshaped CFR matrix
$\widetilde{H}_{i,j}$	-	$\widetilde{\mathbf{H}}$ element for i transmitting and j receiving modes
$\mathbf{H}_m$	-	MIMO CFR matrix at the m-th frequency
$\hat{\mathbf{H}}_m$	-	MIMO CFR plus noise matrix at the m-th frequency
H_s	-	Ratio between the received and the source voltage
$H_{s_{rx},\Delta_{tx}}$	-	MIMO CFR among Δ_{tx} and s_{rx} modes
$\mathcal{H}(q)$	-	Entropy of the quantity q
$\mathbf{I}_N$	-	Identity matrix of dimensions $N \times N$
I_{tx}	A	Current phasor vector at the transmitter port
$\mathrm{Im}\{\cdot\}$	-	Imaginary operator
$\mathcal{I}_{ON}$	-	Set of active sub-carriers
κ	-	Keyhole or pinhole point

(continue on the next page)

(continued from the previous page)

Symbol	Unit	Definition
k	-	Hyperbolic fit coefficient
$\mathbf{K}_m$	W/Hz	Transmitted signal covariance matrix at m-th frequency
$\hat{\mathbf{K}}_m$	W/Hz	Optimal matrix for $\mathbf{K}_m$
$\mathcal{K}$	-	Auto-covariance function
$\dot{\mathcal{K}}$	-	Normalized covariance function
$\mathcal{K}^{\Delta}_{\ell,p}$	-	Covariance among Δ_ℓ and Δ_p modes
λ	-	Eigen-spread of the singular values d_i
$\Lambda(\theta)$	-	Likelihood function with parameter θ
$\mathcal{L}$	dB	Path loss of the CFR
$\mathcal{L}_{dB}$	dB	Logarithmic version of the path loss
μ_x	-	Mean of the quantity x
m	-	Discrete frequency index
M	-	Number of discrete frequency samples
M_1	-	Discrete frequency sample correspondent to f_1
M_2	-	Discrete frequency sample correspondent to f_2
$\mathcal{M}$	-	Maximum number of secret messages
n	-	Discrete time index
n_x	V	Noise in time domain experienced by x
N	-	Number of discrete time samples
$\mathbf{N}_m$	W/Hz	Noise covariance matrix at m-th frequency
N_{s_ℓ}	V/Hz	Fourier transform of the noise on the mode s_ℓ
N_M	-	Number of measurements
N_R	-	Number of receiving modes
N_T	-	Number of transmitting modes
N_U	-	Number of users
$\mathcal{N}(\mu, \sigma^2)$	-	Normal distribution with mean μ and variance σ^2
$p(x\|\theta)$	-	Fitting distribution pdf evaluated at samples x given θ
ψ	-	Normalized users covariance function
ψ_x	-	ψ for channels sharing the same $x \in \{tx, rx\}$ port
ψ_x^{amp}	-	Same as ψ_x but considering the CFR amplitude
P_e	-	Error probability
P_m	W/Hz	PSD mask at the m-th frequency
P_t	W/Hz	Transmitted power spectral density
$\overline{P}_t$	W/Hz	Average allocated power for a set of realizations
$\hat{P}_t$	W/Hz	Optimal power allocation strategy
$P_{t,m}$	W/Hz	Transmitted power on the m-th frequency sample

(continue on the next page)

(continued from the previous page)

Symbol	Unit	Definition
$\mathbf{P}_t$	W/Hz	Transmitter power allocation vector
$\mathbf{P}_X$	W/Hz	Power allocation vector for the user X
P_w	W/Hz	Noise power spectral density
P_T	W	Total available power
$\Pr[\cdot]$	-	Probability operator
$\mathcal{P}$	s^{-1}	Power delay profile
q	-	General fitting function model
$\mathbf{Q}_m$	W/Hz	Diagonal power allocation matrix at m-th frequency
$\hat{\mathbf{Q}}_m$	W/Hz	Optimal power allocation matrix at m-th frequency
$\mathcal{Q}$	-	Covariance matrix of $\widetilde{\mathbf{H}}$
$\dot{\mathcal{Q}}_{x,y}$	-	Normalized covariance matrix among x and y variables
ρ_P	-	Pearson correlation coefficient
ρ_S	-	Spearman correlation coefficient
r	-	Rank of a matrix
R	Ω	Real part of the line impedance
R_e	bps	Equivocation rate at the wiretapper
R_S	bps	Secrecy rate
$R_{S,X}$	bps	Secrecy rate for the user X
R_S^{sum}	bps	Sum secrecy rate in broadcast channels
R_S^{wgh}	bps	Weighted sum secrecy rate
$\mathrm{Re}\{\cdot\}$	-	Real operator
$\mathcal{R}$	Hz	Deterministic auto-correlation function
σ_τ	s	Root-mean-square delay spread
$\overline{\sigma}_\tau$	s	Average value of σ_τ among the considered database
σ_x	-	Standard deviation of the quantity x
σ_x^2	-	Statistical power of the quantity x
s_{rx}	-	MIMO star-style receiving modes $rx \in \{1, \ldots, 4\}$
$\mathbf{s}_m$	V	Vector of precoded MIMO signals at m-th frequency
S	-	Matrix of the scattering parameters
S_{21}	-	Forward scattering parameter, namely the CFR
$\mathcal{S}$	-	Secret message
t	s	Continuous time
T	s	Resolution in time
$\mathcal{T}$	-	Modified matrix $\dot{\mathcal{Q}}$ according to Pearson-Spearman equality
$\mathbf{U}$	-	Left-singular vectors unitary matrix of the SVD
$\mathcal{U}(a, b)$	-	Uniform distribution in (a, b)

(continue on the next page)

(continued from the previous page)

Symbol	Unit	Definition
V_s	V	Source voltage phasor vector
V_{rx}	V	Voltage phasor vector at the receiver port
V_{tx}	V	Voltage phasor vector at the transmitter port
$\mathbf{V}$	-	Right-singular vectors unitary matrix of the SVD
$\mathbf{w}_m$	V	MIMO AWGN noise at m-th frequency
$\mathbf{x}_m$	V	Vector of transmitted MIMO signals at m-th frequency
X	Ω	Imaginary part of the line impedance
$\mathcal{X}$	-	Input alphabet of the transmitted signal x
$\mathbf{y}_m$	V	Vector of received MIMO signals at m-th frequency
$\mathcal{Y}$	-	Output alphabet of the legitimately received signal y
ζ	-	Percentile value
$\mathbf{z}_m$	V	Vector of equalized MIMO signals at m-th frequency
Z_{IN}	Ω	Line impedance
$\mathcal{Z}$	-	Output alphabet of the eavesdropped received signal z

Abstract

Nowadays, we live in a highly interconnected world, where the information exchange is the milestone that has pushed and drives the incredible growth experienced by our society. This huge amount of generated data traffic will be expected to grow even further in the next few years. In order to meet these future requirements and the customers needs, the telecommunications systems must evolve and improve. Although twisted pair copper and wireless technologies represent an established and widespread solution, extensively adopted for today's communication systems, they cannot achieve these goals alone. The desire to provide a new technology that would be able to exploit what was already existing and deployed, has led to the development of the power line communication (PLC) systems.

The PLC technology exploits the existing power delivery infrastructure in order to deliver high speed and reliable data communication. Although the energy distribution grid is worldwide widespread, being able to reach each consumer around the world, it has not been conceived for data transmission at high frequencies. This leads to a challenging transmission environment, characterized by strong attenuation, high selectivity, with significant fading effects, and a great deal of noise. Despite these detrimental effects, a reliable and secure high speed communication can be established. However, in order to design and develop the best next generation devices, able to overcome the environment and medium limitations, a thoroughly knowledge and a comprehensive analysis of the PLC channel is fundamental. All the collected information enables the development of new and effective models, able to faithfully describe a real communication scenario, allowing to save money and time in the development process.

The aim of this thesis is to provide a detailed PLC channel characterization, considering several environments belonging to both the indoor and the outdoor environments. Among the indoor scenarios, that identify a confined communication environment, the in-home, the in-car and the in-ship networks are analyzed. Furthermore, concerning the outdoor scenario, both the low voltage (LV) and medium voltage (MV) distribution grids are investigated. The properties of the noise that typically affects the different PLC environments are assessed. The study mainly focuses on the broadband frequency spectrum (BB-FS), although some comparisons with the narrowband frequency spectrum (NB-FS)

are also tackled. The extensive analysis of the PLC network, performed for each considered scenario, allows to highlight the main properties and relationships that enable the development of new and effective channel models, herein described.

The first part of this work deals with the characterization of the in-home single-input single-output (SISO) PLC channel, considering a large database of measurements that was carried out during a measurement campaign performed in Italy. A statistical analysis is presented in terms of normality test, channel frequency response (CFR) distribution and phase behavior. Moreover, the main and most commonly used statistical metrics, namely average channel gain (ACG), root-mean-square delay spread (RMS-DS) and coherence bandwidth (CB), are assessed and compared to each other in order to highlight the typical relationships. Then, the performance that can be achieved are computed, inferring the relation between the geometrical distance and the maximum achievable rate, as well as the improvements due to the bandwidth extension. Furthermore, the correlation that can be experienced by channels belonging to the same network, but connecting different nodes, is discussed. Finally, the line impedance is investigated, identifying the main existing relationships between the resistive and the reactive part.

Then, the attention is moved to the multiple-input multiple-output (MIMO) transmission scheme, still within the in-home environment. The signal transmission over all the three commonly available wires, typically deployed in domestic premises, is discussed and explained. The CFR statistics and characteristics are assessed basing on the channels collected by the special task force (STF) 410 of the ETSI during an experimental measurement campaign across Europe. Also the noise properties are discussed, providing a novel method to simulate the noise correlation among the spatial receiving modes, which is based on the actual noise measurements provided by the STF-410. In addition, the general processing system is discussed, describing the optimal transmission and reception scheme under two hypothesis, full channel state information (CSI) knowledge and no CSI knowledge. The performance, in terms of maximum achievable rate, are computed for both the cases.

Afterwards, the focus is turned to in-vehicle communications, where two typical application scenarios, namely car and ship, are discussed and compared. In particular, a fundamental distinction is made among the electric car (EC) and the conventional car (CC) scenarios. Both channel and noise measurements that we carried out on a compact electric car are analyzed. The results are compared to an online available database of measurements concerning a conventional fuel car. A similar analysis is tackled considering measurements that we acquired on a large cruise ship. Finally, the two environments are compared in terms of statistical metrics relationship and average performance.

Later, the outdoor communication context is addressed, investigating and comparing LV and MV distribution grids in both the narrow-band (NB) and broad-band (BB) spectra. The characterization of this transmission scenario is of fundamental importance since it

has become very attractive, especially in recent times, for smart grid applications. The properties of one of the most known outdoor LV database and two MV set of measurements, that were carried out in two completely different network sites, are firstly discussed. Then, a comparison in terms of path loss, line impedance and background noise is tackled for the LV and MV networks in both the NB and BB frequency ranges. Some features of the main network devices usually deployed in the outdoor networks are also discussed. The final comparison, in terms of achievable rate, aims to assess if some improvements can be obtained by exploiting the BB-FS instead of the NB-FS.

In order to provide an overall overview and a general comparison among all the previously discussed environments, the main channel properties and the statistical metrics relationships are shown together and distinctly discussed. Also the differences in terms of background noise properties are summarized. The channel and noise knowledge allows the computation of the SISO channel capacity distribution for all the environments, which is later compared to the MIMO channel capacity distribution for the in-home scenario. Two different noise types are considered for the MIMO capacity computation, namely spatially uncorrelated and correlated, relying on the ETSI STF-410 noise measurements.

The second part of this work focuses on the channel modeling, which represents a quick and easy testing tool for the development and the simulation of standards and devices. This translates into a considerable saving in terms of costs and time, avoiding on-field measurements. All the detailed information previously collected, as well as the highlighted relationships, are the foundations on which we develop an extremely synthetic channel model, able to faithfully emulate a real MIMO PLC channel with a reduced set of parameters. The proposed model consists of a pure top-down approach, without any physical connection. It is extremely synthetic since it is able to numerically generate channel realizations, that are equivalent to the measurements, simply basing on the CFR amplitude and phase statistics and on their corresponding properties, such as the correlation exhibited among the frequencies, as well as between the different spatial modes.

A final fundamental aspect is also taken into account. In a world based on a massive and constant flow of information, where usually the communications are private and confidential, ensuring the security of the exchanged data is of paramount importance. Towards this end, the concept of secure data communication is introduced focusing on the secrecy granted at the physical level, named physical layer security (PLS). As it is discussed, this concept completely differs from the secrecy ensured at the application layer, thus, exploiting encryption protocols through the use of keys. The main concepts underlying the secure data communication are discussed. In this respect, the wiretap channel is defined, evaluating the performance that can be achieved among a transmitter and an intended receiver, without releasing any information to a third counterpart. This quantity is known as secrecy capacity. The main differences between the conventional capacity and the secrecy capacity, and among the wireless and PLC scenarios, are highlighted. Furthermore, the

detrimental influence on the secrecy capacity due to the typical PLC channel phenomena, such as the frequency selectivity and the multiple user (MU) correlation, as well as to the network topology, which gives rise to what is known as keyhole effect, are assessed. Afterwards, a typical MU broadcast scenario is considered, discussing and computing the achievable secrecy rate region under a total power and a quality of service (QoS) constraints. Finally, in an attempt to overcome all the PLC scenario limitations, a MIMO transmission scheme, a bandwidth extension, as well as a more fair background noise assumption are assessed, relying on experimental channel and noise measurements. The achievable secrecy rate is computed considering both an alternating optimization (AO) algorithm and a uniform power allocation approach. The results are compared to the SISO case, as well as to the conventional capacity, without secrecy constraints.

1 Introduction

In recent years we have assisted at the worldwide increasing demand of data connectivity, not only for information exchange and multimedia services, but also by "smart" devices deployed almost everywhere, that need to communicate each other. This huge request of high speed and reliable data traffic has pushed and drives the industry and the research community to develop and provide new devices, specify new standards, and exploit different communication mediums in order to meet these requirements. Moreover, the desire to deliver new communication services, without requiring significant investments in the expansion of the telecommunication infrastructure, motivates the development and the exploitation of the already existing structures.

The twisted pair copper systems represent an established and widespread solution. Furthermore, the wireless technology has become a promising, simple and cost effective technique that has gathered great success, especially nowadays. Anyway, these solutions will not be enough to manage and maintain this massive and increasing amount of information exchange demand. Furthermore, as a matter of fact, there are several applications and contexts in which other transmission techniques represent a better and more powerful solution, being also able to aid and support the existing technologies. One of these, that has attracted the attention of industries, especially in the last few years, exploits the existing power delivery infrastructure in order to convey high speed data content. This technology is known as power line communication (PLC).

1.1 The PLC Technology

This thesis deals with PLC, a transmission technique that is becoming more and more widely and successfully deployed, and that has been recently recognized as a key technology to enable reliable communications, especially within the smart grid context [1]. PLCs have experienced several developments and different implementing strategies over the years, depending on the use they were designed for. The main historical steps towards

the realization of the modern PLC concept are briefly summarized in the following.

1.1.1 Brief History

The idea of exploiting the power delivery infrastructure as a communication medium originates in 1918. Thus, PLC is not a recent concept and it was initially used by power utilities for command and control applications over high and medium voltage lines between remote stations [2]. Since then, the application areas have significantly expanded [3]. For example, broadband internet access offered by PLC over the distribution network that feeds houses and buildings was considered of great interest, especially in the first decade of the new millennium. Furthermore, advanced technology was deployed and it proved to be a technically valuable solution.

In parallel, it was recognized that high speed data coming from last mile communication systems, e.g., digital subscriber line (DSL) and optical fiber, might have found a bottleneck at the house door. Thus, the exploitation of the power delivery structure, which is worldwide widespread, more than the common twisted pair cables or the optical fibers, represents a strength point for the PLC technology. Indeed, high speed in-home connectivity was also desirable, allowing the home gateway to provide uninterrupted flow of heterogeneous traffic between the outdoor and the indoor networks, hence among the service provider and the end user, as a typical DSL internet connection.

Wi-Fi has fostered such a paradigm and it has been largely researched, developed and marketed as stated, for example, by the evolution of the Institute of Electrical and Electronics Engineers (IEEE) 802.11 standard [4]. However, wireless technology may also experience complications, mostly due to unfavorable propagation conditions and limited radiated power for safety reasons that do not allow to grant full coverage at the promised speeds, e.g., in multiple floor dwellings with the presence of reinforced concrete floors.

Although the market is already highly penetrated by DSL, typically deployed at the final customers as asymmetric DSL (ADSL), and wireless technologies, which may relegate PLC in few areas, still some good chances exists about its wide use, especially in emerging countries. Especially in recent years, indeed, a novel and increasing interest is moving towards the PLC technology, in particular concerning smart grid applications. This is since, as seen, one of the main advantages of the PLC technique is the exploitation of the already existing wired electrical infrastructure in order to provide communication capabilities. Thus, the smart grid represents one of the most appealing application contexts for PLC and, consequently, a lot of effort has been spent by the research community in this area. In particular, some feasibility and experimental studies were carried out in [5–11]. Similarly, smart city [12], in-home automation [13] and telemetry [14] applications can also benefit from the avoidance of dedicated cabling deployment and can further overcome the wireless propagation issues. Consequently, complementary technologies were researched and PLC found a fertile market where to prove its own validity. Initially, a

number of proprietary solutions were developed, but noting that the key strategy for a wide deployment is standardization.

1.1.2 Standardization

The diversity of grid contexts and application domains to which PLC systems can be applied has naturally led to a large ecosystem of specifications, many of whose have been adopted by standards-developing organization (SDO) authorities. Regulatory activities are essentially concerned with coexistence with other systems that also use the power grid (i.e. machines and appliances that draw electricity) and wireless systems operating in the same frequency bands as PLC. The frequency range used for PLC starts as low as 125 Hz and reaches as high as 250 MHz. A useful classification of PLC systems according to frequency bands has been introduced in [1] that distinguishes between ultra narrow band (UNB), narrow-band (NB) and broad-band (BB) PLC systems, operating between about 125–3000 Hz, 3–500 kHz and 1.8–250 MHz, respectively. Most recent developments in standardization and regulation activities over the past twenty years apply to NB and BB PLC systems, and we will focus on these in the following.

Narrowband PLC

There are numerous industry specifications for narrowband PLC (NB-PLC) systems that support link rates of up to a few kbps and operate in the application space of home and industry automation and for utility applications, e.g. see [15, Ch. 7], [16, Ch. 2.2] and [17]. Several of these were adopted as international standards in the late nineties and early 2000s, establishing a track record for PLC as a proven technology for low data-rate and reliable applications.

The development and standardization of broadband PLC (BB-PLC) systems have been followed by a wave of activity to specify NB-PLC solutions for relatively high data-rate (HDR) transmission. These efforts have been driven by the demands for an effective smart grid communication infrastructure [18], [19, Ch. 4]. Figure 1.1 provides an overview of the development of the major industry specifications and SDO authorities for such HDR NB-PLC systems. Within this context, the HDR term means that data rates of tens to hundreds of kbps are achieved using the 3–500 kHz frequency band. In particular, in accordance with the frequency bands available in different regions of the world, the specifications listed in Figure 1.1 have defined different bandplans.

Concerning the European community, the standard European Norm (EN) 50065 (EN 50065-1:2011) [20] was issued by the European Committee for Electrotechnical Standardization (CENELEC) (3–148.5 kHz), which specifies four frequency bands for PLC systems. Namely, band A (3–95 kHz) is reserved exclusively to power utilities; band B (95–125 kHz) can be used for any application; band C (125–140 kHz) is dedicated to

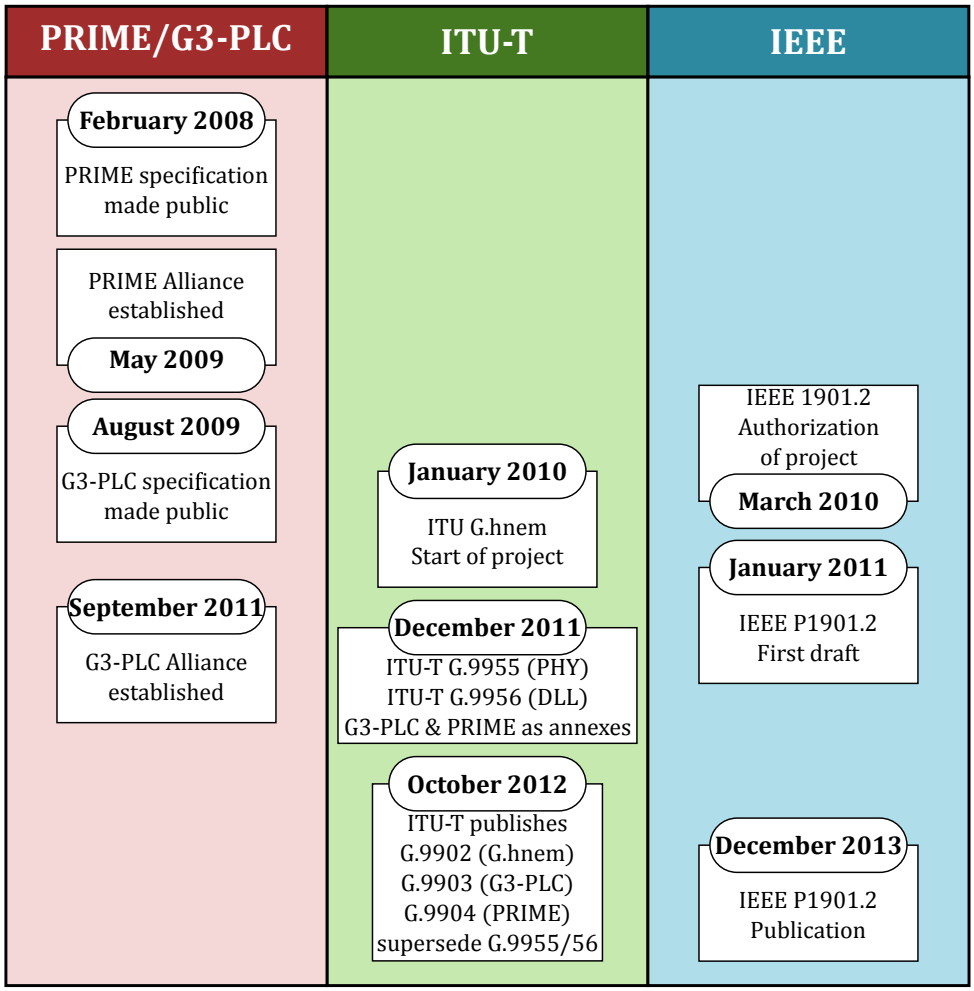

Figure 1.1: Overview and development time-line of the main NB-PLC specifications and standards for PRIME/G3-PLC, ITU-T and IEEE SDO authorities..

in-home networking systems; band D (140–148.5 kHz) is reserved to alarm and security systems. Instead, in the United States (USA) the NB spectrum is regulated by Federal Communications Commission (FCC), Title 47, Part 15 (47 CFR §15) (9–490 kHz), while in Asia by the Standard T84 issued by the Japanese Association of Radio Industries and Businesses (ARIB) (10–450 kHz) [21], that allow PLC devices to work in the 3–500 kHz band. Also within the narrowband frequency spectrum (NB-FS) the so called NB-PLC technology has been standardized. Although the first solutions deployed single carrier modulation (e.g. frequency-shift keying (FSK) in the International Electrotechnical Commission (IEC) 61334 standard [22]), orthogonal frequency division multiplexing (OFDM) was chosen to provide higher speeds.

The most popular standards are Power Line Intelligent Metering Evolution Alliance (PRIME) (International Telecommunication Union (ITU)-T G.9904) [23] and Électricité Réseau Distribution France (ERDF) G3-PLC (ITU-T G.9903) [24], which are specified for working over low voltage (LV) networks in the CENELEC-A frequency band. In NB-PLC systems differential modulation is used. This avoids the need for channel estimation and is

thus better suited for transmission of shorter messages and is also more robust to channel variations. Furthermore, emphasizing simplicity, convolutional coding is used. In case of PRIME, even this is optional, while G3-PLC adds an outer Reed-Solomon (RS) code. G3-PLC also specifies a robust mode that uses additional repetition. Such a mode has been added to the latest version of PRIME.

In order to provide a worldwide standard, in 2011 the ITU-T published recommendations, ITU-T G.9955 for the physical layer (PHY) and ITU-T G.9956 for the link layer, which included PRIME and G3-PLC as well as the new G.hnem technology. The latter uses coherent transmission. For NB-PLC up to 500 kHz two standards, that incorporate the features of the previous ones, have been developed, namely the ITU-T G.hnem (ITU-T G.9902) [25] and the IEEE P1901.2 (IEEE 1901.2-2013) [26] (ratified at the end of 2012 and 2013, respectively), as shown in Figure 1.1. They offer data rates in the order of hundreds kbps, reaching about 500 kbps in some special conditions and through the use of OFDM. Moreover, as outlined in [1], the IEEE P1901.2 and G3-PLC are sufficiently different to be non-interoperable.

Broadband PLC

The late nineties saw a boost of activities in the PLC community, developing BB-PLC solutions for the access and in-home domains, eventually targeting data rates of hundreds of Mbps [27, 28]. This resulted in several industry specifications, mainly those backed by the HomePlug Powerline Alliance (HP), the Universal Powerline Alliance (UPA) and the High-Definition Power Line Communication Alliance (HD-PLC). A first relevant industry standard was promoted by the HP that developed a BB solution operating in the 2–28 MHz band based on OFDM, starting with the HomePlug 1.0 released in June 2001 [29, 30]. This standard was capable to deliver 14 Mbps, with a peak rate of 200 Mbps, and was adopted by the Telecommunications Industry Association (TIA) as the international standard TIA-1113 in 2008. However, the existence of different non-interoperable specifications has not been ideal for broad market success. Against this background, the consolidation of BB-PLC systems in international standards was started by the IEEE P1901 Corporate Standards Working Group in June 2005, followed by the ITU-T standardization project G.hn in April 2006 [31, 32]. In 2010, this resulted in the publication of the IEEE P1901 [33], the ITU-T G.9960 (known as ITU-T G.hn) [34] and the G.9961 [35] standards, which specify the physical and data link layers, as well as coexistence mechanisms and power spectral density (PSD) masks.

The IEEE standard uses the 2–30 MHz frequency band with an optional extended band of up to 50 MHz. It includes two multicarrier physical layers, which are commonly referred to as OFDM via fast Fourier transform (FFT) OFDM and Wavelet OFDM, respectively. The former is classic (windowed) OFDM, while the latter is a discrete wavelet multitone (DWMT) modulation [36]. They are non-interoperable but their coexistence

has been ensured by an inter-system protocol (ISP). The FFT-PHY applies a Turbo code for forward error correction (FEC), while the Wavelet-PHY uses a concatenated RS and convolutional code, which can optionally be replaced by a convolutional low-density parity check (LDPC) code. The physical layers support multiple signal constellations and spectral masking, as required by regulations. On top of these two physical layers resides, via PHY convergence protocols, a common media access control (MAC) layer that enables both carrier-sense multiple access (CSMA) and time-division multiple access (TDMA).

While IEEE P1901 has provisions for in-home and access networks, ITU-T G.hn applies specifically to home networking. It does not apply only to PLC, but also to communication over phone lines and coaxial cables. For PLC, it includes three band-plans, from 2 MHz to 25, 50, and 100 MHz, respectively. The spectral mask, in order to comply with the emission limits, is consistent with that used in IEEE P1901. Also, as in IEEE P1901, windowed OFDM with flexible bit loading is applied, and CSMA and TDMA are used for medium access. As it can be noted, the IEEE P1901 and ITU-T G.hn standards are non-interoperable. However, the coexistence is enabled through the ISP specified in the IEEE P1901 and ITU-T G.9972 [37].

On the way towards Gbps transmission, a multiple-input multiple-output (MIMO) transmission extension to G.hn has been specified as ITU-T G.9963 [38]. Similarly, HomePlug published the HomePlug AV2 (HPAV2) standard [39], which is backward compatible with HPAV and IEEE P1901, and promises 2 Gbps of peak rate. Such impressive performance is made possible by the adoption of state-of-the-art communication solutions as multicarrier modulation, bandwidth extension up to 86 MHz, multiple wire transmission, precoding (using powerful Turbo codes) and adaptation. This, together with an efficient notching, a power back-off to reduce emissions and a number of advanced techniques at the MAC layer. At the other end of the data-rate spectrum, ITU-T G.9960 includes a low-complexity profile for reduced component cost and power consumption targeting the smart grid market. Similarly, a simplified low-power version of the BB HomePlug standard, called HomePlug Green PHY [40], has been developed as a subset of the HPAV standard for low power consumption and low cost, targeting the home-area network domain of smart grids. In this respect, this standard has been adopted as a reference for communications between an electric vehicle and the charging station.

Figure 1.2 summarizes the mentioned standards along the time-line of their publication dates. The left column shows some important steps in the evolution of HP specifications, the second column considers the ITU-T standard development, while the third one concerns the IEEE standardization process. Within this thesis the focus will be on the broadband frequency spectrum (BB-FS), making just some hints about the NB-FS.

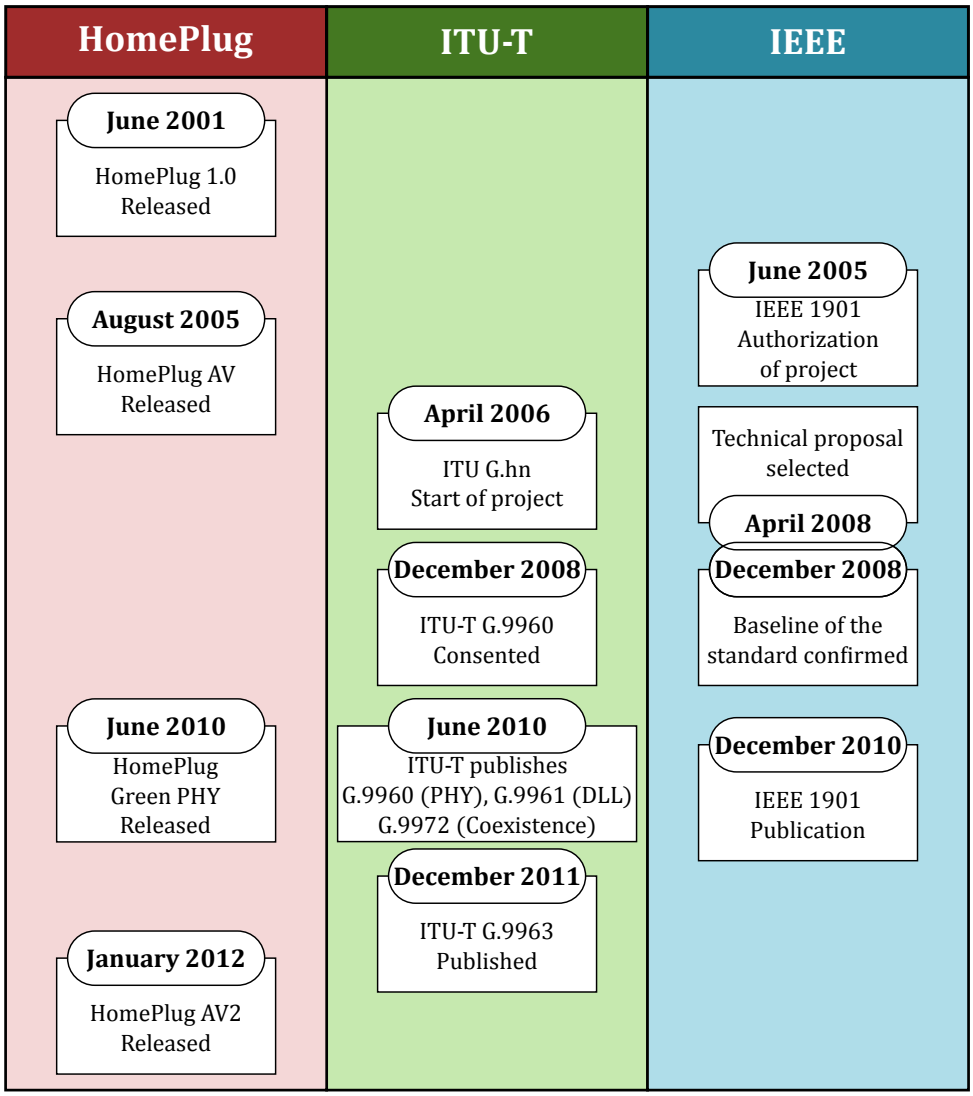

Figure 1.2: Overview and development time-line of the main BB-PLC specifications and standards for HP, ITU-T and IEEE SDO authorities.

1.2 PLC Application Contexts

The PLC enables the delivery of a broad range of services by exploiting the existing power delivery grids. Moreover, since power lines are pervasively and worldwide deployed, the use of PLC is potentially ubiquitous.

In general, PLC can be applied to provide two-way communication in all the three smart grid domains, namely transmission, distribution and user domains, exploiting high voltage (HV), medium voltage (MV) and LV lines [19]. As previously stated, typically PLC is divided into two classes: NB and BB. NB-PLC operates in the range of frequencies below 500 kHz, and it is used for low rate applications, as command-and-control, remote monitoring and automatic meter reading. BB-PLC, instead, may signal up to 86 MHz and it enables the streaming of high-speed multimedia content.

In particular, PLC can be used to deliver several applications, for instance, remote

fault detection, remote station surveillance, or state estimation. It can provide communication capabilities between sensors located in substations so that status can be monitored, and faults detected and isolated. PLC can also be exploited for the detection of islanding events. The main application in the LV part of the network is automatic/smart metering. For this application, PLC has already enjoyed a great deployment success, with about 90 million meters installed in Europe, and many more installed worldwide. Sensing, command, and control applications are also of great interest for applications inside homes or buildings. The in-home PLC network can be exploited for energy management purposes, together with a wide set of home automation applications for increasing security, comfort and life quality. These scenarios, along with the smart grid contexts, correspond to one of the most studied areas for the applicability of PLC networks [41–44].

Two further PLC application areas lie in the management and control of micro grids (e.g. local generation grids using renewable energy sources, such as solar cells and wind turbines), and in the connection between electrical vehicles and the grid, which can offer a wide set of applications. In this respect, there are several scenarios in which the PLC technology can be applied. A promising alternative, although it is not significantly exploited yet, is represented by in-vehicle communication, where in-vehicle PLC refers to the set of applications devoted to establish data links inside any means of transportation [45], [15, Ch. 10]. Within this context, PLC networks have been explored for vehicular environments usages. The investigation of in-car PLC has been documented in [46–52]. The in-ship environment is less investigated. Some results are shown in [53, 54]. Moreover, PLC can find application in more unconventional scenarios, such as planes [55, 56], trains [57, 58] and space crafts [59]. All the above listed works testify that the PLC technology can provide high-speed data connectivity via the exploitation of the existing power network, with clear potential benefits in terms of cost and weight reduction.

However, the applicability of PLC networks is not restrained to the above mentioned scenarios. A range of novel applications have been proposed for PLC networks, including robotics [60], authentication [61], security systems in mining [62], as well as uses within inductive coupling [63], contactless communication [64] and wireless power transfer [65].

As an overall final remark, it can be noted as the PLC represents a valuable solution to deliver both high speed entertainment, or multimedia services (especially for the in-home premises), and low data rate, reliable and robust communications (e.g. for information exchange among sensors). Furthermore, it represents a cost effective and flexible solution, capable to overcome the detrimental effects and to adapt at the different properties exhibited by the great multitude of possible application contexts.

1.3 PLC Scenario Characterization

Despite the existence of commercial PLC systems and recently released standards, PLC can still evolve and advanced solutions can be identified to better solve the open challenges, which mostly rely on the full understanding of the hostile communication medium, the development of ad hoc modulation and coding techniques and the definition of MAC protocols for lossy channels with time variant behavior in terms of traffic, noise sources and topology changes.

Further improvements require the detailed knowledge of the communication medium. Indeed, the variability of the wiring structures and of the possible application scenarios translates into an extreme variability of the PLC channel features and noise properties. For example, line discontinuities and unmatched loads generate multipath fading effects [3, 66]. This translates into severe frequency selectivity, although, differently from the wireless case, PLC channels are mostly static (no mobility). In this respect, the characterization of the PLC channel and noise is of fundamental importance.

1.3.1 Channel Features

In the literature, a lot of effort has been spent on the channel analysis. A first characterization of the PLC channel was presented in [67]. The study was based on measurements up to 60 MHz. In [68], the feasibility of high-speed PLC was tested for the in-home USA scenario. The test was carried out with prototype devices in the 1.8–30 MHz frequency range, which is that deployed by most of BB-PLC commercial systems. New standards enable communications up to 60 MHz, e.g., IEEE P1901 [33], and even up to 100 MHz, such as ITU-T G.hn [34]. Moreover, some studies discuss the PLC applicability even beyond 100 MHz, as for example it has been promoted by the ITU-R in [69].

A characterization of the PLC channel up to 100 MHz was presented in [70]. The analysis was based on a measurement campaign that was performed in France and it yielded the classification of the channels into nine classes according to the channel capacity. In [71], the classes were described in terms of associated root-mean-square delay spread (RMS-DS) and coherence bandwidth (CB). More recently, in [72], it was shown that the RMS-DS is negatively related to the average channel gain (ACG). This result was confirmed in [73], where the statistics of the PLC channel in USA networks was further compared to that of phone lines, coaxial cables and MV lines. Both [72] and [73] targeted the 1.8–30 MHz frequency band. An analysis of the RMS-DS, the ACG and the normality of the channel frequency response (CFR) in dB of a set of measured channels was also reported in [74]. The database consists of 200 measurements that were performed in Spain (ESP). All previous contributions address the in-home PLC scenario, with the exception of [73] that also considers MV grids and phone lines. An accurate characterization of the outdoor PLC channel was performed by the Open PLC European Research Alliance

(OPERA) [75], and the results were presented in [76]. The work provides an experimental channel and noise characterization for both the LV and MV sides of the distribution grid. More recently, the line impedance of the LV distribution grid was investigated in the NB frequency range [77].

As previously mentioned, the throughput achieved by the PLC technique can be increased by signaling in the extended frequency band between 1.8–86 MHz, making use of advanced multicarrier modulation schemes based on OFDM, but also by enabling the use of MIMO solutions to further extend coverage, or to provide higher data rates with respect to (w.r.t.) more conventional single-input single-output (SISO) PLC systems. Indeed, a MIMO communication can be established by exploiting the presence of multiple conductors, such as the phase (P), the neutral (N) and the protective earth (E) [34,39,78]. A preliminary analysis of the improvements due to the use of a 2×4 MIMO communication method in the 4–30 MHz band is reported in [79], while [80] considers precoded spatial multiplexing (beamforming) with zero forcing (ZF) detection and [81] describes the MIMO feasibility study, recently extended in [82]. The frequency extension up to 100 MHz and a fair background noise assumption are discussed in [83]. Later, an experimental measurement campaign, that was performed across Europe to collect information about the MIMO PLC channel, has been described in [78, 84], providing some characterization results in [85]. Some further considerations concerning the channel characterization and the spatial correlation analysis within the in-home MIMO PLC scenario were discussed in [86] and [87], respectively. Finally, some details regarding the MIMO PLC channel capacity computation are presented in [88].

Though still understudied, considerable effort is invested in the vehicular environment characterization, especially in recent times. In this respect, probably the most well-known and deeply analyzed scenario is the in-car context, with a sharp distinction among conventional car (CC), fueled by combustion engine, and electric car (EC), powered by a battery. Indeed, CC and EC exhibit several differences due to a different wiring structure, especially concerning the wired part needed for feeding the electric motors, which inject a great deal of noise. Some studies, based on experimental measurement campaigns, that characterize the PLC channel response and the noise of an EC are assessed in [89, 90], while [46] discusses an online available database concerning a CC.

All the previously discussed works focus on the BB-FS, where PLC is typically deployed for high-speed data connectivity. For what concerns the NB-FS, namely below 500 kHz, a detailed channel characterization analysis has been carried out in [91] for the indoor scenario. Looking at the outdoor scenario, the utility companies have fostered the development of low-rate PLC technologies in order to support remote automatic meter reading and network management via command and control applications. These application scenarios represent the perfect context for NB-PLC technologies, that are generally preferred, as proved by the multitude of commercial standards [92, 93].

Besides the channel characteristics, in order to evaluate the performance achieved on PLC networks, e.g. in terms of data throughput, it is of fundamental importance to analyze and assess the noise that affects the considered scenario.

1.3.2 Noise Properties

The PLC networks are affected by several noise components: the stationary (or background) noise and the non-stationary (referred to as impulsive) noise, with both periodic and aperiodic components, which are introduced by noisy loads, switching devices and plug-in/plug-out procedures [3]. That is, the noise is dominated by a mixture of active noise components injected in the network by the loads connected to it. Also the vehicular environment is influenced by noise, especially if considering the electric vehicles, where the drives that control the motors powertrain inject a great deal of noise. Noise impairments for the CC were modeled in [49], taking into account the periodic components, as well as in [94]. Contrariwise, some studies based on experimental measurement campaigns, which characterize the PLC channel response and the noise of an EC, were discussed in [89] and [90]. Furthermore, measurements concerning the background noise observed within the in-ship scenario were carried out in [53, 95].

Non-Stationary (Impulsive) Noise

The impulsive noise can be cyclostationary, with a repetition rate that is equal to, or double, that of the mains period; bursty and cyclostationary, with a repetition rate that is high, namely between 50 and 200 kHz; or aperiodic. The first two components are referred to as periodic noise, synchronous and asynchronous with the mains frequency [96]. The periodic synchronous noise originates from silicon controlled rectifiers (SCR) in devices, while the asynchronous noise is due to the switching activity of power supplies. The characterization, in the time and frequency domain, of the PLC noise can be done by observing it at the receiver port [97] or at the source [98]. The aperiodic noise is the most unpredictable component and it is due to the connection and disconnection of the appliances from the power delivery network. The amplitude of the aperiodic noise can be significantly larger than that of the other impulsive noise components. Beside the amplitude, the aperiodic impulsive noise is typically described by the duration and the inter-arrival time [99]. The statistics of these quantities depends on how the impulsive noise events are identified and measured.

A model for the periodic noise terms that is based on a deseasonalized autoregressive moving average is presented in [100]. The distribution of the amplitude in the time-domain can be fitted by the Middleton's class A [101] or the Nakagami-m distribution [102]. Some further studies reveal that the normal assumption on the noise statistics holds true if the periodic time-variant nature of the noise is accounted for [103], and the impulsive

noise contributions are removed from the measures [104]. In [96] a Markov-chain model is proposed to model the ensemble of components. In [105] the noise at the source is modeled as in [106] and then the noise at the receiver is obtained by filtering it with the channel generated with a top-down channel response generator. In [107] a top-down channel generator is used, instead, to filter the source noise.

Stationary (Background) Noise

The background noise, instead, is a combination of conducted noise and coupled radio signal contributions. Often, the overall noise contribution is estimated by an equivalent average (stationary) Gaussian noise, averaged over a long period of time, providing its PSD profile. The colored exponentially decreasing noise PSD profile can be modeled through a polynomial expression as in [106] for the in-home scenario, or as in [76] for the outdoor LV and MV scenarios.

The noise in the MIMO context has not been thoroughly studied yet. Experimental results in the domestic scenario are reported in [85, 108] and an extension to the 0–100 MHz frequency band with the assumption of colored noise, instead of white noise, is done in [83]. Furthermore, a model to account for the spatial correlation of the noise of a 2×4 MIMO channel is proposed in [109]. While, a MIMO noise PSD profile is modeled according to an exponential function of frequency in [83].

1.4 Modeling and Simulation

The characterization of the PLC channel is very important since it allows the development of effective models and the design of appropriate PHY transmission technologies. The specific properties depend on the application scenario and on the used transmission bandwidth. The models allow generating channel responses that are consistent with the experimental ones, thus are able to fairly reproduce a real communication scenario. Therefore, new developed prototypes or updated standards can be simply tested, in an analytic or numerical way, without the on-field measurements need. This strategy translates into a considerable saving in terms of production times and costs.

The literature reports a variety of PLC channel models, for both the channel impulse response (CIR) and the CFR quantities, but essentially two approaches can be followed, that are referred to as top-down and bottom-up. Initially, deterministic models were developed, but more recently statistical models have been proposed. Obviously, the most investigated environment concerns the domestic premises. However, there are also some examples of channel modeling for the vehicular scenario. In particular, in-car PLC channel models that follow a top-down and a bottom-up approach were described in [47] and [48], respectively. While, the noise impairments were modeled in [49] taking into account the periodic components.

1.4.1 Bottom-Up Approach

The bottom-up approach models the channel transfer function (CTF) between two outlets of a network exploiting the transmission line (TL) theory, under the transverse electromagnetic (TEM) or quasi TEM mode assumption. Therefore, bottom-up modeling offers a tight connection with the physical propagation of PLC signals. Thus, its application requires the knowledge of the network topology in terms of wiring cables and loads.

First attempts in the NB-FS were discussed in [110] for the in-home scenario, and in [111] for the outdoor LV scenario. The literature discusses both time and frequency domain bottom-up approaches. The first relies on the multipath propagation model, describing all the reflection effects that a transmitted signal can encounter [112]. While, the second faces the same propagation problem in frequency domain, basing on the scattering matrix (or S-parameters) [113] or ABCD-matrix [106, 114, 115]. In particular, [106, 113, 114] consider the BB-FS, while [115] discusses the NB-FS exploiting a time-domain validation. Moreover, the ABCD approach allowed also to model the channel periodic time variations by adding a number of time variant loads, as it was done in [116].

In terms of practical usability, the actual CFR among two specific plugs is not of fundamental interest. It is more interesting to have an overall idea of the network behavior in order to design and test novel devices or communication algorithms. Thus, the bottom-up approach can be statistically extended in order to obtain a random channel generator model. A first attempt to use a bottom-up statistical channel generator was presented in [106] for the American indoor scenario, satisfying the National Electric Code (NEC) wiring norms, where an abstract statistical description of a simple topology was made. A more realistic statistical description of in-home networks, through a random channel generator obtained combining a random topology generator algorithm and an efficient channel response computation method, was detailed in [117]. Herein, a voltage-ratio approach was also proposed to efficiently obtain the CTF in complex networks with many nested branches. Instead, the statistics of the in-home channel were inferred in [118] as a function of different network parameters, as wiring structures, size, and loads. In addition, grounding practices, typical of the USA scenario, were modeled in [114], while the time-variance was accounted in [116]. Furthermore, since multiple conductors are available between two nodes, a MIMO communication can be exploited.

Concerning the MIMO scenario, the first use of the multi-conductor TL theory to model a MIMO PLC channel was discussed in [119, 120]. Another MIMO PLC channel model, following a bottom-up approach, was described in [121]. The work in [121] practically extends the two-conductor TL theory channel simulator discussed in [115], that exploits the method of the modal expression for the electrical quantities, to the MIMO transmission scheme. However, although the bottom-up approach is able to faithfully describe a transmission channel, it requires a large amount of information about the

underlying network structure and it is even computationally intensive.

1.4.2 Top-Down Approach

The bottom-up approach limitations represent the primary reasons underlying the choice of the dual approach, referred to as top-down, which is able to overcome these limitations and it is also attractive for its low complexity. In the top-down approach, the channel response is obtained by fitting a certain parametric analytic function with data coming from the experimental measures. Thus, it represents a more phenomenological approach.

One of the first and few examples of NB-PLC channel model, based on measurements, is discussed in [122]. Otherwise, concerning the BB-FS, a deterministic multipath propagation model was firstly proposed in [123] and later improved in [66], where the CFR was modeled taking into account the multipath nature of the signal propagation, as well as the cables losses. The idea of developing a statistical top-down model by introducing some variability in the model in [66] was firstly presented in [124]. Then, the refinement of such a model to fit experimental data from an in-home measurement campaign up to 100 MHz was done in [125]. Concerning the MIMO transmission scheme, one of the first attempts to model a 2×4 MIMO channel, according to a top-down approach, is described in [126]. Furthermore, inspired by [124], a 3×3 MIMO statistical top-down model was presented in [127], basing on actual measurements carried out in France.

Alternative SISO top-down channel models were discussed in [70] and [128], while a simple time-domain multipath random generator for the CIR was presented in [73] via the exploitation of the statistics of the measurements presented in [68]. Recently, it has been shown that also the MIMO PLC channel can be modeled via a set of statistically simulated parameters, as discussed in [88, Chap. 5]. It is therefore foreseen that refined top-down models will be developed in the future.

1.5 Main Contributions and Outline

The purpose of this first part has been to collect the works related to the state-of-the-art in the PLC environment, highlighting the main findings concerning this communication scenario. This is done in order to provide a thorough overview of the main concepts that will be discussed within this thesis. In the following paragraphs, instead, a brief outline of the work is presented, highlighting the main goals and objectives. Then, in Section 1.6, the research papers that we published on scientific journals or conference proceedings, as well as the book contributions, are listed. These papers document the main findings and results carried out during the research activity.

The aim of this thesis is to assess features and performance that concern the PLC technology, considering different communication environments under actual and real constraints. The main purpose is to go beyond the state-of-the-art represented by the existing

scientific works, with the final goal of providing a simple and effective PLC channel model, better than the existing ones. In particular, the published scientific contributions listed in Section 1.6, whose results underlie the content of this thesis, provide new information about the PLC scenario. The intent is to foster the refinement of the existent channel knowledge and the development of updated models, that either follow a top-down or a bottom-up approach.

It is known that the PLC channels exhibit a time-variant behavior [116], that is more pronounced especially at low frequencies, i.e. in the NB-FS. However, within this thesis the focus will be on the BB-FS, namely above 2 MHz, where the channels are less affected by the temporal variation. This is also confirmed by our experimental observations. The same applies for the noise. Hence, the PLC channel, as well as the noise PSD, will be considered as stationary within this work. Furthermore, as a matter of fact, most of the initial part of the work is devoted to assess and compare the properties and the performance of different scenarios, putting them in comparison, accounting on the same assumptions and relying on the same computational procedures.

The analysis is performed considering different measurements databases collected by our laboratory group during the years. In particular, for the in-home scenario, the database of 1266 measurements discussed in [129] has been considered. Concerning the in-home MIMO PLC channel, we contributed to the experimental measurement campaign that was performed by the special task force (STF)-410 across Europe [78], collecting 353 MIMO channel measurements. With reference to the vehicular environment, two different measurement databases were carried out, namely 84 measurements concerning a compact electric car [89], and a total amount of 92 measurements within the in-ship context [54]. Furthermore, measurements were also performed considering the outdoor MV scenario, providing two distinct databases. One consists of 98 measurements and considers the industrial complex where the laboratories of a public company are located, as discussed in [130]. While, the other concerns 122 channel measurements collected in northern Italy in a real-life underground MV scenario [131].

All the above listed databases of experimental channel measures enable a fair and actual comparison among the different environments, providing an overall view about the PLC behavior within different application contexts. In the following, an outline of the structure of this thesis is provided, summarizing the main contents and the concepts that will be detailed in the rest of the work.

Chapter 1: Introduction

In recent decades, PLCs have attracted considerable attention from the research community and industry, as well as from regulatory and standardization bodies. The overall introductory part, discussed at the beginning of this chapter, provides and explains the basics about the power line context, giving an overview of the main concepts that will be

discussed and analyzed in the rest of this work. The preliminary discussion recalls a brief historical outline about the PLC technology and its standardization process. Then, the main possible application contexts are highlighted, making clear and precise references to the most significant scientific works. Furthermore, since the core of this work is devoted to the PLC channel characterization in various environments and different frequency bands, the most relevant contributions concerning this branch are reported, along with a short description of their contents. Another key point of this thesis is the comparison among all the considered scenarios, especially in terms of performance (e.g. of achievable transmission rate). Hence, also the main findings and studies concerning the noise properties are needed and herein summarized. Finally, the detailed study carried out within this work, digging into the PLC channel characterization, has enabled the collection of accurate and precise information with the aim of develop a new simple and effective PLC channel model. Accordingly, the typical strategies, as well as the main scientific contributions, related to the PLC channel modeling, have been summarized.

Chapter 2: Preliminary Definitions

Most of the published scientific works, which are the foundation of this thesis, aim to characterize and analyze the PLC network and channel in different application contexts. In this respect, the same well-known and widely accepted metrics for the statistical analysis have been accounted, namely ACG, RMS-DS, CB and the achievable capacity (throughput). Thus, this chapter it is proposed to summarize and explain, providing an analytic formulation, all these statistical metrics, which will be used and recalled along the entire work. Furthermore, sometimes the method followed to compute certain quantities, such as the CIR, is not always detailed. This renders rather difficult to replicate the measurement setup and to compare the results, as mentioned in Chapter 1. Within this chapter, the procedures for the computation of the physical quantities (metrics) that characterize the channel, starting from the measurements in the frequency domain, are detailed. Lastly, the differences that can be obtained when considering different computation procedures and/or system parameters are highlighted through an example.

Chapter 3: In-Home Scenario

This chapter focuses on the statistical characterization of the PLC channel within the well-known in-home scenario. The detailed study examines a wide set of measured channels in the 1.8–100 MHz frequency band, providing new insights on the relation between the line impedance and the CFR as well as among the channels that share either the transmitter or the receiver outlet. Furthermore, the validity of some results presented in the literature, that are limited to the 30 MHz band, is confirmed. The study comprises the most frequently used statistical metrics, as well as the relation between such quantities.

Moreover, closed-form expressions are provided to model the quantities and their relations. Furthermore, most of the results presented in the literature are not strictly and directly comparable because of some differences in terms of frequency range, network topology and measuring methodology. For instance, the method used to compute the CIR is not always detailed and can change. Thus, it is rather difficult to replicate the measurement setup and to compare the results. This is the reason why a detailed procedure for the computation of the physical quantities (metrics) that characterize the channel from the measurements (in the frequency domain) were herein provided. Finally, the coverage, i.e. the relation between the maximum achievable rate and the distance, as well as the achievable rate gain offered by the bandwidth extension up to 300 MHz, are studied.

Chapter 4: MIMO Extension

The focus is always on the domestic environment, but the attention is turned to the MIMO transmission scheme. The performance improvements provided by the use of precoding schemes in MIMO PLC channels and in the presence of additive colored and correlated Gaussian noise are investigated. A PSD constraint compliant with the HPAV2 standard is assumed, considering a 2×4 Δ-style to star-style MIMO system. Thus, the additional common mode is also exploited at the receiver side. The performance (in terms of capacity) for different power allocation strategies, as well as for the SISO, MIMO and reduced-dimension MIMO configurations, are compared. The results are based on experimental measurements carried out during a measurement campaign across Europe.

Chapter 5: In-Vehicle Scenario

The in-vehicle environment is investigated, where PLCs can provide high-speed data connectivity via the exploitation of the existing power network, with clear potential benefits in terms of cost and weight reduction. The focus is on two scenarios: an electric car and a cruise ship. An overview of the wiring infrastructure and network topology in these two scenarios is provided. The main findings reported in the literature, related to the channel characteristics, are reported. Noise is also assessed with emphasis to the EC context. Then, new results from the statistical analysis of measurements made in a compact EC and in a large cruise ship are shown in terms of average statistical metrics. Finally, an overall comparison is made, highlighting similarities and differences taking into account also the CC, with combustion engine, and the largely investigated in-home scenario.

Chapter 6: Outdoor Scenario

Besides the indoor scenario, there is another environment, even more widespread, where the PLC technology can be successfully applied, namely the outdoor scenario. This is

even more true if the smart grid context is considered, that has gained high momentum especially in the recent years. However, the high amount of applications to be implemented in the smart grid context require bi-directional connectivity between a multitude of nodes with a reliable, high speed, low latency, energy efficient and cost effective communication technology. PLC has the potentiality to meet the requirements. Indeed, there exists space for PLC technology improvements able to overcome the challenges mostly due to a hostile communication medium. There are two considered frequency spectra, namely the NB spectrum (3–500 kHz) and the BB spectrum (1.8–86 MHz), that are exploited by current PLC technology. In this chapter, the usage of these spectra, both in LV and MV networks, are discussed. Pros and cons are highlighted, advocating the realization of an adaptive technology that can cognitively make the best usage of available resources so that the requirements of reliability, latency and coverage can be met.

Chapter 7: Scenarios Comparison

The purpose is to provide an overview of the PLC channel properties for all the previously discussed environments, highlighting strengths and weaknesses. In particular, the main characteristics of both the indoor channel, namely in-home, in-ship and in-car, and the outdoor LV and MV scenarios, are reported and compared. This detailed characterization and comparison is fundamental since the thorough knowledge of the medium properties, as well as the relationships between the most representative channel metrics, allow the development of effective and reliable models. Indeed, as it will be discussed, modeling is a key strategy in order to easily develop and test new standards and devices. Results are provided concerning different available measurement databases, carried out in different countries and scenarios. The focus is on the BB-FS for both indoor and outdoor scenarios.

Chapter 8: Channel Modeling

The increasing amount of data connectivity demand motivates the development of new and effective channel models, able to faithfully describe the communication medium. These models allow to quickly develop and test new devices, allowing a considerable saving in terms of costs and time. Thus, the attention is moved towards the modeling and the emulation of real PLC environments. Differently from the typical models discussed in the literature, which usually consider a SISO scheme, the focus is on the MIMO transmission technique, relying on real channel and noise PSD measurements. In particular, the experimental channels and noise acquisitions were carried out in several in-home PLC scenarios are considered. The aim is to provide an extremely synthetic channel model that follows a purely top-down approach. To this end, the MIMO channel frequency response is expressed in amplitude and phase. The corresponding statistical behavior of these two quantities and their intrinsic relationships, in terms of both frequency and spatial cor-

relation, are assessed. Then, the most commonly used average statistical metrics and the capacity distribution are computed for both the experimental measurements and the simulated channels. The results validate the proposed model as an effective and simple PLC network emulator.

Chapter 9: Beyond Capacity: Security

The confidential data communication over PLC networks is considered. In particular, rather than analyzing cryptographic techniques, the focus is on the security provided at the physical layer, named physical layer security (PLS). Although the PLS has been deeply investigated for wireless systems, it is not the same for the PLC environment. The well-known wireless results are applied to the PLC context, considering the SISO and single carrier case. The differences among conventional capacity and secrecy capacity, as well as between the secrecy capacity achieved on wireless channels (Rayleigh distributed) and PLC channels (log-normally distributed) are highlighted. Both optimal and uniform power allocation strategies are considered. Then, the results are extended to the multicarrier SISO transmission system and to the multiple user (MU) broadcast channel, in the 2–28 Mz band and under additive white Gaussian noise (AWGN). The effects of the typical PLC channel phenomena, such as frequency and MU correlation, as well as the influence of the underlying network structure, in the form of the keyhole effect, are assessed in terms of secrecy rate distribution. To provide experimental evidence, the measurements obtained in an in-home measurement campaign are considered. Also the secrecy rate region for the MU broadcast channel and the average secrecy rate under a quality of service (QoS) constraint, considering both simulated channel realizations and channel measurements are assessed. Finally, the performance improvements attainable with the use of the MIMO transmission scheme, the extended 2–86 MHz band and the beneficial effect of correlated noise are investigated. A comparison between the secrecy rate attained exploiting an alternating optimization (AO) algorithm or an uniform power allocation, as well as with the channel capacity, achieved without secrecy constraints, is also performed. The experimental results are provided relying on measured noise and channel responses.

1.6 Publications

In the following, the main results discussed in this thesis, that have been published on scientific journals, conferences proceedings and technical books, are collected and listed. In particular, [J6] deals with the channel characterization of the in-home SISO channel in the 1.8-100 MHz frequency range. The analysis is extended to the MIMO scheme in [C4]. While, [J4] and [C1] dig into the channel characterization of the in-vehicle scenario,

focusing on car and ship environments, and the outdoor LV and MV networks, respectively. The collected results led to the development of an extremely synthetic channel model discussed in [J2]. The work in [J1], instead, proposes a modeling strategy based on a well-known multipath propagation model, providing its descrying parameters statistics. The secure communication and the PLS concepts concerning the PLC scenario are detailed in [C5], [J7] and [B1] for the single carrier channel, the multicarrier and MU systems, and for the MIMO scheme under colored and correlated noise, respectively.

Journal Papers

J1 A. Pittolo and A. M. Tonello, "In-Home Power Line Communication Model: Statistical Analysis and Numerical Emulation," to be submitted to *IEEE Transactions on Communications*, 2015.

J2 A. Pittolo and A. M. Tonello, "In-Home MIMO PLC Channel: An Extremely Synthetic and Effective Model," to be submitted to *IEEE Communication Letters*, 2015.

J3 C. Cano, A. Pittolo, D. Malone, L. Lampe, A. M. Tonello, and A. Dabak, "State-of-the-art in Power Line Communications: from the Applications to the Medium," submitted to *IEEE Journal on Selected Areas in Communications*, 2015.

J4 A. Pittolo, M. De Piante, F. Versolatto, and A. M. Tonello, "In-Vehicle PLC: In-Car and In-Ship Channel Characterization," in press to *IEEE Vehicular Technology Magazine*, Special Issue on the State of the Art in Propagation and Mobile Channel Modeling, 2014.

J5 A. M. Tonello, A. Pittolo, and M. Girotto, "Power Line Communications: Understanding the Channel for Physical Layer Evolution Based on Filter Bank Modulation," *IEICE Transactions on Communications*, vol. E97-B, no .8, pp. 1494–1503, August 1, 2014.

J6 A. M. Tonello, F. Versolatto, and A. Pittolo, "In-Home Power Line Communication Channel: Statistical Characterization," *IEEE Transactions on Communications*, vol. 62, no. 6, pp. 2096–2106, June 2014.

J7 A. Pittolo and A. M. Tonello, "Physical layer security in power line communication networks: an emerging scenario, other than wireless," *IET Communications*, vol. 8, no. 8, pp. 1239–1247, May 22, 2014.

Conference Papers

C1 A. M. Tonello and A. Pittolo, "Considerations on Narrowband and Broadband Power Line Communication for Smart Grids," in *Proc. of 6th IEEE International Conference on Smart Grid Communications (SmartGridComm)*, November 2015.

C2 A. Pittolo and A. M. Tonello, "New Results in Channel Modelling," in *Proc. of 9th Workshop on Power Line Communications (WSPLC)*, October 2015.

C3 A. Pittolo and A. M. Tonello, "Physical Layer Security in MIMO-ME PLC Networks with Alternating Optimization," in *Proc. of Workshop on Communication Security (WCS)*, Ancona, Italy, September 11-12, 2014.

C4 A. Pittolo, A. M. Tonello, and F. Versolatto, "Performance of MIMO PLC in Measured Channels Affected by Correlated Noise," in *Proc. of 18th IEEE International Symposium on Power Line Communications and its Applications (ISPLC)*, March 2014, pp. 261–265.

C5 A. Pittolo and A. M. Tonello, "Physical Layer Security in PLC Networks: Achievable Secrecy Rate and Channel Effects," in *Proc. of 17th IEEE International Symposium on Power Line Communications and its Applications (ISPLC)*, March 2013, pp. 273–278.

Book Chapters

B1 A. Pittolo and A. M. Tonello, "Physical Layer Security in Power Line Communication Networks," in *Physical and Data-Link Security Techniques for Future Communication Systems*, ser. Lecture Notes in Electrical Engineering, M. Baldi and S. Tomasin, Eds. Springer International Publishing, 2016, vol. 358, pp. 125–144.

Preliminary Definitions

2

This chapter summarizes the quantities, the main statistical metrics and the most common statistical tests that have been used along the entire work. In particular, in Section 2.1 the CFR, the line impedance and the CIR are introduced. Typically, in the past, the available databases and the channel measurements were provided in the time domain. However, especially in recent time, the frequency domain acquisition is largely used and preferred since it enables to carry out both channel and impedance measurements. Since, as seen, the CIR properties depend on the computational method, within this section a detailed calculation procedure is described. Moreover, an example on how and how much the computational method and the system parameters choice affects the CIR is discussed. Different types of correlation quantities are also defined, namely the frequency, the MU and the spatial correlation functions. Then, Section 2.2 provides a concise description of the most commonly used statistical metrics, namely the ACG, the RMS-DS, the CB and the maximum achievable rate (or capacity). The concept of geometrical distance in the PLC context is also discussed. Finally, the main statistical tests that have been used in order to study the PLC channel, i.e. the log-likelihood and the q-q plot, are presented in Section 2.3.

2.1 Network Quantities

A PLC system can be easily modeled as a two-port network between the transmitter and the receiver sides, as depicted in Figure 2.1. In the following, the main quantities that will be analyzed and investigated along the rest of this thesis, such as the CFR, the line impedance and the CIR, as well as the channel properties as the frequency, the MU and the spatial correlation, are defined and discussed. Typically, the frequency domain is considered. Thus, for the rest of this work f, $f_1 > 0$, $f_2 > 0$ and B denote the continuous frequency, the start and the stop signaling frequencies, and the transmission bandwidth, respectively.

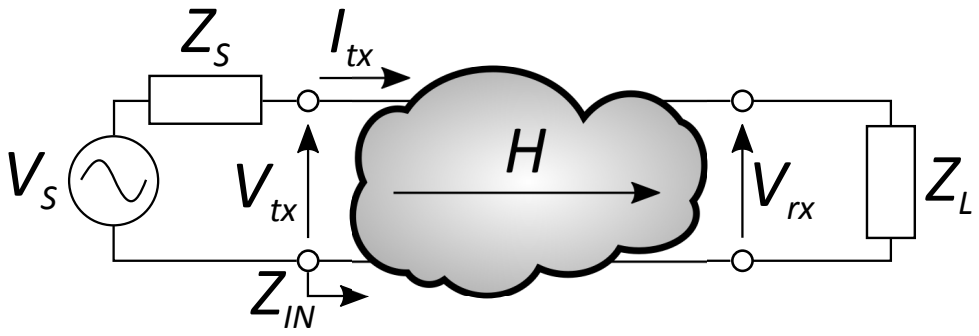

Figure 2.1: Schematic representation of a typical power delivery network.

2.1.1 Channel Frequency Response

With reference to the scheme shown in Figure 2.1, the CFR at the f-th frequency is defined as the ratio between the voltage at the receiver outlet $V_{rx}(f)$ and the voltage at the transmitter outlet $V_{tx}(f)$. Thus, it is given by

$$H(f) = \frac{V_{rx}(f)}{V_{tx}(f)}. \tag{2.1}$$

The CFR can be expressed in real plus imaginary part, but sometimes it is more convenient to represent it in magnitude (or amplitude) and phase terms, as follows

$$H(f) = A(f)e^{\varphi(f)}, \tag{2.2}$$

where $A(f) = |H(f)|$ is the amplitude, while $\varphi(f) = \angle H(f)$ represents the phase at frequency f. Sometimes, $A(f)$ is referred to as CTF, which is usually provided in dB scale as $A_{dB}(f) = 10\log_{10} A(f)$. Moreover, also the path loss (PL) can be defined as $\mathcal{L}(f) = |H(f)|^2$, with the corresponding dB version given by $\mathcal{L}_{dB}(f) = 10\log_{10}\mathcal{L}(f)$.

Although it is desirable, unfortunately the voltage at the transmitter port is not equal to that at the source port, provided by the generator. Thus, the ratio between the source voltage $V_s(f)$ and $V_{rx}(f)$ is given by

$$H_s(f) = \frac{V_{rx}(f)}{V_s(f)}, \tag{2.3}$$

and in general, $H_s(f) \neq H(f)$. Anyway, the two quantities can be related through the line impedance, defined in the following.

2.1.2 Line Impedance

The line impedance is the load seen by the transmitter side. It is defined as the ratio between the voltage and the current at the transmitter port, formulated as

$$Z_{IN}(f) = \frac{V_{tx}(f)}{I_{tx}(f)}, \tag{2.4}$$

where $I_{tx}(f)$ is the current at the transmitter port, as shown in Figure 2.1. Contrariwise the CFR, the line impedance is usually expressed in real (resistive) plus imaginary (reactive) part, so that it reads $Z_{IN}(f) = R(f) + jX(f)$.

Typically, the line impedance is computed referring to a 50 Ω source (Z_S) and load (Z_L) impedances at the transmitter and receiver sides, respectively. This is because the network analyzer, which is commonly used for the network parameters measurement (e.g. the scattering matrix S), has a built-in 50 Ω impedance at each of its ports.

Usually, a finite number of frequency points is available due to the precision of the measuring instrumentation. Thus, sometimes, a discrete-frequency representation of the above mentioned quantities is more convenient, especially for a computational implementation. The discrete frequency index m indicates the frequency $f = m\Delta f$, where $m = 0, 1, \ldots$ and Δf is the resolution in frequency. Furthermore, $f_1 = M_1\Delta f$, $f_2 = M_2\Delta f$, with a total number of samples equal to $M = M_2 - M_1$.

2.1.3 Channel Impulse Response

The real CIR is obtained from the CFR by means of processing, i.e., by windowing the CFR, applying an inverse discrete Fourier transform (IDFT), and truncating the less significant tails. In detail, the procedure that we adopt is detailed in the following.

1. First, the focus is on the CFR in the frequency range from 0 to f_2. The CFR is defined in the discrete-frequency domain and the number of CFR samples is M_2+1. From 0 to f_1, the CFR is set equal to zero. Since the CIR is real, the CFR is supposed to be Hermitian, hence its positive spectrum, from 0 to f_2, has been extended to the negative part of the spectrum, between $-f_2$ and 0, by applying the Hermitian symmetry. This leads to $2M_2 + 1$ frequency samples.

2. At this step different types of low-pass or band-pass filers can be applied, for example a raised-cosine filter. The use of this kind of filter enables reducing the side-lobe effect that will be introduced by the inverse Fourier transform [132]. However, we chose not to introduce any kind of filtering in order to obtain results that are comparable to those obtained by other published works. Hence, in practice, it is like applying a rectangular window.

Table 2.1: Average RMS-DS for different transmission bands and threshold coefficients.

Band (MHz)	$\alpha_{\mathcal{E}}$	σ_τ (μs) min	mean	max
0–30	1	0.133	1.257	5.360
	0.98	0.030	0.942	5.294
	0.9	0.008	0.574	5.002
1.8–30	1	0.114	0.581	1.825
	0.98	0.033	0.394	1.524
	0.9	0.012	0.278	0.957
0–100	1	0.114	1.153	5.284
	0.98	0.018	0.842	5.210
	0.9	0.002	0.500	4.909
1.8–100	1	0.056	0.502	1.613
	0.98	0.017	0.337	1.280
	0.9	0.001	0.239	0.926

3. Then, the IDFT of the CFR is computed to obtain the real CIR at time instant $t = nT$, namely $h(n)$, where $n = 0, \ldots, N$, with $N = 2M_2$. The resolution in time is denoted with T. The CIR is defined in the discrete time domain with temporal resolution $\Delta t = 1/[(N+1)\Delta f]$.

4. To cut the tails introduced by the IDFT we proceed as follows. Firstly, the pulse is shifted in order to bring the anti-causal tails introduced by the IDFT to the beginning of the CIR. Then, the normalized cumulative pulse energy is computed as $\mathcal{E}_C(n) = \sum_{k=0}^{n} |h(k)|^2 / \sum_{k=0}^{N} |h(k)|^2$. Finally, we set $h(n) = 0 \ \forall \ n$ subject to $\mathcal{E}_C(n) \leq (1-\alpha_{\mathcal{E}})/2$ or $\mathcal{E}_C(n) \geq \alpha_{\mathcal{E}} + (1-\alpha_{\mathcal{E}})/2$. In the analysis carried out in this thesis, the value $\alpha_{\mathcal{E}} = 0.98$ is used.

Practically, with the last step the side lobe effects are reduced by cutting the CIR tails as follows. Given the channel energy, computed as

$$\mathcal{E} = |H(0)|^2 + 2\Delta f \sum_{m=M_1}^{M_2} |H(m)|^2, \tag{2.5}$$

the CIR is limited to the one that includes the 98 % of the channel energy.

The definition of a detailed procedure is motivated by the fact that processing affects the results and, in turn, the statistics of the metrics that are computed from the CIR. As an example, Table 2.1 reports the minimum, mean and maximum value of the RMS-DS (defined in Section 2.2.2) computed from impulse responses obtained with different processing procedures. As it can be noted, the RMS-DS becomes larger when the bandwidth decreases. Besides, it drastically increases when the lower frequencies in the 0–1.8 MHz band are considered for its computation. This leads to values that are approximately twice those obtained considering the same spectrum without the frequencies below the

1.8 MHz. This happens because when the very low frequencies are considered, the CIR duration increases due to the long temporal modes influence, which are introduced by the non-negligible low frequency coefficients. That CIR behavior involves a greater energy dispersion, translating into a higher RMS-DS. Furthermore, as intuition suggests, the RMS-DS decreases when less channel energy is accounted by the CIR, due to the tail cut operation ($\alpha_{\mathcal{E}}$ factor). In this respect, the case $\alpha_{\mathcal{E}} = 1$ shows that the side lobes introduced by the rectangular window, applied in frequency, corrupt the RMS-DS calculation.

2.1.4 Frequency Correlation

In order to obtain a detailed and comprehensive channel characterization, also the intrinsic medium dependencies, e.g. among frequencies, or between the different communication links belonging to the same network, need to be assessed. Towards this end, the evaluation of the frequency correlation plays a fundamental role.

The statistical auto-correlation function (SAF) of the CFR is defined as

$$\Phi(f, \lambda) = E\left[H(f)H^*(\lambda)\right], \tag{2.6}$$

where $\{\cdot\}^*$ is the complex conjugate and $E[\cdot]$ denotes the expectation operator w.r.t. the available measurements. However, especially for the generation process, the auto-covariance function is considered. This is since it enables to directly generate correlated variables with the proper variance. The CFR covariance function, that shows the strength of the linear relation among the considered quantities, resembles the SAF expression in (2.6), but without the bias of the CFR mean value, and is given by

$$\mathcal{K}(f, \lambda) = E\left[\left(H(f) - m_H(f)\right)\left(H(\lambda) - m_H(\lambda)\right)^*\right], \tag{2.7}$$

where $m_H(f) = E[H(f)]$ is the mean value of the CFR at the f-th frequency. However, in order to better magnify the degree of correlation exhibited by the involved quantities, the normalized covariance function is used, which is defined as

$$\dot{\mathcal{K}}(f, \lambda) = \frac{E\left[\left(H(f) - m_H(f)\right)\left(H(\lambda) - m_H(\lambda)\right)^*\right]}{\sigma_H(f)\sigma_H(\lambda)}, \tag{2.8}$$

where $\sigma_H(f)$ is the standard deviation of the CFR at the frequency f. The values assumed by $\dot{\mathcal{K}}$ are limited within the range $[0, 1]$, where 0 stands for no correlation, while 1 means completely correlated. This facilitates the understanding of the degree of the exhibited correlation. Typically, the above mentioned functions are represented through a matrix formulation, with f and λ being the row and column matrix indexes, respectively, while the elements represent the Pearson product-moment correlation coefficient (or linear correlation) among the corresponding CFRs. Potentially, the knowledge of the

SAF can allow to model the channel in a certain frequency band as a vector of correlated random variables with a given correlation. This is what it will be discussed in Chapter 8.

2.1.5 Multiple Users Correlation

PLC channels, associated to different pairs of outlets of the same site, may share part of the signal path, namely the backbone, because the propagation takes place on the same electrical circuit. Thus, they are supposed to experience similar reflection effects. In this respect, the aim is to verify whether channels of the same site, or that share the transmitter or the receiver outlet, are correlated. This information is fundamental when more than two nodes are involved in the communication, e.g., to study realistic multiple user schemes or relaying techniques.

Towards this end, the space-frequency MU correlation function is defined. This unusual terminology is used to distinguish this type of correlation from the spatial correlation, which refers to the correlation between the possible transmitting and receiving wires, as described in Section 2.1.6. Indeed, there is a slightly, but significant, difference. Both the correlation functions concern different communication links, but the spatial correlation is referred to the wires belonging to the same bundle of cables, namely phase, neutral and protective earth. These cables connect the same transmitter and receiver outlets and are usually exploited to implement a MIMO transmission scheme in the PLC scenario. While, the MU correlation identifies the correlation between different SISO communication links, belonging to the same network, but having different transmitter or receiver outlets, or even both.

Similarly to (2.8), the normalized MU covariance function can be defined as follows

$$\psi(f,\lambda) = \frac{E_{i,j}\left[\left(H_i(f) - m_{H_i}(f)\right)\left(H_j(\lambda) - m_{H_j}(\lambda)\right)^*\right]}{\sigma_{H_i}(f)\sigma_{H_j}(\lambda)}, \tag{2.9}$$

where $i \neq j$ and the expectation in i, j (i.e. the measurements indexes) is across the channel realizations of the same site. As it can be noted, the value of ψ has not only a frequency dependence, but it is also influenced by the set of considered channels, e.g. that share the same transmitter, or receiver, or none, as it will be assessed in Section 3.4.

2.1.6 Spatial Correlation

Since the electrical power network of nearly all dwellings consist of three different wires, namely phase, neutral and protective earth, a MIMO transmission scheme can be implemented. Thus, in this case, the evaluation of the spatial correlation between the different wires highlights connections and dependencies that allow a better channel understanding, and hence the improvement of the communication medium exploitation.

The expression of the normalized spatial covariance function is similar to the expression in (2.9), but with some differences. It is defined as

$$\chi_{\ell,p}(f) = \frac{E\left[\left(H_\ell(f) - m_{H_\ell}(f)\right)\left(H_p(f) - m_{H_p}(f)\right)^*\right]}{\sigma_{H_\ell}(f)\sigma_{H_p}(f)}, \tag{2.10}$$

where $\ell \neq p$ and with ℓ and p referring to the different possible transmitting and receiving modes, respectively, that are related to the three deployed cables. In this case the mean is performed among all the realizations within the same site and for the same frequency f. The meaning of this quantity will be clarified in Section 4.1.3, where the spatial correlation among the MIMO transmitting and receiving modes is assessed.

Alternatively, the spatial correlation can also be computed for a single MIMO channel, rather than for a set of measurements, which is more related to a given environment. In this case, the average is performed over the frequency samples of the considered MIMO CTF and not on the set of different measurements. However, the PL should be normalized in order to obtain proper results, as it has been discussed in [87]. In this thesis, the first definition, computed as in (2.10), has been used since it provides the average correlation value among all the different transmission and reception modes at each frequency sample. This quantity, in our opinion, is more representative of the phenomena that occur in a typical PLC scenario, which is what we aim to characterize. Moreover, the expression in (2.10) is able to capture all the fluctuations over the frequency domain, unlike the correlation computed relying on a single MIMO channel.

2.2 Statistical Metrics

In the following, the most common and used metrics, that provide a statistical characterization of the PLC channel, namely ACG, RMS-DS, CB and maximum achievable rate, are described. In particular, the ACG and the CB are computed relying on the CFR, while the RMS-DS is calculated from the CIR. Furthermore, the concept of channel capacity, as well as the meaning of geometrical distance, are also introduced.

2.2.1 Average Channel Gain

The ACG is a scalar metric that describes the average attenuation, averaged along frequencies, of the channel. Typically, the ACG in dB scale is used, which is defined as

$$\mathcal{G} = 10\log_{10}\left(\frac{1}{B}\int_{f_1}^{f_2} |H(f)|^2 df\right) \quad \text{[dB]}, \tag{2.11}$$

when the bandwidth B, between f_1 and f_2, is considered. Often, the discrete-frequency representation of the CFR is used, which is computed as follows

$$\mathcal{G} = 10\log_{10}\left(\frac{1}{M}\sum_{m=M_1}^{M_2}|H(m)|^2\right) \quad [\text{dB}], \tag{2.12}$$

In [74], an alternative definition of the ACG is provided as the mean of the dB-version of the CFR. From the literature, it has been shown that $\mathcal{G}$ is expected to be normally distributed [72]. This result is confirmed in Section 3.2.1.

2.2.2 RMS Delay Spread

The RMS-DS accounts for the energy dispersion of the CIR. It is computed relying on the power delay profile (PDP) that is calculated from the CIR as

$$\mathcal{P}(t) = \frac{|h(t)|^2}{\int_0^D |h(u)|^2 du} \quad [\text{s}^{-1}], \tag{2.13}$$

where D represents the duration of the CIR. If the CIR is not limited, D goes to infinity. Hence, the RMS-DS is defined as

$$\sigma_\tau = \sqrt{\int_0^D t^2\mathcal{P}(t)dt - \left(\int_0^D t\mathcal{P}(t)dt\right)^2} \quad [\text{s}]. \tag{2.14}$$

Usually, the RMS-DS is computed basing on the CIR evaluated through the IDFT of the CFR in the discrete-frequency domain. Thus, the discrete-time expression of the RMS-DS reads

$$\sigma_\tau = T\sqrt{\sum_{n=0}^{N}(n)^2\mathcal{P}(n) - \left(\sum_{n=0}^{N}n\mathcal{P}(n)\right)^2} \quad [\text{s}], \tag{2.15}$$

In the literature, it has been shown that the RMS-DS of the PLC channel can be modeled as a log-normal random variable [72]. From experimental observations, the validity of such a model is confirmed in Section 3.2.1.

2.2.3 Coherence Bandwidth

The CB can be defined starting from two different correlation functions. A first approach is to use the deterministic auto-correlation function (DAF) of the CFR, as

$$\mathcal{R}(\lambda) = \int_{f_1}^{f_2} H(f+\lambda)H^*(f)df, \tag{2.16}$$

where $\{\cdot\}^*$ denotes the complex conjugate operator and $H(f) = 0$ outside the frequency range $[f_1, f_2]$. The discrete-frequency version of (2.16) is given by

$$\mathcal{R}(k) = \Delta f \sum_{m=M_1}^{M_2} H(k+m)H^*(m). \tag{2.17}$$

Hence, the CB at level ξ, namely $\mathcal{B}_C^{(\xi)}$, is the frequency λ_ξ beyond which the absolute value of $\mathcal{R}$ falls to a value that is ξ times (with $\xi < 1$) its maximum, i.e.,

$$\mathcal{B}_C^{(\xi)} = \lambda_\xi \quad \text{such that} \quad |\mathcal{R}(\lambda_\xi)| = \xi|\mathcal{R}(0)|. \tag{2.18}$$

The average CB, namely $\overline{\mathcal{B}}_C^{(\xi)}$, is obtained by averaging $\mathcal{B}_C^{(\xi)}$ across the ensemble of channels, i.e. $\overline{\mathcal{B}}_C^{(\xi)} = E[\mathcal{B}_C^{(\xi)}]$.

Another approach is to compute the CB from the CFR SAF, which is defined in (2.6), as formally done in [133]. In the presence of uncorrelated scattering, which is a typical situation in wireless communications, $\Phi(f, \lambda)$ is a function of the difference $\Delta = f - \lambda$. In the PLC scenario this assumption does not apply, therefore, similarly to [125], the averaged correlation function can be defined as

$$\overline{\Phi}(\lambda) = \int_{f_1}^{f_2} \Phi(f, \lambda) df. \tag{2.19}$$

In this case the CB, referred to as $\hat{\mathcal{B}}_C^{(\xi)}$, can be computed as in (2.18) by substituting $\mathcal{R}(\lambda)$ with $\overline{\Phi}(\lambda)$.

Differently from (2.6), (2.16) is specific to a given channel realization and it is only a function of the frequency difference λ. In order to distinguish the two different methods, $\mathcal{B}_C^{(\xi)}$ is referred to as deterministic CB, while $\hat{\mathcal{B}}_C^{(\xi)}$ as statistical CB. For example, the statistical CB was used to fit the model in [125] to the measures. Some experimental works, e.g. [71], deal with the deterministic CB because the number of acquisitions does not allow for the expectation computation in (2.6). A numerical comparison between $\hat{\mathcal{B}}_C^{(\xi)}$ and $\overline{\mathcal{B}}_C^{(\xi)}$ is reported in Section 3.2.2. In this respect, it can be noted as the two quantities are, in general, different.

2.2.4 Maximum Achievable Rate

In order to provide an overall scalar quantity that synthesizes the performance obtainable on a PLC network, the maximum achievable rate, namely the capacity, is used. Under the assumption of a normally distributed transmitted signal and a stationary additive Gaussian noise, which is in general colored on PLC networks, the Shannon capacity reads

$$\mathcal{C} = \int_{f_1}^{f_2} \log_2 \left(1 + \frac{P_t(f)|H(f)|^2}{P_w(f)}\right) df \quad \text{[bps]}, \tag{2.20}$$

where $P_t(f)$ and $P_w(f)$ are the transmitted signal and the noise PSD values at frequency f, respectively. While, the discrete-frequency capacity expression is given by

$$\mathcal{C} = \Delta f \sum_{m=M_1}^{M_2} \log_2 \left(1 + \frac{P_t(m)|H(m)|^2}{P_w(m)}\right) \quad \text{[bps]}. \tag{2.21}$$

The maximum achievable rate is widely deployed in the literature, though, in most of the cases, simplified noise models are used. In [70] and [73], the noise is assumed to be white, with a PSD of -140 dBm/Hz and -120 dBm/Hz, respectively. Some other papers, instead, account for the colored nature of the noise, as in [83]. Finally, it should be noted that the actual PHY data rate can differ from the capacity estimated by (2.20) due to the following reasons.

- The Shannon gap, which accounts for the modulation scheme non-idealities, is not taken into account.
- The transmission header or the hardware impairments are not considered.
- Not all the noise disturbances, such as the impulsive noise or the NB and frequency modulation (FM) broadcast radios, are accounted.

2.2.5 Geometrical Distance

Typically, with distance it is intended the euclidean norm between the three-dimensional coordinates of the transmitter and the receiver outlets that, in general, do not correspond to the length of the backbone, i.e. the shortest signal path (or cable) that connect the pair of outlets. The three dimensions are required because the sites can consist of multiple floors. In this thesis, the geometrical distance between the transmitter and the receiver outlet is simply referred to as distance and denoted with $\mathcal{D}$.

2.3 Statistical Tests

Beside the previously described statistical metrics, other more classical statistical tools can be exploited in order to infer the distribution of a CFR. In this respect, the likelihood and the quantiles plot methods are used in order to assess the statistics exhibited by the quantities under test. These are the most commonly used methods that enable a quick and effective way to provide the statistical behavior of a quantity.

2.3.1 Likelihood

In this thesis, in order to assess the distribution of the measured CFR amplitude, the data measurements are fitted with the most common and well-known distributions, such as,

exponential, Gamma, log-normal, normal, Rayleigh, Weibull and log-logistic. In order to provide a comparative result between the various distributions, that allows to determine which one is the best, the maximum likelihood estimates of the distribution parameters are taken into account. The likelihood function is computed as [134, Chap. 2]

$$\Lambda(\theta) = \prod_{x \in \mathbb{X}} p(x|\theta), \tag{2.22}$$

where $x \in \mathbb{X}$ is the set of measured samples, $p(\cdot)$ is the probability density function (pdf) of the fitting distribution and θ represents the parameters of the fitting distribution, that were obtained by the estimation. The higher the likelihood function value in (2.22), the better the parameters fit the measured distribution. The limits of (2.22), when dealing with models having different complexities, namely that are described with a different number of parameters, are neglected. Typically, the analysis is performed as a function of frequency and considering the logarithmic value of the function in (2.22), namely the log-likelihood.

2.3.2 Q-Q Plot

In statistics, the quantile-quantile (q-q) plot is a graphical technique for determining if two data sets come from populations that have a common distribution. The q-q plot is a plot of the quantiles of the first data set against the quantiles of the second data set, where quantile means the fraction (or percentage) of points below a given value. In particular, a k-th q-quantile for a random variable is a value x such that the probability that the random variable will be less than x is at most k/q. An example of the q-q plot usage is discussed in Section 3.2.1.

3 In-Home Scenario

As stated in Section 1.1.1, we have assisted at the development of increasingly powerful and performing PLC devices, which exploit advanced modulation techniques. Especially in recent years, PLCs have gained success as a valuable solution to deliver high-speed multimedia content through the existent wiring infrastructure. However, further improvements require a detailed knowledge of the communication medium. In this respect, the statistical characterization of the PLC channel is of fundamental importance.

In the literature, a lot of effort has been spent on this topic. However, unfortunately, many of the proposed results are not strictly comparable because of some differences. For instance, [70] considers the bands 0.03–100 MHz and 2–100 MHz, [72] and [73] the band 1.8–30 MHz, while [74] the band 2–30 MHz. Furthermore, the method used to compute the CIR is not always detailed. Thus, it is rather difficult to replicate the measurement setup and to compare the results in terms, for instance, of RMS-DS. In this chapter, the aim is to provide a detailed procedure for the computation of the physical quantities (metrics) that characterize the channel starting from the measurements in the frequency domain. Hence, the statistical analysis of a large set of in-home PLC channels, that we measured in Italy (ITA), is presented. The results are compared to those provided in the literature, highlighting, when necessary, the differences in the setup. The focus is on the 1.8–100 MHz frequency range because this is the band of interest of current and next-generation PLC standards and devices. A further analysis, beyond 100 MHz and up to 300 MHz, is provided in order to quantify the potentiality of the bandwidth extension in terms of achievable rate improvement. The final goal of this characterization work is to provide new information about the PLC channel, in order to foster the refinement of the existent models that either follow a top-down or a bottom-up approach.

We collected a database of nearly 1300 channel responses in different premises, performing measurements in the frequency domain up to 300 MHz. Some preliminary results of the CFR analysis were reported in [135], [129]. Namely, in [135], the relation between the channel statistics and the physical distance, between the transmitter and the receiver

outlet, was presented. The work focused on the 2–100 MHz frequency band. Instead, in [129], some partial results concerning the statistics of the channel response and the line impedance were discussed. In this chapter, a more comprehensive analysis and a reconciliation of previous results are reported. Compared to previous contributions, the main advances to the knowledge of the PLC channel with this work can be summarized as follows.

- The statistics of the amplitude of the CFR is studied up to 100 MHz. The distribution that best fits (among the known ones) the measured CFR amplitudes is studied, and a closed-form expression for the mean and the standard deviation distributions is provided, as a function of frequency.

- The ACG, the RMS-DS, the CB and their relations are studied in the band 1.8–100 MHz. The main reported findings concern the relation between the ACG and the RMS-DS, and between the CFR phase slope and both the ACG and the RMS-DS, as well as the frequency behavior of the statistical CB. Furthermore, the two CB definitions, referred to as statistical and deterministic CB, are assessed and compared. As seen in Section 2.2.3, they are obtained from the study of different correlation functions of the CFR. In particular, the introduction of the statistical CB is motivated by the work in [125], where the quantity is exploited to fit a top-down model. In addition, the frequency correlation exhibited by the channel measurements is also assessed.

- The maximum achievable rate dependencies on the frequency band and on the distance between the end nodes are shown. In this respect, it should be noted that the distance is defined in terms of difference between the position of the transmitter and receiver outlet, as discussed in Section 2.2.5, and, in general, it does not match with the length of the path followed by wirings.

- The MU correlation discussed in Section 2.1.5, i.e., the correlation between the channels connecting different outlet pairs of the same network, is investigated. Several quantities are considered, i.e., the correlation between channels of the same site, the correlation between the channels that share the same transmitter outlet and the correlation between the channels that share the same receiver outlet. To remove the randomization due to the phase, the last two quantities are evaluated considering only the amplitude of the CFR.

- The line impedance behavior, discussing both resistive and reactive components, is assessed. A statistical characterization of these two quantities is also provided. Furthermore, the relation between the CFR and the line impedance is investigated, detailing a method to determine the high probability regions in the scatter plots of the line impedance real and imaginary parts.

- In order to facilitate the comparison of the measured data, and following the spirit of replicable research, closed-form expressions are provided to model the statistical quantities and their relations. Furthermore, a script is made available on-line [136]. The script computes the CIR and the main statistical metrics from the measures of the CFR. The aim is to share a common tool that may allow for future comparisons.

The analysis that follows is time-invariant. The PLC channel exhibits, in general, a linear and periodically time variant behavior [137–139], but, from the experimental observations, we found that the time-dependency is not pronounced in the considered frequency band. This finding is validated by other experimental results, e.g., [140], where it was shown that channel time variations are mostly experienced below 2 MHz. Therefore, in the following, the channel is assumed to be stationary without loss of generality.

The chapter is organized as follows. Section 3.1 provides some details concerning the measurement campaign. In Section 3.2, the channel characterization and its properties, as well as the main statistical metrics distribution and their relationships, are assessed and compared. Furthermore, Section 3.3 discusses the performance achievable on the in-home PLC channel in connection with the geometrical distance and the improvements due to the bandwidth extension. Moreover, Section 3.4 analyzes the MU correlation exhibited by the channels when considering the same site, the same transmitter, or the same receiver outlet. Finally, Section 3.5 describes the line impedance characteristics and statistical behavior.

3.1 Measurement Campaign

We performed an experimental measurement campaign in Italy on single-phase in-home networks. Three sites were considered as representatives of small flats and detached houses of the urban and suburban scenario. The area of the sites ranges between 50 and 200 m^2. For each site, all the available outlets were considered to provide a comprehensive view. In this respect, we did not limit the set of outlets to those that were considered most probable for a PLC transmission, as for instance, it was done in [70].

Measurements were carried out in the frequency domain with an Agilent E5061B vector network analyzer (VNA). The transmit power was set to 10 dBm. Multiple acquisitions were performed on different band portions in order to keep the maximum resolution in frequency, given the fixed number of samples acquired by the instrument. Couplers were used to protect the equipment from the mains and extension cables, with characteristic impedance of 50 Ω, enabled to assess distant outlets. The couplers are BB high-pass filters and they exhibit an attenuation lower than 5 dB up to 100 MHz. The effects given by the couplers and the cables were removed by measuring first their ABCD matrix and then deconvolving them from the overall measurement. For further details concerning the measurement setup the reader is referred to [141].

For each channel, 16 subsequent acquisitions were averaged to obtain the actual scattering (S) parameters. From experimental observations, 16 acquisitions were sufficient to cope with noise impairments. From the S-parameters, the CFR, and the line impedance were obtained. A total number of 1266 acquisitions were carried out. A discrete-frequency representation is used according to the fact that the VNA acquires a finite number of points, regardless the frequency span. The index m denotes the frequency sample $f = m\Delta f$, where Δf is the resolution in frequency. Unless otherwise stated, the start and stop frequencies are denoted with $f_1 = M_1\Delta f = 1.813$ MHz and $f_2 = M_2\Delta f = 100$ MHz. For the 1.8–100 MHz frequency range $\Delta f = 62.5$ kHz, $M_1 = 29$ and $M_2 = 1600$. Acquisitions beyond 100 MHz and up to 300 MHz were also performed and are discussed in Section 3.3.3. In this case, $f_1 = 1.875$ MHz, with $\Delta f = 187.5$ kHz, $M_1 = 10$ and $M_2 = 1600$.

3.2 Channel Properties

In this section, the results of the channel characterization are reported basing on the metrics definition and the statistical tests detailed in Section 2.2 and Section 2.3, respectively. Unless otherwise specified, the study is limited to the frequency range between 1.8 and 100 MHz, namely the band of interest of current and next generation PLC systems. Firstly, the focus is on the channel attenuation, then the channel phase slope and its relationships are assessed.

3.2.1 Statistical Tests

Herein, the statistical behavior of the CFR amplitude, in linear scale, is investigated. The distribution of the measured amplitudes is fitted with the most common and well-known distributions, namely, exponential, Gamma, log-normal, normal, Rayleigh, Weibull and log-logistic. Basically, for each distribution, the maximum likelihood estimates of the distribution parameters is obtained through the computation of the likelihood function as in (2.22). The higher the values assumed by the likelihood function in (2.22), the better the parameters fit the measured distribution.

The analysis is performed as a function of frequency and the values of the logarithmic version of (2.22), obtained with the set of the distribution parameters that yields the best fit, are reported in Figure 3.1. The log-normal distribution provides the highest likelihood value almost in the entire frequency range, i.e., a result that was already mentioned in [129]. Only the few low frequencies, between 1.8 and 2 MHz, are better fitted by the Weibull distribution, which gets a slightly higher score. However, also other statistical distributions besides the Weibull one, such as log-logistic and gamma, obtain similar scores. This is due to their pdf shape, which is very similar, with the main differences limited

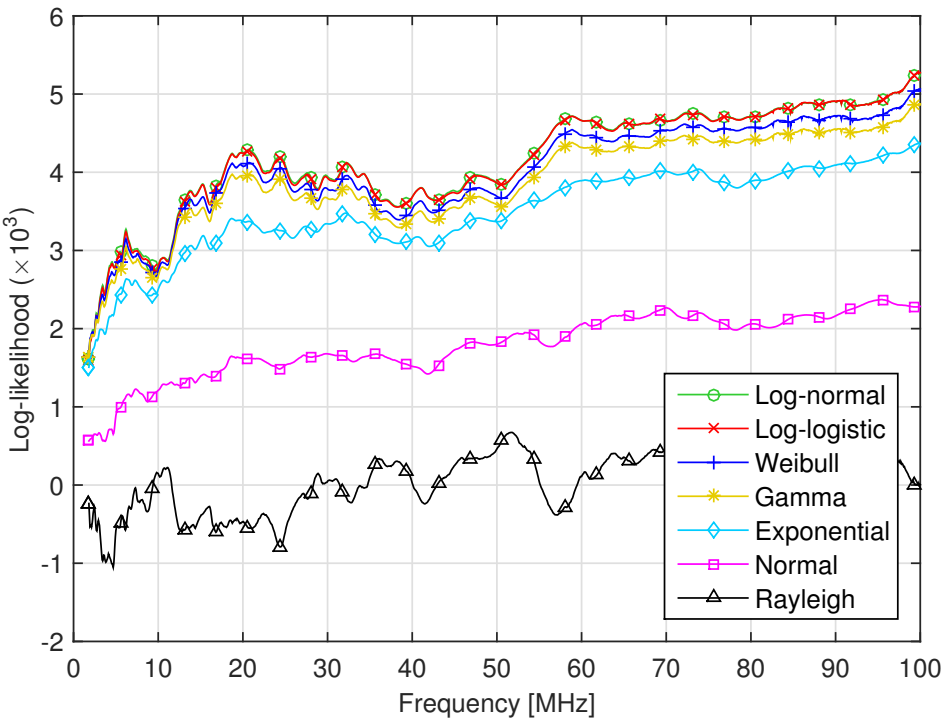

Figure 3.1: Log-likelihood value for the best fitting of the measured CFR amplitude. Different distributions are considered.

to the tails. Since the network structure, the loads, the reflections and the propagation effects can be different in different scenarios, log-normality does not strictly apply in all contexts. However, in this case, the measured PLC channel amplitudes are log-normally distributed with good approximation [72], a result that is validated in [129]. It is further noticeable that the PLC channels do not exhibit Rayleigh fading, contrariwise to what happens in the wireless case [142].

It is obvious that wireless and PLC scenarios are not strictly comparable. Indeed, in wireless networks the channel varies because of large-scale effects, such as environmental changes (slow fading), but also due to the users mobility or small-scale changes (fast fading). Contrariwise, in PLC networks there are no mobility effects since the network topology is fixed. However, due to the loads connection/disconnection, as well as to their operability, some fluctuations in the CFR can be noticed. Hence, to make a comparison with the wireless case, the above detailed statistical characterization of the PLC channel resembles the situation in which the user can be hypothetically connected to any different plug of the considered network. Anyway, since the overall PLC network has an effect on the single CFR, regardless of the measuring plugs, in our opinion this phenomenon is more related to the fast fading in wireless (which is Rayleigh distributed), rather than to the slow fading effect.

Figure 3.2 shows the mean μ_A and the standard deviation σ_A of the best log-normal fit of the channel amplitude in linear scale, as a function of frequency. Both the quantities exhibit an exponentially decreasing behavior that can be modeled as $q(f) = a_q f^{b_q} + c_q$.

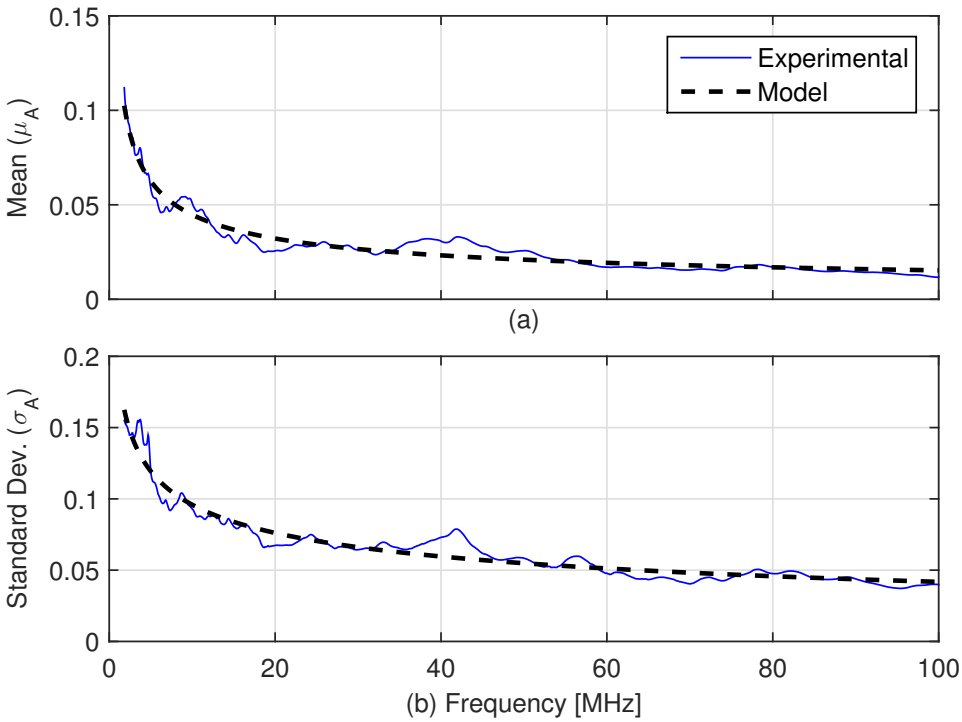

Figure 3.2: Experimental mean and standard deviation of the best log-normal fit of the measured CFR amplitudes (in linear scale), as a function of frequency. The model for both the quantities is also shown.

Table 3.1: Mean and standard deviation coefficients of the best log-normal fit of the CFR amplitude.

Parameter (q)	a_q	b_q	c_q ($\times 10^{-3}$)
μ_A	0.537	-0.496	1.512
σ_A	0.445	-0.256	-25.574

The variable q identifies the corresponding parameter μ_A or σ_A, while a_q, b_q, and c_q are constant coefficients. Table 3.1 reports the value of a_q, b_q and c_q.

In terms of mean value, the channel attenuation, in linear scale, increases exponentially with frequency, confirming that the power line cables have a low pass behavior. In terms of standard deviation, the channel statistics is less spread at higher frequencies. In the following, instead, the statistical behavior of the main statistical metrics, namely the ACG and the RMS-DS, are assessed and discussed. Regarding the properties of these statistical metrics, the q-q plot is considered in Figure 3.3. As discussed in Section 2.3.2, it graphically compares the quantiles of the considered quantity with those of a chosen distribution, e.g. normal, log-normal, and so on.

Firstly, let us focus on the ACG ($\mathcal{G}$). Figure 3.3a shows the quantiles of the ACG (in dB scale), named A_{dB}, versus the standard normal quantiles. The following observations can be made. First, the ACG ranges between -7.6 dB and -57 dB. The mean and the standard deviation of the best normal fit of the ACG in dB scale read $\mu_{\mathcal{G}} = -35.412$ dB and $\sigma_{\mathcal{G}} = 10.521$ dB, respectively. Furthermore, most of the samples lie on the dash-

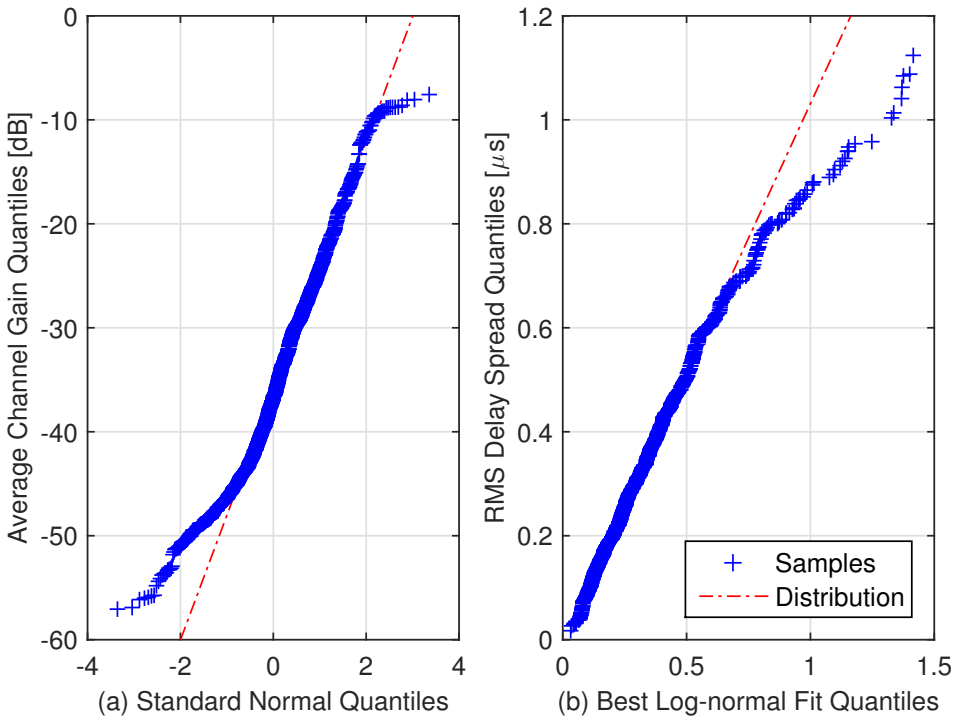

Figure 3.3: On the left (a), scatter plot of the ACG versus the standard normal quantiles. On the right (b), scatter plot of the RMS-DS versus the quantiles of the best log-normal fit.

dotted line. This would suggest that $\mathcal{G}$ is normally distributed, though the normality is not strictly confirmed by tests that have been performed on the measured data, as Kolmogorov-Smirnov, that reject always the null hypothesis. This is mainly due to the strictness of the above mentioned test and to the slight asymmetry, which is limited to the tails of the measured distribution.

Now, the attention is moved towards the RMS-DS (σ_τ). Figure 3.3b shows the quantiles of the measured RMS-DS versus the quantiles of the log-normal distribution, which provides the best fit. Most of the samples are closed to the dash-dotted line. This confirms that σ_τ is log-normally distributed with good approximation, as pointed out in [73]. The mean and the standard deviation of the best log-normal fit are $\mu_{\sigma_\tau} = 0.346$ μs and $\sigma_{\sigma_\tau} = 0.260$ μs, but these values are strongly dependent on the CIR computation method, as shown in Section 2.1.3.

3.2.2 Statistical Metrics Comparison

Now, the focus is on the well-known and most commonly used statistical metrics. The relation between the RMS-DS and the ACG, computed basing on the experimental channels, is shown in Figure 3.4a. Basically, Figure 3.4a is the scatter plot (circles) of the RMS-DS as a function of the ACG (in dB scale). The robust fit is also reported. The two quantities are negatively related. In [73] and [74], a similar study was performed for two

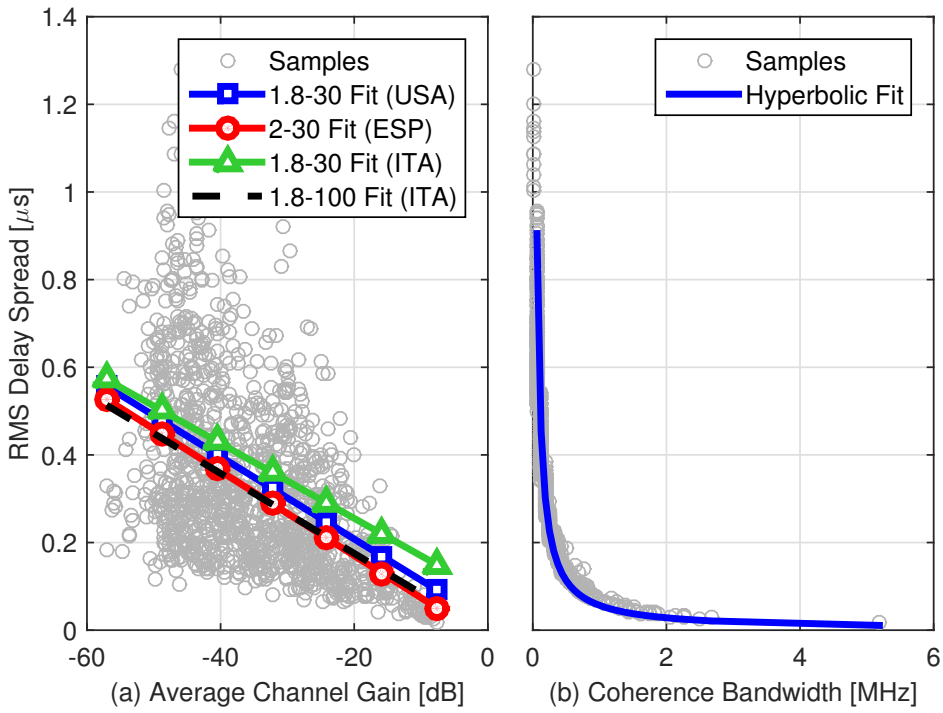

Figure 3.4: On the left (a), RMS-DS versus ACG and robust regression fit for the measurements in both the 1.8–30 MHz and 1.8–100 MHz bands. The 1.8–30 MHz USA [73] and 2–30 MHz ESP [74] robust regression fits are also shown. On the right (b), RMS-DS versus deterministic CB with the hyperbolic fit.

Table 3.2: Robust fit parameters for the RMS-DS versus the ACG in dB scale.

Country	Band (MHz)	slope ($\times 10^{-3}$) (μs/dB)	y-intercept (μs)
USA [73]	1.8–30	−9.400	0.020
ESP [74]	2–30	−9.630	−0.022
ITA	1.8–30	−8.545	0.084
ITA	1.8–100	−9.129	−0.007

sets of experimental data. The former work is the result of a measurement campaign in the USA for the 1.8–30 MHz band. The latter concerns networks in ESP for the 2–30 MHz band. In order to compare the results, the robust regression fit of our data in the 1.8–30 MHz frequency range is also shown in Figure 3.4a. A good agreement, especially with the ESP case, can be observed. Slight deviations of the lines slope and y-intercept may be due to the different frequency range and to the differences in the adopted procedure for the CIR computation, which reflects to the RMS-DS values. The robust fit parameters, for each frequency band and scenario, are listed in Table 3.2. It can be noted as the values are all very similar among the different measurement databases, especially if considering the same frequency band.

Table 3.3: Comparison among the statistical CB and the mean deterministic CB for different values of ξ, namely 0.9, 0.8 and 0.7.

ξ	$\overline{\mathcal{B}}_C^{(\xi)}$ (MHz)	$\hat{\mathcal{B}}_C^{(\xi)}$ (MHz)
0.9	0.288	0.438
0.8	0.545	0.938
0.7	0.846	1.563

Coherence Bandwidth

As discussed in Section 2.2.3, there are two alternative ways to compute the CB, depending on the type of auto-correlation function used for their computation, namely deterministic or statistical, that are labeled accordingly in the following. Figure 3.4b shows the relation between the RMS-DS and the deterministic CB at a level 0.9, i.e. $\mathcal{B}_C^{0.9}$, for the experimental channels. The focus is on $\mathcal{B}_C^{0.9}$ for consistency with previous analysis [71]. As it can be noted from the scatter plot (circles), the samples are distributed according to a hyperbolic trend, as highlighted by the hyperbolic fit that reads

$$\mathcal{B}_C^{0.9} = \frac{0.057}{\sigma_\tau} \quad [\text{Hz}]. \tag{3.1}$$

A similar result was pointed out in [71] for a set of channels measured in France. In detail, in [71], it was shown that the relation $\mathcal{B}_C^{0.9} \cdot \sigma_\tau = 0.055$ holds, which is very close to (3.1).

Differently from the deterministic CB, evaluated from the DAF in (2.16), which is function only of the frequency difference λ, the statistical CB is computed basing on the SAF in (2.6), which depends on the couple of considered frequencies. From the analysis of the SAF of the experimental data, it has been verified that the $\Phi(f, \lambda)$ expression in (2.6) does not depend only on the difference $f - \lambda$, as it will be clarified in Section 3.2.4. Therefore, the uncorrelated scattering assumption does not hold true. The presence of correlated scattering can be justified by the fact that signal reflections share part of the same network path, namely the backbone. Thus, instead of having a unique value of deterministic CB, it is possible to compute the statistical CB for each frequency sample, as it will be discussed in Section 3.2.4. The statistical CB trend over frequency and for different levels ξ, namely 0.9, 0.8 and 0.7, is depicted in Figure 3.5. As highlighted by the robust regression fit, the statistical CB has an increasing trend with a slope that increases with the level ξ. Although a similar behavior can be noted between the different levels, increasingly wide variations are exhibited with increasing levels of ξ, with the highest transitions encountered when considering the level $\xi = 0.9$.

Finally, Table 3.3 shows the comparison between $\overline{\mathcal{B}}_C^{(\xi)}$ and $\hat{\mathcal{B}}_C^{(\xi)}$. The average deterministic CB ($\overline{\mathcal{B}}_C^{(\xi)}$) is closer to the statistical CB ($\hat{\mathcal{B}}_C^{(\xi)}$) for higher values of ξ where they can be, to some extent, interchanged. This result can be exploited to fit the model in [125].

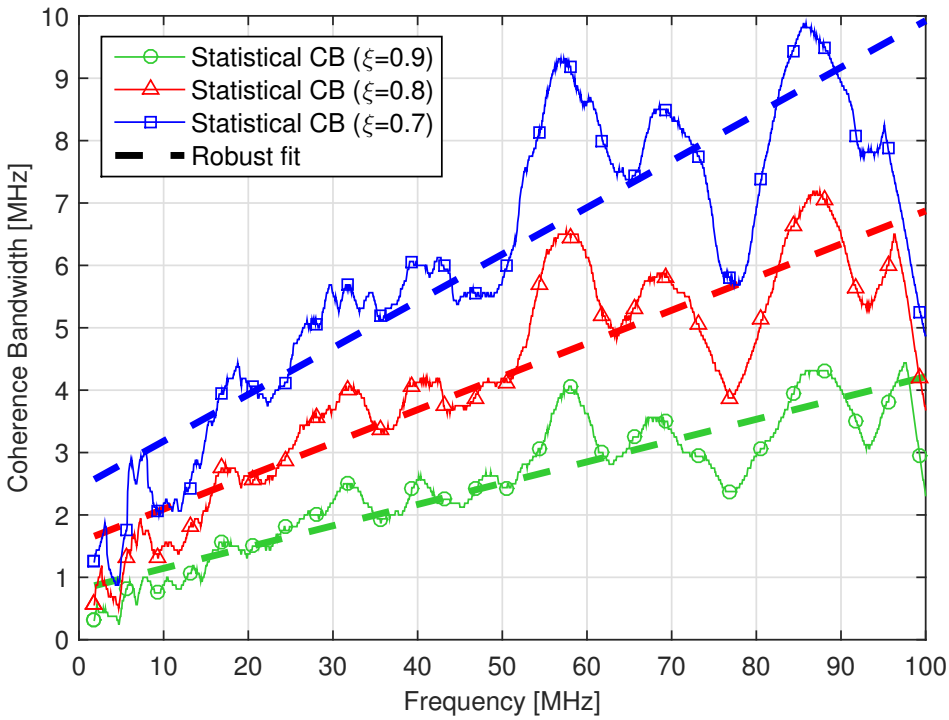

Figure 3.5: Statistical CB ($\hat{\mathcal{B}}_C^{(\xi)}$) at three different ξ levels, namely 0.9, 0.8 and 0.7, along frequency. The robust regression fit is also shown.

3.2.3 Phase Slope Statistics

As discussed in Section 3.2.1, beyond the amplitude of the CFR, also the phase needs to be assessed. In particular, the analysis of the phase of the CFR reveals that it can be modeled as uniformly distributed in $(-\pi, \pi)$ for each sample over the entire frequency range.

In the following, the focus is on the slope of the unwrapped phase that consists of the radiant phase angles corrected by adding 2π when the jumps between consecutive elements are lower than, or equal to, the jump tolerance of $-\pi$ radians, i.e. $\Delta\varphi \leq -\pi$, while subtracting 2π when $\Delta\varphi > \pi$. These adjustments allow the phase to accumulate without limit, producing an unwrapped phase. Figure 3.6 depicts the typical unwrapped phase behavior for a number of measured CFRs and their average trend, averaged over the entire set of measurements. It can be noted as, depending on the considered realization (different line), the decreasing trend can be more or less pronounced. This is related to how and how much the considered channel shifts the transmitted signal phase.

The phase slope brings some information on the delay introduced by the channel and thus on the length of the backbone, namely the shortest electrical path between the transmitter and the receiver. The delay increases with the distance of the path followed by the signal towards the receiver. Similarly, the channel attenuation is supposed to increase with the distance due to the effect of the non-ideal deployed cables and the impact of the branches connected to the backbone.

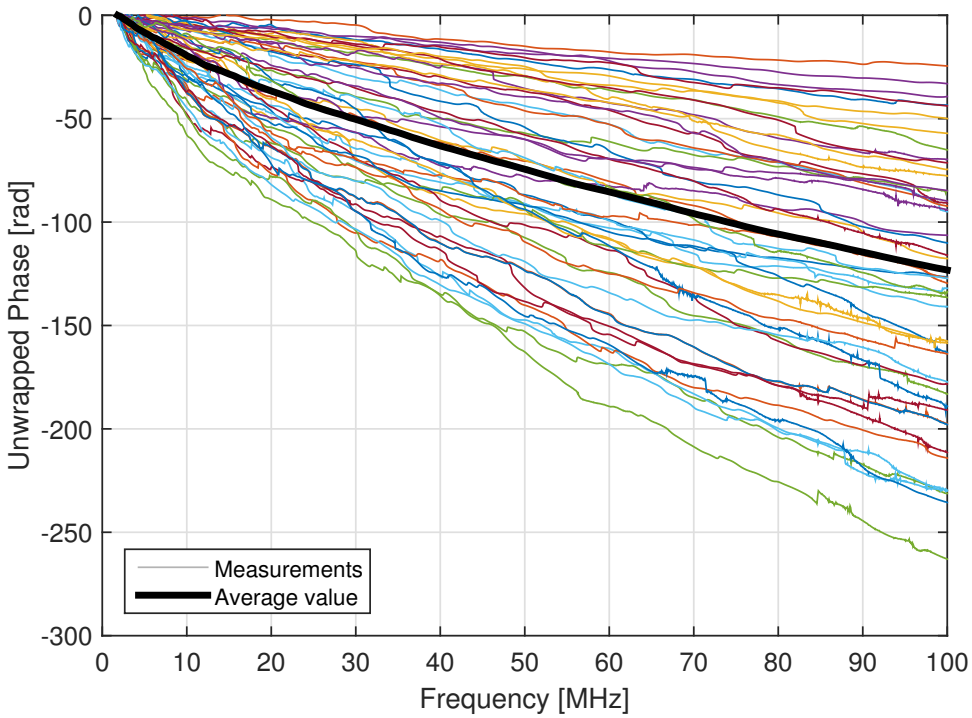

Figure 3.6: Unwrapped phase behavior over frequency for a reduced set of measurements. The average trend is also depicted.

Table 3.4: Robust fit parameters for ACG and RMS-DS versus the phase slope.

Metric	slope (rad/(MHz·x))	y-intercept (rad/MHz)
$\mathcal{G}$	0.038 ($x \equiv$ dB)	0.203
σ_τ	-1.842 ($x \equiv \mu$s)	-0.510

These observations are validated by the results. In particular, Figure 3.7 shows the relation between the phase slope versus the ACG and the RMS-DS. The phase slope is defined as the slope of the robust fit of the unwrapped phase exhibited by the CFR. The robust regression fit is also shown.

The scatter plot in Figure 3.7a depicts the relationship between the phase slope and the RMS-DS. The robust regression fit highlights as these quantities are negatively related. The greater the phase slope (in absolute value), the higher the RMS-DS (or channel dispersion). This effect is due to the long deployed cables and to the high number of branches, in agreement with the above discussion. Instead, Figure 3.7b shows the relation between the phase slope and the ACG. In this case the metrics are positively related, indeed, high phase slope values (in absolute value) involve low ACG values (or high attenuation). The robust fit parameters, for both the ACG and the RMS-DS versus the phase slope, are listed in Table 3.4.

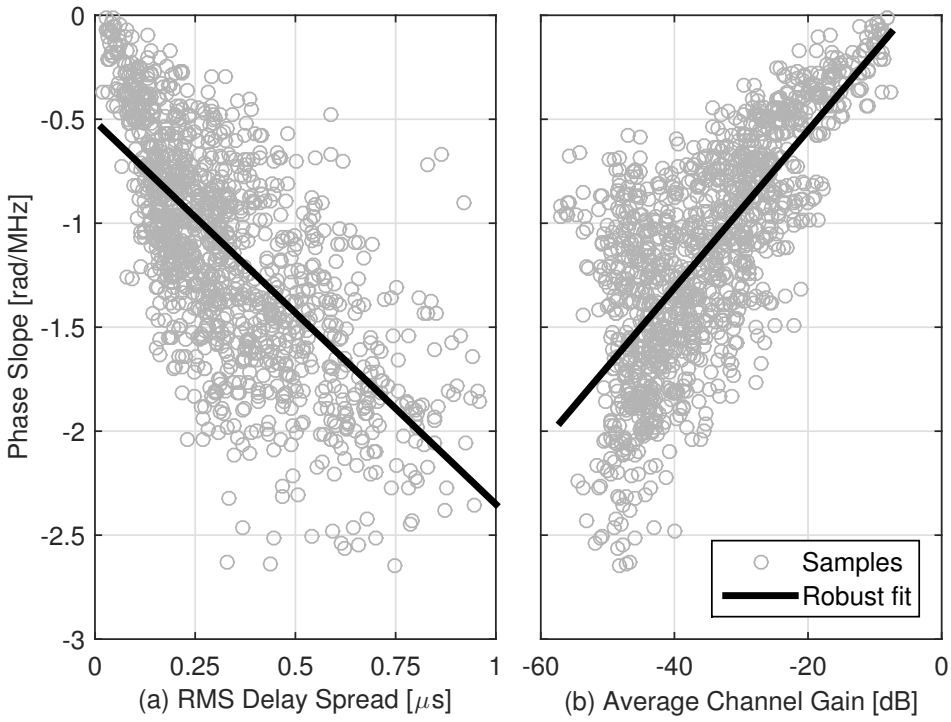

Figure 3.7: On the left (a), scatter plot of phase slope versus RMS-DS. On the right (b), phase slope versus ACG. The robust regression fit is also shown.

3.2.4 Frequency Correlation

As previously discussed, this thesis focuses on the BB-FS. Typically, BB-PLC systems adopt multicarrier modulation at the physical layer. The most commonly used modulation scheme is based on OFDM transmission, as envisioned by the HPAV [29] and HPAV2 [39] standards. In OFDM schemes the BB channel is partitioned in a number of parallel sub-channels, or frequencies, whose responses can be correlated. The degree of this correlation can be evaluated in terms of normalized covariance matrix, namely $\dot{\mathcal{K}}(f, \lambda)$, between the f-th and λ-th frequencies, which is given by (2.8), as discussed in Section 2.1.4. The average of the expectation operator in (2.8) is performed on the entire set of channel measurements.

The normalized covariance matrix depicted in Figure 3.8 is evaluated on the logarithmic (or dB) version of the channel measurements, which are normally distributed with good approximation, as discussed in Section 3.2.1. The analysis is performed in dB scale since the logarithmic version of the CFR measurements, and their corresponding properties, facilitates the simulation procedure considered in the modeling generation process, as it will be discussed in Chapter 8. It can be noted as certain frequencies (or sub-channels) are more related to some others, such as those at 3 and 8 MHz, where the colors become warmer (yellow and red). A higher degree of correlation can be noted also in the upper right corner, thus at high frequencies. This phenomenon is mainly due to the cross-talk among the wires and to the coupling effects, which become increasingly prominent at

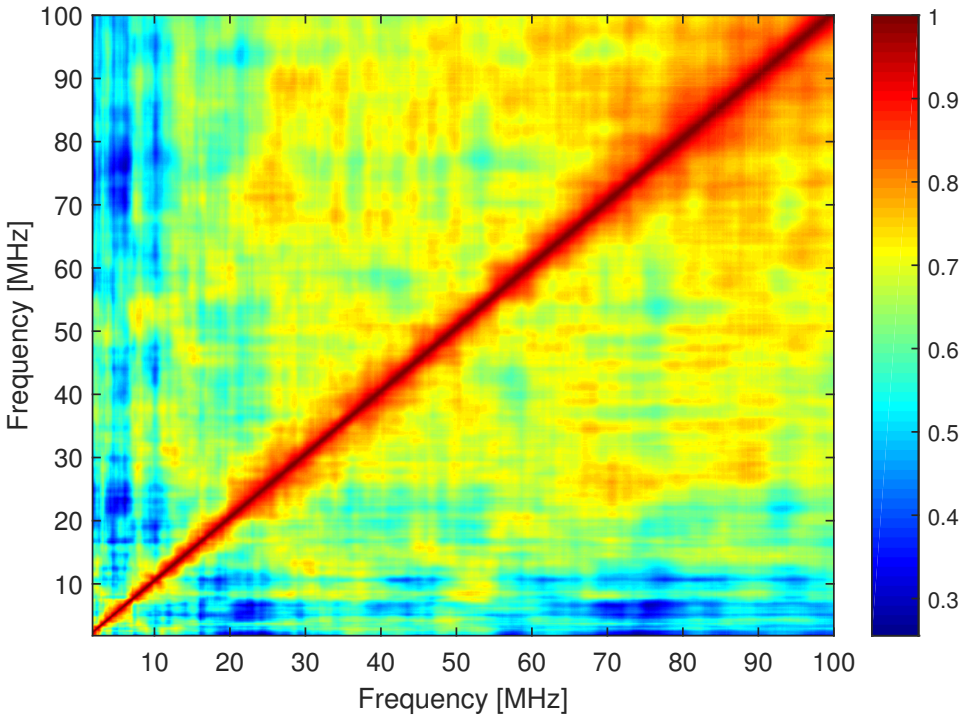

Figure 3.8: Normalized covariance matrix for the channel measurements in dB scale.

higher frequencies.

Furthermore, the normalized covariance matrix is directly connected to the SAF $\Phi(f, \lambda)$, as discussed in Section 2.1.4. Thus, looking at Figure 3.8, it is clearly noticeable as $\Phi(f, \lambda)$ does not depend only on the frequency difference $f - \lambda$, as stated in Section 3.2.2.

3.3 Channel Performance

In the literature, the most widely deployed metric for the performance description is represented by the maximum achievable rate, i.e. the capacity $\mathcal{C}$, which is defined as in Section 2.2.4. In the following, the performance that are achievable on the experimental channels described in Section 3.1 are computed. The results are assessed in conjunction with the geometrical distance, as well as considering a frequency band extension in order to evaluate the data rate enhancements.

3.3.1 System Specifications

In the following the capacity has been computed as in (2.20), assuming a PSD profile at the transmitter side, namely $P_t(f)$, equal to 10^{-5} mW/Hz (-50 dBm/Hz) up to 30 MHz, and to 10^{-8} mW/Hz (-80 dBm/Hz) above 30 MHz. The PSD reduction is required in order to satisfy and comply with the regulations on the radiated emissions [143].

The constraints on the transmitting PSD are not sufficient for the capacity evaluation,

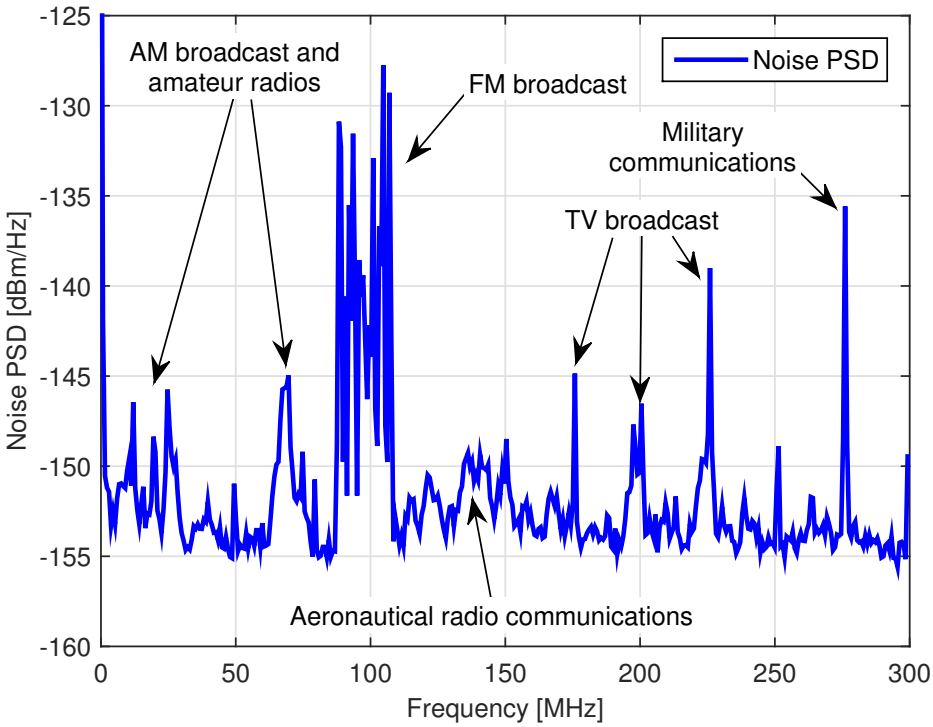

Figure 3.9: Typical PSD profile of a measured background noise in the 0–300 MHz band.

also the noise that affects a PLC network must be considered. A typical background noise PSD profile that can be observed in the 0–300 MHz frequency band is depicted in Figure 3.9. The typical exponentially decreasing PSD profile exhibited by the background noise in PLC networks (colored noise) is not clearly detectable due to the wide considered frequency range. The considered bandwidth, indeed, gives emphasis to the noise floor and highlights the most common disturbances that affect the PLC scenario.

The typical background noise PSD exponential decreasing profile experimented in PLC networks (colored noise) is not so clearly detectable due to the wide considered frequency range that gives emphasis to the noise floor and highlights the most common disturbances that affect the PLC scenario. The main NB disturbances that usually interfere with the PLC environment can be easily observed in Figure 3.9. They are mainly due to radio and television broadcast transmissions, as well as to military and aeronautical communications. Among these, the FM broadcast is the dominant one, increasing the PSD floor, equal to -155 dBm/Hz, of more than 25 dB.

In most of the cases, however, a simplified noise model is used in place of a real background noise assumption, in order to simplify the system. In [70] and [73], the noise is assumed to be white, with a PSD of -140 dBm/Hz and -120 dBm/Hz, respectively. Some other papers, instead, account for the colored nature of the noise, which consists of an exponentially decreasing profile along frequency. We adopt the additive colored

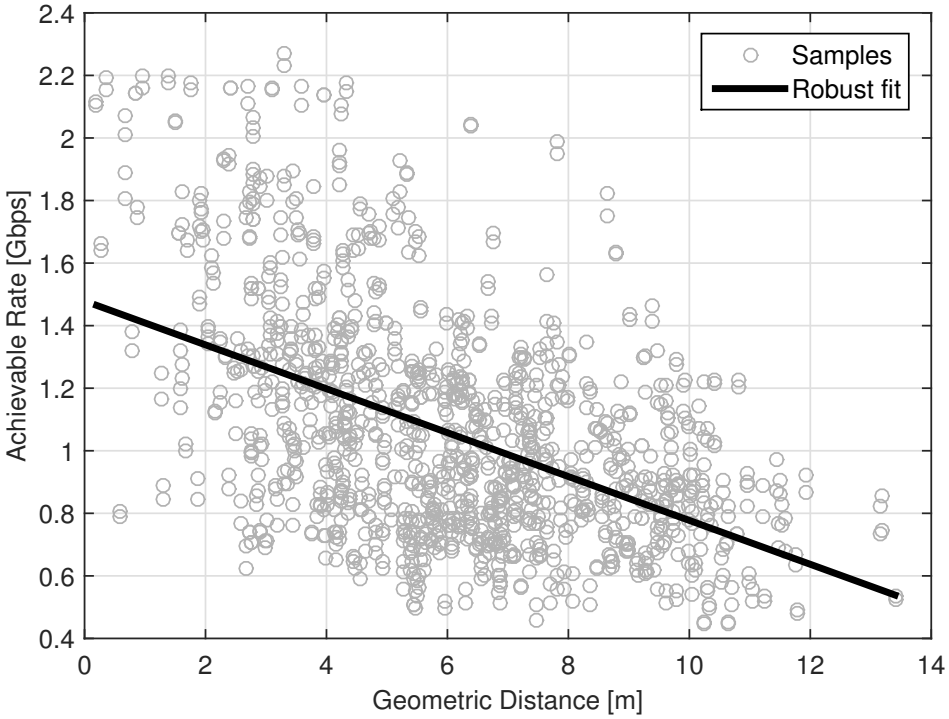

Figure 3.10: Scatter plot of the capacity as a function of the geometrical distance. The robust fit is also shown.

Gaussian noise model presented in [83] that models $P_w(f)$ as follows

$$P_w(f) = \frac{1}{f^2} + 10^{-15.5} \quad [\text{mW/Hz}]. \tag{3.2}$$

The capacity $\mathcal{C}$ is computed according to the expression in (2.20), as detailed in Section 2.2.4, considering the corresponding geometrical distance between the transmitter and receiver outlets, as well as three different transmission bandwidths. However, it should be noted that, since there are several noise disturbances, whose statistical characterization has not been thoroughly assessed yet, the true PLC channel capacity may be overestimated by (2.20) if the noise model in (3.2) is used. More in detail, we do not account for the contribution due to NB and FM broadcast radios.

3.3.2 Capacity versus Geometrical Distance

Firstly, the aim is to study the relation between the maximum achievable rate and the geometrical distance (see Section 2.2.5 for details), in order to infer the achievable coverage. In this respect, the capacity of all the available measurements is computed.

The scatter plot in Figure 3.10 displays the capacity against the geometrical distance, with the corresponding robust regression fit as a function of the distance. Interestingly, the achievable rate decreases with the geometrical distance, with a maximum $\mathcal{C}$ value of 2.27 Gbps. The slope of the robust regression fit reads -68.7 Mbps/m. Moreover, for

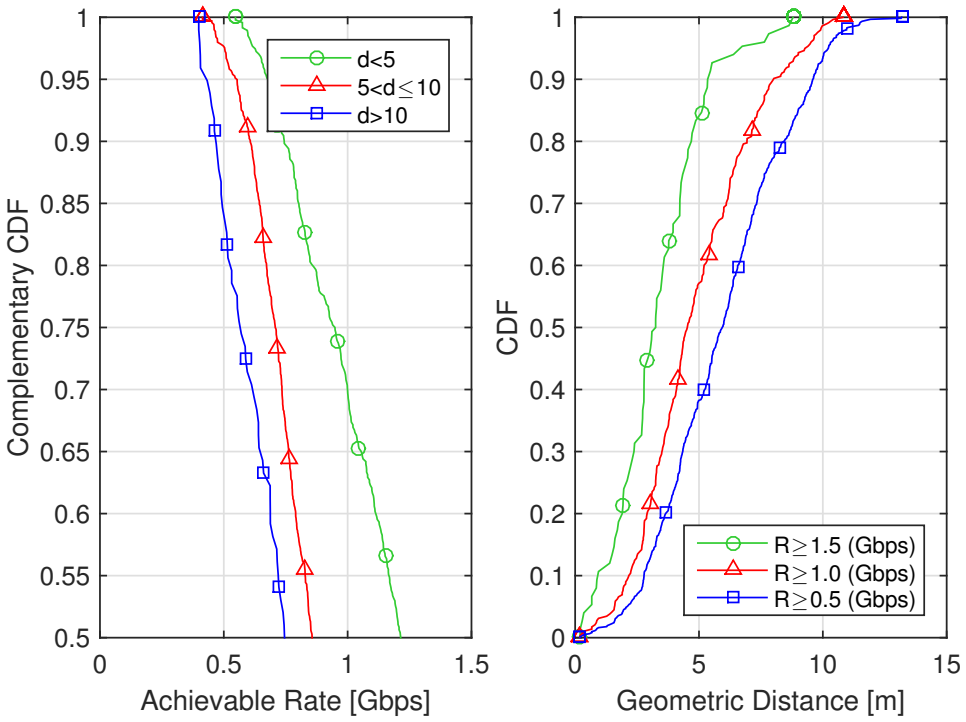

Figure 3.11: On the left (a), C-CDF of the achievable rate conditioned on the distance. On the right (b), CDF of the distance conditioned on the achievable rate.

distances greater than 11 m, the capacity is always lower than 1 Gbps.

In order to infer the PLC coverage similarly to the wireless scenario, the maximum achievable rate is computed in connection to the geometrical distance between the transmitter and receiver positions of the considered channel. In this respect, the complementary cumulative distribution function (C-CDF) of the maximum achievable rate, conditioned on the distance, as well as the cumulative distribution function (CDF) of the geometrical distance, conditioned on the maximum achievable rate, have been computed and depicted in Figure 3.11.

In particular, Figure 3.11a shows the results for three values of distance, i.e. smaller than 5 m, between 5 and 10 m and greater than 10 m. A similar result was already shown in [135]. The differences in the maximum achievable rate values are amenable to the different noise model and transmitted PSD level assumptions. It is worth to note that in the 70 % of the cases the channels associated to distances between outlets shorter than 5 m exceed 1 Gbps.

In a dual manner, Figure 3.11b shows the geometrical distance CDF conditioned by the maximum achievable rate of the channel, namely larger than 0.5, 1, or 1.5 Gbps. Interestingly, data rates larger than 1.5 Gbps can be achieved with high probability by channels shorter than 5 m. Therefore, in the considered sites, PLC can provide a real good option for very high speed connectivity between outlets that are nearly placed.

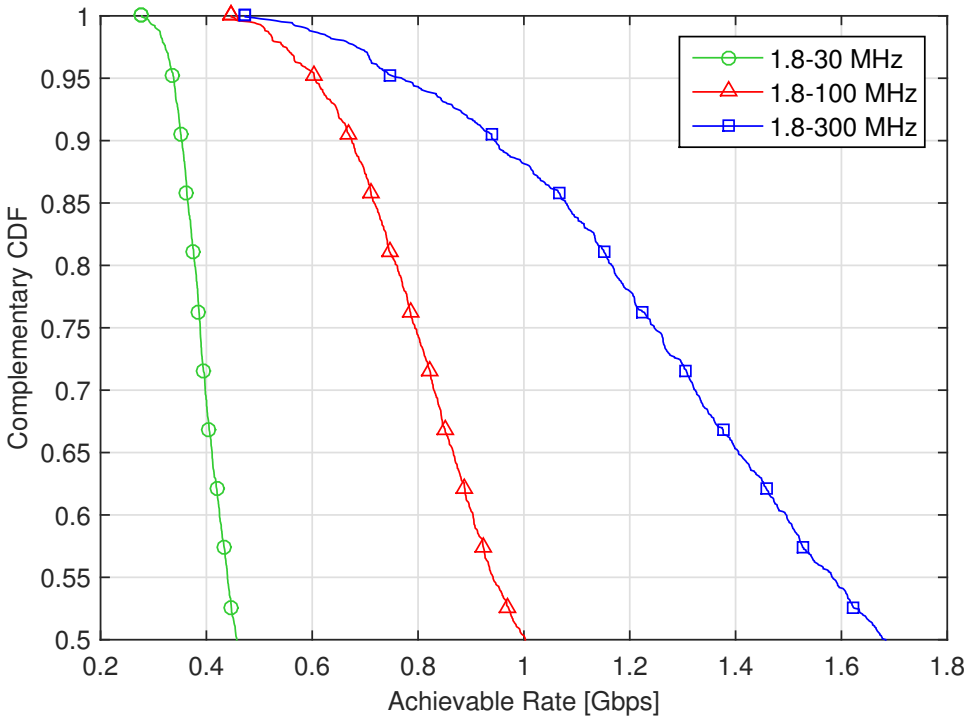

Figure 3.12: C-CDF of the maximum achievable rate for three different transmission bandwidths, i.e. up to 30, 100 or 300 MHz.

3.3.3 Bandwidth Extension

In the following, the improvement provided by the bandwidth extension beyond 100 MHz is assessed. The channel measurements acquired in a wider spectrum, up to 300 MHz, as detailed in Section 3.1, were considered. For what concerns the transmitting power constraint, the same PSD profile specified in Section 3.3.1 has been assumed. Concerning the background noise profile, to our knowledge, there is no model up to 300 MHz presented in the literature. Thus, the noise model in (3.2) is extended up to 300 MHz.

The capacity C-CDF evaluated considering three different transmission bandwidths, namely 1.8–30 MHz, 1.8–100 MHz and 1.8–300 MHz, is depicted in Figure 3.12. The plot limits the C-CDF values to those greater than 0.5. Thus, it is easily observable that in the 50 % of the cases a maximum achievable rate greater than 457 Mbps, 1 Gbps and 1.68 Gbps can be achieved for the three corresponding bandwidths. These values appear to be quite high due to the low level of noise PSD that has been considered, having a floor equal to -155 dBm/Hz.

The 20-th, 50-th and 80-th percentiles of the capacity distribution, for all the three considered bandwidths, are listed in Table 3.5. As it can be noted, the maximum achievable rate improves significantly, but the increase provided by the bandwidth enlargement is not proportional to such a bandwidth extension. In this respect, let us define the average spectral efficiency η as the ratio between the average maximum achievable rate and the transmission bandwidth. Table 3.5 reports the spectral efficiency coefficient for

Table 3.5: Achievable rate percentiles and mean spectral efficiency for three transmission bandwidths, i.e. up to 30, 100 or 300 MHz.

Band (MHz)	20-th (Mbps)	50-th (Mbps)	80-th (Mbps)	η (bps/Hz)
1.8–30	331	410	525	15.27
1.8–100	714	956	1282	10.47
1.8–300	1121	1637	2721	6.50

the three cases. It can be seen as, on average, the spectral efficiency decreases as the bandwidth increases. This is due to the large attenuation exhibited by the PLC channels at very high frequencies, although the noise PSD level is quite lower.

3.4 Multiple User Correlation

As discussed in Section 2.1.5, usually, different PLC links exhibit a certain degree of correlation due to the fact that channels, associated to different pairs of outlets (and thus users) within the same site, may share part of the communication medium, namely the backbone. This involves a certain degree of correlation among the channels that connect different users belonging to the same network. In the rest of the thesis, this type of correlation is referred to as MU correlation in order to differentiate it from the spatial correlation. The latter concerns the correlation exhibited by the different channels (or modes) connecting the same transmitting and receiving outlets in a network deploying multiple wires, i.e. in a MIMO transmission scheme.

In order to simplify the analysis, for the rest of this section the MU correlation between channels of the same site, namely $\psi(f, \lambda)$, is studied imposing $f = \lambda$, i.e., $\psi_x(f, f) \equiv \psi_x(f)$. From the measurements analysis, the absolute value of the MU correlation, i.e. $|\psi(f)|$, obtained through the expression in (2.9), has been found to be small. This can be noted looking at Figure 3.13, where $|\psi(f)|$ assumes values always below 0.05, regardless of the considered site or frequency. This result reflects the large variability and heterogeneity of the in-home PLC scenario. Indeed, in-home networks consists of many branches that cause multipath propagation and several signal reflections. These phenomena involve that, on average, the channels are not correlated.

To limit the variability and get useful information, we propose to focus only on the channels that share the same transmitter or receiver outlet. The first case is representative of a broadcast down-link scenario, while the second case of a scenario where multiple transmitters, e.g. video cameras, send data to a concentrator. We denote with $\psi_x(f, \lambda)$, where $x \in \{tx, rx\}$, the correlation of the CFR between the frequencies f and λ for the channels that share the same transmitter outlet, i.e., $x = tx$, or for channels that share the same receiver outlet, i.e., $x = rx$. Hence, $\psi_x(f, \lambda)$ is computed as in (2.9), but limiting the expectation in i, j over the channels that share the same transmitter outlet

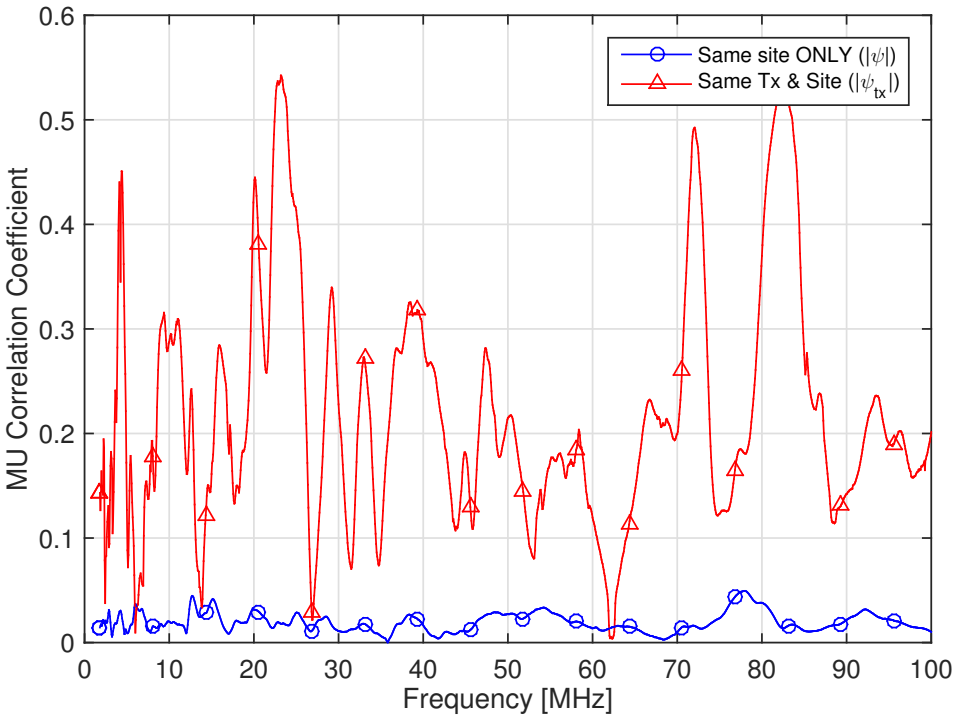

Figure 3.13: Absolute value of the MU correlation $|\psi(f)|$ and $|\psi_{tx}(f)|$ as a function of frequency. One single site is considered, as an example.

for ψ_{tx} and over channels that share the same receiver outlet for ψ_{rx}. Also in this case $\psi_x(f, f) \equiv \psi_x(f)$ has been considered. An example of the correlation value $\psi_{tx}(f)$, for the channels sharing the same transmitter within one site, is depicted in Figure 3.13. It can be noted as the maximum absolute value of the MU correlation is one order of magnitude larger if the constraint of sharing the same transmitting outlet is assumed. This can be highlighted considering the statistics of $\psi_{tx}(f)$ for the overall set of available sites.

In Figure 3.14a, the 20-th, 50-th and 99-th percentile profiles of the CDF of $|\psi_{tx}(f)|$, as a function of frequency, are shown. The numerical results confirm that, if a spatial constraint is added, a higher correlation might be found. Indeed, also in this case, the maximum value of $|\psi_{tx}(f)|$ is one order of magnitude larger than $|\psi(f, \lambda)|$. Therefore, as intuition suggests, the correlation between channels that share the same transmitter outlet is non-negligible. We speculate that this is because of the random contribution of the phase of distinct channels, which is uniformly distributed in $(-\pi, \pi)$. Therefore, we also study the correlation $\psi_x^{amp}(f)$ that is defined as $\psi_x(f)$, with $x \in \{tx, rx\}$, but considering the amplitude of the CFRs, i.e., $|H_i(f)|$ and $|H_j(\lambda)|$, within the expectation at the numerator of (2.9).

The values of $\psi_{tx}^{amp}(f)$ are depicted in Figure 3.14b, which shows the same percentile profiles considered in 3.14a. Note that, by definition, $\psi_{tx}^{amp}(f)$ is a real quantity. Interestingly, the correlation is large. Therefore, the low values experienced by $\psi_{tx}(f)$ are due to the random phase of the channels. Furthermore, $\psi_{tx}^{amp}(f)$ decreases as the frequency increases. Similar results are found for the correlation between the amplitude of the chan-

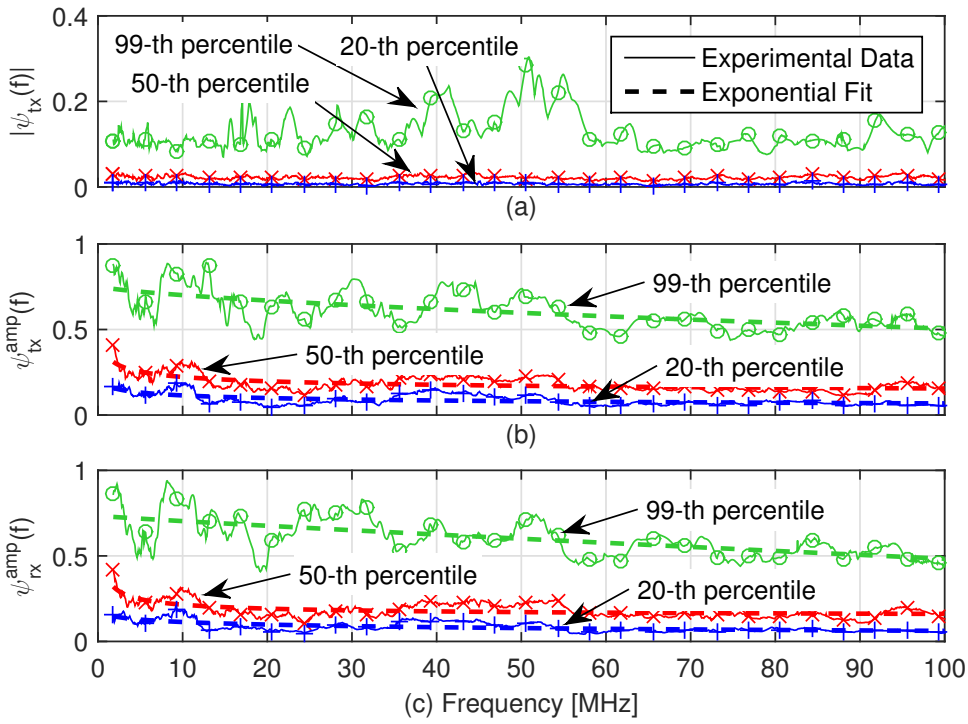

Figure 3.14: 20-th, 50-th and 99-th percentile of the MU correlation $|\psi_{tx}(f)|$ (a), $\psi_{tx}^{amp}(f)$ (b) and $\psi_{rx}^{amp}(f)$ (c) as a function of frequency. For $\psi_{tx}^{amp}(f)$ and $\psi_{rx}^{amp}(f)$ the best exponential fit is also shown.

Table 3.6: Parameter values of the best exponential fit of the MU correlation quantiles for $\psi_{tx}^{amp}(f)$ and $\psi_{rx}^{amp}(f)$.

Correlation (q)	Percentile (ζ)	a_{q_ζ}	b_{q_ζ}	c_{q_ζ}
$\psi_{t,abs}(m)$	99-th	-1.873×10^{-3}	0.663	0.755
	50-th	0.602	-0.290	0.085
	20-th	0.357	-0.119	-0.080
$\psi_{r,abs}(m)$	99-th	-0.315×10^{-3}	0.906	0.735
	50-th	0.981	-0.496	0.136
	20-th	-0.274	0.057	0.480

nels that share the receiver outlet, $\psi_{rx}^{amp}(f)$, as shown in Figure 3.14c, where the same percentiles are reported.

The experimental profiles of $\psi_{tx}^{amp}(f)$ and $\psi_{rx}^{amp}(f)$ can be fitted with an exponential function, namely $q_\zeta(f) = a_{q_\zeta} f^{b_{q_\zeta}} + c_{q_\zeta}$, where q_ζ stands for $\psi_{tx}^{amp}(f)$ or $\psi_{rx}^{amp}(f)$, while ζ indicates the percentile value. The corresponding fitting profiles are shown in both Figure 3.14b and Figure 3.14c, whose parameters are reported in Table 3.6.

3.5 Line Impedance

Not only the channel response properties are important, but also the line impedance characterization is required for the design of the analog front-end of a transmitter modem.

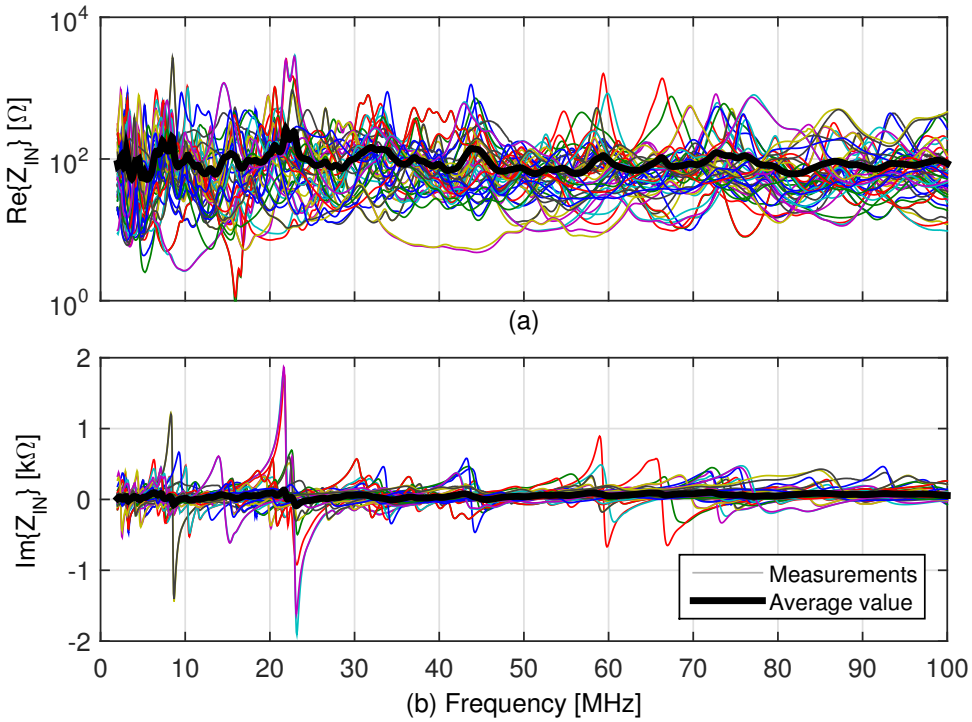

Figure 3.15: Real part (a) and imaginary part (b) of the input line impedance for the in-home scenario in the BB frequency range 1.8–100 MHz.

Indeed, a low line impedance at the transmitter port makes the injection of the voltage signal challenging. The line impedance Z_{IN}, defined as in Section 2.1.2, spreads over a broad set of values across the 1.8–100 MHz spectrum. In the following, the real part $R(f)$ and the imaginary part $X(f)$ of the line impedance are separately discussed as a function of the frequency f.

The measurement results have shown that the line impedance can be significantly low, in the order of few ohms, especially at low frequencies. For instance, in the access network, this is due to the fact that the home network acts as many parallel loads attached to the access port [3]. Within the in-home network scenario, the line impedance at the outlets exhibits a highly frequency dependent behavior, as shown in Figure 3.15.

Both the resistive (on top) and the reactive (on bottom) components, namely $R(f)$ and $X(f)$, are represented as a function of frequency. The different colors represent the several line impedance measurements, while the thick black line corresponds to the average profile along frequency, averaged over the 1266 measurements, for both $R(f)$ and $X(f)$. Interestingly, the reactive part behavior is mostly inductive and the real part slightly increases at high frequency. Therefore, it is expected that BB-PLC can be less affected by the signal injection issue than NB-PLC. Furthermore, the BB-FS can provide channel and impedance diversity that can simplify the design of impedance adaptation techniques [144].

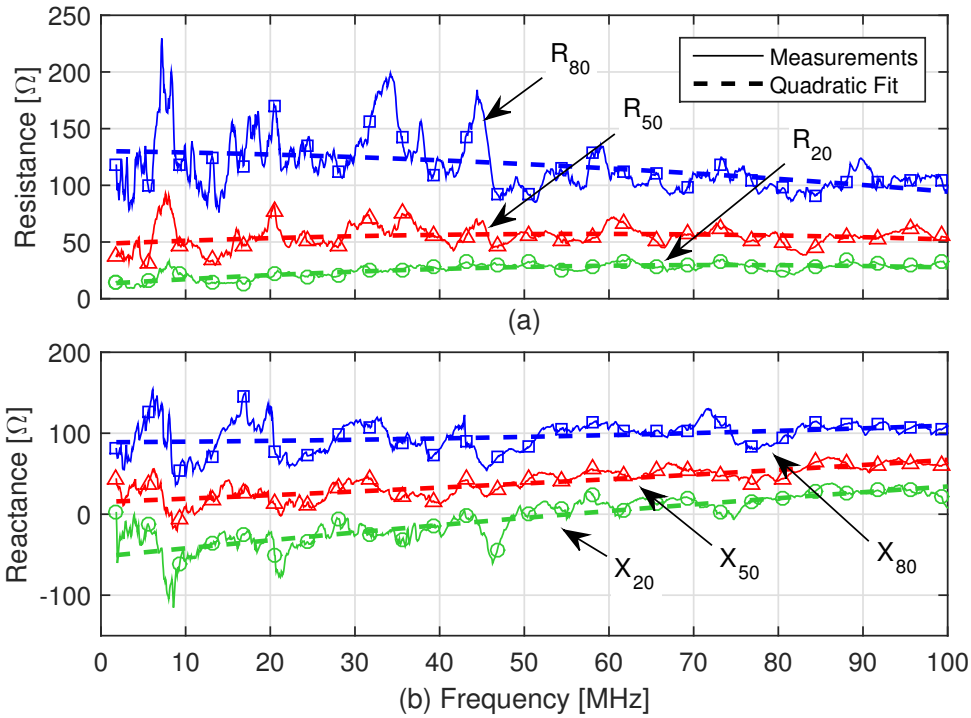

Figure 3.16: 20-th, 50-th and 80-th percentiles of the resistive (a) and reactive (b) part of the line impedance. The best polynomial fit is also shown.

3.5.1 Statistical Analysis and Properties

In order to analytically describe the statistical behavior of the line impedance measured in a typical in-home PLC network, the CDF of $R(f)$ and $X(f)$ is studied. A similar characterization has been performed in [91] for the NB-FS. Figure 3.16 shows the 20-th, 50-th and 80-th percentiles of both the resistive and reactive components of the line impedance as a function of the f-th frequency, i.e. $R(f)$ and $X(f)$, respectively. The best polynomial fit modeled as $q_\zeta(f) = a_{q_\zeta} f^2 + b_{q_\zeta} f + c_{q_\zeta}$ is also shown. The variable q_ζ represents the percentile at value ζ of the quantity $q \in \{R, X\}$, while a_{q_ζ}, b_{q_ζ} and c_{q_ζ} are constant parameter values. Basically, the resistive component is less spread at high frequencies and the lowest quantile increases with frequency. Instead, the reactive quantiles exhibit a frequency increasing behavior, that turns into an inductive like nature.

In Table 3.7 the parameters values of the best polynomial fit for both $R(f)$ and $X(f)$, and for all the three considered percentiles, are summarized. This table facilitates the comparison between the different fits, providing all the coefficients that are essential for the replicability and the simulation of the $R(f)$ and $X(f)$ values, in agreement with their approximated profiles.

Finally, the relationship between the resistive and reactive part is assessed. In particular, Figure 3.17 shows the scatter plot for the values $R(f)$ versus $X(f)$, expressed in kΩ, at the same frequency. All the frequency samples and the available measurements are considered. The resistive part is displayed in logarithmic scale in order to emphasize the

Table 3.7: Quadratic fitting parameter values of the line impedance components.

Quantity (q)	Percentile (ζ)	a_{q_ζ} ($\times 10^{-5}$) (Ω)	b_{q_ζ} (Ω)	c_{q_ζ} (Ω)
R	20	-1.213	0.029	12.926
	50	-1.053	0.019	48.303
	80	-1.004	-0.006	130.229
X	20	-0.7045	0.065	-52.387
	50	0.5036	0.024	15.118
	80	0.5705	0.004	88.825

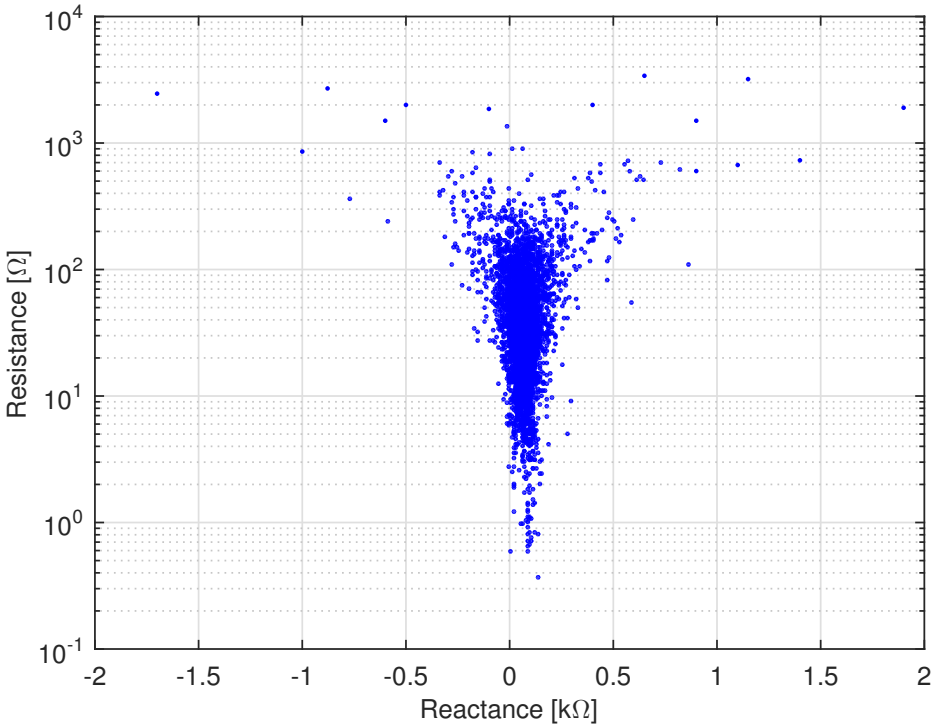

Figure 3.17: Scatter plot of the resistive part, in logarithmic scale, against the reactive part, expressed in kΩ, of the line impedance.

rang of low values, i.e. below 10 Ω. It can be noted as $R(f)$ ranges between 0.6 Ω and 3.4 kΩ, while $X(f)$ ranges between -1.7 and 1.9 kΩ. Furthermore, high reactive values imply high resistive values. Instead, when the resistive component is low, in the order of few Ohm, the reactive part is positive and approximately equal to 120 Ω. Deepening the analysis of the impedances database, it has been observed that these low resistance values correspond to an almost series resonance, which occurs in the neighborhood of 16 MHz, as it can be clearly observed in Figure 3.15. Since it is not a perfect resonance, the imaginary part is not exactly zero and, in this case, equals 120 Ω. Thus, the network loads seen at the input port of the considered channel measurements involve an input impedance that exhibits a more inductive behavior at the 16 MHz frequency, while the resistive part approximately decreases to zero.

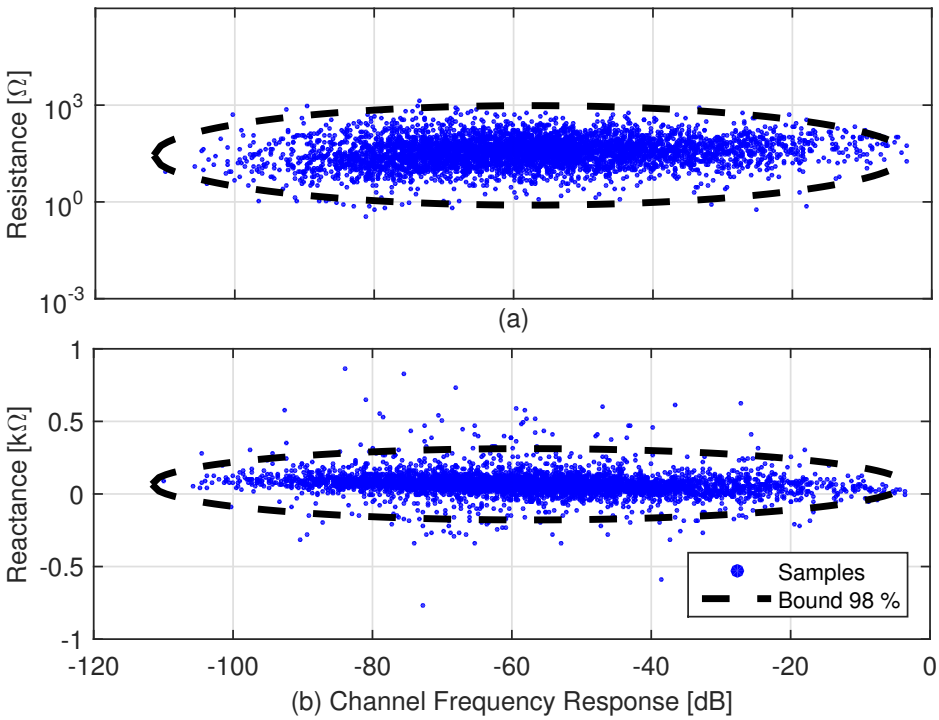

Figure 3.18: Scatter plot of the resistive (a) and the reactive (b) component of the line impedance versus the CFR. The high-density regions are also shown.

3.5.2 Impedance versus CFR

In addition to the relationship between the line impedance real and imaginary parts, it is also interesting to analyze whether and how the line impedance is related to the CFR. Figure 3.18 shows the scatter plot of the line impedance components $R(f)$ and $X(f)$ versus the CFR, evaluated at the same frequency f. The plot has been obtained gathering the samples from all frequencies. Despite the high variability, we identify high-density regions to which 98 % of the samples belong. The intent is to identify a range of possible real values that can be used as a constraint for the simulation process, or that can act as a reference bound. The region borders are shown in the figure. Similar results can be obtained by applying the same analysis frequency by frequency.

The target frequency range is 1.8–100 MHz, considering the dB-version of the CFR amplitude versus the logarithmic representation of the resistive component or versus the reactive component in linear scale. Also in this case, the reactive part is represented in kΩ, while the resistive part is considered in logarithmic scale in order to magnify the behavior at lower values. The border of the high density region can be modeled, from the experimental evidence, as an ellipse that reads

$$\frac{(x-m_x)^2}{u^2}+\frac{(y-m_y)^2}{w^2}=1, \tag{3.3}$$

where x and y are the variables denoting the CFR and the line impedance component

Table 3.8: Parameters of the high-density regions for the line impedance components versus the CFR in dB scale.

Component	m_x (dB)	u (dB)	m_y	w
R	-45.336	44.618	1.709	1.154
X			47.216	325.016

values (R or X), respectively. All the other terms are constant coefficients. The parameter m_x is the mean value of the measured CFR in dB scale, namely $m_x = E[A_{dB}(f)]$. Similarly, m_y is the mean of the impedance component, i.e., $m_y = E[\log_{10} R(f)]$ for the resistance, and $m_y = E[X(f)/10^3]$ for the reactance. The expectation $E[\cdot]$ is performed across all the frequency samples and the channel realizations. The other coefficients in (3.3) are obtained as follows.

According to the results of Section 3.2.1, the dB version of the CFR is normally distributed with good approximation. It is well-known that, for a normally distributed random variable, more than 99 % of the samples are within three times the standard deviation. In this respect, $u = 3\sigma_{A_{dB}}$, where $\sigma_{A_{dB}}$ is the standard deviation of the CFR. Substituting m_x, m_y and u in (3.3) with the values above described, w reads

$$w = \sqrt{\frac{u^2(y - m_y)^2}{u^2 - (x - m_x)^2}}. \tag{3.4}$$

The relation in (3.4) can be computed for all x and y values. The result is a set of values of w that are collected in a vector named $\boldsymbol{w}$. The value that models w is chosen as the 98-th percentile of the CDF of $\boldsymbol{w}$. Table 3.8 reports the values of the constant coefficients in (3.3) for the resistive and the reactive component. Clearly, m_x and u are identical in both cases. From the analysis of the coefficients in Table 3.8, we note the followings. First, the average value of the CFR, the resistance and the reactance are about -45.336 dB, $51 = 10^{1.709}$ Ω and 47.216 Ω, respectively. Furthermore, the standard deviation of the CFR is $14.87 = 44.618/3$ dB.

3.6 Main Findings

A statistical characterization of the in-home PLC channel has been presented relying on a set of 1266 measures acquired in Italy. The analysis brings new insights on the channel behavior, confirming some prior results presented in the literature that were obtained from measurement campaigns carried out in other countries. The aim is to allow a precise comparison between the results of this analysis and those from other campaigns. In this respect, the need of common processing procedures and the importance of using the same definition for the physical quantities to be analyzed has been pointed out. This

formulation is intended to be used for the analysis of the results of future measurement campaigns, providing results that are consistent with the ones herein presented. Besides the processing procedures, a detailed statistical analysis has been carried out.

In particular, it has been shown as the PLC channel is significantly frequency selective in the 1.8–100 MHz band. The magnitude of the CFR is log-normally distributed. The log-normality applies also to the RMS-DS, while the ACG (in dB) is normally distributed with good approximation. This confirms previous results reported in the literature, obtained in other measurement campaigns. Furthermore, the parameters of the best fit of such quantities and the robust regression fit coefficients of their relations have been analytically described and listed. The hyperbolic relationship between the CB and the RMS-DS has also been assessed and modeled. In addition, the differences between two CB definitions, namely the statistical CB and the deterministic CB, have been discussed.

The in-home wiring, connecting a pair of outlets, can follow "unpredictable" paths, so that the electrical and the geometrical distances do not coincide. Nevertheless, the geometrical distance between two outlets can be statistically related to the maximum achievable rate. This allows to infer the coverage offered by a PLC systems similarly to the wireless scenario. For example, in the tested scenario, rates in excess of 1 Gbps can be sustained between outlets at distances smaller than 5 m. This application scenario is not uncommon, e.g., the connectivity between a set-top box and a TV. Moreover, signaling above 100 MHz, in particular up to 300 MHz, can provide achievable rate improvements. However, the spectral efficiency, i.e. the data rate per-unit-frequency, decreases significantly.

The correlation among channels that share, or not, the same transmitting or receiving plug, has been analyzed. The overall ensemble of pair of channels belonging to a given site is essentially uncorrelated. However, if the pair of channels are constrained to be associated to the same transmitter (broadcast channel), then a more pronounced correlation is found. Furthermore, even larger correlation is found if the latter study is limited to the amplitude of the CFR. It follows that the random phase of the channel significantly reduces the MU correlation. Similar results apply to the channels that share the same receiver outlet.

Finally, the line impedance in the range 1.8–100 MHz is discussed, showing that it can assume a broad set of values but, in general, the spread is more pronounced in the lower frequency range. Furthermore, the analysis of the reactive component highlights an inductive behavior. Instead, no clear relation between the line impedance and the CFR has been identified. However, the scatter plot of the line impedance components versus the CFR (in dB) highlights a high probability region that can be analytically described.

MIMO Extension

4

As discussed in the Introduction and then validated through numerical results in Chapter 3, the PLC technique is an established solution to convey high speed data content exploiting the existent power delivery infrastructure. Recent PLC standards, as HPAV2 [39], showed that it is possible to ensure data rates of about 1 Gbps and up to a maximum of 2 Gbps at the PHY. Such an impressive throughput is obtained by signaling in the extended frequency band between 2–86 MHz, making use of advanced multicarrier modulation schemes based on OFDM, and by enabling the use of MIMO solutions to further extend coverage or to provide higher data rates w.r.t. more conventional SISO PLC systems. Basically, a 2×4 MIMO communication can be established by exploiting the presence of multiple conductors, usually three, that reach each plug of the network. They are the phase (P), the neutral (N) and the protective earth (E). The latter is commonly used in many countries in order to provide a return path for the power supply short-circuit alternated currents (50 Hz) that take place in the presence of an insulation fault.

At the transmitter side, the signal is injected between pairs of wires. The transmission modes are referred to as delta, Δ. Due to the Kirchhoff's laws, only two Δ signals can be injected at the same time. At the receiver, the signal is observed between one conductor and a reference plane. The configuration is referred to as star-style and the number of star-style modes is three, as the number of wires. Typical devices that implement a large metal plane, which can act as a reference plane, are those that deploy large screens, e.g. modern televisions. Fortunately, this type of devices are exactly those that usually require a high speed data communication in order to deliver multimedia services. Therefore, they can enjoy the performance improvements introduced by the MIMO transmission. Furthermore, coupling between the wires and the physical earth, due to unbalanced parasitic capacities given by grounded devices, can be exploited to get another receiver mode, namely the common mode (CM) [78]. Basically, the CM flows with the same intensity and direction through P, N and E. With CM, the number of available modes at the receiver side is four. In order to clarify the deployed scheme,

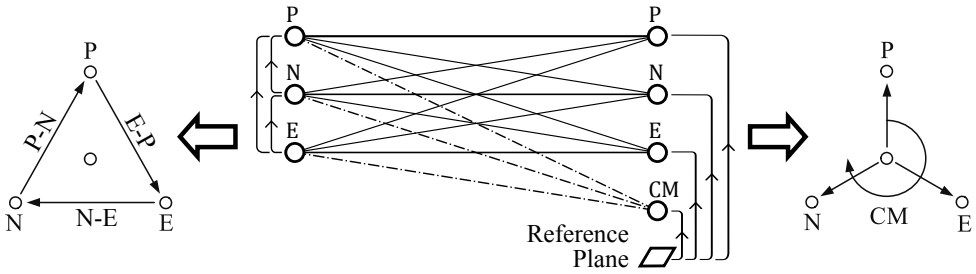

Figure 4.1: MIMO transmitting and receiving modes, according to STF-410.

the transmitting and receiving modes, which also comply with the special task force 410 (STF-410), are depicted in Figure 4.1. Due to electromagnetic interference (EMI) reasons, the CM is used only at the receiver side.

A preliminary analysis of the performance improvements achieved through the use of a 2×4 MIMO communication method, in the 4–30 MHz frequency band and in comparison with the SISO system, is reported in [79]. Herein, AWGN is assumed and spatial multiplexing, through beamforming at the transmitter side and ZF detection at the receiver, is discussed. Under the same system assumptions, precoded spatial multiplexing is considered in more detail in [80], while [81] describes implementation and results of the MIMO PLC feasibility study. Otherwise, this chapter aims to investigate the effect of a colored and correlated noise (rather than AWGN), as well as the performance improvement provided by the frequency extension up to 86 MHz, considering the MIMO PLC channel capacity. The 2×4 Δ-style to star-style MIMO communication channel is considered. An extension to the 0–100 MHz frequency band, and the assumption of colored noise, instead of white noise, was already done in [83]. However, in this case, the 2×2 MIMO channel with a Δ-style mode configuration, at both the transmitter and the receiver ends, was taken into account.

The purpose of this chapter is to evaluate the MIMO PLC performance in the extended frequency range 2–86 MHz that is foreseen by the latest PLC standards [39] for the next generation PLC systems. A comparison is performed between different MIMO configurations and precoding schemes, taking into account a 2×4 MIMO communication channel, thus, exploiting the additional CM at the receiver side. The focus is on a Δ-style feeding mode and a star-style receiving mode. Furthermore, the presence of a colored (in frequency) and correlated (between different receiving modes) Gaussian noise is assumed. Concerning the channel, the database that was collected by the STF-410, which is part of the European Telecommunications Standards Institute (ETSI), during an experimental measurement campaign across Europe [78] is exploited. This allows to obtain fair results that estimate with good approximation the performance that are achievable on real PLC networks. The measurements were performed in the 1–100 MHz frequency range. As for the in-home SISO case in Section 3.2, a concise statistical analysis of the MIMO channels is provided, in addition to what has been already done in [85]. Namely, we study the CDF

of the ACG and the mean value of the eigen-spread, as a function of frequency. Concerning the noise, we model it from the experimental results reported in [85] and [108]. It should be noted that in [85] the channel capacity distribution was evaluated assuming an equal PSD constraint over the whole frequency range, as well as an uncorrelated AWGN noise. Otherwise, we consider a PSD constraint compliant with the HPAV2 standard [39], as specified in Section 4.4, and a colored and correlated noise.

The comparisons are made assuming both perfect or no channel state information (CSI) knowledge at the receiver side. The results are provided in terms of maximum achievable rate, which is the channel capacity under the Gaussian background noise assumption [145]. In [108] and [126], other performance analysis were made assuming the channel configuration to be Δ-style at both the transmitter and the receiver ends. While, in our case, the Δ-style and star-style structures are considered at the transmitter and the receiver sides, respectively. Moreover, the optimal joint design of the transmit and receive signal processing scheme is discussed and the capacity, through numerical simulations, is evaluated. Finally, the performance improvements provided by the use of MIMO schemes w.r.t. SISO are assessed.

The remainder of the chapter is structured as follows. First, in Section 4.1, we deal with MIMO channel characterization. Later, in Section 4.2, the MIMO noise covariance matrix model, that we have derived from the experimental evidence, is detailed. In Section 4.3, the system architecture is presented. Then, in Section 4.4, the numerical results are provided. Finally, the main findings of this chapter follow.

4.1 MIMO Channel Properties

The MIMO PLC system is studied from an experimental basis. Firstly, the idea behind the MIMO transmission scheme, when applied to the PLC context, is described. Then, a concise statistical characterization of the MIMO CFR is proposed. Finally, a model for the MIMO noise covariance matrix generation is presented and detailed. In this respect, we remark that the channel analysis is based on the knowledge of the actual measured channel responses, while the noise model has been derived from the main findings reported by the STF-410 and in [108].

4.1.1 System Principle

When more than two conductors are present, a communication over multiple wires can be established. In general, due to Kirchhoff's laws, with N conductors, only $N-1$ channels are linearly independent, and thus, available for transmission. Contrariwise, all the 4 star-style receiving modes can be used, although only three of them are linearly independent and the fourth one is a linear combination of the other three modes. However,

the exploitation of the fourth mode at the receiver provides a noticeable signal-to-noise ratio (SNR) improvement, as it will be shown in Section 4.4.

We follow the approach that was proposed by the STF-410. The resulting MIMO modes are depicted in Figure 4.1. Basically, PLC devices can signal differentially between pairs of wires P, N and E, namely, P-N, P-E and N-E, and receive between P or N or E and the reference plane. To enforce the physical earth path, at the receiver, the coupler is connected to a ground plate of approximately one squared-meter area. In this respect, we note that flat TVs are equipped with big metal backplanes that can act as a ground plate [146]. Moreover, the CM can be used as a further received signal in order to obtain a 2×4 MIMO communication system. The feeding and receiving configurations are referred to as Δ and star, respectively. The Δ-style modes P-N, P-E and N-E are labeled as Δ_{tx}, with the corresponding index $tx \in \{1,2,3\}$, while the star-style modes P, N, E and CM as s_{rx}, with $rx \in \{1,2,3,4\}$, respectively. Given the aforementioned Kirchhoff's constraint, we focus only on the feeding modes Δ_1 and Δ_2. Instead, we consider all the star-style receiving modes, plus the CM, in order to assess the performance improvements due to the CM exploitation, although it is linearly dependent from the other three modes.

4.1.2 CFR Statistics

We contributed to the experimental measurement campaign that was performed by the STF-410 across Europe to collect information about MIMO channels. A total amount of 353 MIMO channels were acquired. For further details the reader is referred to [78].

Measurements were performed in the frequency domain, according to the measurement procedure that was detailed in [78] and followed by all members of the STF-410 to collect data. We collected 1601 frequency samples of the scattering parameters, in the 1–100 MHz frequency range, for each one of the 353 acquired MIMO channels. Therefore, the resolution in frequency is $\Delta f = 61.875$ kHz. In this work, we focus on the 2–86 MHz frequency range, as specified by the HPAV2 standard [39], and we define the CFR as the scattering parameter S_{21}. The quantity $H_{s_{rx},\Delta_{tx}}(f)$ denotes the CFR between the Δ-style transmitting port Δ_{tx} and the star-style receiving port s_{rx} at frequency f, where $tx = 1, 2$ and $rx = 1, 2, 3, 4$. Hence, the 4×2 CFR matrix $\mathbf{H}(f)$ is defined, in which the (s_{rx},Δ_{tx})-th element corresponds to $H_{s_{rx},\Delta_{tx}}(f)$.

In the following, the statistics of the measured channels is investigated. Unlike what has been done in [82] and [85], that assess the overall CFR distribution of the entire database of collected measurements, we focus on the ACG that is computed, according to equation (2.12), for each transmitter-receiver mode pair in the considered MIMO scheme, as follows

$$\mathcal{G}_{s_{rx},\Delta_{tx}} = 10\log_{10}\left(\frac{1}{M}\sum_{m=M_1}^{M_2}|H_{s_{rx},\Delta_{tx}}(m)|^2\right) \quad \text{[dB]}, \tag{4.1}$$

where $M_1\Delta f = 2$ MHz, $M_2\Delta f = 86$ MHz and $M = M_2 - M_1$. Figure 4.2 shows the

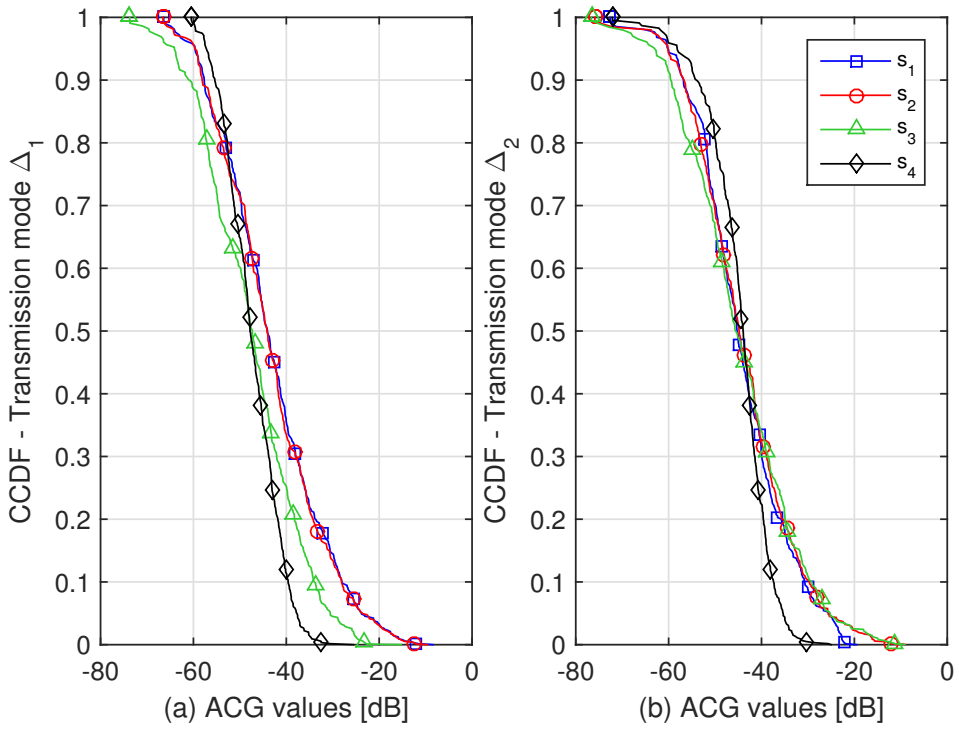

Figure 4.2: C-CDF of the ACG as a function of the MIMO modes. From left to right, results for Δ_1 (a) and Δ_2 (b) transmission modes are shown.

C-CDF of the ACG as a function of the signaling mode. We note the followings. First, in terms of ACG, s_1 and s_2 are equivalent. Second, when the transmission mode is Δ_1, the ACG of s_3 is 3 dB less than that of s_1 and s_2. Instead, when the transmission mode is Δ_2, the distribution of the ACG of s_3 is close to that of s_1 and s_2. Third, the ACG of s_4 is less spread than that of the other receiver modes. Indeed, the ACG of the CM is nearly -30 dB for both the Δ_1 and Δ_2 modes, whereas that of the other modes spans up to -20 dB. Finally, the ACG of s_4 behaves similarly regardless the transmission mode. Note that the values in Figure 4.2 concern an average gain, computed as in (4.1), and not the effective CFR gain.

Now, we perform the analysis of the singular value decomposition (SVD) of the MIMO channels in terms of eigen-spread. In comparison to [82] and [85], that assess both the singular values and their eigen-spread distribution for all the measurements and frequency samples together, we provide the eigen-spread percentiles for each distinct transmitter-receiver mode pair, as a function of frequency. The aim is to magnify the frequency dependence for each MIMO transmission-reception modes combination. The SVD of the channel matrix $\mathbf{H}(f)$ reads

$$\mathbf{H}(f) = \mathbf{U}(f)\mathbf{D}(f)\mathbf{V}^{\dagger}(f), \tag{4.2}$$

where $\mathbf{V}$ and $\mathbf{U}$ are unitary matrices, $\mathbf{D}$ contains the singular values of $\mathbf{H}$, and $\{\cdot\}^{\dagger}$ denotes the hermitian operator. The channel matrix $\mathbf{H}$ is a 4×2 matrix, therefore, the maximum number of singular values is 2. We denote the singular values of $\mathbf{H}(f)$ with $d_i(f)$, where

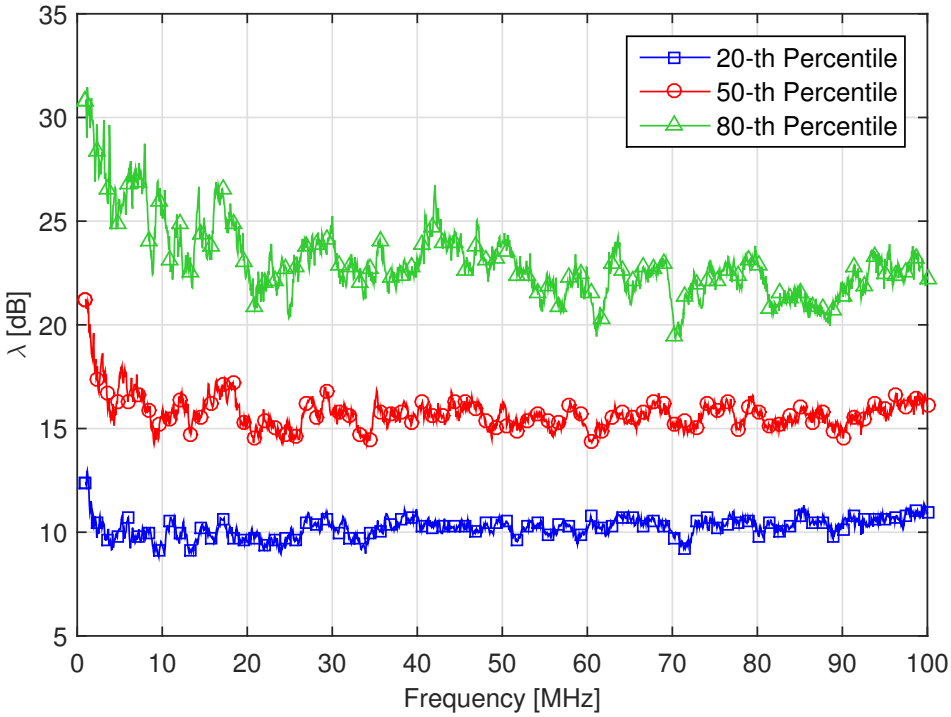

Figure 4.3: 20-th, 50-th and 80-th percentile of the eigen-spread as a function of the frequency.

$i = 1, 2$, and we define the eigen-spread as $\lambda(f) = d_1(f)/d_2(f)$ [108]. Without loss of generality, we assume $d_1(f) > d_2(f)$, computing λ for all channels and frequencies to obtain its statistics.

Figure 4.3 depicts 20-th, 50-th and 80-th percentiles of λ, in dB scale, as a function of frequency. We note that the channels are slightly more correlated in the lower frequency range, where λ is more spread. Instead, the 20-th percentile is almost frequency independent.

4.1.3 Spatial Correlation

In the MIMO scenario, the PLC channels are correlated due to the symmetry and determinism of the wiring structure. Within the considered frequency range, the correlation is provided in terms of normalized spatial covariance $\chi_{\ell,p}(f)$, defined as in (2.10). The different MIMO channels are identified by $\ell, p \in \{\text{P, N, E, CM}\}$, which refer to the different considered star-style receiving modes, given the same Δ-style transmitting mode. For example, the label P⇒N indicates the correlation among the channels to the phase and neutral star-style modes, having the same Δ transmitting mode, in practice $\chi_{\text{P,N}}(f)$.

The spatial correlation along frequency, between all the possible combinations of different star-style receiving modes and the two possible Δ-style transmitting modes, namely P-N (Δ_1) and P-E (Δ_2), are reported in Figure 4.4 and Figure 4.5, respectively. The figures show very high levels of $\chi_{\ell,p}(f)$ for all the combinations, especially at high fre-

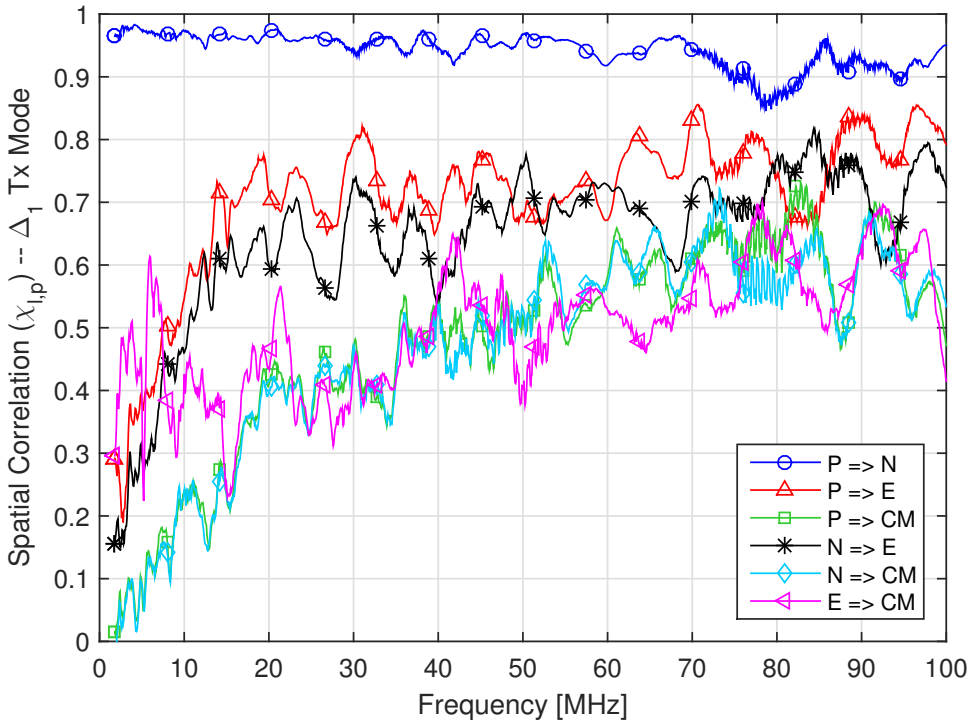

Figure 4.4: Spatial correlation, along frequency, for all the possible star-stile receiving modes, namely N, P, E, and CM, given the same Δ-style transmitting mode P-N.

quencies, where the cross-talk effects become prominent. In particular, when considering the P-N Δ-style transmission mode, depicted in Figure 4.4, high levels of correlation are exhibited among the channels P⇒E and N⇒E, with the highest values experimented among the P⇒N channels responses, especially for lower frequencies. Contrariwise, if the other Δ-style transmitting mode P-E is considered, the highest level of correlation is exhibited among the P⇒E CFRs, as it can be noted in Figure 4.5. The correlation among the channels P⇒N and N⇒E is still high, but slightly lower, as happens for the P⇒E and N⇒E channels for the Δ_1 transmission in Figure 4.4. However, the frequency dependent behavior of $\chi_{\ell,p}(f)$ for all the receiving combinations when considering the Δ_2 transmission mode in Figure 4.5 is limited compared to the profiles exhibited assuming the Δ_1 transmission mode in Figure 4.4. Furthermore, the P⇒N correlation for the Δ_1 (P-N) mode is slightly higher than the P⇒E correlation for the Δ_2 (P-E) mode.

The above mentioned differences in the correlation values and profiles are due to the fact that the power is delivered through the phase (P) and the neutral (N) wires, which are positioned one next to the other and follow the same path from the transmitter to the receiver. Contrariwise, although the protective earth (E) wire follows almost the same path, it further comprises the device chassis (for grounding purposes in case of faults), as well as the wires branches deployed for an overall grounding to the physical earth. Furthermore, the fact that the correlation values among the same receiving modes pair depend on the considered transmission mode, especially between the channels with the corresponding receiving star-style modes exploited at the transmitter side (in Δ configu-

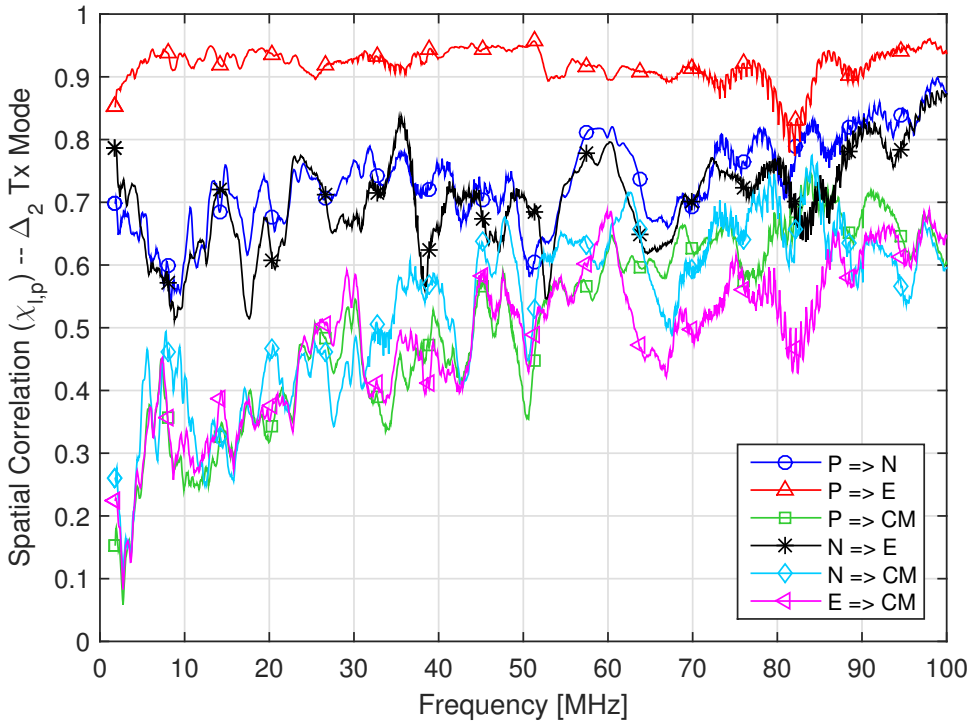

Figure 4.5: Spatial correlation, along frequency, for all the possible star-stile receiving modes, namely N, P, E, and CM, given the same Δ-style transmitting mode P-E.

ration), is justified by the following considerations.

According to the adopted measurement setup, the network scattering parameters matrix (S), and thus the CFR, among one Δ-style transmitting port and one star-style receiving port are measured referring to a 50 Ω load, while closing all the other unused ports always on a 50 Ω impedance. Thus, when measuring the CFR between the same Δ-style transmitting port and each one of the two star-style receiving modes corresponding to the wires supplied at the transmitter, it is almost like considering the same electrical circuit. This is due to the Kirchhoff's law for the voltages and the currents in the network. Hence, since these measured CFRs approximately refer to the same underlying electrical circuit, the correlation exhibited among the corresponding star-style receiving modes is very high. However, the degree of correlation is less than one, i.e. full correlation, since the considered measurement point for the two CFRs is not exactly the same and because part of the signal, injected in the measurement process, couples with the other passive conductors in different ways. This different energy dispersion experienced by the two modes involves that the correlation coefficient is less than the unity. Now, it is easy to understand why the correlation among the P⇒N channels given the P-N Δ-style transmitting mode, depicted in Figure 4.4, experience such high correlation values, similarly to what happens for the P⇒E channels when assuming the P-E Δ-style transmitting mode, represented in Figure 4.5.

Obviously, in addition to the spatial correlation, also the MU correlation, defined as in Section 2.1.5 and assessed in Section 3.4 for the SISO case, should be considered. Indeed,

as detailed in Section 2.1.5, these two quantities refer to different concepts. In particular, the MU correlation refers to a multi-point communication channel towards different outlets, while the spatial correlation concerns a point-to-point transmission exploiting a MIMO communication channel, i.e. the multiple wires that connect the same transmitting and receiving plugs. Furthermore, as an additional effect, not only the MIMO channel responses are correlated, but also the noise, as discussed in the next section.

4.2 Noise Covariance Matrix Generation

The noise in the MIMO context has not been thoroughly investigated yet. However, some experimental results for the in-home scenario are reported in [85] and [108]. The analysis of Section 4.4 requires the knowledge of the covariance matrix of the noise experienced by the star-style modes. In this respect, since we own only the ETSI database of channel measurements and not that of the noise PSD profiles, we propose a model strategy that exploits both the experimental evidence reported in [85] and [108]. We proceed as follows. We assume the noise to be Gaussian with zero mean and we focus on the frequency domain, denoting the covariance between the noise of the modes s_ℓ and s_p with $\mathcal{K}_{\ell,p}(f) = E[N_{s_\ell}(f)N^*_{s_p}(f)]$, where $\ell, p = 1, \ldots, 4$ and $N_{s_\ell}(f)$ is the Fourier transform of the noise experienced by the mode s_ℓ. We let the main-diagonal elements of the covariance matrix, namely $\mathcal{K}_{\ell,\ell}(f)$, be equal to the PSD of the measured noise. In this respect, we exploit the results provided by the STF-410 in [85] that are depicted in Figure 4.6. As it can be noted, the noise PSD floor sharply increases in the neighborhoods of 87 MHz for all the modes due to the interference of the FM broadcasting radio. Moreover, the CM experiences the highest noise. According to [85], the auto-correlation of mode CM, i.e. $\mathcal{K}_{44}(f)$, is approximately 5 dB greater than the noise experienced by the other modes.

Now, we focus on the cross-correlation terms, i.e., $\mathcal{K}_{\ell,p}(f)$ with $\ell \neq p$. The noise received on different ports is correlated [85]. Therefore, $\mathcal{K}_{\ell,p}(f) \neq 0$. We model the covariance matrix element $\mathcal{K}_{\ell,p}(f)$ as

$$\mathcal{K}_{\ell,p}(f) = \alpha_{\ell,p} \left(\mathcal{K}_{\ell,\ell}(f) + \mathcal{K}_{p,p}(f) \right), \tag{4.3}$$

where $\alpha_{\ell,p}$ is a constant coefficient that can be obtained as follows. We validate the model proposed in (4.3) starting from the correlation coefficient [108]

$$\Phi_{\ell,p}(f) = \frac{\left| \mathcal{K}^{\Delta}_{\ell,p}(f) \right|}{\sqrt{\mathcal{K}^{\Delta}_{\ell,\ell}(f)\mathcal{K}^{\Delta}_{p,p}(f)}}, \tag{4.4}$$

where $\mathcal{K}^{\Delta}_{\ell,p}(f) = E[N_{\Delta_\ell}(f)N^*_{\Delta_p}(f)]$ is the covariance between the noise of the modes Δ_ℓ and Δ_p, with $\ell, p = 1, 2$. Note that $N_{\Delta_1}(f) = N_{s_1}(f) - N_{s_2}(f)$, and similar relations hold for the other Δ-mode noise terms. In [108], it was shown that $\Phi_{\ell,p}(f)$, as well as

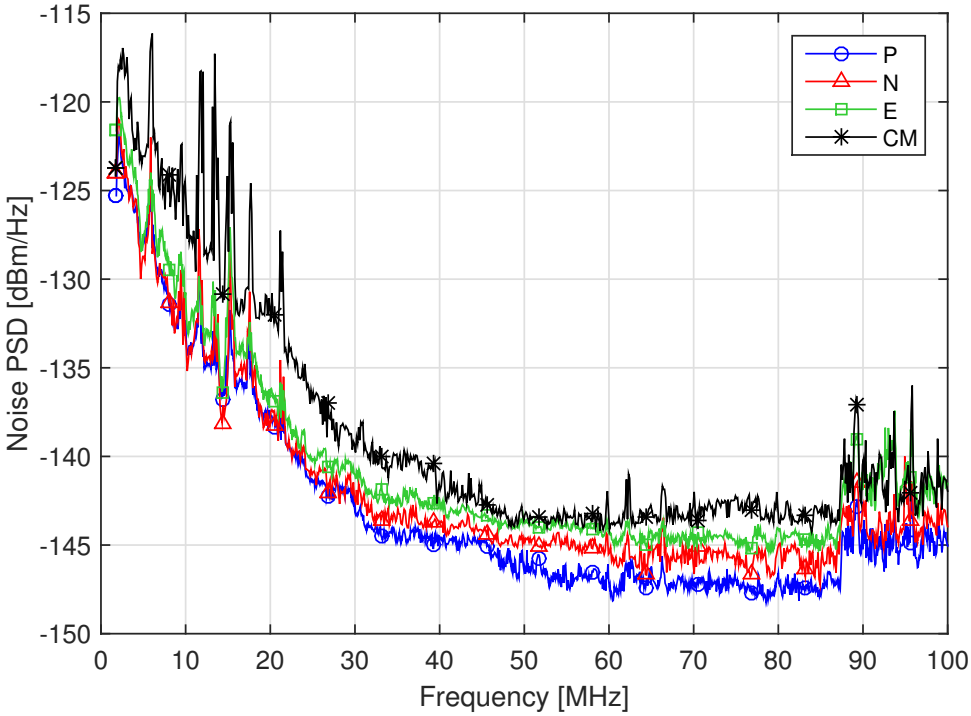

Figure 4.6: Noise PSD profile for all the star-stile receiving modes, namely N, P, E, and CM, provided by the ETSI STF-410 in [85].

$\mathcal{K}^{\Delta}_{\ell,\ell}(f)$, exhibit approximately the same frequency-decreasing profile, regardless the pair of considered modes. Therefore, we speculate that $\mathcal{K}^{\Delta}_{12}(f)$, $\mathcal{K}^{\Delta}_{13}(f)$ and $\mathcal{K}^{\Delta}_{23}(f)$ differ by a constant value from each other. Let us compute

$$\mathcal{K}^{\Delta}_{12}(f) - \mathcal{K}^{\Delta}_{13}(f) = \mathcal{K}_{11}(f) + \mathcal{K}_{22}(f) - 2\mathrm{Re}\{\mathcal{K}_{12}(f)\}, \tag{4.5}$$

where $\mathrm{Re}\{\cdot\}$ denotes the real operator. We note that the left side of (4.5) is a constant value, regardless frequency. Therefore, both sides of relation (4.5) are frequency independent and $\mathcal{K}_{12}(f)$ should compensate the frequency variations due to $\mathcal{K}_{11}(f)$ and $\mathcal{K}_{22}(f)$. We extend the conclusion to all star-style modes. This proves the model in (4.3).

Now, we focus on the coefficient $\alpha_{\ell,p}$. We introduce the time domain correlation coefficient $\phi_{\ell,p}$, given by [85]

$$\phi_{\ell,p} = \frac{E[n_{s_\ell}(t)n_{s_p}(t)] - m_{s_\ell}m_{s_p}}{\sqrt{\sigma^2_{s_\ell}\sigma^2_{s_p}}} = \frac{\int \mathcal{K}_{\ell,p}(f)df}{\sqrt{\int \mathcal{K}_{\ell,\ell}(f)df \int \mathcal{K}_{p,p}(f)df}}, \tag{4.6}$$

where μ_{s_ℓ} and $\sigma^2_{s_\ell}$ are the mean and the variance of the noise $n_{s_\ell}(t)$ (in the time-domain) experienced by the mode s_ℓ. Hence, we substitute (4.3) in (4.6) and we obtain

$$\alpha_{\ell,p} = \phi_{\ell,p}\frac{\sqrt{\int \mathcal{K}_{\ell,\ell}(f)df \int \mathcal{K}_{p,p}(f)df}}{\int \mathcal{K}_{\ell,\ell}(f)df + \int \mathcal{K}_{p,p}(f)df}, \tag{4.7}$$

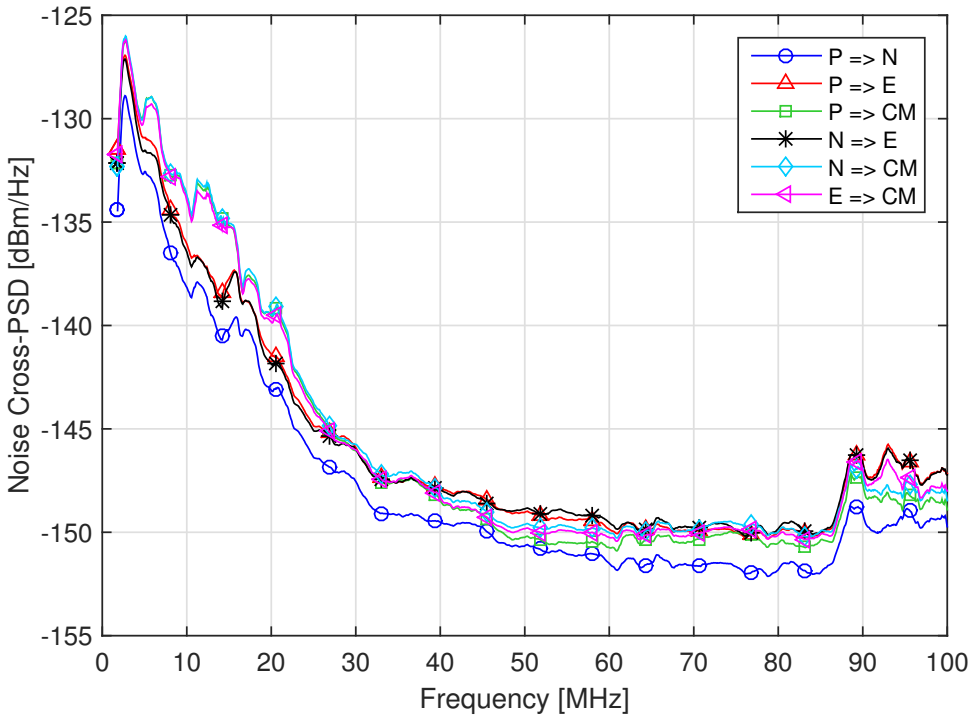

Figure 4.7: Noise C-PSD profile for all the combinations of star-stile receiving modes, computed according to the proposed generation process.

where $\phi_{\ell,p}$ is the time-domain correlation coefficient that we define as in [85]. We generate $\phi_{\ell,p}$ randomly, according to the statistics that was presented in [85].

In order to have an idea of how and how much the noise modes are correlated at the receiver side, the cross-PSD (C-PSD) values, i.e. the behavior, along frequency, of the covariance matrix out-of-diagonal elements, generated according to the above detailed procedure, are depicted in Figure 4.7. The C-PSD allows us to highlight the spatial cross-correlation that exists between the noise signals. In particular, the C-PSD terms are computed assuming the average value of $\phi_{\ell,p}$ for each possible combination, in order to obtain an average profile. As for the channel spatial correlation discussed in Section 4.1.3, the different labels correspond to all the possible combinations of the noise star-style receiving modes. For example, P⇒N refers to the C-PSD profile exhibited between the noise modes P and N, when the same Δ-style transmitting mode is considered.

From Figure 4.7, it can be noted as the C-PSD profiles resemble the PSD profiles depicted in Figure 4.6, even if slightly shifted downwards. The shift effect is mainly due to the time-domain correlation coefficient $\phi_{\ell,p}$ that ranges in between 0 and 1. Instead, the similar trend, w.r.t. the PSD profiles in Figure 4.6, is an expected result since the out-of-diagonal elements are a linear combination of such PSD profiles, i.e. the diagonal elements of $\mathcal{K}_{\ell,p}$, according to (4.3). Furthermore, the lowest C-PSD profile is exhibited by P⇒N. This is, since, the corresponding PSD profiles, reported in Figure 4.6, are the lowest ones. Instead, the combinations with the CM show the highest trend, which is similar for all the combinations. However, Figure 4.7 shows as the C-PSD exhibits

non-negligible levels and significant differences for almost all spatial modes combinations.

4.3 System Model

We consider an OFDM-MIMO PLC channel with N_T transmit and N_R receive signals. For each sub-carrier m, the general processing scheme is shown in Figure 4.8.

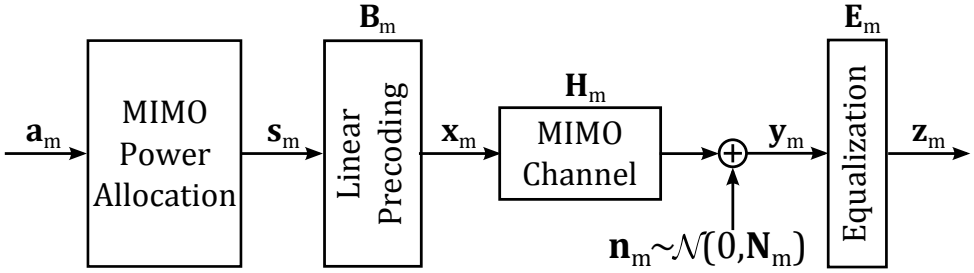

Figure 4.8: MIMO PLC coding scheme at each m-th sub-carrier.

The N_T transmitted symbols at the m-th frequency, expressed by the $N_T \times 1$ vector $\mathbf{a}_m$, are weighted by the power allocation coefficients and precoded by the $N_T \times N_T$ matrix $\mathbf{B}_m$ (beamforming), yielding the $N_T \times 1$ transmitted signal $\mathbf{x}_m$.

We assume zero mean and unit energy uncorrelated symbols, i.e. $E[\mathbf{a}_m \mathbf{a}_m^\dagger] = \mathbf{I}_{N_T}$, which is the $N_T \times N_T$ identity matrix. Thus, the matrix $\mathbf{Q}_m = E[\mathbf{s}_m \mathbf{s}_m^\dagger]$ of the signal $\mathbf{s}_m = \mathbf{Q}_m^{1/2} \mathbf{a}_m$ is diagonal and represents the power allocation strategy of the total available power P_T. In our system $P_T = P_m$, where P_m is the PSD mask at the m-th carrier.

At each frequency, the $N_R \times 1$ received signal $\mathbf{y}_m$ at the m-th sub-carrier is equal to

$$\mathbf{y}_m = \mathbf{H}_m \mathbf{x}_m + \mathbf{n}_m, \tag{4.8}$$

where $\mathbf{n}_m \sim \mathcal{N}(0, \mathbf{N}_m)$ is the $N_R \times 1$ additive Gaussian noise with zero mean and covariance matrix $\mathbf{N}_m = E[\mathbf{n}_m \mathbf{n}_m^\dagger]$. The noise is colored in frequency and correlated in the spatial domain, the reader is referred to Section 4.2 for details. At the receiver, $\mathbf{y}_m$ is equalized by the $N_T \times N_R$ matrix $\mathbf{E}_m$ to yield the $N_T \times 1$ detected vector $\mathbf{z}_m$. For an OFDM transmission system the capacity of the MIMO channel can be computed, similarly to (2.21), as [145]

$$\mathcal{C} = \Delta f \sum_{m \in \mathcal{I}_{ON}} \log_2 \left[\det \left(\mathbf{I}_{N_R} + \mathbf{N}_m^{-1} \mathbf{H}_m \mathbf{K}_m \mathbf{H}_m^\dagger \right) \right], \tag{4.9}$$

where $\mathcal{I}_{ON}$ is the set of all active sub-carriers and $\mathbf{K}_m = E[\mathbf{x}_m \mathbf{x}_m^\dagger]$ is the covariance matrix of the transmitted signal at the m-th carrier. We assume a sufficiently high number of sub-channels so that the impact of the cyclic prefix (CP) on the overall capacity can be neglected. Anyway, the consideration of the CP overhead leads to a linear reduction on

the effective capacity observed by the end user. Therefore, the actual performance can be trivially obtained from the overall capacity results provided in the following.

4.3.1 Full CSI Knowledge at the Transmitter

The optimal processing scheme assumes perfect knowledge of the channel response and the noise covariance matrix at the transmitter side [147]. When this information is available, we can allocate the total available power in the most efficient way, as follows. First, we whiten the noise pre-multiplying the received signal by $\mathbf{N}_m^{-1/2}$, where $\mathbf{N}_m^{-1} = \mathbf{N}_m^{-1/2}\left(\mathbf{N}_m^{-1/2}\right)^*$. We obtain

$$\mathbf{N}_m^{-1/2}\mathbf{y}_m = \hat{\mathbf{H}}_m\mathbf{x}_m + \mathbf{w}_m, \tag{4.10}$$

where $\hat{\mathbf{H}}_m = \mathbf{N}_m^{-1/2}\mathbf{H}_m$ is the resulting channel matrix, which combines the effect of noise correlation and the channel attenuation, while $\mathbf{w}_m \sim \mathcal{N}(0, \mathbf{I}_{N_R})$ is the AWGN noise.

Then, we compute the SVD of the matrix $\hat{\mathbf{H}}_m$, i.e. $\hat{\mathbf{H}}_m = \mathbf{U}_m\hat{\mathbf{D}}_m\mathbf{V}_m^\dagger$, and we exploit the water-filling algorithm to obtain the optimal power allocation. The optimal precoding matrix $\mathbf{B}_m$ is the unitary matrix $\mathbf{V}_m$ [147]. Hence, the optimal transmitted signal covariance matrix reads $\hat{\mathbf{K}}_m = \mathbf{V}_m\hat{\mathbf{Q}}_m\mathbf{V}_m^\dagger$. At the receiver, after the whitening filter, we apply ZF equalization through the matrix

$$\hat{\mathbf{H}}_m^+ = \left(\hat{\mathbf{H}}_m^\dagger\hat{\mathbf{H}}_m\right)^{-1}\hat{\mathbf{H}}_m^\dagger, \tag{4.11}$$

where $\hat{\mathbf{H}}_m^+$ is the pseudo inverse of the channel matrix $\hat{\mathbf{H}}_m$. Under the optimal allocation strategy and according to the described linear precoding scheme, the MIMO PLC channel capacity in (4.9) becomes

$$\mathcal{C} = \Delta f \sum_{m\in\mathcal{I}_{ON}} \log_2\left[\det\left(\mathbf{I}_{N_R} + \hat{\mathbf{D}}_m\hat{\mathbf{Q}}_m\hat{\mathbf{D}}_m^\dagger\right)\right], \tag{4.12}$$

where the MIMO channel has been diagonalized into $r = \text{rank}[\mathbf{H}_m]$ spatially parallel subchannels, since $\hat{\mathbf{D}}_m$ is a diagonal matrix. For the MIMO transmission scheme exhibited by our channel measurements, the multiplexing order is $r = \min(N_T, N_R) = 2$.

4.3.2 No CSI Knowledge at the Transmitter

When the transmitter has no knowledge about the channel, the optimal power distribution is the uniform one, namely $\mathbf{K}_m = P_T/N_T\mathbf{I}_{N_T}$. In this case, no linear precoding is possible, i.e. $\mathbf{B}_m = \mathbf{I}_{N_T}$. Furthermore, at the receiver side, ZF detection is accomplished according

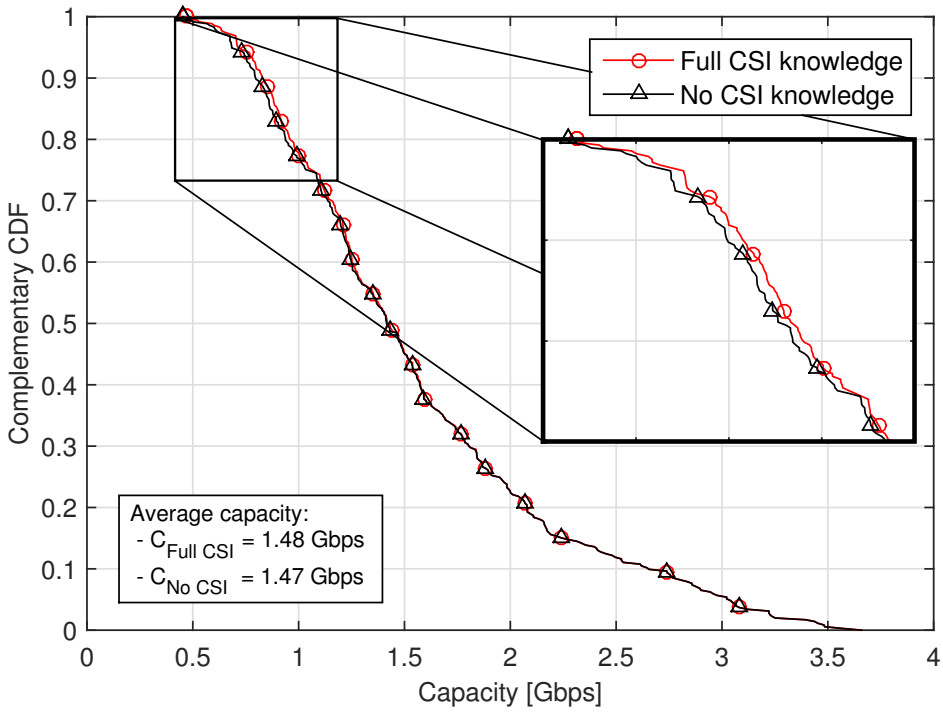

Figure 4.9: Capacity C-CDF with and without the CSI knowledge at the transmitter side, exploiting a 2×4 MIMO scheme. The average capacity is also reported.

to (4.11), where we substitute $\hat{\mathbf{H}}_m$ with $\mathbf{H}_m$. The capacity formulation turns into

$$\mathcal{C} = \Delta f \sum_{m \in \mathcal{I}_{ON}} \log_2 \left[\det \left(\mathbf{I}_{N_R} + \frac{P_m}{N_T} \mathbf{N}_m^{-1} \mathbf{H}_m \mathbf{H}_m^{\dagger} \right) \right], \tag{4.13}$$

where P_m is the power (in Watt) drawn from the PSD constraint at the m-th sub-carrier.

4.4 Numerical Results

In this section, the performance of the coding schemes, when the transmitter has perfect knowledge about the CSI or when it does not have any CSI information, are discussed. Furthermore, the performance of different MIMO configuration schemes are putted in comparison. The results are provided in terms of capacity, computed as described in Section 4.3. To this aim, we fulfill the specifications of the HPAV2 standard [39]. Namely, we consider the frequency range 2–86 MHz with a PSD limit of -50 dBm/Hz and -80 dBm/Hz in the range 2–30 MHz and 30–86 MHz, respectively. This is a constraint on the total transmit power per carrier, which could be divided among the different Δ-style spatial transmissions modes. Furthermore, the noise is assumed to be colored in frequency and spatially correlated, among the different star-style receiving modes, according to the model described in Section 4.2.

Figure 4.9 shows the differences between the capacity distribution achieved when the transmitter has perfect CSI knowledge, thus of both channel ($\mathbf{H}_m$) and noise covariance

($\mathbf{N}_m$) matrices for all $m \in \mathcal{I}_{ON}$, and when no CSI is available at the transmitter side. For both cases the optimal power allocation scheme has been implemented, i.e. water-filling and uniform, respectively. The two curves appear to almost overlap, but this is not true for low target rates. Indeed, the average difference in capacity, averaged among all the considered realizations, is in the order of 10 Mbps. Instead, the two curves actually overlap each other for high target rates, achieved with low probabilities. This is due to the high SNR exhibited in the range 2–30 MHz, which involves the optimal power allocation to be uniform. Thus, the capacity increase, due to CSI knowledge at the transmitter, becomes significant in the range 30–86 MHz, affected by low SNR. Moreover, there are a maximum of two equivalent and independent spatial SISO channels, obtained through the SVD. Thus, the optimal allocation strategy can be applied only between these two equivalent spatial channels, assuming the PSD limit at a certain frequency as a total power constraint for the spatial domain at the same frequency. This limitation further reduces the benefits of the optimal allocation, when compared to the uniform one. Anyway, the optimal power allocation leads to rates roughly 0.63 % greater in our simulations. The results in Figure 4.9 suggest that for high SNRs the feedback of the CSI and its overhead, as well as the linear precoding (beamforming) at the transmitter, can be avoided using an uniform power allocation, yet yielding high rates. This translates into a complexity reduction.

The advantages provided by MIMO w.r.t. single-input multiple-output (SIMO) and SISO schemes are depicted in Figure 4.10. Concerning MIMO, we feed two Δ-style modes and we receive all, or some, of the star-style modes. Instead, in the SIMO configuration we feed only Δ_1, whereas in the SISO implementation we assume that both the transmitter and the receiver are configured in Δ-mode. As Figure 4.10 shows, the larger the number of used ports by both sides (transmitter and receiver), the greater the capacity. In particular, it can be noted a significant increase in capacity going from single-input to multiple-input systems, taking into account multiple-output configuration. This is due to the doubling of the multiplexing order, or rank of the channel matrix, which changes from 1 to 2. Furthermore, the 2×4 MIMO case (HPAV2 standard) approximately doubles the capacity of the SISO scheme (HPAV specifications). This is a significant improvement, compared to conventional SISO systems, able to meet the increasing demand of high speed data communication requested by multimedia services.

4.5 Main Findings

We have discussed the use of the MIMO scheme in PLC networks when additive colored and correlated Gaussian noise is present. A brief CFR characterization, concerning the MIMO scenario, has been discussed. Additionally, the degree of correlation exhibited by the MIMO channels, when considering all the possible star-style receiving mode pairs and

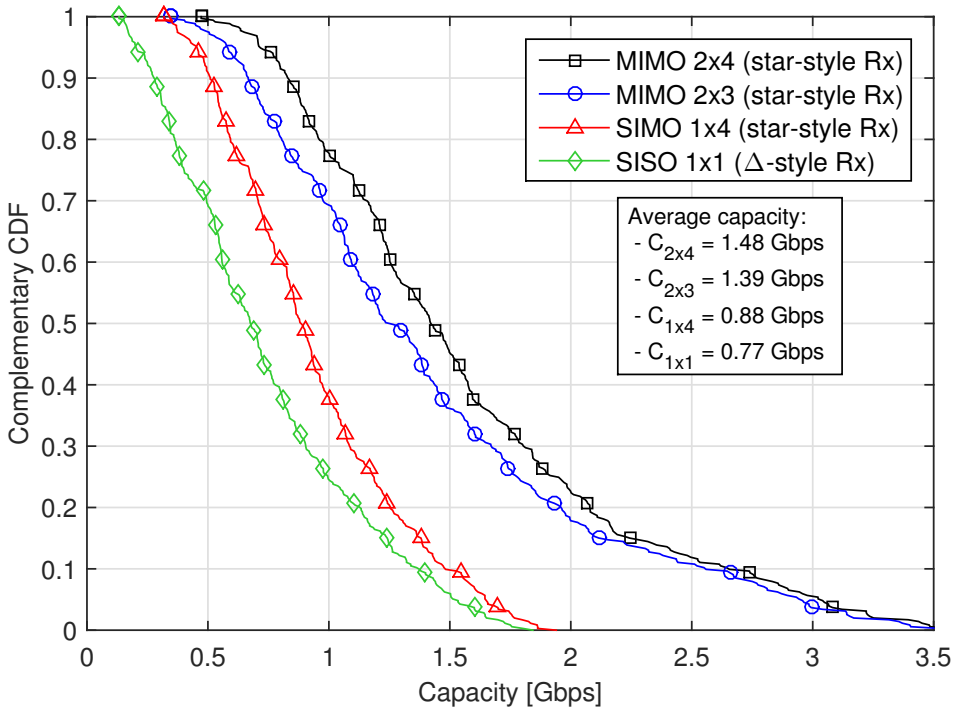

Figure 4.10: Capacity distribution comparison among SISO, SIMO and two different MIMO system configurations. The average capacity for each configuration is also shown.

the same transmitting mode, has been assessed. A detailed procedure for the computation of the MIMO noise covariance matrix, basing on noise measurements, has also been discussed.

The availability of both MIMO channel and noise PSD measurements allow the capacity evaluation, providing significant results, which are representative of the performance achievable on a real PLC scenario. In particular, we have compared the performance between different coding schemes that exploit, or not, the CSI to perform the optimal spatial allocation of the available power. The simulation results show that the CSI knowledge translates into a significant increase in performance only for bad channel realizations and low SNR values. For a high SNR, the uniform allocation strategy is optimal and no CSI feedback is required. Furthermore, we have shown that the increase in capacity, due to the exploitation of all the possible transmit and receive ports (2×4 in our case), outperforms any other coding scheme. Particularly, the 2×4 MIMO experimental channels analyzed in this chapter achieve a capacity that almost doubles that of a conventional SISO scheme.

5 In-Vehicle Scenario

The transformation of the conventional vehicles into efficient and intelligent systems requires the deployment of smart electronic components and the establishment of high-speed reliable data links for their interconnectivity. Up to now, this is typically achieved through dedicated wired data buses, e.g., local interconnect network (LIN) bus, controller area network (CAN) bus. However, the car wiring infrastructure is the third factor that contributes to the overall vehicle weight, immediately after the engine and the gearbox. Likewise, in the naval context more than 20 % of the total weight is due to the electric cables mass.

The increase of weight has a negative impact on the performance of vehicles and, ultimately, on the energy efficiency. Therefore, it is of great importance to develop communication technologies that can reduce the amount of wiring. Other than wireless, PLC promises to be a valuable candidate, as it can provide robust and reliable communication links by exploiting the existent in-vehicle power delivery infrastructure to convey data. Thus, it can enable the deployment of advanced automotive control applications that need relatively high-speed, flexibility and scalability, or distribute high-speed data streams from internet access, as well as support video streaming from cameras and multimedia or entertainment services. PLC channels are characterized by multipath propagation, generated by line discontinuities due to multiple branches and unmatched loads [3]. This translates into severe frequency selectivity, although, differently from the wireless case, PLC channels are mostly static (no mobility).

The most investigated areas of PLC have been so far related to home networking and communications for the (smart) power grid. Despite the intuitive feeling that PLC can be used for in-vehicle connectivity, no dedicated technology has been developed and not many research results have been published yet. As seen, in general, PLC is divided into two classes, namely NB and BB [3]. NB-PLC operates in the range of frequencies below 500 kHz and it is used for low rate applications, while BB-PLC enables the streaming of high-speed multimedia content, signaling up to 86 MHz, as proposed by the recent HPAV2

standard [39]. Moreover, a simplified low-power version of the BB HomePlug standard, called HomePlug Green PHY [40], can also be used as a valuable alternative to NB-PLC for low rate applications. In this respect, this standard has been adopted as a reference for communications between the electric vehicle and the charging station.

5.1 Related Research and Main Goals

In-vehicle PLC refers to the set of applications devoted to establish data links inside any means of transportation, i.e., cars, ships, planes, or trains. The investigation of in-car PLC has been documented in [46–50]. The in-ship environment is less investigated. Some results are shown in [53]. Moreover, PLC systems can find application also in more unconventional scenarios, such as in planes, in space crafts and in trains, as discussed in [55], [59] and [57], respectively.

In this chapter, the focus is on the in-car and the in-ship PLC scenarios. In-car PLC is challenged by a mixture of high channel attenuation, high levels of noise and by low values of the line impedance. The characterization of such quantities is of great importance for the design of optimal transmission techniques. In this respect, an online available database of 193 measurements, performed in a conventional car (CC), i.e. with combustion engine, was analyzed in [46]. Instead, in-car PLC channel models that follow a top-down and a bottom-up approach were described in [47] and [48], respectively. Moreover, noise impairments were modeled in [49] taking into account its periodic components.

Almost all the above cited papers deal with the CC, equipped with a fossil fuel combustion engine. In comparison, the EC scenario shows several differences, in terms of wiring structure, which is more pervasive due to the need of feeding the electric motors, and because of the presence of a number of electric machines, such as current drives and power converters, that inject a great deal of noise. Some studies, e.g. [89] and [90], characterize the PLC channel response and the noise of an electric car (EC) basing on experimental measurement campaigns. In [89], the line impedance and the noise introduced by the DC-DC converter of a compact EC, equipped with a lithium battery pack that provides up to 70 km of autonomy, were additionally analyzed. While, measurements of the CFR between the vehicle and the external grid, during battery charging, are performed in [90] together with the symbol error rate evaluation concerning a proposed CFR simulation model.

The aim of this chapter is to investigate and assess differences and similarities among the in-car and the in-ship scenarios. The measurement databases and the initial results reported in [89] and [54], which consider the in-car and the in-ship scenarios, respectively, are exploited and briefly recalled in Section 5.2 and Section 5.3. However, the analysis is more focused on how the network topology and the physical phenomena influence the channel characteristics, the statistical metrics, as well as the noise properties. In

particular, a thorough study on the metrics relationships, on the achievable performances and a detailed discussion on the background noise experienced by the EC, related to the motors state, are tackled. Furthermore, the investigation is performed under the same assumptions in order to provide results that can be compared among each other, as well as to other results computed considering different measurement databases. The analysis starts concerning the EC scenario, describing the network structure, the channel and line impedance properties, as well as the noise generated by the DC-DC converter and by the motor drives. The results are compared to the findings reported in [46], that refer to a CC. Then, the same analysis is performed for the in-ship scenario, reporting the main results computed relying on the measurements made in a large cruise ship [54]. The focus is on the channels belonging to the LV part of the distribution network. The BB frequency range is considered. Moreover, the channel response characteristics are studied in terms of ACG, RMS-DS, CB, and maximum achievable rate, i.e. the channel capacity.

Finally, an overall comparison is made considering also the conventional car and the in-home scenario. It will be shown that, despite the differences in network size and topology, as well as in channel characteristics and noise properties, the PLC, applied to the in-car and the in-ship scenarios, can achieve high and similar performance. The same transmitting power constraints, as those typically used in home networks, are considered.

5.2 In-Car Scenario

The in-car scenario is heterogeneous since it comprises vehicles with different powertrains and power grids. It includes EC, supplied by batteries, and CC, powered by fossil fuel, whose power grid characteristics significantly differ. Despite the great differences, reliable PLC is possible in both the environments, as shown by the results presented and discussed in the next sections.

Conventional cars are characterized by a massive wiring infrastructure, with an overall length of several kilometers, but with a limited number of junctions and small single cables length. Furthermore, the return conductor is often missing, since the vehicle chassis is used for it. The noise coming from the powertrain is limited and mainly due to the activity of the spark plugs and the control unit [49, 94].

Electric vehicles, where the powertrain comprises electric motors controlled by drives, are more affected by noise. The power grid consists of two sub-networks. The high-power sub-network feeds the motors and it is directly connected to the battery pack. The low-power LV sub-network feeds the remaining loads, as the derivation panel, the auxiliary devices and the lights. Both sub-networks are direct current (DC), and the low-power sub-network is fed from the high-power sub-network via a DC-DC converter, as depicted in Figure 5.1. Therefore, the two circuits are not separated and the large noise components, generated by the motor drives, propagate and radiate toward the low-

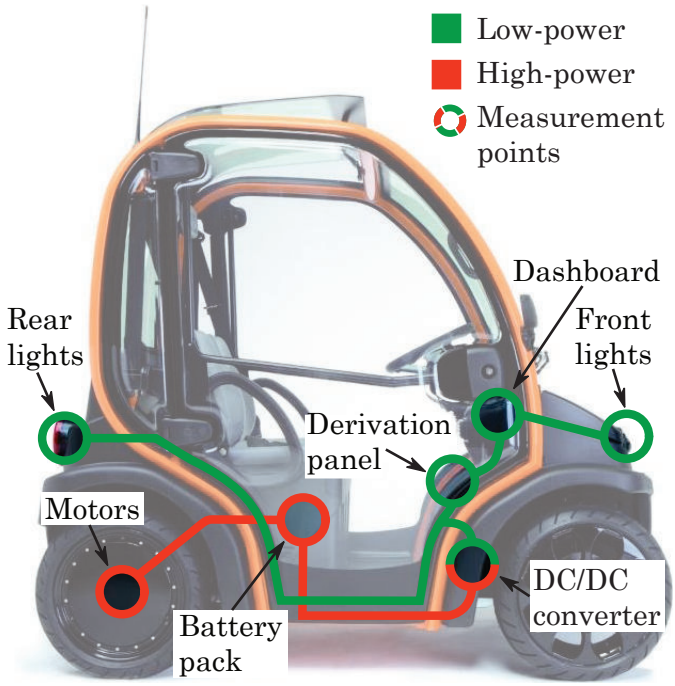

Figure 5.1: Vehicle under test, namely the Estrima Birò. The power distribution grid scheme and the measurement points are also depicted.

power sub-network, where PLC devices are connected. The resultant noise exhibits both periodic and impulsive components [89].

Figure 5.1 shows the power grid scheme and the measurement points of the electric vehicle under test. The vehicle is a best seller in its market, namely the Estrima Birò, a compact 4-wheels electric car manufactured in Italy. The car is equipped with three-phase brushless electric motors, one for each of the two rear wheels. The electric motors are connected to the 48 V high-power sub-network (in red). A DC-DC converter feeds the 12 V low-power sub-network (in green).

In the 12 V sub-network, the DC-DC converter is connected to the derivation panel, which, in turn, feeds all the peripherals, as the lights and the dashboard. Therefore, the 12 V sub-network exhibits a star-style structure, with the derivation panel being the center. Peripherals are connected to the derivation board through both positive and negative feeding conductors, with nearby devices exploiting the same negative wire. In general, the underlying network deploys cables with length up to 3 meters.

5.2.1 In-Car Channel Properties

In this section, the CFR of the 84 measurements obtained from [89] are shown and discussed. The measurements were acquired through a coupler with a flat frequency response up to 100 MHz and using a VNA in the 1.8–100 MHz frequency range. During the measurement campaign, two different motor states, i.e. on or off, and various equipment

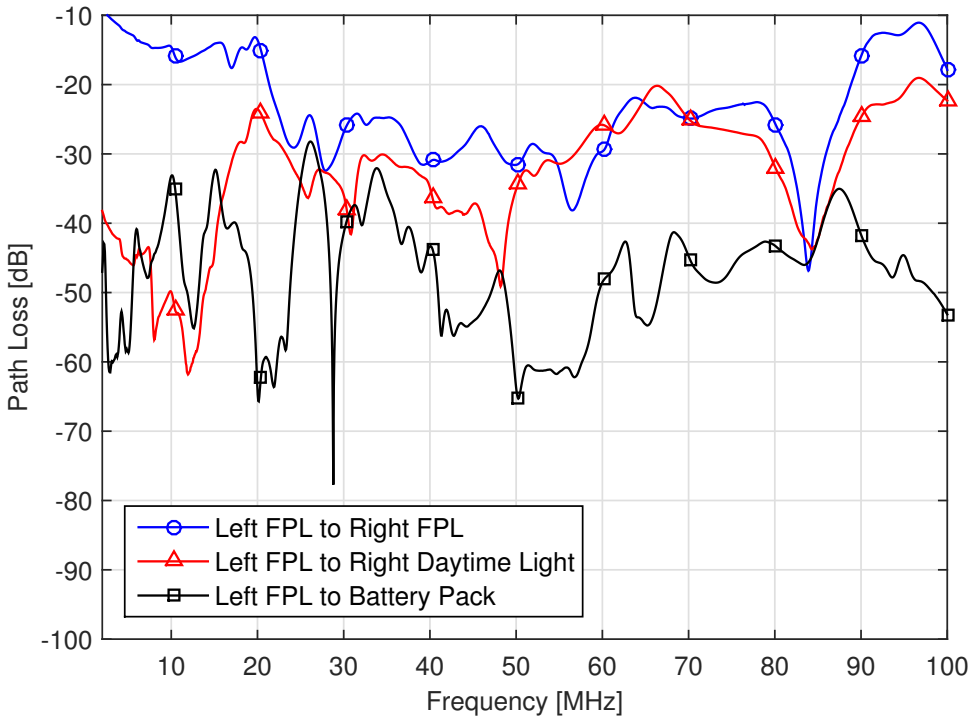

Figure 5.2: Path loss of three representative in-car channels [89].

activity were considered, as it is detailed in the following. Communications within the low-power sub-network and between the low-power and high-power sub-networks, across the DC-DC converter, are considered. The former case targets the propagation of the PLC signal in the 12 V circuit. In the latter case, there is a lack of electric continuity. In fact, the DC-DC converter can be modeled, and acts, as a low pass filter, since it is designed for the DC signal conversion only. Thus, the propagation of the broadband high-frequency signal through the DC-DC converter can only be due to coupling and radiated effects.

The measurements analysis has shown that the channels can be classified in three different classes, according to the attenuation they exhibit. As known, the attenuation is one of the primary factors that determine the system capacity. However, other classification criteria can be used. The classes make a distinction between low, medium and high-attenuated channels. In general, channels within the 12 V circuit belong to the first two classes, regardless the physical length of the electric paths. Instead, channels across the DC-DC converter belong to the third class, the most attenuated. This result is not surprising since, in this case, the propagation is only due to radiated effects.

Figure 5.2 shows a representative PL profile, in dB scale, for each considered class. The PL is defined as $\mathcal{L}(f) = |H(f)|^2$, where $H(f)$ is the CFR, while its logarithmic version is computed as $\mathcal{L}_{dB}(f) = 10 \log_{10} \mathcal{L}(f)$. In the figure, the low-attenuated channel refers to the link between the left front position light (FPL) to the right FPL. The medium-attenuated channel refers to the link between the left FPL to the right daytime

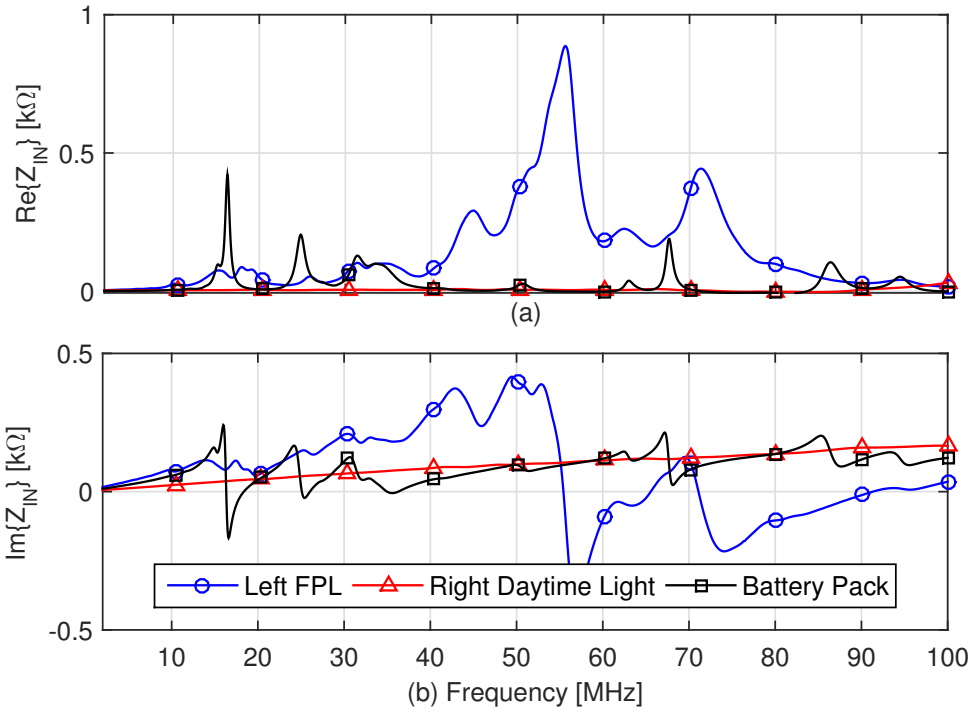

Figure 5.3: Impedance of three representative EC channels [89].

running light. The high-attenuated channel refers to the link between the left FPL to the battery pack. Interestingly, it can be noted that, despite the large attenuation of the channel across the DC-DC converter, some low-attenuated frequency windows exist. Moreover, although the channels exhibit a moderate selective behavior, due to the reduced multipath propagation into a star-style network structure deploying short cables, a low ACG is observed, as discussed in Section 5.4.1. The PL range and behavior depicted in Figure 5.2 is consistent with that reported in [90], although the latter refers to different car states (key ignition positions) and for frequencies up to 30 MHz.

Figure 5.3 reports the impedance as a function of frequency. The line impedance is an important quantity since it describes the load seen by the transmitter. Low impedance values make the signal injection challenging. In this respect, the signal transmission in a BB-FS is desirable because the real part of the line impedance reaches significant high levels at middle frequencies, as depicted in Figure 5.3a. Moreover, the imaginary part of the impedance in Figure 5.3b exhibits an inductive behavior for frequencies up to 55 MHz and a capacitive behavior for higher frequencies. The inductive behavior is explainable considering that light bulbs are built with a metallic wire wounded as a coil. The capacitive behavior, instead, is due to the parasitic capacitance of the small bulbs of the FPL lamps.

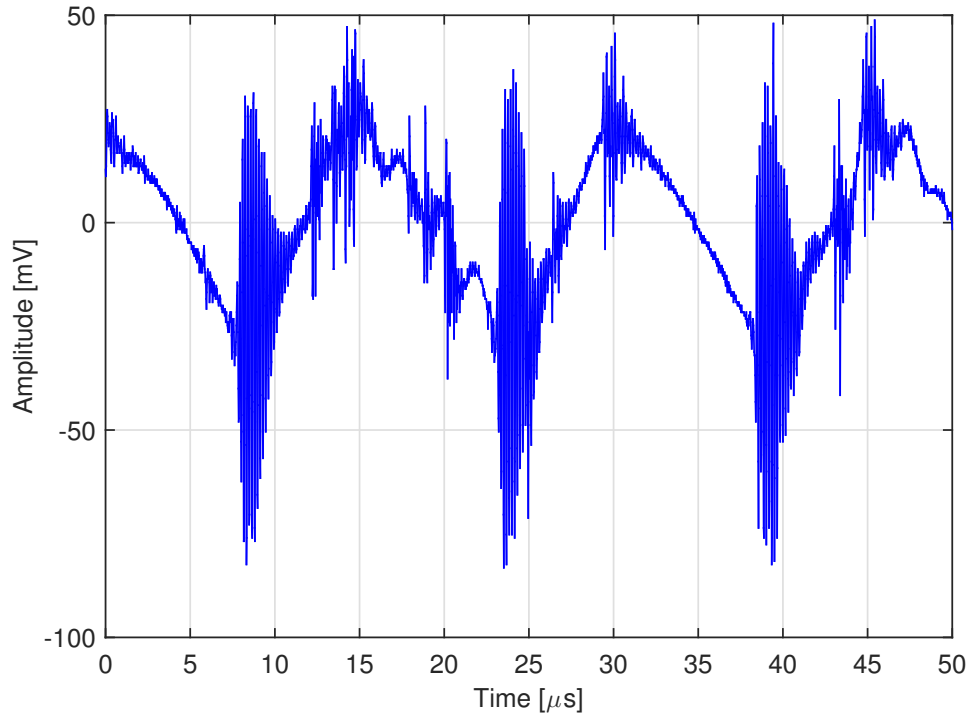

Figure 5.4: In-car noise voltage waveform measured at the DC-DC converter (12 V side), with motors and equipment switched on.

5.2.2 In-Car Noise Properties

In the following, the noise is discussed focusing on the EC. Differently from conventional cars, PLC in electric vehicles is more affected by noise impairments due to the activity of the electric drives. For the noise experimental acquisition, a digital storage oscilloscope (DSO), with a bandwidth of 1 GHz, was used and connected to each test point highlighted in Figure 5.1.

Figure 5.4 shows a time-domain noise waveform measured close to the DC-DC converter, on the 12 V sub-network side, depicted in Figure 5.1, when the car is in movement with all the equipment switched on. As it can be noted, the noise is characterized by a dominant triangular signal plus sharp and fast fluctuations. The former component reflects the switching activity of the DC-DC converter. Basically, it is due to the charge/discharge current that flows in the inductor within the DC-DC converter and is not properly filtered, so that it propagates in the 12 V side of the network.

The sharp fluctuations, instead, are the sum of two contributions, the coupled noise due to the motor drives and the overshooting ripples due to, again, the DC-DC converter. When the car is moving and the motors are running, a large amount of current flows from the battery pack to the motors. Such relevant currents generate a significant magnetic field that concatenates itself with the remaining power plant of the car. This translates into a coupled noise component observable along the ramps. These spikes, induced by the motors activity, have approximately the same periodic behavior described in [90], which,

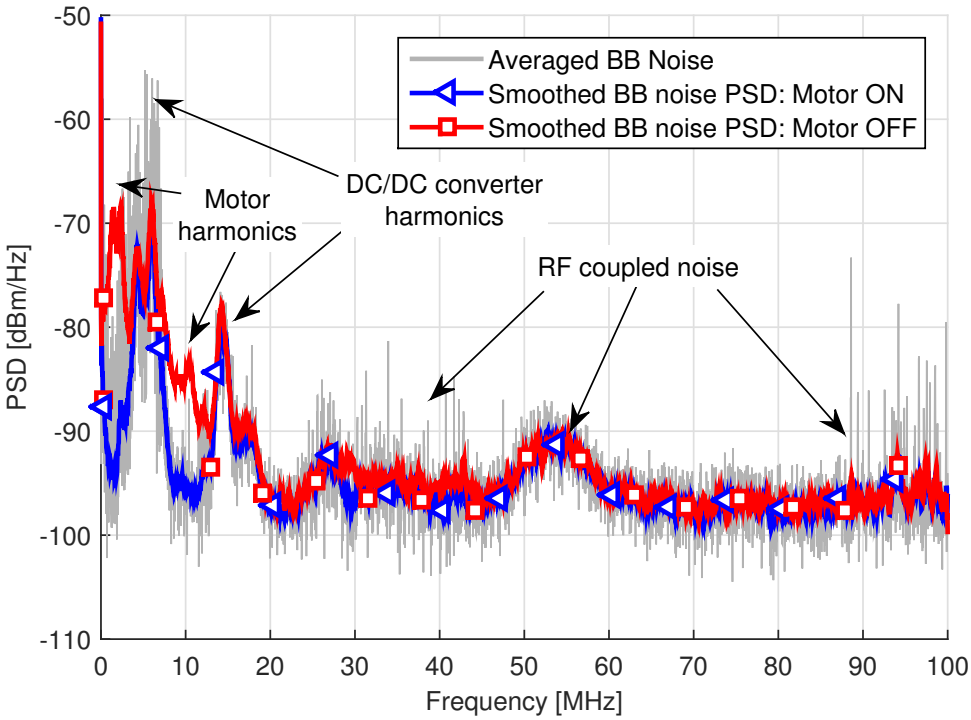

Figure 5.5: BB in-car noise PSD for two motor states. The average PSD value is also shown.

however, does not consider the DC-DC converter operability. Instead, the overshooting ripples confined on the triangular waveform switching discontinuities are due to further resonance effects within the DC-DC converter.

The triangular-shape and the coupled noise components, due to the motors, can be analytically described in terms of Fourier series expansions, showing that their effects are limited to the lower frequency range, where the harmonics are concentrated, as detailed in [89]. This effect is noticeable in Figure 5.5 that shows the BB noise PSD for two motor states, namely on and off. The differences are confined at low frequencies. The displayed PSD has been obtained by averaging the noise PSD profiles over all the measurement points, represented in Figure 5.1, and all the considered equipment configurations, as well as for both the motor states.

Contrariwise, the noise contribution due to the overshooting ripples, caused by the DC-DC converter, translates into a high-frequency component centered around 5 MHz, as shown in Figure 5.5. Moreover, the harmonics of these overshooting ripples can be observed in the 15 MHz band. Beside such noise contribution, Figure 5.5 highlights a large noise component between 50 and 60 MHz that is not related to the vehicle activity. Rather, it is amenable to coupled radio frequency (RF) signals that were present in the laboratory site during measurements. Likewise, the PSD components in the range 30–40 MHz and above 87 MHz are due to amateur and broadcast radio transmissions, respectively. If a CC is considered, the noise PSD is tens of dB lower than the one experimented in the EC described in this section, as reported, for instance, in [94].

5.3 In-Ship Scenario

In this section, the attention is turned to the in-ship environment, where the main results obtained from the measurement campaign carried out in a large cruise ship [54] are discussed. The focus is on the channel characterization considering the LV part of the power line distribution network.

5.3.1 In-Ship Channel Properties

A total of 92 time-domain measurements were carried out using a signal pulser together with a DSO (with a sampling rate of 200 Msamples/s), that were connected via a capacitive coupler having a CFR with a flat behavior up to 50 MHz. The vehicle under test was the 116,000 tonnes cruise ship depicted in Figure 5.6. In this scenario, the power is supplied by asynchronous diesel generators via MV lines connecting MV/LV substations and distributed to the decks through LV three-phase wires with non-distributed neutral. In detail, the power is vertically distributed from the substation switchboard (SS) to all decks, reaching the distribution boards (DBs) through cables that range from 80 to 100 meters. Each DB is then connected via a bus-bar, with a length of about 40 meters, to the room service panels (RPs), which serve a small number of rooms each [54]. Therefore, the network topology is the ensemble of two differently structured sub-networks, namely a star-style network from the SS to the DBs and a bus-style network from the DB to the RPs. The channels referred to these sub-networks are referred to as SS-DB and DB-RP, respectively. Since the underlying structure is completely different, these two sub-networks are separately considered in the rest of this section.

The measurements in [54] concern only the LV distribution network, as depicted in Figure 5.6. Since there are three available conductors, denoted with R, S, and T, a 2×2 MIMO channel can be established transmitting and receiving among the R and T conductors, as well as between the S and T conductors, in a differential mode. For the measurements, the two direct links and the two cross-links responses were measured using a SISO configuration and closing the other two ports on a known 50 Ω load.

The best and the worst PL profiles of the channels belonging to the two sub-networks are reported in Figure 5.7. Due to the coupler CFR and to the measurement procedure, the frequency range is limited to 1.8–50 MHz. As it can be noted, the PL ranges between -10 and -60 dB, as happens for the in-car scenario discussed in Section 5.2.1, despite a larger network with much longer cables. However, the in-ship ACG value listed in Table 5.1 is the highest (lowest attenuation) w.r.t. both the in-home and the in-car scenarios. This is due to the limited amount of branches in the SS-DB sub-networks and to a better quality of the deployed cables. Contrariwise, the frequency selectivity is higher than that observed in the in-car scenario, as stated by the low average CB level listed in Table 5.1, although for the best PL profile reported in Figure 5.7 it is quite small. This is because

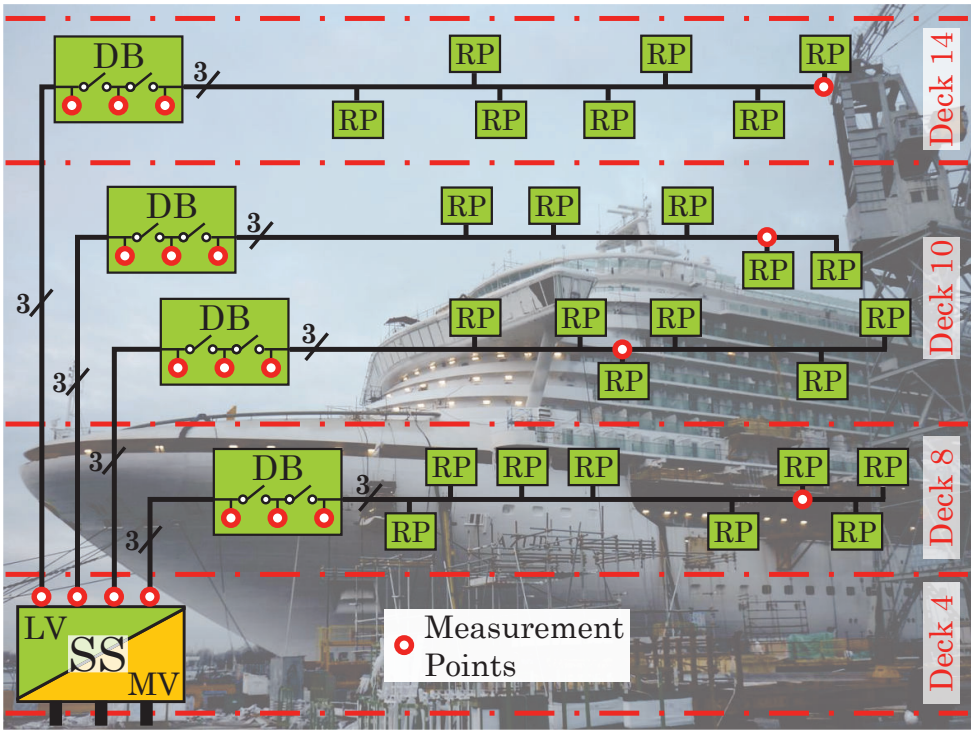

Figure 5.6: Power distribution grid scheme of the cruise ship Azura, built by Fincantieri. The measurement points are also shown.

such channels are associated to cable links without derivations, where the reflection effects are less pronounced.

5.3.2 In-Ship Noise Properties

Noise measurements were carried out through the use of a spectrum analyzer and selecting a number of points in order to evaluate the typical PSD profile. Three representative background noise PSD profiles, which correspond to a different measurement point, namely to a RP, a DB, or to a SS location, are depicted in Figure 5.8. Two states of the ship were considered, namely with switched on or off diesel generators. However, small variations of the noise PSD level along frequency were found, with a floor ranging between -135 dBm/Hz and -145 dBm/Hz, depending on the node position, as represented in Figure 5.8. It can be noted as the PSD levels measured at the three representative points exhibit almost a flat profile. Thus, the background noise can be assumed as AWGN with a certain level. This assumption holds true in the bandwidth of interest, i.e. 1.8–50 MHz, also displayed in the figure. Contrariwise, for lower frequencies, namely below 1.8 MHz, the noise PSD drastically increases. This is probably due to the great deal of noise injected into the network by the activity of the diesel generators or by the big employed machines that, due to their operability, act as strong disturbance sources especially at low frequencies.

It has to be said that the ship was not in navigation conditions. In such a case, the

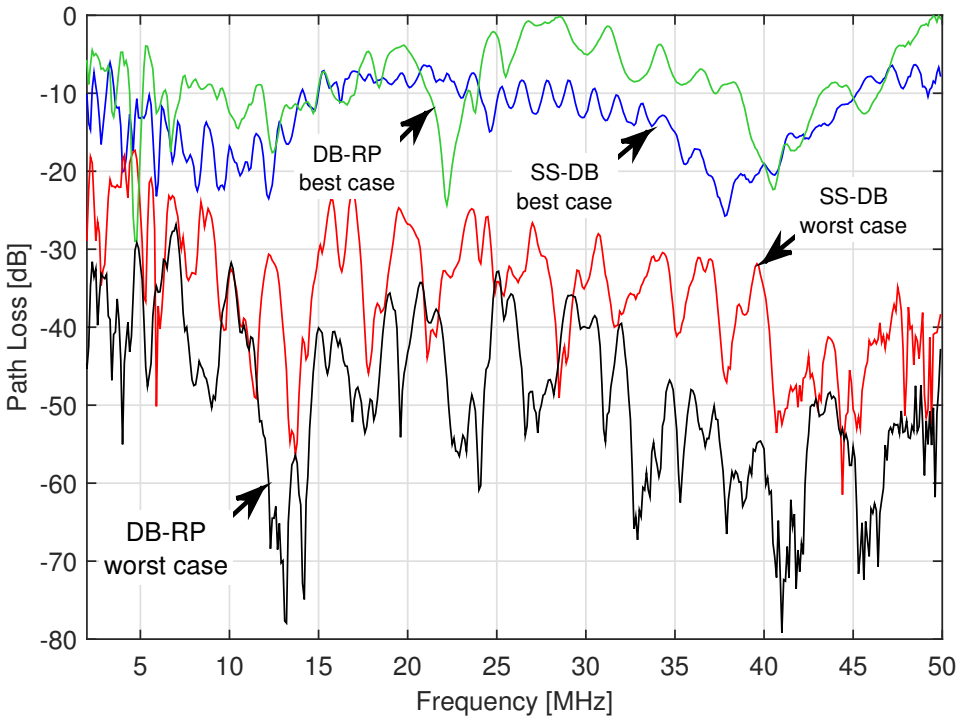

Figure 5.7: Best and worst PL profile for the two in-ship power sub-networks (i.e., SS-DB and DB-RP).

experienced noise may be higher due to loads and people activity. Thus, a noise PSD with a conservative floor value of -110 dBm/Hz can be considered, as it will be done in the following performance analysis section. This value appears to be an appropriate compromise between the -95 dBm/Hz measured in [53] and the nearly -132 dBm/Hz floor observed in [95].

5.4 Statistical Analysis and Performance

In order to statistically assess and characterize the PLC channel in the considered in-car and in-ship scenarios, the most commonly used metrics, i.e. ACG, RMS-DS, CB and capacity, defined as in Section 2.2, are analyzed in this section. In this chapter the level $\xi = 0.9$ is considered for the CB metric, thus only $\mathcal{B}_C^{(0.9)}$ is discussed. A final discussion, comparing the most commonly used average statistical metrics, is also performed. In order to perform a fair comparison, in the following the considered frequency range is 1.8–50 MHz for all the scenarios, unless otherwise stated.

5.4.1 Metrics Relationships and Capacity Distribution

In this section, the aim is to compare the in-car and the in-ship scenarios, assessing the dependencies and evaluating the corresponding capacity distribution. In particular, in Figure 5.9, the RMS-DS is analyzed w.r.t. the ACG (on the left side) and the CB (on the

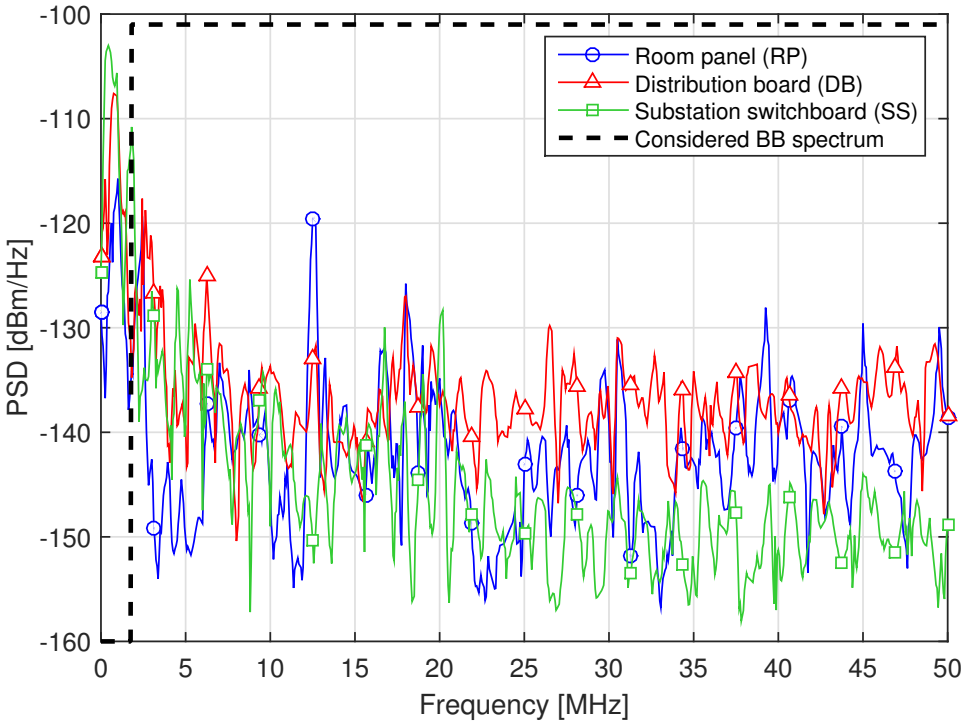

Figure 5.8: Representative background noise PSD profiles corresponding to a RP, a DB, or a SS measurement point. The considered BB spectrum is also depicted as a reference.

right side) for two different scenarios, in-car (on top) and in-ship (on bottom). The fit of the CC measurements discussed in [46] is also depicted (dashed line). The scatter plots (circles) correspond to the measurements. As it can be noted, the RMS-DS and the ACG are negatively related, as shown by the robust regression fit (solid line). In particular, a slightly lower attenuation is exhibited by the conventional car compared to the electric car, as later clarified in Table 5.1. The slope of the robust fit line for the in-ship scenario in Figure 5.9c is roughly five times the slope of the in-car scenario in Figure 5.9a. This significant difference is due to the fact that both these environments exhibit almost the same ACG, but the in-ship scenario shows a considerably greater RMS-DS, mainly due to the underlying network structure, as it will be clarified in Section 5.4.2. Indeed, the in-car scenario experiences only a slightly higher attenuation, since values are more shifted towards the left bottom corner w.r.t. the in-ship case. This is even more noticeable looking at the average metrics reported in Table 5.1, later described. The reasons underlying these properties are detailed in Section 5.4.2. Furthermore, on the right hand side of Figure 5.9, it can be noted as the CB is inversely related to the RMS-DS, as shown by the hyperbolic fit (solid curve).

Now, the focus is turned to the performance evaluated in terms of achievable capacity. Figure 5.10 shows the capacity C-CDF computed using the electric car channel and noise measurements (labeled with EC) in both the 1.8–50 and 1.8–100 MHz bands. As a further term of comparison, the capacity C-CDF of the conventional car (labeled with CC) in the 1.8–50 MHz, is also shown. In order to provide smoother C-CDF trends, the

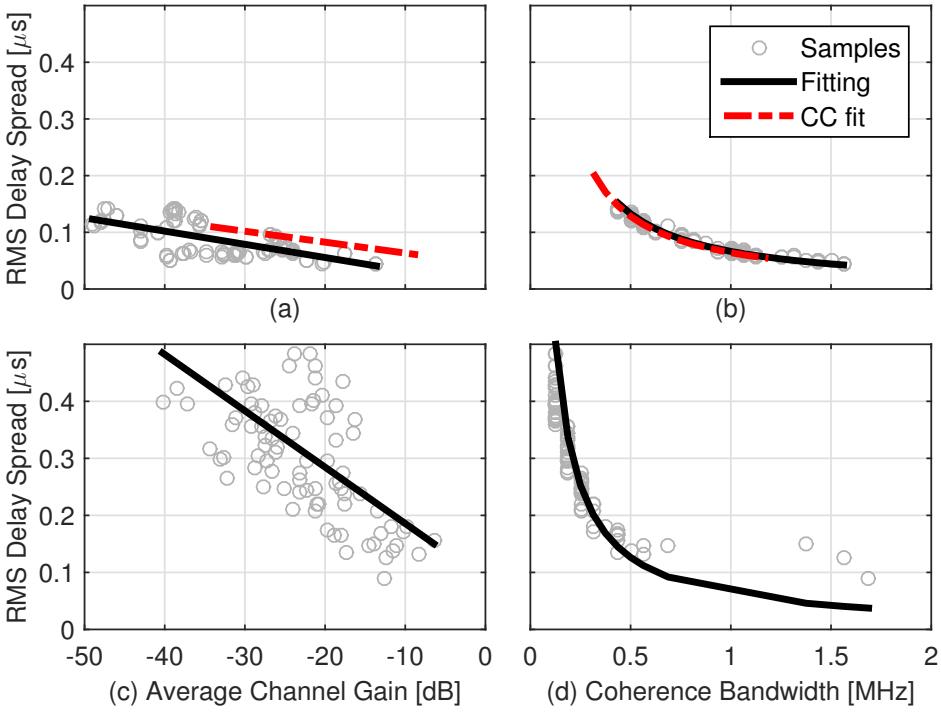

Figure 5.9: Comparison among the EC, (a) and (b), and the in-ship, (c) and (d), scenarios. The CC measurements fit [46] is also depicted.

corresponding fitting curves are also displayed. The distribution that provides the best fit, i.e. with the highest likelihood value computed as in (2.22), is used for the approximation. In particular, the capacity C-CDF fits in Figure 5.10 correspond to a Weibull distribution. The capacity is computed assuming a transmitted signal PSD of -50 dBm/Hz and the measured noise PSD in Figure 5.5 for the EC. For the CC, a flat noise PSD level of -120 dBm/Hz is considered [46]. It should be noted that the CC outperforms the EC, when the 1.8–50 MHz band is considered, since the motor states (on or off) and a higher noise affect the latter. Nevertheless, high link capacity is achievable. This is even more prominent when considering the 1.8–100 MHz frequency range for the EC. No measurements beyond 50 MHz are available for the conventional car. In fact, for the EC, with probability 0.9 the capacity can exceed 500 Mbps in the 1.8–100 MHz band, which doubles the value of 220 Mpbs achieved in the 1.8–50 MHz band.

Conversely, the capacity C-CDF obtained considering the in-ship channel measurements is reported in Figure 5.11. Also in this case, the fitting C-CDF curves correspond to a Weibull distribution. The capacity is computed assuming a transmitted signal with a PSD of -50 dBm/Hz and an AWGN with a PSD equal to -110 dBm/Hz, which is a conservative floor value, as discussed in Section 5.3.2. Since three phases (or wires) are available, the capacity is estimated for the PLC links that use the same phase (direct links), and the links that use different phases at the transmitter and receiver sides (coupled links). It can be noted, in Figure 5.11, as the capacity of the direct links outperforms that of the coupled ones for both the considered sub-networks. Moreover, if

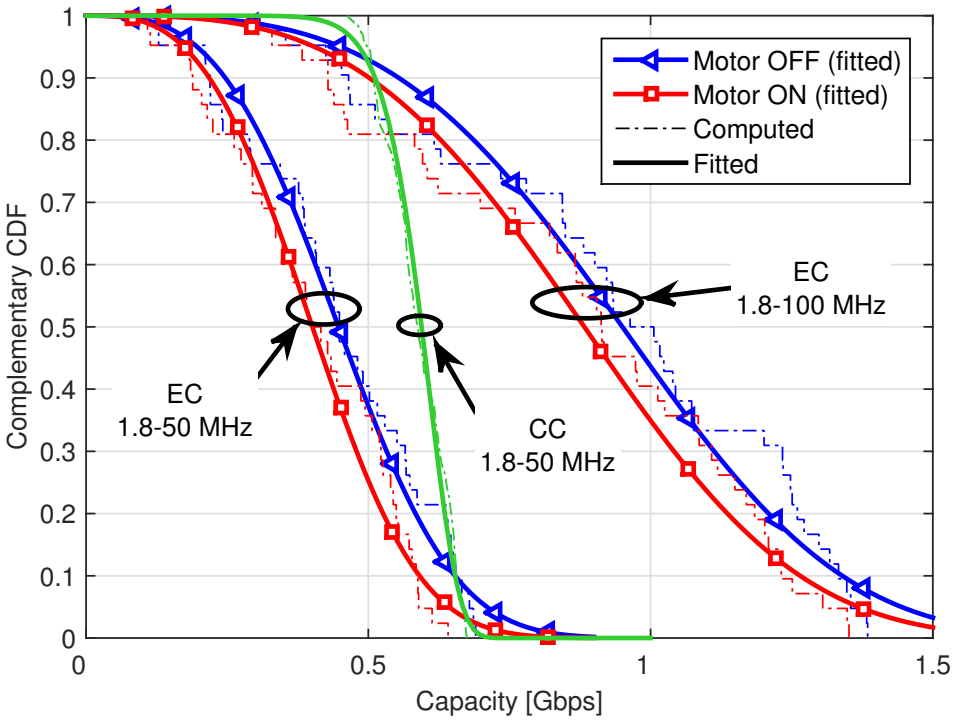

Figure 5.10: EC PLC performance in terms of capacity C-CDF for 1.8–50 MHz and 1.8–100 MHz frequency ranges. The CC capacity C-CDF in the 1.8–50 MHz band is also shown.

MIMO transmission is used, under the same SISO assumptions and dividing the available power equally among all the possible spatial transmitting modes, namely two as discussed in [54], the capacity will have the potentiality to almost double, compared to the SISO case.

5.4.2 Overall Comparison

In this section, the average values of the statistical metrics discussed in Section 2.2 are evaluated and discussed. As a further comparison, the metric values for the more popular in-home case, considering the 1266 measurements discussed in Chapter 3, and for the online available database of 193 measurements analyzed in [46], which concerns a conventional car, are also listed. In particular, Table 5.1 summarizes the average value of the performance metrics computed from the measurements in each considered scenario, where $\overline{\{\cdot\}}$ indicates the average, in the bandwidth 1.8–50 MHz.

It is interesting to note the following. First, the in-ship channels exhibit the higher average ACG ($\overline{\mathcal{G}}$). Second, both the in-car scenarios have a $\overline{\mathcal{G}}$ value similar to the in-home case. Third, the high average RMS-DS ($\overline{\sigma}_\tau$) value and the low average CB ($\overline{\mathcal{B}}_C^{(0.9)}$) value for the in-ship case, caused by the large amount of branches in the DB-RP sub-networks, are very similar to those of the in-home scenario. Moreover, the lower attenuation exhibited by the in-ship channels is due to the limited amount of branches in the SS-DB sub-networks,

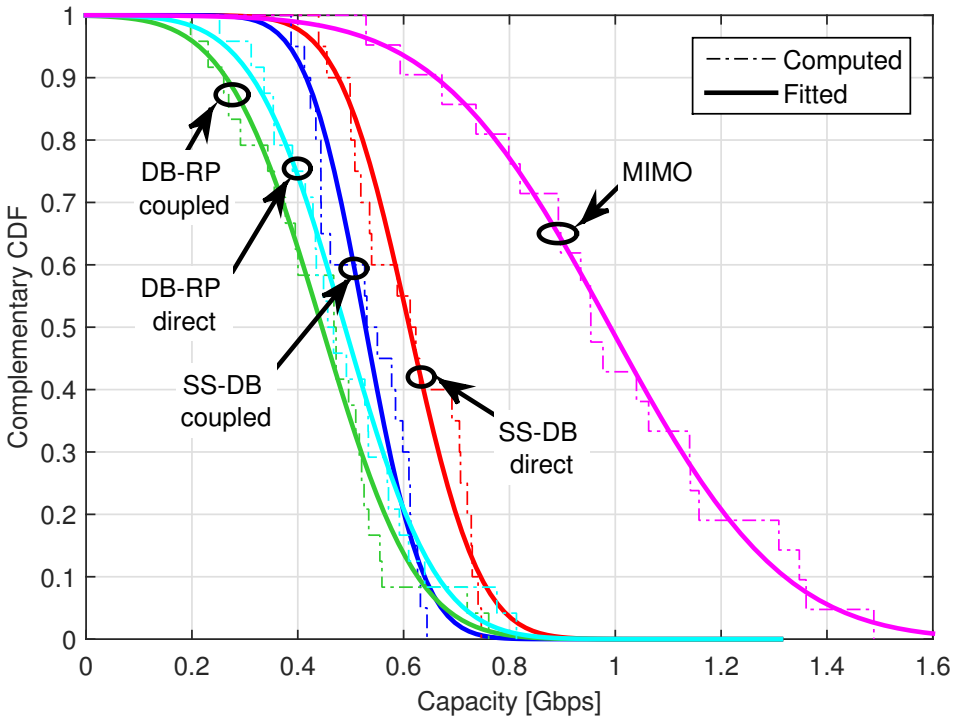

Figure 5.11: Capacity C-CDF for the two different in-ship sub-networks, in SISO configuration, and for the 2×2 MIMO transmission, both in the 1.8–50 MHz band.

Table 5.1: Average statistical channel metrics for different scenarios.

Scenario	B (MHz)	$\overline{\mathcal{G}}$ (dB)	$\overline{\sigma}_\tau$ (μs)	$\overline{\mathcal{B}}_C^{(0.9)}$ (kHz)	$\overline{\mathcal{C}}$ (Mbps)
In-home	1.8–50	−33.10	0.357	251.48	539.11
In-car (EC)	1.8–50	−33.25	0.086	874.26	425.67
In-car (CC)	1.8–50	−27.33	0.102	677.14	589.97
In-ship	1.8–50	−22.89	0.320	258.83	511.23

to a better cables quality and to a simpler topology, despite the length. Conversely, the lower RMS-DS and the higher CB values, obtained for both the in-car scenarios, are due to the low multipath propagation into short cables length. While, the high attenuation in the EC context is due to poor electric wiring characteristics, to the low line impedance values in Figure 5.3 and to the attenuation introduced by the DC-DC converter.

Finally, looking at the average capacity ($\overline{\mathcal{C}}$) reported in Table 5.1, it can be noted as all the considered scenarios exhibit similar performance (of about 500 Mbps), despite the different network structure, channel properties and noise sources. The $\overline{\mathcal{C}}$ value for the EC is slightly lower than the others. This is mainly due to the strong effect of the measured background noise in Figure 5.5.

5.5 Main Findings

The PLC channel in the vehicular context has been discussed. In particular, two environments have been considered, the in-car scenario, with focus on the electric car, and the in-ship scenario. It has been shown that, in both cases, PLC has the potentiality to offer high-speed data connectivity, despite the different nature of the underlying network structure and background noise properties. The measurements analysis has shown that, although the in-car network has a compact size, the PLC channel is affected by frequency selective fading and high attenuation. Contrariwise, the in-ship channels exhibit, on average, less attenuation thanks to fewer discontinuities and to better quality cables, despite the length. Moreover, the background noise of the EC has been analyzed, showing a prominent and severe influence at low frequencies, especially where NB-PLC operates. This is primarily due to the switching activity of the DC-DC converter, together with the electric drives for the motors. The DC-DC converter noise affects also the BB-PLC spectrum, in particular at 5 MHz and at its harmonics. The measurements and the literature have shown that the in-ship scenario exhibits a noise PSD, in the 1.8–50 MHz, with a floor ranging from -95 to -145 dBm/Hz. Moreover, the presence of a three-phase distribution network allows the usage of MIMO transmission techniques that have the potentiality of almost doubling the channel capacity, as for the MIMO transmission within the in-home scenario discussed in Chapter 4. Similar capacity improvements can be obtained in the in-car scenario by extending the transmission bandwidth to 1.8–100 MHz.

6 Outdoor Scenario

In the first part of this thesis the indoor scenario, which considers each type of confined environment, such as homes and vehicles, has been thoroughly discussed and characterized. However, the PLC technology can play a significant role even when considering the energy distribution part of the network, namely the outdoor scenario. The communication over the power distribution lines has become attractive, especially in the latest years, due to the increasing momentum gained by the smart grid applications. In particular, the realization of the smart grid requires the deployment of bi-directional communication links that interconnect the nodes of the grid. PLC is a technology that is capable to meet this goal by exploiting the existing grid infrastructure and thus, potentially, reducing investment costs. A pervasive deployment of PLC systems is envisioned especially in the distribution network that comprises LV and MV lines. In this scenario, a large number of "smart" devices, i.e. active loads, sensors, actuators, etc., will be present and generate an overall high amount of data.

Recently, industry has turned the attention towards the development of multipurpose PLC modems that, for example, can provide connectivity for monitoring and protection (e.g., faults detection), monitoring of islanding effects, advanced metering, power management, home energy management and micro-grid control. Generally, the power supply generated from power plants is pervasively distributed to the end customers through a well planned network infrastructure that comprises HV overhead lines, MV lines and LV lines that reach the final customer. A schematic representation of a typical power distribution grid is depicted in Figure 6.1. Although the power lines can be used as a transmission medium, they have not been conceived for this use. Therefore, their exploitation typically faces several issues, which depend on the specific application context, network topology and operating frequency band. They include:

- channel attenuation and frequency selectivity due to multipath propagation, which depend on the considered frequency band and underlying grid topology;
- channel time variations that mainly depend on the loads connection/disconnection

and operability;

- low line impedance values that challenges the injection of the voltage signal into the network;
- high levels of background noise, caused by the devices connected to the network;
- high interference coupled into the lines, which is generated by RF transmissions or emissions;
- radiation effects due to the transmission of high frequency signals that causes the wires to behave as transmitting antennas.

6.1 Applications and Requirements

The PLC can be used to offer a number of services in the grid. Monitoring and control, enabled by PLC, allow fault detection, power quality monitoring and islanding effects avoidance. The energy management allows decentralized production and the control of storage and electrical vehicles charge. Smart metering, instead, is the key component for demand side and demand response management, dynamic pricing and acquisition of user behavior. Furthermore, smart building solutions can be realized with automation and control within them.

All these applications have different constrictions in terms of data rate, latency and reliability. Although each single connection may have low data rate requirements, the overall traffic can be high, especially when fast real time services have to be granted. Furthermore, the data rate balance depends not only on the sensor/actuator needs, but also on the redundancy introduced by the network protocol, including the need of implementing security/privacy mechanisms, as it will be discussed in Chapter 9.

The amount of data traffic to be carried by a link depends, finally, on the considered PLC network segment. For instance, the concentrator in a MV/LV substation has to collect the traffic from all LV nodes (houses), which can easily exceed 1 Mbps and much higher if fast demand side management has to be realized. Other applications, as control of islanding situations, fault detection and circuit breakers control, do not have high data rate requirements, but must be handled with extreme reliability and with fast response, namely below 100 ms.

It is therefore not obvious if a NB solution can handle all these applications, or if a combination of NB and BB has to be deployed. For instance, a NB solution can be adopted for the LV network segment, while a BB solution for the MV segment [148].

6.1.1 Main Purposes and Organization

As extensively discussed in Section 1.1.2, current PLC technology can exploit both the so called NB-FS, operating at frequencies below 500 kHz, and the BB-FS, which uses the 1.8–100 MHz frequency band, in order to provide data connectivity. As it has been detailed, the market and the industries offer a variety of NB standards (e.g. ITU-T G.hnem, IEEE P1901.2) and BB standards (e.g. ITU-T G.hn, IEEE P1901, HPAV2). The aim of this chapter is to provide an overview about the challenges that PLC for smart grid applications is facing. Emphasis is given to physical layer aspects, starting from the channel behavior analysis in both the NB-FS and BB-FS. It has to be emphasized that the focus is not on the existing NB-PLC or BB-PLC solutions discussed in Section 1.1.2, but rather on the physical medium characteristics in the considered frequency bands.

The chapter is structured as follows. In Section 6.2 the outdoor power delivery structure is discussed, focusing on the medium aspects. The study digs into the typical PL profile, as well as into the input line impedance values usually exhibited in both the LV and MV networks and for both the NB and BB spectra. Then, the attention is moved towards the main network features and to the analysis of the background noise that affects the different scenarios. Later, in Section 6.3, the average SNR along frequency, exhibited by both LV and MV lines, is computed in order to provide some performance results, in terms of capacity, comparing the NB and BB spectra. Finally, the main findings of the chapter follow.

6.2 Network and Medium Aspects

The design of the PLC network depends on the application scenario and on the grid topology. Focusing on the distribution grid, it comprises both MV and LV sections. Figure 6.1 shows a schematic representation of the distribution grid. Bi-directional PLC services can be established between nodes of the network in a centralized or peer-to-peer fashion, covering different geographical areas.

The HV part of a power distribution grid consists of lines carrying voltages that range between 110 kV and 380 kV, being typically used for nationwide or even international power transfer. Usually, these networks consist of long overhead lines with little or no branches, which translates into a quite good PLC channels that exhibits low energy dispersion and limited attenuation per line length. However, the research community interest in studying the potential of this part of the grid to deliver BB communication services for smart grid applications is still limited. Indeed, as a matter of fact, the PLC over HV networks faces many challenges and issues such as the great deal of noise, introduced by the time-varying arcing and corona effects with noise power fluctuations in the order of several tens of decibels, or the practicalities and costs of coupling communication signals

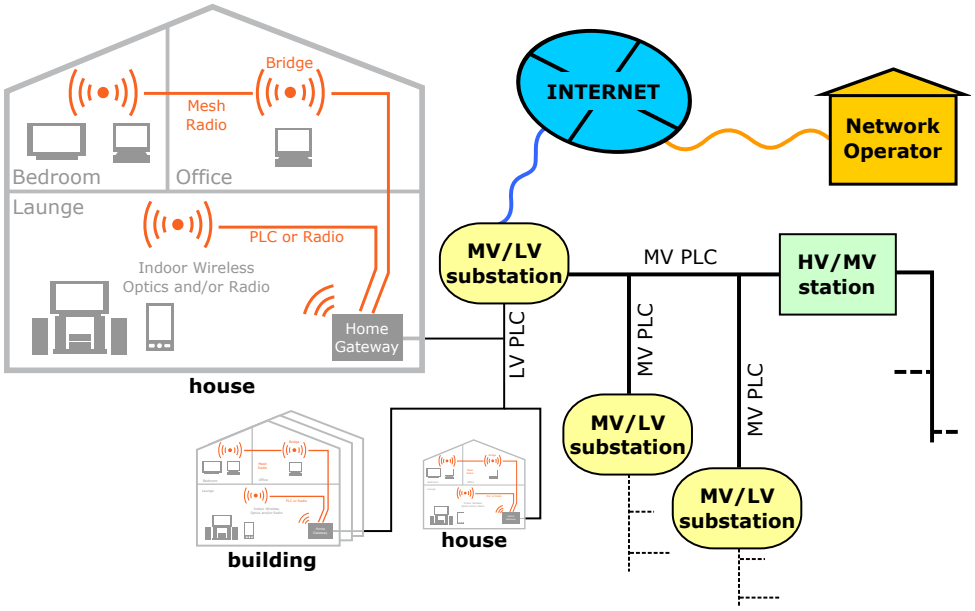

Figure 6.1: Schematic of a typical power distribution grid.

into these lines. Moreover, the interest in this field is limited by the high competition offered by the fiber optical links, which are actually worldwide widespread. However, several successful studies exploiting the HV lines have been discussed and detailed in [149–151].

Otherwise, the MV lines are used to provide power to large aggregations of customers, e.g., towns, neighborhoods and industrial sites. The MV lines carry voltages in the order of tens of kilo Volt and are connected to the HV power supply network via a primary transformer substation [3]. The MV lines can be deployed as underground or overhead cables and the underlying network structure is typically characterized by a tree structure with a low amount of branches. This, as described in Section 6.2.1, translates into a lower channel attenuation and frequency selectivity w.r.t. both indoor and outdoor LV channels. Besides feeding the loads, the MV networks deploy a number of intelligent electronic devices, such as sectionalizers, capacitor banks and phasor measurement units, as well as large distributed energy generators from renewable sources, e.g. solar panels. Depending on how the PLC network nodes are organized, it may be desirable to cross the elements that create propagation discontinuity, as circuit breakers and transformers. The ability to cross such elements depends on the transmission bandwidth, as discussed in Section 6.2.1 and [130].

The LV lines, instead, cover the last part of the power distribution system, delivering the energy to the end customer premises, as houses and buildings. They are connected to the MV lines through secondary transformer substations and typically carry a voltage in the order of hundreds Volt [3]. These transformers act as blocking filters. However, they might be useful to partition the network into cells in order to increase the system capacity. That is, the transformer splits the network and creates two distinct physical cells with the use of a base station (concentrator). Usually, the LV lines are deployed

as underground cables and their underlying network structure is comparable to a bus transmission line, namely a long backbone with short branches connecting the utilities. However, significant differences are found among European and American outdoor LV networks. In Europe the 230/400 V three-phase distribution grid is divided in supply cells served by a MV/LV transformer station. Up to about 300 houses are connected through around 30 branches with a maximum branch length of approximately 1 km. In the Asia and USA the power distribution takes place at 125/250 V with single or split phase. Each supply cell is small, serving less than 10 houses with branch lengths in the order of 100 m. This different network configuration must be taken into account since the number of repeaters/concentrators to be deployed in USA networks is high, which can translate in higher deployment costs. Indeed, this depends on the solution adopted. In fact, the repeater can be a simple bypass coupler or an active PLC modem.

6.2.1 Channel Properties

The aim of this section is to highlight the main differences among the outdoor LV and MV communication media. Concerning the outdoor distribution grids, the analysis of the PLC channel provided in the literature is less comprehensive, if compared to the indoor case. It is however very important to know such characteristics in order to design good PLC solutions [152].

With reference to the LV channels, the measurements performed by the OPERA project [75] are herein considered. From the collected measurements an analytic model was derived, providing eight different reference CFRs. Each CFR has been selected and tabulated considering different length classes and attenuation levels, i.e. short, medium and high. In particular, Figure 6.2a shows the BB PL, in dB scale, of three different OPERA reference channels, corresponding to high (350 m), medium (250 m) and low (150 m) attenuation with decreasing path length. The PL in dB scale is defined as $\mathcal{L}_{dB}(f) = 10\log_{10}|H(f)|^2$, where $H(f)$ is the CFR at the f-th frequency. Also the average PL profile is reported. It is defined as $\overline{\mathcal{L}}_{dB}(f) = 10\log_{10} E[|H(f)|^2]$, where $E[\cdot]$ denotes the expectation over the full set of measurements. As it can be noted, the outdoor LV CFR of the channels introduces high attenuation, since the cable attenuation dominates the multipath fading. Also the average PL profile exhibits this strongly attenuated trend, which decreases linearly with frequency.

Concerning the MV channels, a total amount of 98 measurements are considered. Some of them, namely 42, were carried out in 2010 during the measurement campaign that was described and discussed in [130]. The other 56 measurements were carried out in 2011 considering another part of the previously discussed network. In particular, the considered scenario is a three-phase 20 kV MV network that feeds the industrial complex where the laboratories of the public company Ricerca Sistema Energetico (RSE) are located. The corresponding network structure is representative of a large number of users concentrated

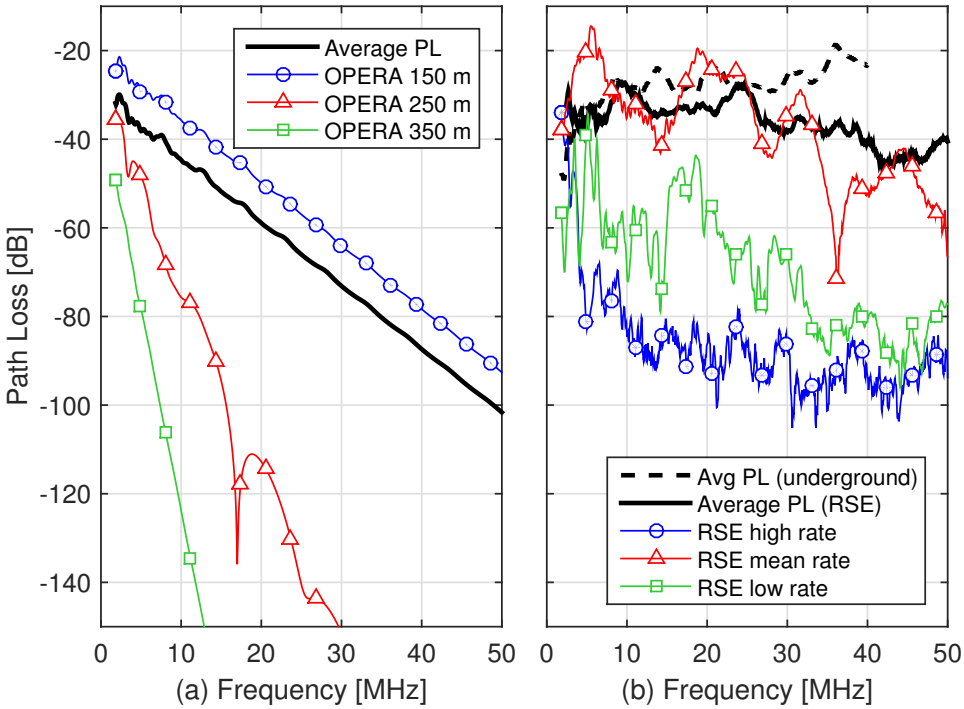

Figure 6.2: PL profiles for the outdoor LV OPERA reference channels (a), and the MV channels feeding the RSE industrial laboratories (b). The average PL profile of the underground MV channels [131] is also depicted.

in a small area. In detail, the underlying network is tree structured with several MV/LV transformers connected to it. The measurements have been performed in time domain providing results that are valid up to 55 MHz, thus for both NB-FS and BB-FS. In particular, the CFR has then been computed through a FFT. However, other analysis of the MV channels can be found in [131] that discusses the 122 responses carried out during a measurement campaign performed in northern Italy in 2013. The measurements were acquired in two different real-life underground MV PLC networks consisting of star-style or tree structured topology, having a reduced number of branches. Although, in general, this scenario is more representative of an actual MV power distribution network w.r.t. the crowded scenario discussed in [130], the measurements validity bandwidth is limited by the pass-band frequency of the capacitive couplers, i.e. 2–40 MHz. Thus, these results are valid and usable only within the BB-FS. However, given the considerable number of measurements, this database is statistically representative and it will be considered for the PLC channel discussion, in the BB-FS, assessed in Chapter 7.

In Figure 6.2b, the PL, in dB scale, for a good, a medium and a bad outdoor MV channel realization, ranked according to the capacity they offer, as well as the average PL ($\overline{\mathcal{L}}_{dB}$), are depicted for the RSE measurements. It should be noted that such channels are less attenuated than the LV outdoor channels in Figure 6.2a. The frequency selective behavior is mainly due to the great number of connected premises, as well as to the influence of the noise in the time-domain measurements acquisition. Furthermore, the

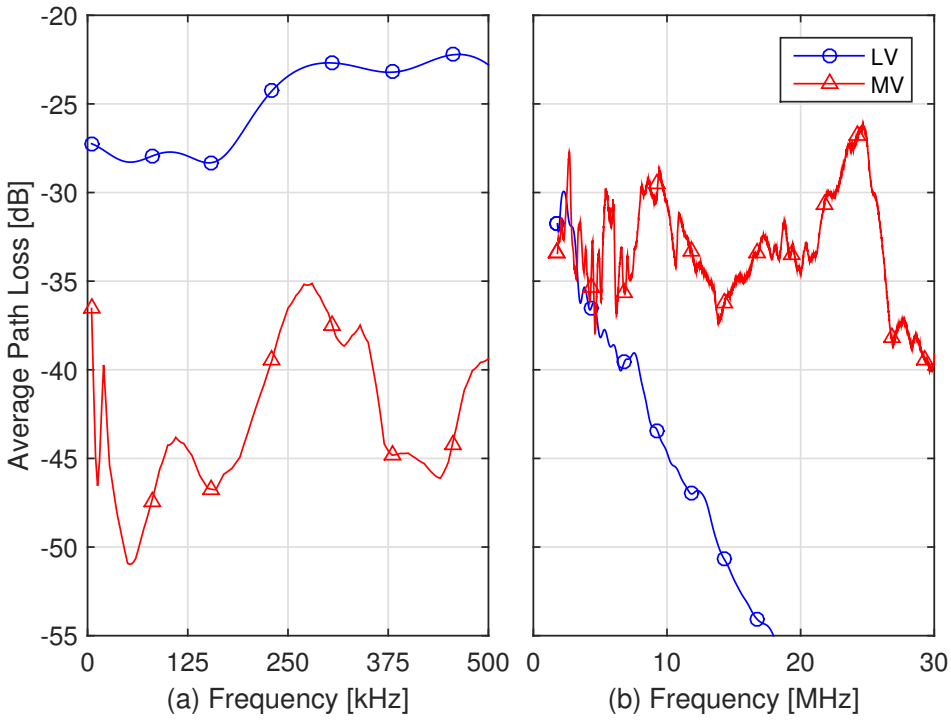

Figure 6.3: Average PL profile for outdoor LV and MV lines in both the NB (a) and BB (b) frequency range.

average PL profile for the measurements corresponding to the MV underground scenario, discussed in [131], is also depicted. It can be noted as the computed $\overline{\mathcal{L}}_{dB}$, corresponding to the two different MV networks, exhibits a similar profile along frequency, especially in the 5–30 MHz band. Moreover, for the underground network, $\overline{\mathcal{L}}_{dB}$ exhibits a large attenuation below 5 MHz that reflects the high-pass behavior of the couplers. For the rest of this chapter, the measurements carried out at the RSE laboratories [130] are considered for the outdoor MV scenario, unless otherwise stated. The reason underlying this decision is that these measurements are valid not only for the BB-FS, but also for the NB-FS, i.e. below 500 kHz. Contrariwise, the measurements acquired on the underground networks [131] cannot be used below 2 MHz, due to the coupler high-pass behavior. Furthermore, concerning the BB-FS, the frequency is limited up to 30 MHz in order to comply with the other measurements range, such as the impedance values. This is done in order to adopt a common frequency range along the entire chapter with the aim of helping the comparison and the analysis. The LV and MV (RSE) average PL profile, in dB scale, for both the NB and BB frequency spectrum, is shown in Figure 6.3 as a function of frequency. On the left hand side, in Figure 6.3a, the NB case is considered, while on the right hand side, in Figure 6.3b, the BB case is considered.

In the NB-FS case (up to 500 kHz), the MV channels exhibit higher attenuation w.r.t. LV ones. This is mainly due to the longer cable length deployed in MV networks, which translates into a larger signal degradation. Moreover, the MV PL shows a more pronounced frequency selective behavior, if compared to the smoother LV PL profile.

This is, since, the underlying network topology is different, namely tree structured for the MV case, while bus structured for the LV scenario. The high number of branches of the considered MV network translates into a pronounced frequency selectivity, greater than the LV scenario, although, usually, LV networks are characterized by many short interconnections to the final premises. However, if the underground outdoor MV network discussed in [131] is considered, which deploys a topology that is closer to a typical outdoor MV grid, lower dispersion, and thus less selectivity, is found w.r.t. the LV case, as it will be confirmed in Section 6.2.2.

The same selectivity behavior can be noted considering the BB case in Figure 6.3b. In contrast to the NB frequency range, the PL dominates the LV scenario for larger frequencies. In particular, beyond 5 MHz, the LV channels are affected by an attenuation higher than the MV ones. As before, this is mainly due to network structure and topology. Instead, since the considered LV lines deploy short three-phase cables, in which each phase wire is close to each other, high resistance values at high frequency are introduced by the spread parallel resonance. This effect produces the prominent PL degradation, as it will be discussed in Section 6.2.3 considering the input line impedance. Also the MV channels exhibit a frequency decreasing PL profile. This behavior is not clearly noticeable in Figure 6.3b due to the great PL exhibited by the LV channels and to the limited bandwidth up to 30 MHz. However, this trend can be easily detectable looking at the average PL profile reported in Figure 7.1 labeled as “Outdoor MV (RSE)”, which considers the same measurements database in the extended 1.8–50 MHz band.

6.2.2 Metrics Relationship and Overall Remarks

In order to deeply investigate the existing differences between the outdoor LV and MV scenarios and within the MV PLC notwork itself, the three different databases discussed in Section 6.2.1 are herein compared in terms of the most commonly used statistical metrics. The scatter plot of the RMS-DS versus ACG, computed basing on the outdoor MV measurements, namely RSE laboratories [130] and underground networks [131], are depicted in Figure 6.4. In particular, the former are identified by the red triangles, while the latter by the green squares. The corresponding robust regression fit is also depicted, even for the OPERA outdoor LV reference channels.

Focusing on the robust fit, it can be noted as the three different scenarios show different relationships. In particular, the slope of the LV scenario is roughly 8 times greater than that of the underground MV networks, but the half w.r.t. the RSE measurements. This huge difference in slope within the same MV scenario is mainly due to the underlying network structure. Indeed, underground networks are star-style structured with very few branches, as usually happens in outdoor MV distribution grids. This translates into a lower dispersion, confirmed by the fact that the values are all confined in the lower region of Figure 6.4, which corresponds to a low RMS-DS, as clarified in Table 6.1.

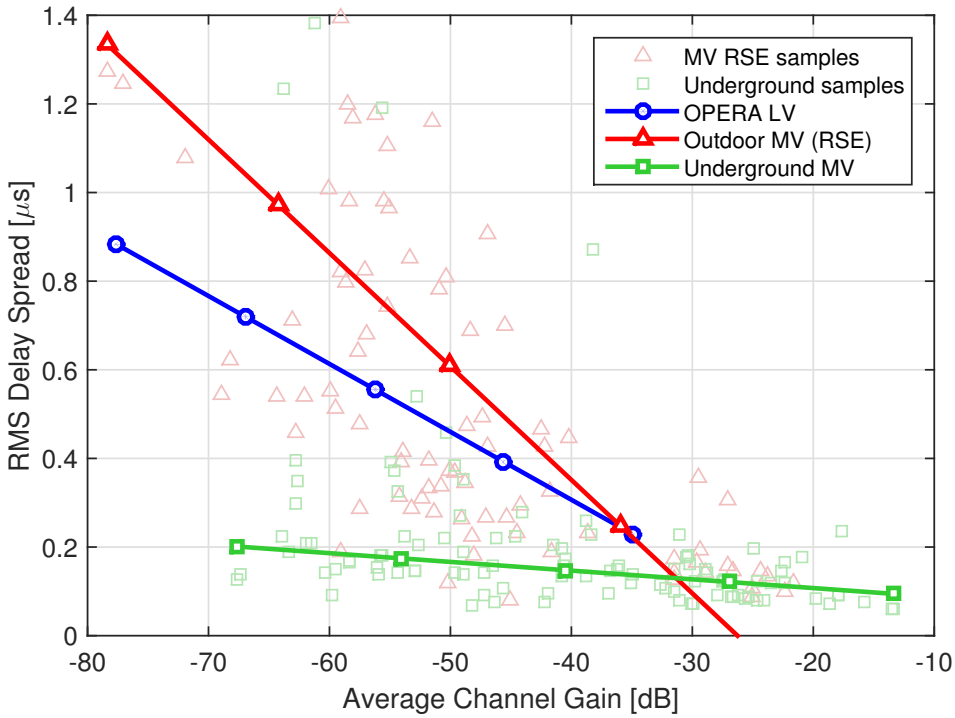

Figure 6.4: Relationship between RMS-DS and ACG for two outdoor MV measurements, i.e. RSE laboratories and underground networks, and the corresponding robust regression fit. The robust fit of the OPERA LV channels is also shown.

Contrariwise, the network connecting the RSE industrial laboratories consists of many branches, connecting a large number of users within a small area. This configuration is more close to an American network structure or to a LV network layout, as confirmed by the robust fit slope proximity among LV and MV scenarios. The great number of interconnections involves high values of RMS-DS, as summarized in Table 6.1. Finally, it can be noted as the LV robust fit line is shifted to the left if compare to the MV robust fits. This means that the outdoor LV scenarios exhibits a lower ACG, and thus an higher attenuation, as listed in Table 6.1.

The average value of the most commonly used statistical metrics, namely ACG, RMS-DS and CB, averaged over the corresponding measurements database, are listed in Table 6.1 for each considered outdoor scenario. The corresponding bandwidth is also highlighted. As expected by the above discussions, the underground MV channels exhibit the lowest RMS-DS, and thus the highest CB. Furthermore, they show the highest ACG, or lowest attenuation. This is aided by the limited number of branches and the good quality of deployed cables, despite the length. Conversely, both outdoor LV and MV RSE scenarios show a high RMS-DS caused by the large number of interconnections. Moreover, the topology, together with the bad quality of the cables, leads to high values of attenuation (low ACG), especially for the LV scenario. The listed results provide an overview of the possible average behaviors that can be encountered in different outdoor scenarios and network configurations.

Table 6.1: Average statistical metrics for the different outdoor LV and MV scenarios in the corresponding bandwidths.

Scenario	Band (MHz)	$\overline{\mathcal{G}}$ (dB)	$\overline{\sigma}_\tau$ (μs)	$\overline{\mathcal{B}}_C^{0.9}$ (kHz)
Outdoor LV	1.8–50	−56.96	0.581	140.63
Outdoor MV (RSE)	1.8–50	−50.36	0.741	200.89
Underground MV	2–40	−40.92	0.207	487.26

6.2.3 Input Line Impedance Characteristics

In order to be able to couple and inject the PLC signal into the power network, the line impedance must have a suitable value. Very low impedance values involve that the signal generator at the transmitter side must inject very high current values in order to transfer appreciable values of voltage to the load and, therefore, to the receiver port [144]. Thus, it is of fundamental importance to analyze the line impedance (Z_{IN}), defined as in Section 2.1.2. Typical values of the magnitude and the phase of the line impedance are reported in Figure 6.5. We consider both the MV and the LV scenario for both the NB and BB spectra. The profiles in Figure 6.5 have been obtained considering the most typical trend among those reported in [153] (LV and MV BB), [154] (LV NB) and [155] (MV NB). Unfortunately, most of the impedance analysis reported in the literature that concern the MV lines refer to the characteristic impedance of the deployed cables and do not discuss the input line impedance seen at the transmitter side. Thus, we were not able to retrieve any substantial information concerning the phase of the input line impedance for the MV lines in the NB-FS.

From Figure 6.5 it can be firstly noted that the line impedance is significantly low in the NB case. The two peaks, in correspondence of the edge frequencies of the MV case in Figure 6.5a, are mainly due to resonance effects induced by mismatches among the channel characteristic impedance and the line terminations, such as open-circuit and short-circuit. Nevertheless, as specified in [155], the characteristic impedance of the differential mode is very low, with values of few Ohm.

Contrariwise, the BB spectrum exhibits much higher values of impedance, although the Z_{IN} behavior is frequency selective, which reflects into a more benign situation for the modem line driver. It is interesting to note that there is a serial resonance when the magnitude, in Figure 6.5b, approaches zero, while the phase, in Figure 6.5d, is zero. Contrariwise, the magnitude drastically increases in correspondence of a parallel resonance, when the phase is zero. This is the reason of such high values of input impedance.

Another aspect that can be observed for the BB spectrum is that the LV and MV networks exhibit almost a dual reactive behavior. Indeed, for lower (up to 2.2 MHz) and higher (over 15.5 MHz) frequencies, LV lines have a capacitive behavior, while MV lines for lower (up to 8.5 MHz) and higher (over 21.5 MHz) frequencies exhibit an inductive

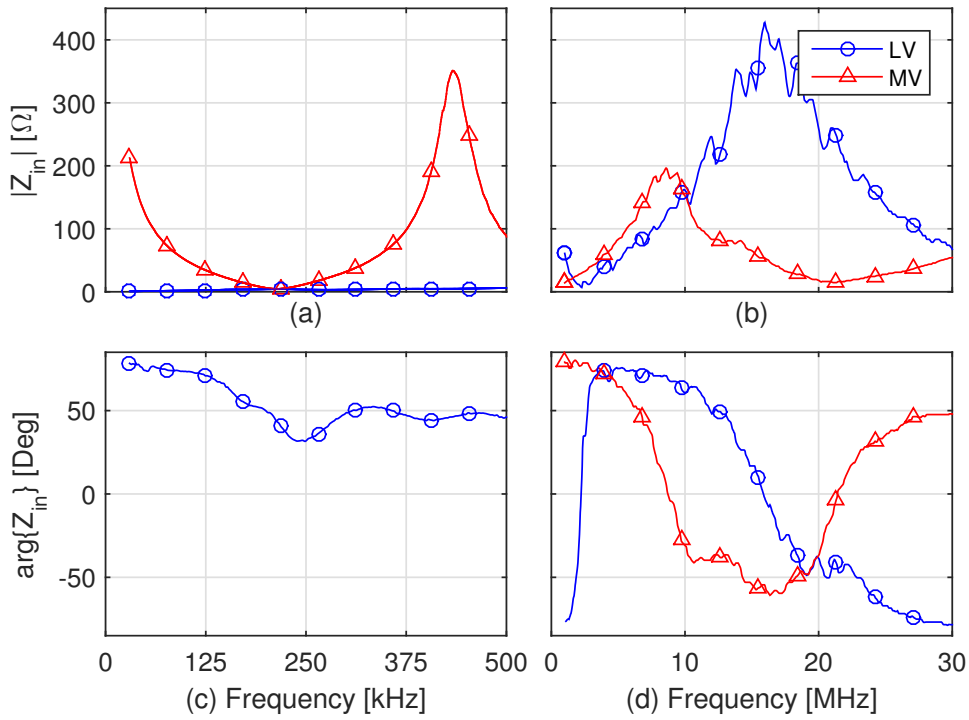

Figure 6.5: Magnitude (on top) and phase (on bottom) of the input impedance for outdoor LV and MV lines in the NB (left side) and BB (right side) spectra.

behavior. Contrariwise, in the middle frequency range. This effect is mainly due to the network configuration and structure, as well as to the specific loads connected to the network. For example, the transformers act as a high parallel inductance at low frequencies. Finally, for long cables, as those typically deployed in MV networks, and high frequencies, the line impedance is dominated by the characteristic impedance of the cable.

6.2.4 Network Transformers and Discontinuities

As said, circuit breakers and transformers may act as discontinuity elements for the PLC signal propagation. While this is not necessarily a negative aspect, since the overall network can be partitioned into cells and therefore increase the overall system capacity, in certain circumstances it is desirable to let the PLC signal propagate uninterruptedly through the circuit breaker and through the transformer.

It has been claimed that the transmission in the NB-FS has a better ability to bypass such elements. However, it should be observed that such an ability is actually increased at high frequencies, where electromagnetic coupling effects are more pronounced. This is shown in Figure 6.6, where the attenuation introduced by a circuit breaker in open and closed configuration, together with the attenuation between the primary and secondary ports of a MV/LV transformer, are depicted. It can be noted as the attenuation is less than -40 dB, for frequencies above 10 MHz, although the open state of the circuit breaker is

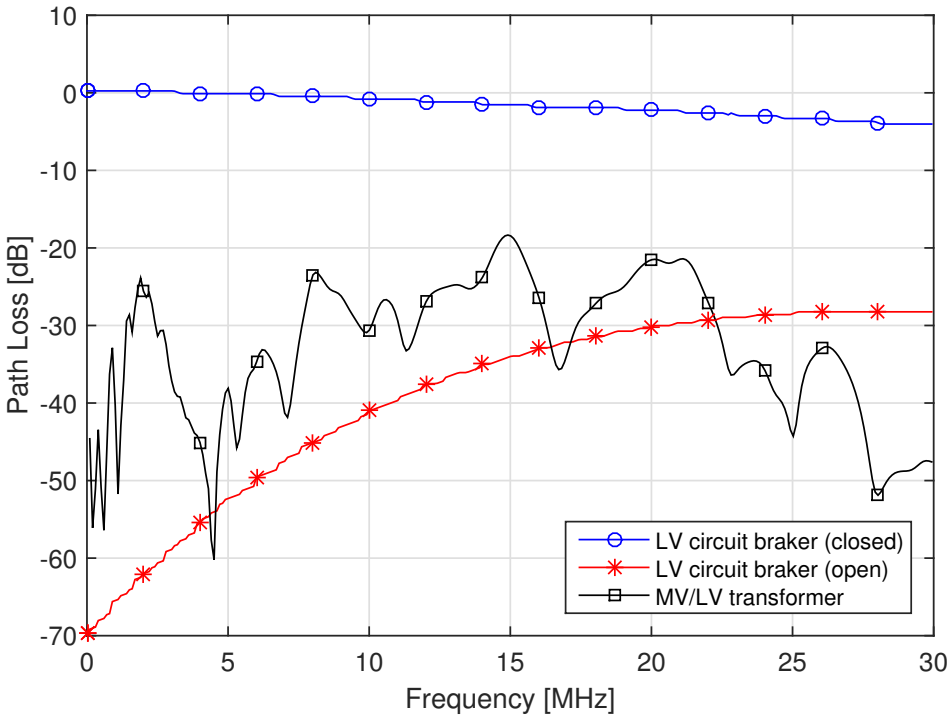

Figure 6.6: Path loss of a LV circuit breaker, for both open and closed configurations, and of a bypass MV/LV transformer, along frequency.

considered. Contrariwise, the attenuation significantly increases at low frequencies. Also for the transformer the lower attenuation is located at lower frequencies. Again, this shows that transmitting in the BB frequency range has higher potentiality to bypass circuit discontinuities.

6.2.5 Background Noise

PLC networks are affected by several noise components, namely the background noise and the impulsive noise with both periodic and aperiodic components, introduced by noisy loads or switching devices [3], as discussed in Section 1.3.2. That is, the noise is dominated by a mixture of active noise components injected in the network by the loads connected to it. Typically, an equivalent average (stationary) colored PSD profile is used to describe the overall noise experienced at the receiver side. This is represented in Figure 6.7 considering both the LV and the MV scenarios. According to the OPERA measurement campaign in [76], the noise PSD can be analytically modeled as

$$q(f) = a_q + b_q e^{f c_q} \quad [\text{dBm/Hz}], \tag{6.1}$$

where the frequency f is in MHz, while the constant parameters a_q, b_q and c_q to obtain the OPERA LV and MV profiles are reported in Table 6.2.

Furthermore, some time domain noise traces were also measured in one of the out-

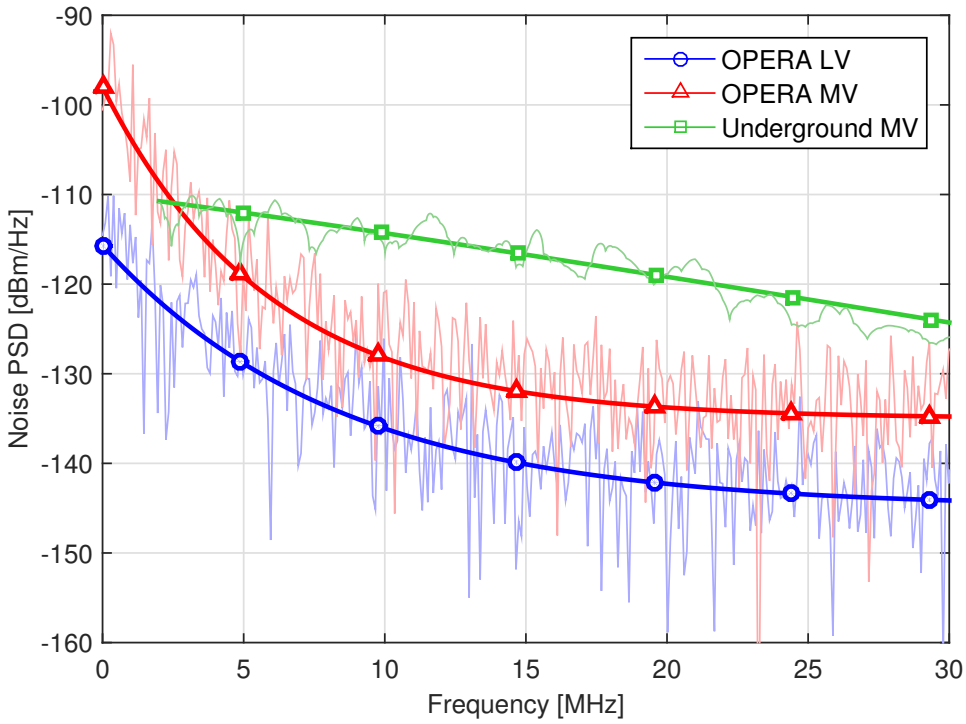

Figure 6.7: OPERA LV and MV [76], as well as underground MV [131], background noise PSD profiles. The exponential model is also shown.

door underground MV networks sites discussed in [131]. In particular, the noise PSD is obtained through the Fourier transform. As usually happens in PLC networks, the measured noise PSD exhibits a frequency decreasing profile, though some outliers exist. The PSD measurements profiles have been averaged and then fitted via the expression

$$q(f) = a_q + b_q f^{c_q} \quad [\text{dBm/Hz}]. \tag{6.2}$$

Also in this case, the frequency f is in MHz. Comparing the OPERA noise model in (6.1) with the underground MV noise expression in (6.2) it can be seen as the dependence on the frequency f is different. In particular, (6.1) is characterized by an exponential dependence, while (6.2) by a power dependence. Although differences exist, the noise PSD shows a frequency decreasing trend in all the considered cases, as clarified in Figure 6.7.

A typical noise PSD and the corresponding fitting model are depicted in Figure 6.7 for the outdoor LV and MV OPERA scenario, as well as for the underground MV network. Concerning the latter environment, the frequency range is limited down to 2 MHz since the validity bandwidth for these noise measurements is the same of the channels discussed in Section 6.2.1, i.e. 2–40 MHz, due to the pass-band behavior of the deployed couplers. It is important to note as the MV channels experience a higher PSD level w.r.t. LV channels. This is probably related to the fact that MV lines deploy long cables that can capture RF disturbances. Moreover, load unbalances or device activities can directly inject great amounts of noise, with harmonics along the entire frequency range, more than in a LV

Table 6.2: Parameter values of the best exponential fit concerning the background noise PSD for different measurement databases and scenarios.

Parameter (q)	a_q	b_q	c_q
OPERA LV	-114.941	29.282	-0.120
OPERA MV	-105.000	37.000	-0.170
Underground MV	-110.000	-0.351	1.090

network. Furthermore, the noise drastically increases at lower frequencies, having high impact on the NB-PLC schemes. This is most evident looking at the OPERA background noise, that assumes very high values at low frequencies.

The constant parameters a_q, b_q and c_q for both the discussed models in (6.1) and (6.2) and for both the considered LV and MV scenarios are summarized in Table 6.2. This allows to easily generate a background noise PSD profile that is equivalent to the measured one, depending on the considered environment.

6.3 NB and BB Performance Comparison

Although it has been shown that BB channels are more attenuated than NB channels, the noise PSD is higher in NB than in BB. Thus, these information are not sufficient, by themselves, in order to highlight all the strengths and weaknesses of the different environments. In order to put in comparison the NB and the BB transmission technologies, as means for data communication, the SNR and the performance are assessed.

6.3.1 Signal-to-noise ratio

In communications, what is relevant is the SNR at the receiver side [144]. Hence, beside the channel properties, also the influence of noise must be considered. It is well-known as PLC networks are affected by a great deal of noise, especially when considering the outdoor MV scenario [3]. Figure 6.8 shows the SNR values at the receiver side, as a function of frequency, for both the outdoor LV (OPERA [75]) and MV (RSE [130]) scenarios in the BB-FS. The values are computed relying on the average channels depicted in Figure 6.3 and on the noise models, corresponding to the OPERA measurements analyzed in [76], which are displayed in Figure 6.7. In particular, the background noise model profiles for the outdoor LV and MV scenarios are generated according to the expression in (6.1) using the corresponding coefficients listed in Table 6.2. However, despite they are sufficiently representative, other situations can be encountered, depending on the considered scenario. For example, as discussed in Section 6.2.5, the outdoor underground MV background noise measurements reported in [131] exhibit a slightly different frequency behavior. Finally, a transmitter PSD of -50 dBm/Hz has been considered.

Figure 6.8 shows that for both the considered scenarios the SNR has a concave trend,

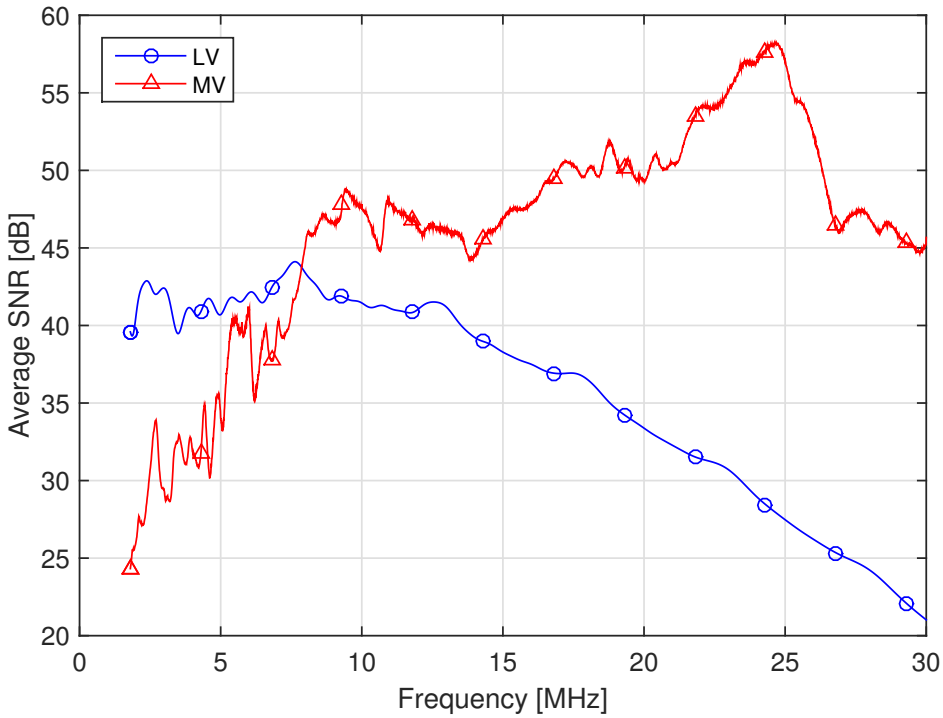

Figure 6.8: SNR trend for LV and MV scenarios in the BB frequency range.

due to the combination of an increasing channel attenuation and a decreasing noise PSD profile along frequency. The maximum values are centered around 7.5 MHz and 24.5 MHz for the LV and MV scenario, respectively. Furthermore, as shown in Figure 6.3, the LV average PL profile is dominated by the attenuation, especially at high frequencies, this behavior reflects also to the LV SNR trend depicted in Figure 6.8.

It should be observed that the low line impedance exhibited in the NB spectrum exacerbates the difference in terms of SNR when compared to the BB spectrum. Thus, higher voltage levels of at the source must be granted in order to overcome the coupling losses, rendering the scheme less energy efficient. Thus, the SNR value is not the only parameter to take into account when a certain technology, or device, is developed. Indeed, beyond the theoretical studies and targets, also the physical implementation challenges must be tackled in order to provide and design proper devices.

6.3.2 Capacity

It is of primary interest to evaluate the performance that a given transmission scheme can provide. In this respect, the maximum achievable rate, i.e. the capacity, is the most common and used metric. It has been evaluated as discussed in Section 2.2.4, according to the expression in (2.20). Since the channel capacity in (2.20) is directly connected to the SNR, the trend depicted in Figure 6.8 motivates the study of the achievable performance when transmission is performed in the NB-FS or in the BB-FS. In particular, we assume to keep the signal bandwidth equal to 500 kHz, but to adapt the central carrier so that

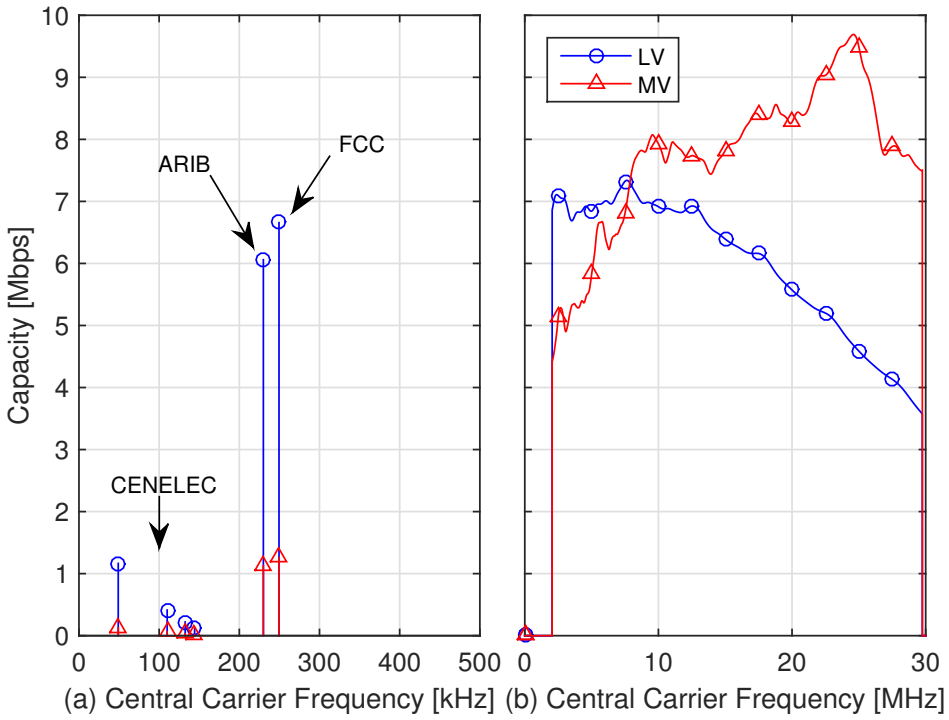

Figure 6.9: Capacity for LV and MV scenarios in the NB (a) and BB (b) frequency range. For the BB case a bandwidth of 500 kHz is considered.

the BB-FS can be occupied. This is a form of adaptive modulation that cognitively uses the available spectrum in an optimal manner. This is shown in Figure 6.9b, together with the capacity offered by the individual CENELEC, ARIB and FCC bands in Figure 6.9a.

In order to comply with the regulations on the radiated emissions [143], the constraint on the transmitter PSD is assumed equal to -50 dBm/Hz, as done for the SNR computation discussed in Section 6.3.1. This is done for both the BB transmission and the adaptive NB modulation within the 1.8–30 MHz band. Conversely, there are no unified and overall recognized or standardized levels specifying the transmission PSD limits for the NB-FS, although some reference levels may be inferred by measuring the emission of different commercial devices. However, since our aim is to investigate how the channel and noise properties affect the NB and the BB transmission performance, the same PSD constraint of -50 dBm/Hz is adopted also for the NB-FS.

It can be noted as the capacity trend in Figure 6.9b recalls the SNR curves shape, with the capacity maxima located at the same frequencies of the SNR maxima, for both the corresponding LV and MV scenarios. We do not consider transmission in the 500 kHz–1.8 MHz band since this is currently not possible for regulations. It is evident how the transmission in the BB spectrum can be beneficial. The individual CENELEC bands do not offer high capacity. In general, this is due to the higher SNR that can be experienced in the BB region w.r.t. the NB case. Only in the LV case, the ARIB and FCC NB frequency spectra offer capacity values close to the BB-FS case.

To aid the comparison, the capacity attainable in the NB-FS and BB-FS, when the

Table 6.3: Achievable capacity and total power request for LV and MV scenarios in both NB and BB frequency ranges.

	Bandwidth	Capacity (Mbps)	Total power @ 1 Mbps (dBW)
LV	3–500 kHz	6.87	−64.13
	7.385–7.885 MHz	7.34	−66.20
	1.8–30 MHz	333.41	−68.13
MV	3–500 kHz	1.32	−29.95
	24.35–24.85 MHz	9.69	−80.29
	1.8–30 MHz	432.40	−82.11

central carrier is optimally chosen, are summarized in Table 6.3 for both the LV and MV scenarios. As a further term of comparison, the capacity achieved exploiting the entire BB-FS is displayed. It is from tens to hundreds times higher than that attainable in the NB-FS. Moreover, we report the total power (in dBW) needed in order to achieve a certain target rate, namely 1 Mbps in the considered case. This power value has been computed applying the optimal solution provided by the margin adaptive water-filling algorithm, which minimizes the power required to achieve a given target rate. As it can be noted, the MV-NB case is the most energy hungry environment, requiring more than 50 dBW w.r.t. the BB-FS case, followed by the LV-NB scenario. The differences grow, becoming more than twice, when comparing the NB-FS w.r.t. BB-FS at higher target rates, even of few Mbps.

The results show that transmission at higher frequencies, as well as a bandwidth expansion, can offer higher rates and higher energy efficiency. Consequently, BB transmission can also significantly reduce the transmission delay (latency).

6.4 Main Findings

PLC is a natural choice to deliver bi-directional connectivity in the power delivery network, enabling the use of several different applications for the smart control and management of the grid. Both the NB-FS (3–500 kHz) and the BB-FS (1.8–100 MHz) can be exploited for the realization of PLC solutions. As a matter of fact, the market offers a choice of engineered solutions that are compliant with the NB (ITU-T G.hnem, IEEE P1901.2) or the BB (ITU-T G.hn, IEEE P1901, HPAV) standards. Although both technologies are mature and ready for mass deployment, it is also true that these techniques have to evolve in order to be able to offer increased levels of performance in terms of data rate, latency, robustness and coverage w.r.t. what is achieved today.

It is often said that most smart grid applications require low data rates and therefore NB solutions are the right choice. It should be recognized that BB solutions offer higher

flexibility and a better trade-off between data rate, latency, robustness and energy efficiency. Adaptive, scalable and flexible solutions, which can smartly use the spectrum and operate in different spectrum portions, e.g. in both the NB-FS and BB-FS, are the right approach for the evolution of current PLC technology. It is a matter of fact that the low frequency bands, e.g. CENELEC-A, show a low channel attenuation, but a high noise. These challenges, within the NB-FS, are mainly due to the increasing number of emissions from active loads, a time variant behavior and a low impedance, which challenges the realization of robust PLC modems and line drivers. On the other side, transmission in the BB-FS enjoys lower noise, much higher line impedance and it offers frequency diversity. However, transmission at high frequencies, at the moment, may be challenged by radiation limits, especially in overhead conductors and by coexistence problems that can be solved by following a cognitive approach and developing low-power solutions. In this respect, filter bank modulation and impulsive PLC solutions are two promising approaches.

Complexity is also another point to consider and the associated requirements can be defined depending on the application and on costs. NB solutions can be realized on re-configurable digital signal processing (DSP) architectures. BB solutions may require application-specific integrated circuit (ASIC) realizations, or mixed ASIC-DSP architectures. The cost difference vanishes as massive production and deployment takes place. Indeed, for certain applications, e.g. elementary sensor/actuator networks, or extremely simple devices, embeddable solutions are desirable.

The overall system performance depends on layer 1, but also on layer 2. A key role is played by the media access scheme and, in this respect, a combination of TDMA and frequency-division multiple access (FDMA) with adaptive scheduling, rather than simple CSMA, can offer benefits [156]. Routing mechanisms, implemented at layer 2, or eventually at layer 3, are also fundamental to achieve the high coverage requirements in large grids. Overall, it is of paramount importance to design light protocols that allow fast responses and network configuration, especially in smart grids, where the network recovery has to be immediate in the event of faults and blackouts.

7 Scenarios Comparison

In recent years we have assisted at the huge demand of data connectivity requested by users, but also by the widespread use of "smart" devices that need to exchange information. The desire to deliver new communication services, without requiring significant investments in the expansion of the telecommunication infrastructure, has pushed towards the development of no-new-wire technologies. Besides wireless and twisted pair copper systems, an attractive solution is represented by the information transmission over the power delivery infrastructure, namely the PLC, which plays an important role and is becoming more and more popular.

By exploiting the power delivery grid, the PLC enables the delivery of a broad range of services, such as remote metering or station surveillance, local area networks, home networking and automation, as well as a wide range of smart grid applications. PLC can be applied to provide a two-way communication in all the three smart grid domains, namely transmission, distribution and user domains, exploiting HV, MV and LV lines [19]. Furthermore, it can provide communication capabilities between sensors located in substations, so that status can be monitored, and faults detected and isolated. PLC can also be exploited for the detection of islanding events. The main application in the LV part of the network is automatic/smart metering. For this application, PLC has already enjoyed a great deployment success, with about 90 million meters installed in Europe, and many more installed worldwide. Sensing, command, and control applications are also of great interest for applications inside homes or buildings. The in-home PLC network can be exploited for energy management purposes, together with a wide set of home automation applications for increasing security, comfort and life quality. Two further PLC application areas lie in the management and control of micro grids, e.g. local generation grids using renewable energy sources, such as solar cells and wind turbines, and in the connection between electrical vehicles and the grid, which can offer a wide set of applications. Finally, there are a number of other PLC applications among which a promising one, but not yet significantly exploited, is in-vehicle (car, ship, plane, train) communication. Since power

lines are pervasively deployed, the use of the PLC technique is potentially ubiquitous.

7.1 Open Challenges and Contributions

Despite the existence of commercial PLC systems and recently released standards, PLC can still evolve and advanced solutions can be identified to better solve the open challenges. These latter mostly rely on the full understanding of the hostile communication medium, the development of ad hoc modulation and coding techniques and the definition of MAC protocols for lossy channels with time-variant behavior in terms of traffic, noise sources and topology changes. Indeed, in order to provide reliable services, design proper devices and define new and effective standards, it is of fundamental importance to assess the channel properties, highlighting their specific features for different environments. This is even more true when considering PLC networks, where the different wiring structure and network topology, as well as the line discontinuities and the unmatched loads, imply an extreme channel variability. Thus, a thorough knowledge of the transmission medium is needed in order to develop reliable channel models, able to faithfully describe a real network.

This chapter focuses on the BB frequency range, considering both indoor (in-home and in-vehicle) and outdoor (low and medium voltage) scenarios. The aim is to provide and summarize the main results in terms of channel and noise properties, considering different databases and comparing several scenarios. All the collected information are exploited in order to develop simple and effective channel models, as it will be discussed in Chapter 8. In particular, the main results in terms of channel characterization and metrics relationship are summarized and compared in Section 7.2 for each considered scenario, separately. The same is done in Section 7.3 concerning the background noise PSD. Afterwards, the performance, in terms of maximum achievable rate, are inferred in Section 7.4. The SISO channel measurements of all the previously considered environments, under the corresponding average noise PSD profile, are considered. Finally, the improvements due to the MIMO extension and to a fairer colored and correlated background noise assumption, are assessed.

7.2 Channel Characteristics

The characterization of the PLC channel is very important since it enables the models development and the design of appropriate physical layer transmission technologies. The specific characteristics depend on the application scenario and on the used transmission bandwidth. For example, as for the wireless scenario, the PLC channel is intrinsically broadcast. However, it has a number of differences that limit the achievable performance. The main ones are the network topology that, with its structure (such as the number of

branches, the connected loads and the layout), affects the channel properties (such as the statistics and the frequency and spatial correlation). Indeed, typically, PLC channels are log-normally distributed, as detailed in Section 3.2.1, while wireless channels are Rayleigh distributed [142].

In general, the PLC channel exhibits multipath propagation, due to line discontinuities and unmatched loads, which translates in severe frequency selectivity. Differently from wireless, there is no mobility, so that the channel is mostly static. However, changes in the wiring topology and in the connected loads induce a change in the channel response. Furthermore, cyclic time variations with periodicity equal, or double, the mains frequency can be present [137–139]. This is due to the periodic change of the loads impedance with the mains frequency, in particular of those that have rectifying units for the alternating current (AC) and AC/DC converters, which exhibit a bistatic impedance behavior. Such cyclic time variations are mostly visible at frequencies below 2 MHz. This is because most of the active loads deploy EMI filters that, at high frequencies, provide a low and stable value of impedance [157].

Moreover, usually, the PLC network channels share part of the same communication link from a transmitter to different receivers, namely the backbone, that introduces a MU correlation between the various links, as discussed in Section 3.4. This effect must be considered since it involves a certain level of correlation among the PLC channels that, therefore, cannot be assumed independent, as for example occurs in a rich scattering wireless environment. In addition, the cables proximity involves prominent cross-talk phenomena, especially when a MIMO transmission scheme is assumed, as detailed in Chapter 4. Furthermore, besides the above mentioned detrimental effects, a great deal of noise, both coupled and radiated, affects the PLC channel. The channel properties, as well as the surrounding effects, can significantly change from one scenario to another due to the particularities exhibited by the considered application context.

Depending on the considered environment, different network topologies, and thus channel properties, can be observed. In order to give an idea on how much and in which way the considered environment affects the channel properties, all the different and previously discussed environments, such as the indoor scenarios, i.e. a confined structure, as a home, a car or a ship, and the outdoor scenarios, which considers the external distribution grids, as low and medium voltage lines, are compared. In particular, Figure 7.1 depicts the average PL in dB scale ($\overline{\mathcal{L}}_{dB}$) along frequency, averaged among the available channel measurements, exhibited by all the above mentioned scenarios. It can be noted as the average PL profile is confined between -40 and -15 dB, in the 5–40 MHz band, for all the considered scenarios, except for the outdoor LV networks. Furthermore, in order to directly and visibly compare the existing relationships between the most commonly used statistical metrics, the previously discussed results, concerning our measurements, as well as other available databases discussed in the literature, are distinctly represented

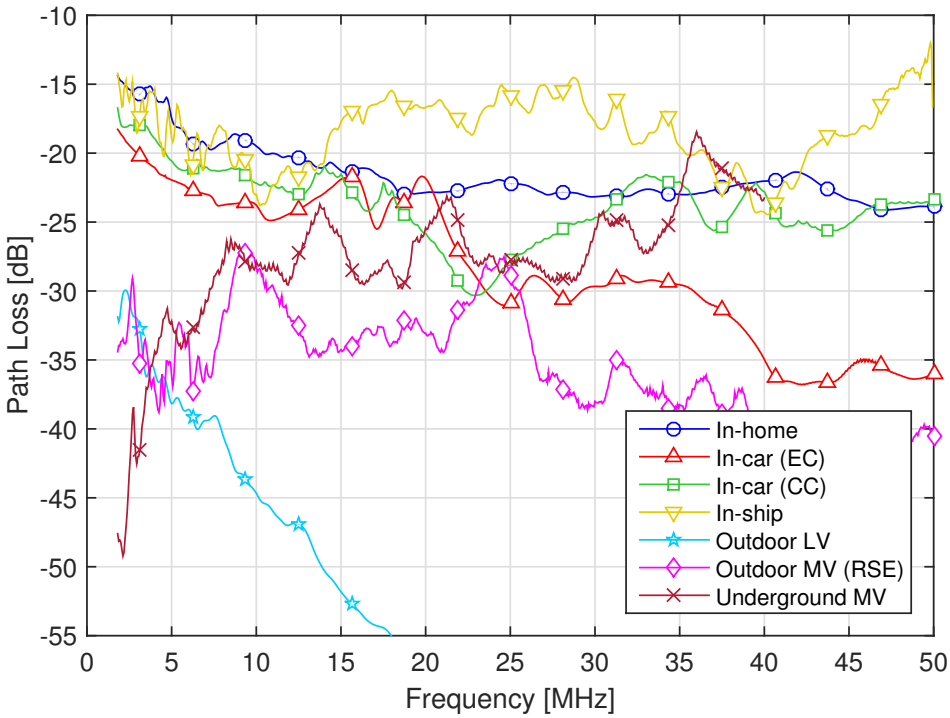

Figure 7.1: Average PL profile, along frequency, for all the considered scenarios, namely in-home, in-car (EC and CC), in-ship and outdoor (LV and MV).

in Figure 7.2.

The figure displays the scatter plots of the relationship between the RMS-DS, i.e. the channel dispersion, and the ACG, representing the channel quality or, inversely, the attenuation. The robust fit of our measurements, represented by the grey circles, and that of other available measurement campaigns, is also displayed, limiting its line ends to the corresponding set of values. This allows a quick understanding of where the points are located and what relationship is exhibited by the set of considered values corresponding to a certain database. In order to clearly discuss the channel properties and the influence of the corresponding scenario particularities on the presented results, the previously mentioned environments are individually discussed in the following sections. Moreover, a final summarizing comparison is briefly described in Section 7.2.4 in terms of average statistical metrics, considering the corresponding measurement databases. The considered bandwidth is limited to the 1.8–50 MHz range since some measurements were carried out up to 50 MHz. This allows a fair comparison among the several environments.

7.2.1 In-Home Scenario

One of the well-known and most investigated scenarios, belonging to the indoor environment, is represented by the in-home premises. The domestic environment represents an attractive research and development area since the more common twisted pair and wireless communication technologies have encountered a bottleneck at the house door,

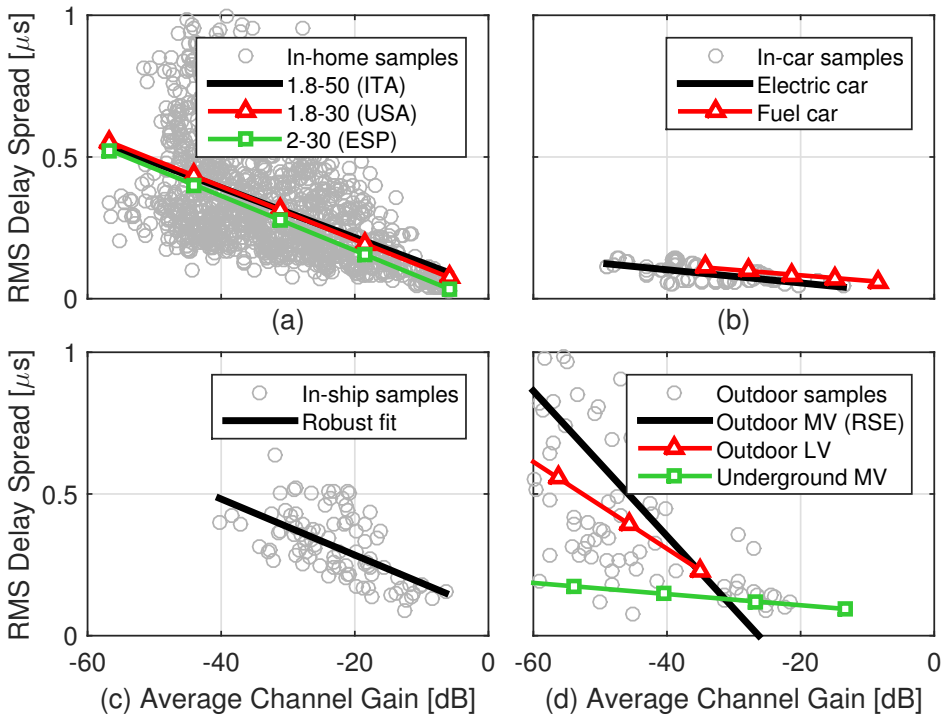

Figure 7.2: RMS-DS versus ACG for in-home (a), EC (b), outdoor MV (c) and in-ship (d) scenarios. The robust fit for the USA and ESP measurements (a), the CC database (b) and the OPERA outdoor LV reference responses (c), is also shown.

also known as last mile. This is even more true when considering groups of houses or buildings.

In-home grids are characterized by a layered tree structure with wires that depart from the main panel, reach derivation boxes and then the final outlets [117]. The presence of many branches give rise to severe frequency selective fading, as discussed in Chapter 3. In Figure 7.1 the average PL of the 1266 CFR measurements acquired in Italian home networks, discussed in Chapter 3, is considered focusing on the 1.8–50 MHz band. It can be noted as the depicted PL is one of the highest, or less attenuated, almost over the entire frequency range and that it is lower only w.r.t. the in-ship case. Furthermore, the PL profile is slightly decreasing along frequency. Instead, the frequency selectivity behavior is not clearly detectable since $\overline{\mathcal{L}}_{dB}$ is obtained averaging over a great number of measurements, namely 1266, that is at least one order of magnitude greater than the number of measurements of the other considered databases. Hence, as known, the average smooths the sharp behavior of the PL profile.

Regarding the statistical metrics, the scatter plot of the relationship between the RMS-DS and the ACG in dB scale, computed considering the same in-home database of measurements, is depicted in Figure 7.2a. The robust fit of the measurements is labeled as ITA in order to distinguish it from the robust fit of the measurement campaigns carried out in the USA for the 1.8–30 MHz band [73] and in ESP for the 2–30 MHz band [74], that are also depicted. A good agreement can be observed among the robust fit of the

different measurements, especially with the Spanish one. Slight deviations of the line slope and y-intercept, reported in Table 7.3, may be due to the different frequency range and to differences on the procedure adopted to compute the CIR, which reflects to the RMS-DS values. Thus, although different network structures and typologies are assessed, a similar behavior can be identified.

Moreover, looking at Figure 7.2a, it can be noted as RMS-DS and ACG are negatively related. Thus, high attenuation values (low ACG) imply high energy dispersion (high values of RMS-DS). This is, since, a low ACG stands for long cables or cables having a large number of branches, which also cause increased RMS-DS values. To aid the comparison, the average statistical metrics, computed averaging the results over the entire set of measurements, are listed in Table 7.1 of Section 7.2.4. In order to fairly compare the different scenarios, the same 1.8–50 MHz frequency band is considered.

7.2.2 Vehicular Environment

As for the in-home case, also the vehicular environment can be classified within the indoor scenario. In particular, the vehicles can be distinguished in multiple categories, such as cars with electric motor or combustion engine, ships, trains, planes, and so on. This application scenario is very attractive, especially in terms of weight reduction, that translates in performance improvement and also in a costs saving.

Within the vehicular context, two different scenarios have been considered in Chapter 5, namely in-car and in-ship. Concerning the in-car scenario, a compulsory distinction must be done among the CC, equipped with a fuel engine, and the EC, powered by a battery. Indeed, in an EC, the motor drives inject a great deal of noise in the low-power network, which is not separated from the high-power supplying network. For the EC case, the 84 measurements carried out in a compact electric car and discussed in [89] are considered. As a term of comparison, also the database of 193 measurements, made online available and described in [46], is considered for the CC scenario.

Concerning the in-ship case, the measurements acquired in a measurement campaign made over the LV distribution network of a large cruise ship, detailed in [54], are considered. The database comprises 92 channel measurements of two types, distinguished by the two different distribution grid sections, namely the one with a star-style topology from the SS to the DB boxes, and the one with a bus bar structure from the DB to the RP cabinets. In order to provide an average result, differently from what has been done in Chapter 5, all the channels are considered together.

Among the considered indoor scenarios depicted in Figure 7.1, the two in-car environments show the lowest PL values, i.e. high attenuation, with the lowest trend exhibited by the EC case. This is noticeable especially above the 30 MHz. Moreover, the PL behavior is smoother with respect to the PL of the other scenarios. This is due to the star-style underlying network topology, having a reduced number of branches, that limits

also the RMS-DS values, as showed in Table 7.1. Furthermore, the dependence between the computed RMS-DS and ACG quantities and the corresponding robust fit for the in-car scenario are represented in Figure 7.2b. The robust fit computed relying on the CC discussed in [46] is also depicted. As it can be noted, the slope of both the robust fits is lower with respect to that of the different in-home scenarios, reported in Figure 7.2a. In practice, it is approximately a fifth, as also stated in Table 7.3. This translates into a lower RMS-DS and a slightly higher ACG, as clearly summarized in Table 7.1. Furthermore, the robust fit for the electric and fuel car show almost the same slope, with the CC robust fit shifted towards right, meaning that in conventional cars a slightly lower attenuation, or higher ACG, is exhibited w.r.t. electric cars.

Concerning the in-ship scenario, the PL profile represented in Figure 7.1 is the highest among all the considered scenarios, as clearly noticeable looking at Table 7.1. This behavior is aided by the star-style network part, which consist of good quality cables with a limited number of branches, despite the significant length, as discussed in Section 7.2.4. A frequency selective behavior is detectable, which is mainly due to the part of the network consisting of a bus-structure with multiple branches. This network configuration leads to high values of RMS-DS, as confirmed by the average results in Table 7.1. In terms of statistical metrics, depicted in Figure 7.2c, the RMS-DS versus ACG values are all moved toward the right hand side w.r.t. the other scenarios, leading to an high ACG, or low attenuation, on average. However, the values are still vertically spread, providing significant RMS-DS values. These statements are also highlighted by the average results listed in Table 7.1, showing as the in-ship scenario is characterized by the highest ACG value, although the RMS-DS is similar to the in-home case, while for the in-car scenarios this value is quite low. Furthermore, it should be noted that the robust regression fit slope of the in-ship scenario is close to that of the in-home case, as listed in Table 7.3.

7.2.3 Outdoor Grids

Differently from the indoor scenario, a less comprehensive analysis of the outdoor PLC channel is available in the literature for what concerns both the LV and MV part of the distribution grid. However, also this part of the power delivery structure is becoming more and more attractive in order to provide and deliver widespread information contents. In this section, the focus is on LV and MV power delivery networks. For the MV scenario, the two different measurement databases discussed in Chapter 6 are considered. The focus is on the 98 MV responses collected at the industrial complex of the RSE laboratories, presented in [130], since the measurements were carried out up to 55 MHz. Although the validity frequency range is 2–40 MHz, due to the couplers pass-band response, also the 122 channel responses discussed in [131], which have been collected in a measurement campaign performed in northern Italy in 2013 over MV underground lines, are considered. Concerning the outdoor LV lines, the measurement campaign performed

by the OPERA project in [75] is considered. In particular, from the measurements, a deterministic model was proposed so that eight reference channel responses have been tabulated. These reference channels are used for the discussion in this section.

Figure 7.1 shows the average PL of the different MV measurements, as well as of the OPERA reference channels obtained from the full set of eight responses. As it can be noted, the LV scenario exhibits a PL dominated by the attenuation w.r.t. multipath fading, especially at high frequencies. This is mainly due to the poor quality and to the length of the deployed cables. However, the great number of branches, discontinuities and unmatched loads, further affect the channel attenuation, beyond the selectivity behavior. Compared to LV, the average PL for the MV scenarios is less attenuated, assuming similar values, for both the considered networks, within the 3–30 MHz band. The differences outside this bandwidth are mainly related to the band-pass behavior of the couplers used during the measurement campaign. These high PL values for the MV lines are due to a good cable quality, to a different network topology, with a reduced number of branches, and to the type and amount of connected loads.

A final comparison is made among the considered outdoor distribution grids. The statistical metrics relationship is shown in Figure 7.2d and concerns the MV channel measurements collected at the RSE laboratories and detailed in [130]. The robust fit for the outdoor LV reference channels derived from the OPERA project measurements [75] and for the underground MV lines [131] is also depicted. Obviously, the robust fit for the underground MV channels has been computed considering the CFRs in the validity band 2–40 MHz. It can be noted as significant differences exist also within the same outdoor scenario. In particular, the robust fit slope exhibited by the LV channels is roughly eight times that of the underground MV channels, as clarified by the values listed in Table 7.3. Contrariwise, the LV slope it is half the slope of the MV robust fit of the RSE measurements. This is due to the different underlying network topology. Indeed, LV networks are typically bus or tree structured with a great number of branches, as usually happens in a domestic (in-home) environment. This is the reason why the robust fit slopes among these two latter scenarios are so similar, except for the attenuation, that is higher for the outdoor LV lines, as reported in Table 7.1. Indeed, the samples are concentrated to the right in Figure 7.2d. The same happens for the MV lines feeding the RSE laboratories, that are deployed in a tree structured fashion, serving a great number of users and resembling the typical LV structure. Contrariwise, the underground MV network layout is more similar to a common MV distribution grid, with a star-style structure with few branches.

7.2.4 Overall Comparison

In order to compare and highlight the main differences among all the previously considered application scenarios, the average statistical metrics, namely ACG, RMS-DS and CB, are

Table 7.1: Average statistical metrics for all the considered scenarios. The BB-FS is considered.

Scenario	$\overline{\mathcal{G}}$ (dB)	$\overline{\sigma}_\tau$ (μs)	$\overline{\mathcal{B}}_C^{0.9}$ (kHz)	$\overline{\mathcal{C}}$ (Mbps)
In-home (ITA)	−33.10	0.357	251.48	359.97
In-car (EC)	−33.25	0.086	874.26	259.18
In-car (CC)	−27.33	0.102	677.14	409.89
In-ship	−22.89	0.320	258.83	353.56
Outdoor LV	−56.96	0.581	140.63	107.60
Outdoor MV (RSE)	−50.36	0.741	200.89	229.67
Underground MV	−40.92	0.207	487.26	197.30

listed in Table 7.1. With the aim of providing a fair comparison, the same 1.8–50 MHz band is considered. Only for the outdoor underground MV lines the considered frequency range is 2–40 MHz.

As it can be noted, the in-home scenario has the lowest ACG, i.e. highest attenuation, within the indoor context, as listed in Table 7.1. This happens since, typically, in-home networks are characterized by a large number of branches and quite long deployed cables, which causes also high values of RMS-DS, as reported. Instead, the in-car context exhibits low values of RMS-DS, due to the reduced number of branches, but high ACG values, due to poor electric wiring characteristics and to low line impedance values. Conversely, the in-ship scenario shows the highest ACG value, despite the cables length, due to the reduced number of branches and to a better cable quality, compared to the in-car scenario. However, the in-ship RMS-DS is similar to the in-home case since part of the considered network is characterized by a great number of branches, that increase and offsets the average value.

Concerning the outdoor channels, it can be seen from Table 7.1 as they show the lowest values of ACG, hence the highest attenuation. This is mainly due to the deployed cables length, compared to the indoor scenarios. In terms of RMS-DS values, instead, the things can change significantly, depending on the deployed underlying topology and on the considered power distribution grid part, i.e. LV or MV. The outdoor LV OPERA channels and the outdoor MV measurements carried out at the RSE laboratories, due to the great number of branches and to the possible mismatches, exhibit the highest levels of RMS-DS among all the considered environments. Conversely, the underground MV network shows a RMS-DS lower than the in-home scenario. This is, since, the underlying structure has a very low number of interconnections. Differently from all the others scenarios, for these channels the considered bandwidth is 2–40 MHz, due to the couplers limitations that were used during the acquiring procedure.

The CB is approximately the inverse of the RMS-DS, thus a low RMS-DS implies a high CB and viceversa, as shown in Table 7.1. The table also reports the average capacity obtained averaging the computed values of maximum achievable rate over the

Table 7.2: Average statistical metrics for different outdoor networks in the NB-FS.

Scenario	Band (kHz)	$\overline{\mathcal{G}}$ (dB)	$\overline{\sigma}_\tau$ (μs)	$\overline{\mathcal{B}}_C^{0.9}$ (kHz)
OPERA LV	9–500	-32.02	2.345	30.69
Outdoor LV [158]	3–500	$-(15 \div 33)$	$2.22 \div 3.96$	-
Outdoor LV [159]	3–95	~ -35	~ 19	~ 4

entire set of measurements within the corresponding scenario. It can be noted as, although the scenarios shows significant differences in terms of channel characteristics, network topology and background noise properties, similar performance are achievable for all the considered PLC networks. In particular, all the achievable rates are in the order of hundreds of Mbps. The highest value is obtained by the CC scenario. This is since the ACG is quite high, i.e. the channel is not too much attenuated, and the considered background noise PSD, that has been assumed AWGN as in [46], shows a level that is low, if compared to the EC scenario. The conjunction of these two effects leads to such an high value. Contrariwise, the lowest capacity is achieved by the outdoor LV channels. This is due to the high levels of attenuation, represented in Figure 7.1, although the corresponding background noise is the lowest among the considered scenarios, as depicted in Figure 7.3. Further results, concerning the capacity distribution, are provided in Section 7.4.

As mentioned, this thesis focuses on the BB-FS, however, also some results concerning the NB-FS have been discussed in Chapter 6, as well as in the literature. Some of the main metrics that concern the outdoor channels, where the NB transmission can play a significant role, are summarized in Table 7.2. The table lists the average ACG, RMS-DS and CB for the outdoor LV scenario in different NB frequency ranges. It is known as, usually, the channel at lower frequencies, i.e. in the NB spectrum of 9–500 kHz, is less attenuated than the channel at frequencies beyond 2 MHz, i.e. the BB channel, both in the indoor and in the outdoor environments. Indeed, considering the same OPERA outdoor LV reference channels, it can be noted as the ACG computed within the NB-FS, and reported in Table 7.2, is considerably lower than the ACG calculated considering the BB-FS, listed in Table 7.1. Nevertheless, high RMS-DS values are found, if compared to the BB-FS. Other results presented in the literature have been summarized in Table 7.2. In particular, [158] discusses NB-PLC measurements carried out in Indian and Chinese outdoor LV sites, while measurements that consider urban, suburban and rural LV environments, in the CENELEC-A band (3–95 kHz), are assessed in [159]. As it can be noted, the computed metrics confirm that, in general, the NB-FS exhibits a lower attenuation, but higher RMS-DS values and thus, dispersion.

Finally, in order to aid the comparison among the statistical metrics relationships depicted in Figure 7.2, the robust fit slope and y-intercept values are listed in Table 7.3 for all the measurements and the available databases that have been considered. The considered bandwidth, as well as the hyperbolic fit coefficient of the dependence between

Table 7.3: Robust fit parameters for RMS-DS versus ACG and hyperbolic fit coefficient for RMS-DS versus CB for all the considered scenarios.

Scenario	Band	Robust fit		Hyperbolic
	(dB)	slope ($\times 10^{-3}$)	y-intercept	fit
In-home (USA)	1.8–30	−9.400	0.020	-
In-home (ESP)	2–30	−9.630	−0.022	-
In-home (ITA)	1.8–50	−8.794	0.040	0.055
In-car (EC)	1.8–50	−2.329	0.009	0.066
In-car (CC)	1.8–50	−1.926	0.044	0.064
In-ship	1.8–50	−9.883	0.087	0.063
Outdoor LV	1.8–50	−15.327	−0.306	0.047
Outdoor MV (RSE)	1.8–50	−24.518	−0.625	0.065
Underground MV	2–40	−1.968	0.068	0.072

RMS-DS and CB, are also reported. By looking at the robust fit slope, it is easy to realize the differences among the several scenarios. Furthermore, it can be noted as the hyperbolic fit coefficient (k) of the relationship among RMS-DS and CB, given by $\mathcal{B}_C^{0.9} = k/\sigma_\tau$, is approximately the same for all the considered environments.

All the analysis performed in this initial part of this thesis aim to characterize the PLC channel, its properties and the relationship between its describing metrics, in several scenarios. This is of fundamental importance in order to develop fair and effective channel models, as it will be discussed in Chapter 8. The reasons underlying the push towards the development of new and simple models is mainly related to the researchers, developers and manufacturers needs, that demand a quick and cost effective way to test the new devices. However, as it has already been discussed within this thesis, the channel characteristics alone are not enough to thoroughly describe a PLC scenario. Also the noise that typically affects a PLC network and the maximum rate that can be achieved on the communication medium represent an important feature.

7.3 Background Noise Properties

As it can be seen in Figure 7.1, all the considered indoor and outdoor channels have a decreasing PL profile along frequency. At the beginning, this fact, together with the necessity to deliver primarily low data rate services, has pushed towards the development of NB-PLC technology, operating at low frequencies. However, it should be observed that what concurs to achieve good performance is not simply a good channel response but also the low presence of noise. In fact, the channel capacity, i.e. the maximum achievable rate obtained by practical transmission schemes, is determined by the SNR at the receiver side. As it has been discussed in Section 1.3.2, the noise in PLC systems is a combination of several contributions, namely the background stationary noise and the impulsive noise with both periodic and aperiodic components, which is introduced by

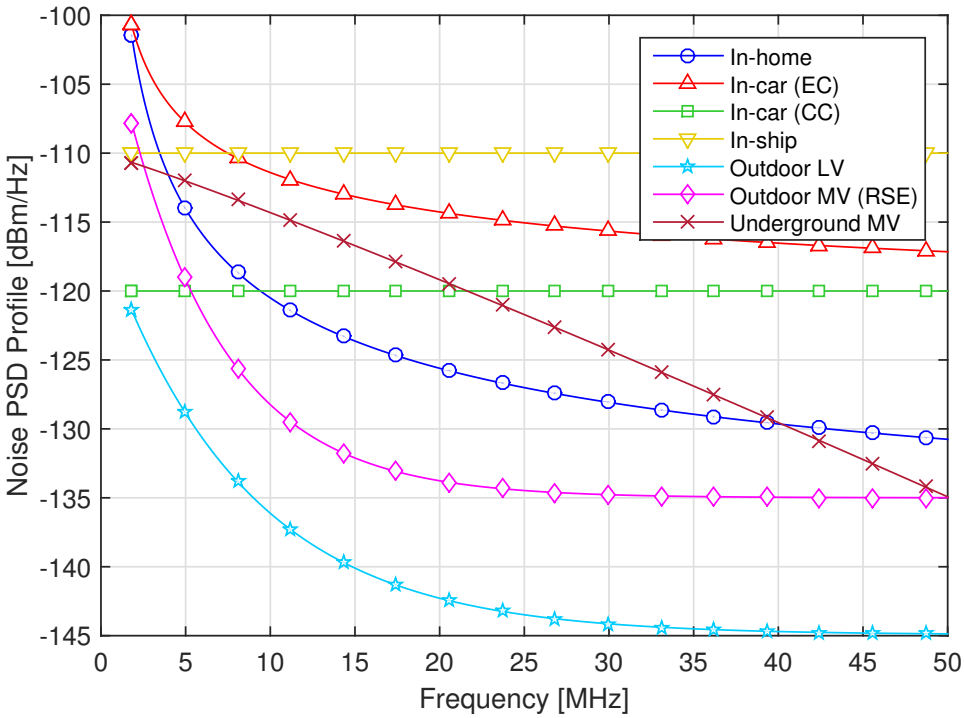

Figure 7.3: Background noise PSD profile assumed for the indoor (worst case), the in-vehicle (EC, CC and in-ship) and the outdoor (LV and MV) scenarios.

noisy loads, switching devices and plug-in/plug-out procedures [3]. As seen, often, the overall noise contribution is estimated by measuring the PSD of the noise, averaged over a long period of time. Typical noise PSD profiles are reported in Figure 7.3 for all the indoor and outdoor considered scenarios.

The figure shows the average background noise PSD profiles encountered within all the several scenarios previously discussed. This noise PSDs are considered for the capacity computation and for the analysis that follows. Depending on the considered environment, the profiles depicted Figure 7.3 where derived from experimental measurements, from the open literature or as an approximated cautionary choice. In particular, both the CC and the in-ship scenarios assume an AWGN background noise profile. In both cases, the noise floor value has been chosen according to on-field measurements and in conjunction with other results provided by the literature. Within the identified noise range, the PSD has been fixed to a conservative level, as discussed in [46] for the CC case, while in Section 5.3.2 and in [54] for the in-ship scenario. However, usually, the noise PSD within the PLC context exhibits an exponentially decreasing profile, which can be modeled essentially in two different ways. For the SISO in-home scenario and from the experimental evidence of the noise measurements carried out on the underground MV lines, discussed in Section 6.2.5 and in [131], as well as on the EC scenario, assessed in Section 5.2.2 and in [89], it has been shown as the average background noise PSD profile can be fitted by the expression in (6.2) [106,131]. The PSD expression in (6.2) exhibits a power dependence on the frequency. Contrariwise, the outdoor LV and MV noise PSD profiles can be expressed

Table 7.4: Model coefficients of the background noise PSD profile for all the different scenarios. The 1.8-50 MHz band is assumed.

Scenario	a_q	b_q	c_q
In-home (best)	−140.000	38.750	−0.720
In-home (worst)	−145.000	53.230	−0.337
In-car (EC)	−103.600	29.820	−0.338
Outdoor LV (OPERA)	−114.941	29.282	−0.120
Outdoor MV (OPERA)	−105.000	37.000	−0.170
Underground MV	−110.000	−0.351	1.090

exploiting the approximation provided by the OPERA project [76] as in (6.1). In this case, the dependence on the frequency is exponential. As seen in Section 6.2.5 for both the models in (6.2) and (6.1), the frequency f must be expressed in MHz, while the quantities a_q, b_q and c_q are the constant parameters to obtain the desired profile. For simplicity, the values for each corresponding scenario are listed in Table 7.4.

In Figure 7.3 only the worst (highest) in-home noise PSD profile is considered in order to perform a worst case analysis identifying the lower limit for the performance that are discussed in the next section. However, the constant coefficients for the best in-home profile are also listed in Table 7.4. Concerning the outdoor underground MV networks, the noise exhibits a frequency decreasing trend that is approximately linear with frequency. This can also be noted looking at Table 7.4, which shows that the c_q coefficient is nearly 1. Among all the scenarios, the highest noise PSD is that assumed for the in-ship scenario, for frequencies higher than 8 MHz. Although the noise PSD was not measured with the ship in full operation (the diesel engines were switched on but without the people activity), this level represents a good compromise between the noise profiles highlighted in other measurement campaigns, as stated in Section 5.3.2. Such a high level can be justified by the heavy loads and by the amount of connected devices typically deployed in a vessel that, although large, represents a confined and very crowded environment. Also the EC environment is affected by sever noise levels, mainly due to the motor drives and to the DC-DC converters operability. It is important to note that the EC noise PSD profile depicted in Figure 7.3 is only an equivalent average level w.r.t. the noise PSD measurements discussed in Section 5.2.2. Instead, the noise within the CC context is lower since the engine is not directly connected to the PLC network, as instead happens for the EC motors. The lower noise is experimented by the outdoor LV and MV lines, according to the OPERA model, with the lowest PSD showed by the LV scenario. This situation occurs since, in outdoor networks, the number of connected loads and noise sources is limited, if compared to any indoor scenario. Furthermore, the long deployed cables, although act as antennas, capturing the noisy RF signals, they also imply a low level of noise experienced at the receiver side, due to the high attenuation exhibited by the outdoor channels.

Finally, it can be observed that the noise PSD floor ranges between −110 and −145

dBm/Hz, while exponentially increases at low frequencies. This shows that a potentially higher SNR can be experienced in the BB-FS rather than in the NB-FS, as discussed in Section 6.3.1. In turn, the BB-PLC has the potentiality to offer higher noise margins and not only higher achievable rates. However, BB-PLC may undergo more severe limitations to grant electromagnetic compatibility (EMC) and coexistence, according to current norms.

7.4 Achievable Performance

From the medium and noise characterization, it is possible to assess and infer the performance at the PHY. This is herein discussed under the assumption of Gaussian background noise, having the PSD profile depicted in Figure 7.3 for each corresponding scenario. The Shannon capacity, computed as discussed in Section 2.2.4, is the common metric used to determine the theoretical achievable rate limit. It has to be emphasized that the true capacity of the PLC channel is still unknown since the statistics of the noise has not been thoroughly investigated yet. For the capacity computation, a transmitted signal PSD of -50 dBm/Hz up to 30 MHz and -80 dBm/Hz beyond 30 MHz has been assumed, according to the HPAV2 standard [39].

The capacity depends on several factors, such as the transmission bandwidth, the considered channel, e.g. SISO or MIMO, and the noise assumptions. In the following the attention is firstly moved towards the SISO channel, assessing the capacity C-CDF for all the previously discussed channels under the corresponding noise assumptions, which are detailed in Section 7.3. Then, the improvements due to the MIMO transmission technique are evaluated focusing on the in-home scenario, where all the multiple deployed wires of the network are exploited for the signal transmission. Furthermore, different background noise properties are considered, such as uncorrelated noise or a more faithful to reality colored (along frequency) and correlated (among the receiving modes) noise.

7.4.1 SISO Transmission Scheme

In order to compare the performance among all the several PLC communication channels, the maximum achievable rate is evaluated for each channel measurement in each considered scenario, according to the expression in (2.20). Since not all the previously discussed environments deploy multiple wires for the point-to-point connection, the SISO transmission scheme is considered. The frequency band is limited to 1.8–50 MHz for all the scenarios, in order to perform a fair comparison, and the corresponding noise PSD profile, depicted in Figure 7.3, is assumed for each scenario. Only for the outdoor underground MV channels the considered bandwidth is 2–40 MHz, due to the couplers limitations. Then, the C-CDF for all the environments is evaluated and depicted in Figure 7.4.

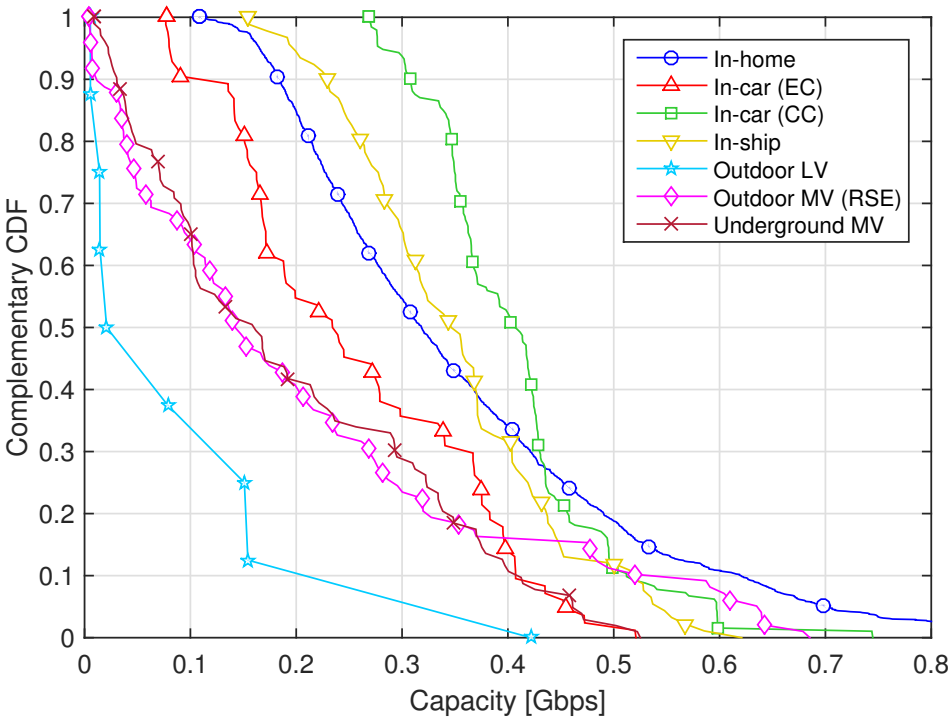

Figure 7.4: Capacity C-CDF for all the considered scenarios in the 1.8–50 MHz band.

It can be noted as the capacity distribution curves are confined approximately in the same region, although some differences in trend exist. The outdoor LV scenario is the only one that greatly differs from the others in terms of capacity C-CDF. The main reason is the high attenuation experienced by the PL depicted in Figure 7.1, despite the low levels of background noise shown in Figure 7.3. The capacity values for the in-home and both the outdoor MV scenarios are the more spread, since the C-CDF curves shows a slowly decreasing profile compared to the others. This is due to a great difference in channel length and properties that can be encountered within these scenarios, which strongly depend on the considered environment and network topology. Conversely, both the in-car scenarios are characterized by networks showing approximately the same structure with comparable cable lengths. Thus, the values are more concentrated and similar, although some differences exist. It can be concluded that, despite the great diversity in terms of channel features, network topology and noise properties of the PLC systems, similar performance are achievable. This statement is also confirmed by the average capacity values reported in Table 7.1.

7.4.2 MIMO versus SISO

In this section, the performance improvements due to the exploitation of the MIMO transmission scheme, discussed in Chapter 4, w.r.t. the SISO case are assessed. The in-home MIMO channels measured by the ETSI STF-410 and presented in [78] are considered. Herein, the effect of the noise when its time and space correlation are taken into account

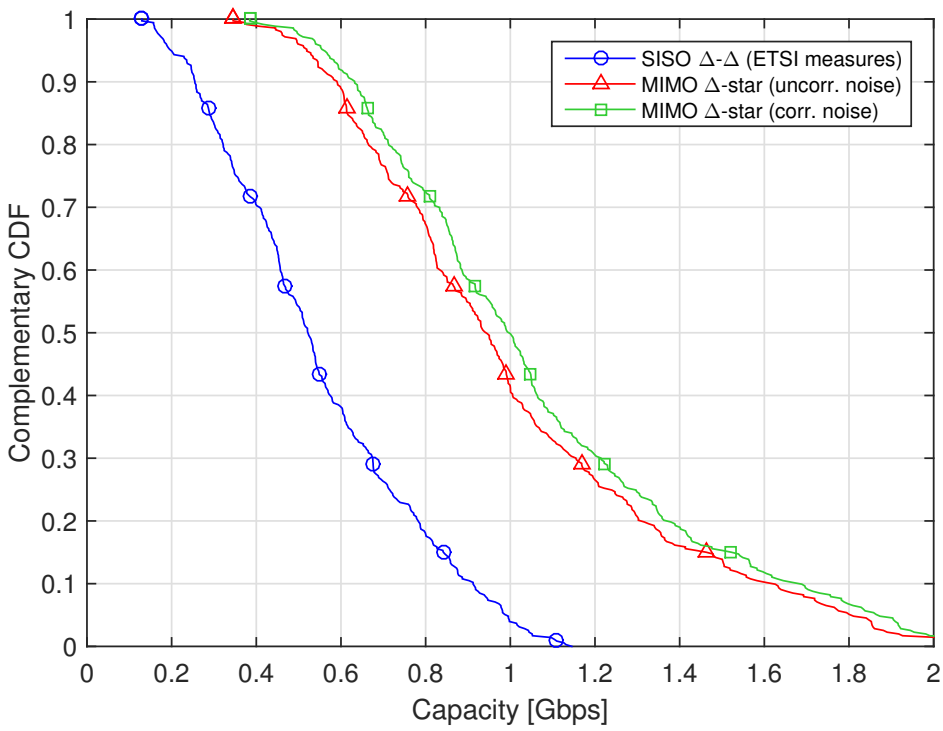

Figure 7.5: Comparison between the in-home SISO and MIMO schemes in terms of capacity C-CDF. The ETSI measurements in the 1.8–50 MHz band are considered. Two different types of colored noise, namely uncorrelated and correlated, are evaluated for the MIMO transmission.

is also evaluated for the MIMO transmission. The spatial correlation of the noise is considered according to the model described in Section 4.2. Figure 7.5 shows that the MIMO transmission provides significant gains over the SISO scheme, under the same PSD constraint. Considering the MIMO transmission, it can be noted as the worst performance is obtained when a colored, but spatially uncorrelated noise, is assumed. While, colored and spatially correlated noise lead to a further capacity improvement, if precoding is implemented. The reason is that the noise correlation renders its cancellation easier at the receiver side.

The marginal differences between the in-home SISO capacity C-CDF results reported in Figure 7.4 and that of the SISO scheme depicted in Figure 7.5 are amenable to the distinct CFR databases and to the different background noise PSD profiles used for each experimental computation. In particular, the SISO capacity C-CDF depicted in Figure 7.5 has been obtained extracting the SISO channel configuration form the MIMO ETSI channel measurements discussed in [78]. In practice, the 2×4 Δ to star style MIMO experimental channels have been converted into a Δ-Δ SISO channel, where the same P-N Δ-style mode have been assumed at both the transmitter and the receiver sides. Then, the SISO capacity in Figure 7.5 has been computed relying on these channels, that obviously differ from the SISO measurements discussed in Chapter 3.

In terms of background noise, the in-home SISO capacity distribution, shown in Fig-

ure 7.4, has been computed assuming the worst-case noise PSD profile, represented in Figure 7.3. This profile has been generated according to the model in (6.2) [106] with the corresponding coefficients listed in Table 7.4. Differently, the Δ-style SISO noise PSD, considered for the SISO capacity computation represented in Figure 7.5, has been extracted from the ETSI star-style MIMO noise PSD measurements depicted in Figure 4.6. Although not directly comparable, it can be noted that the two noise PSD trends differ of approximately 15 dBm/Hz along the entire considered bandwidth. This different background noise PSD level concurs to increase the difference between the two proposed capacity results.

7.5 Main Findings

PLC networks represent a challenging communication environment, mainly due to the channel characteristics and statistical behavior, but also because of the detrimental effect of the noise. However, PLC has become a mature technology that can find application in many different scenarios, from in-home automation and networking, to smart grid applications, as well as to in-vehicle communications. All these several application scenarios are highly heterogeneous, each one having its own features and particularities. In fact, as shown, the channel and noise properties depend on the specific application scenario. However, similar relations and behaviors can be identified for the PLC channel characteristics, such as severe frequency selectivity and high attenuation. Moreover, high levels of noise are experimented, which usually shows an exponentially decreasing profile along frequency. Thus, the noise affects especially the NB-FS, although a higher PL, i.e. low attenuation, is encountered at low frequencies w.r.t. the BB-FS.

Despite the existence of recently standardized NB and BB PLC systems, there exists space for their further evolution. A challenging aspect is the design of reliable communication techniques that can cope with the nasty channel and the detrimental noise effect. Nevertheless, the inferred capacity, under the Gaussian noise assumption, is high and similar among all the considered environments. This, motivates the development of capacity approaching schemes. All the collected information and the highlighted relationships allowed the development of new and effective channel models, able to better emulate a real PLC scenario, as it will be discussed in the next chapter.

Channel Modeling

8

In recent times, the PLC SDO authorities, as well as the industries, have moved their attention towards the study and the development of new PLC devices and transmission strategies, able to exploit all the available wires, through a MIMO transmission technique in an extended frequency range [39]. This, together with precoding, adaptation and a number of advanced techniques at the MAC layer, leads to a great performance improvement, enabling the achievement of much higher data transmission rates, in the order of 2 Gbps of peak rate.

In this perspective, an appropriate channel model can act as a quick and easy technical tool able to simulate, test and develop novel devices or standards. Hence, it is of fundamental importance to provide new and updated models, able to emulate and capture all the different properties that can be encountered in a typical PLC network. Two different methods can be tackled, i.e. deterministic, where everything is fixed, and statistical, where some variability is introduced. Usually, the statistical method is more suitable when a general and comprehensive channel model is desired. This is, since, it is able to statistically emulate the variability that is noticeable in a typical PLC scenario. Among these two methods, two different approaches can be followed, namely bottom-up and top-down.

The bottom-up approach has a strong physical connection and it is able to reproduce a certain CFR by exploiting the TL theory. This method enables a faithful channel reconstruction that closely reproduces the typical CFR behavior exhibited by any two plugs in a certain network. Hence, it provides an excellent approximation of a real communication scenario. Unfortunately, its application requires a fully network topology knowledge in terms of wiring cables length, branches position and connected loads, resulting into a considerable computational effort. An example of such an approach for the SISO PLC channel can be found in [114], or in [117], where the bottom-up approach has been statistically extended.

Contrariwise, the top-down approach considers an analytic expression and fits the the-

oretical model to the actual channel measurements in order to establish the main statistics of the parameters that describe the considered analytic function. This approach leads to a slightly rougher, but more simpler and general, channel approximation, simplifying the statistical extension of the model w.r.t. the bottom-up approach. One of the first and well known top-down approaches was discussed in [66], where the CFR was modeled taking into account the multipath nature of the signal propagation, as well as the cables losses. Later, the model presented in [66], has been statistically extended in [125].

Although a lot of effort has been spent, especially in recent times, in providing new and more faithful channel models, only few proposals have been made for the definition of a general MIMO model so far. A first work, that extends the SISO bottom-up model in [117] to the MIMO case, was described in [119]. While, a first attempt to model a top-down MIMO PLC channel was detailed in [126].

Within this chapter, the focus is on the top-down approach since, in our opinion, it represents a more general solution, if compared to the bottom-up strategy, able to statistically emulate all the possible channel variations that can be encountered in a real PLC environment. Furthermore, it is simpler, since it does not require the full network topology knowledge, and can also be suitable for several application scenarios by changing the parameters statistics. The intent is to provide one of the most simplest and effective top-down models among those already presented in the literature.

The synthetic channel model herein proposed extends the usually analyzed SISO configuration by taking into account the MIMO transmission scheme. A detailed model philosophy is analytically described. The provided theoretical formulation is then applied to a specific experimental context. In particular, the in-home MIMO PLC measurements discussed in Chapter 4 have been considered. This analysis allows to highlight particular channel properties, such as the statistical behavior and the exhibited degree of correlation, that enable some further approximations on the general modeling function, which are then justified by the experimental evidence. Moreover, the validity of the proposed MIMO model is proven comparing the experimental and the simulated channels in terms of achievable performance distribution and also in terms of the most common average statistical metrics. The results show as the developed model is able to quickly and faithfully generate an arbitrarily large number of randomly generated channels, which are statistically equivalent to the real channel measurements. Furthermore, thanks to the MIMO implementation, the proposed modeling strategy can meet the latest standards requirements and it is capable to ease and foster the development and the testing of current and future PLC devices.

The chapter is organized as follows. In Section 8.1 the underlying basic idea of the proposed channel model is discussed. Later, in Section 8.2, the theoretical model is applied to a real in-home MIMO PLC scenario, relying on channel measurements. From the experimental evidence it is possible to highlight certain properties that enable some

further approximations for the proposed model implementation, which can be adopted in order to simplify the generation procedure. Finally, a synthetic description of the model practical implementation and behavior is discussed in Section 8.3. The model validity is also provided through the average statistical metrics and the performance comparison, in terms of capacity distribution, among simulated and experimental channels. The main findings of the chapter follow.

8.1 Model Philosophy

Most of the top-down channel models proposed in the literature are based on an analytic function that relies upon some physical propagation phenomena, such as the signal reflections in a typical PLC network. For example, the authors in [66] exploit a channel analytic modeling function that takes into account the multipath propagation of the transmitted signal, which is due to the presence of multiple branches and mismatches. Thus, these types of solutions, incorporate some basic ideas concerning the bottom-up modeling strategy. Contrariwise to this hybrid mixture of top-down and bottom-up approaches, the basic idea underlying the proposed model is to neglect any physical connection, focusing on a pure top-down solution.

As known, two alternative measurements techniques can be adopted in order to carry out the channel response, differentiated by whether time or frequency domain is considered. The time-domain measurement exploits a signal pulser, together with a DSO, while the frequency-domain measurement uses a VNA, measuring the scattering parameters matrix (S). Typically, the frequency-domain acquisition is preferred, since, compared to the time-domain measurement, it is able to provide not only the CFR, but also the actual propagation delay and the line impedance behavior, which can all be extracted from the S-parameters matrix. Thus, in the following, the focus is on the CFR and on its properties.

The measured SISO CFR at the f-th frequency, namely $H(f)$, is a complex number that is usually expressed in amplitude $A(f)$ and phase $\varphi(f)$, as seen in Section 2.1.1. However, in order to simplify the generation process, the logarithmic version of the CFR, namely $H_{dB}(f) = \log H(f)$, is considered. Thus,

$$H(f) = A(f)e^{i\varphi(f)} \Rightarrow H_{dB}(f) = A_{dB}(f) + i\varphi(f), \tag{8.1}$$

where the real part $A_{dB}(f)$ is the amplitude in dB scale, while the imaginary part is still the phase in radians.

In practice, when considering a real SISO PLC network, the quantity $H(f)$ represents a varying value, which changes according to the investigated scenario, the considered network part, or to the different acquired measurement. Thus, from a statistical perspec-

tive, it can be modeled as a random variable (RV) that can be represented as a column vector, in which each entry represents a different CFR realization. Moreover, since the VNA can measure only a finite number of frequencies, typically, the frequency vector is discretized. Hence, the ensemble of all the frequency samples and measured realizations can be grouped into a $N_M \times M$ channel matrix $\mathbf{H}$ of RVs, where each column represents a frequency sample, whereas each row is a different realization. The constants N_M and M represent the number of acquired realizations and the available frequency samples provided by the VNA, respectively.

From the above discussion, when a database of MIMO PLC channel measurements is considered, the entire set of measured channels can be expressed by a single four-dimensional (4D) matrix $\mathbf{H}$ of RVs, with dimensions $N_M \times N_R \times N_T \times M$. In particular, N_M, N_R, N_T and M represent the number of measurements, receiving modes, transmitting modes and frequency samples, respectively. Thus, any database of measurements is completely described by an equivalent CFR matrix, where the corresponding RVs exhibit a certain statistics and a given degree of correlation. Therefore, it is possible to emulate a real communication scenario by generating a set of simulated channels that exhibit the same statistical behavior and correlation level among the elements corresponding to the experimental quantities. If all these requirements are accomplished, the implemented modeling strategy acts as an effective channel emulator.

In order to simplify the computation, the correlation coefficients between all the possible frequency samples, all the exploited transmitting and receiving spatial modes and for all the combinations of the above mentioned quantities, the 4D matrix $\mathbf{H}$ needs to be reshaped. In particular, the rows of the reshaped matrix $\widetilde{\mathbf{H}}$ correspond to the different measurements, while each column is organized as follows. The first M columns concern all the frequencies, from the first to the last sample, of the first receiving and transmitting mode. Afterwards, the second M columns correspond to the frequencies of the second receiving mode and the first transmitting mode, and so on for all the possible receiving modes. Then, when all the possible receiving modes, concerning the first transmitter, have been reorganized, the samples related to the second transmitting mode are considered for the following columns. Also in this case, all the possible receiving mode combinations, starting from the first, are accounted. And so on for all the possible transmitting modes. Hence, each row of a 4D matrix $\mathbf{H}$, corresponding to a certain measurements database, can be reshaped as

$$\widetilde{\mathbf{H}}^{(rlz)} = [H_{1,1}(\mathbf{f}), \ldots, H_{1,N_R}(\mathbf{f}), H_{2,1}(\mathbf{f}), \ldots, H_{N_T,N_R}(\mathbf{f})], \tag{8.2}$$

where $\{\cdot\}^{(rlz)}$ stands for the realization index indicating a certain measurement. Instead, $H_{i,j}(\mathbf{f})$ represents the vector of RVs corresponding to the vector of frequency samples $\mathbf{f}$ and that are associated to the i-th transmitting and j-th receiving mode. Thus, $\widetilde{\mathbf{H}}^{(rlz)}$ is a vector having dimensions $1 \times N_R \cdot N_T \cdot M$. The overall reshaped matrix is therefore

given by

$$\widetilde{\mathbf{H}} = [\widetilde{\mathbf{H}}^{(1)}, \ldots, \widetilde{\mathbf{H}}^{(N_M)}]^\top, \tag{8.3}$$

where $\{\cdot\}^\top$ denotes the transpose operator. Hence, the reshaped matrix $\widetilde{\mathbf{H}}$ has dimensions $N_M \times N_R \cdot N_T \cdot M$. This organization simplifies the computation procedure.

Once that the matrix has been reshaped, it is possible to compute the covariance matrix of the CFR, in dB scale, as follows

$$\mathcal{Q}(r,c) = E\left[\left(\widetilde{H}_{i,j}(f) - m_{\widetilde{H}}\right)\left(\widetilde{H}_{\ell,p}(\lambda) - m_{\widetilde{H}}\right)^*\right], \tag{8.4}$$

where $\{\cdot\}^*$ is the complex conjugate operator and $E[\cdot]$ denotes the expectation operator w.r.t. the available measurements. Instead, $\widetilde{H}_{i,j}(f)$ is the CFR of the reshaped matrix $\widetilde{\mathbf{H}}$ corresponding to the i-th transmitter and j-th receiver modes at the f-th frequency, with $i = 1, \ldots, N_T$, $j = 1, \ldots, N_R$ and $f = 1, \ldots, M$. Moreover, r and c are the row and column indexes of the covariance matrix $\mathcal{Q}$ that, according to the previously described reshaping method, are function of (f, i, j) and (λ, ℓ, p), respectively. In particular, the row index is given by $r = (i-1)N_R \cdot M + (j-1)M + f$, and the same applies to the column index c for the values λ, ℓ and p.

By substituting the logarithmic expression of the reshaped CFR matrix $\widetilde{\mathbf{H}}$, computed as in (8.1), into (8.4), after some easy algebra the following expression can be found

$$\mathcal{Q} = \mathcal{Q}_{A_{dB}} + \mathcal{Q}_{\varphi} + i\left[\mathcal{Q}^\top_{A_{dB},\varphi} - \mathcal{Q}_{A_{dB},\varphi}\right], \tag{8.5}$$

where $\{\cdot\}^\top$ is the transpose operator, $\mathcal{Q}_{A_{dB},\varphi}$ is the covariance matrix between the amplitude (in dB scale) and the phase, while $\mathcal{Q}_{A_{dB}}$ and $\mathcal{Q}_{\varphi}$ are the auto-covariance matrices of the amplitude (in dB scale) and the phase, respectively. Obviously, in this case, the amplitude and the phase are matrices, reshaped as in (8.2), equivalently to what has been done for the CFR matrix.

It can be noted as the real part of $\mathcal{Q}$ depends only on the amplitude and phase auto-covariance matrices, while the imaginary parts is function of the mutual covariance matrix. Moreover, as previously discussed, the knowledge of the matrix $\mathcal{Q}$, together with a statistical analysis of the CFR, provide a second order characterization of the channel for a given scenario in a certain frequency range. Thus, as stated, a typical PLC network can be emulated through a vector of correlated RVs with a certain covariance matrix and a given statistics. This represents an extremely synthetic model since only the amplitude and phase properties need to be known and reproduced, avoiding the characterization of a large set of parameters in sometimes complex analytic functions.

In the following, the normalized covariance matrix, namely $\dot{\mathcal{Q}}$, is used in order to highlight the degree of correlation exhibited by the RVs corresponding to the channels at different frequencies and for different transmitting and receiving modes. The matrix

$\dot{\mathcal{Q}}$ is given by the covariance matrix in (8.4) normalized by the product of the standard deviations of the corresponding variables. In particular, the elements of $\dot{\mathcal{Q}}$, as an usual linear correlation coefficient, can range from 0 (no correlation) to 1 (fully correlated). This helps to identify the high or low correlation regions and to understand how the considered quantities are correlated.

8.2 Experimental Evidence

In this section, the synthetic channel model described in Section 8.1 is applied to a real PLC scenario. In particular, the database of MIMO in-home experimental channels [78] that has been discussed in Chapter 4 is considered in the 1.8–100 MHz frequency band. First, the measurements database is briefly recalled, assessing the main channels properties and relationships that are required for the generation process. Second, the main issues concerning the random channel simulation procedure, according to the described modeling strategy, are detailed. This analysis highlights other properties that allow a further simplification of the general model proposed in Section 8.1. Finally, these assumptions, in conjunction with the proposed top-down model, are later validated through numerical results in Section 8.3.

8.2.1 Measurement Campaign

As discussed in Section 4.1.1, typically, in-home PLC networks consist of three different wires, two for the power supply, namely P and N, and one for protection in case of an insulation fault, i.e. the E. At the transmitter side a differential Δ-style transmission can be implemented, signaling among pair of wires. Due to the Kirchhoff's law, only two Δ-modes con be used at the same time. At the receiver side, instead, the signal is observed between the wires and a reference plane in a star-style configuration. Beyond the three standard star-style receiving modes, an additional mode, named CM can be extracted [78]. However, as seen, only three out of the four available star-style reviving modes are linearly independent, hence, in the following, the 2×3 MIMO channel is considered.

For the model evaluation, the database of experimental channels that were collected during a measurement campaign across Europe by the STF-410 of the ETSI is exploited [78]. The database consists of 353 MIMO channel measurements in the frequency domain, with 1601 samples in the 1.8–100 MHz frequency range. Concerning the noise, the same colored decreasing PSD profile (along frequency) discussed in [85] is considered. Also the noise correlation, among the three linearly independent receiving modes, is considered and simulated as detailed in Section 4.2. These choices allow to obtain fair and actual results, especially when evaluating the performance in terms of maximum achievable rate.

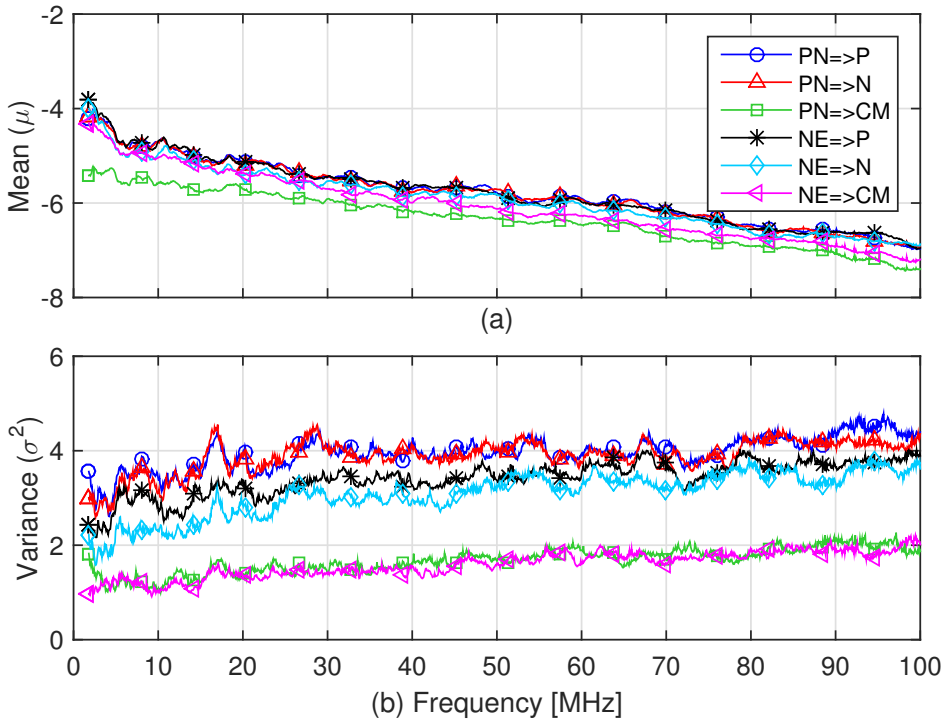

Figure 8.1: Measurements amplitude mean (a) and variance (b) parameters of the best log-normal fit, along frequency, for all the considered transmitter-receiver combinations.

8.2.2 MIMO Channel Properties

From the analysis of the measurements in [78], briefly described in Section 8.2.1 and deeply investigated in Chapter 4, the following properties have been found. The statistical distribution of the experimental channels is established first. As expected, the amplitude is log-normally distributed, as discussed for the SISO channels in Section 3.2.1 and in [72]. Hence, the real part of the logarithmic version of the CFR, which correspond to the amplitude in dB scale and that is computed as in (8.1), is normally distributed. In particular, the mean (μ) and the variance (σ^2) values of the CFR amplitude, for all the considered transmitter-receiver combinations in the band 1.8–100 MHz, are represented in Figure 8.1.

It can be noted as the mean parameter follows approximately the same decreasing profile along frequency, with similar values almost for all the possible transmitting-receiving mode combinations. Only the μ value related to the P-N⇒CM channel amplitude exhibits slightly lower values, especially at lower frequencies. The variance trend, instead, is more spread among the different mode combinations, exhibiting a slightly increasing profile. The lowest values are obtained for both the combinations concerning the CM configuration at the receiver side.

Also the correlation properties of the considered MIMO channel measurements have been assessed. In particular, the normalized covariance matrix of the reshaped channel matrix $\widetilde{\mathbf{H}}$, i.e. $\dot{\mathcal{Q}}$, obtained as described in Section 8.1, as well as the normalized covari-

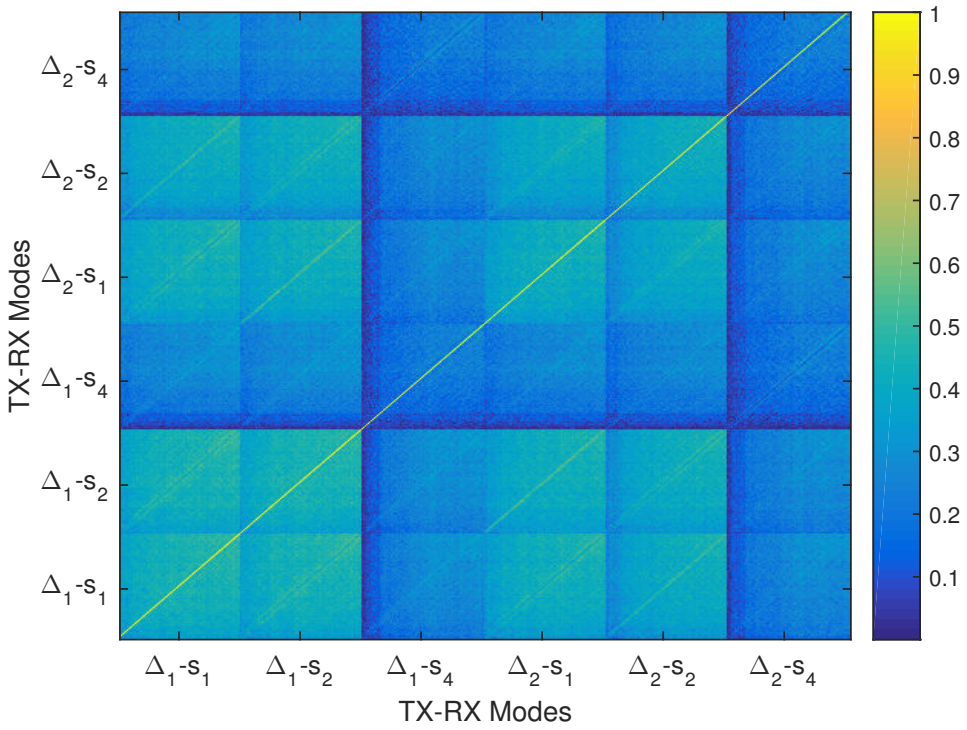

Figure 8.2: Real part of the normalized covariance matrix of the MIMO CFR measurements. All the transmitter-receiver mode combinations are shown.

ance matrix between the amplitude (in dB scale) and the phase of $\widetilde{\mathbf{H}}$, namely $\dot{\mathcal{Q}}_{A_{dB},\varphi}$, are considered. The former is approximately a real quantity, having a maximum and average imaginary value of 0.28 and 0.033, respectively. This observation indicates that the imaginary part of $\dot{\mathcal{Q}}$ in (8.5) is nearly zero. The latter correlation matrix, instead, has a mean value of 0.046, indicating that the relationship between the amplitude (in dB) and the phase can be neglected. Therefore, A_{dB} and φ can be assumed as uncorrelated. In order to further simplify the generation process, these two quantities are assumed as independent. Thus, from the experimental evidence highlighted within this section, the amplitude (in dB scale) and the phase can be independently generated according to the corresponding statistical distribution and with the proper degree of correlation, as it will be clarified in the following section.

As an example, the absolute value of the real part concerning the measurements normalized covariance matrix ($\dot{\mathcal{Q}}$), is depicted in Figure 8.2. As stated, this is the only significant part and depends on both the amplitude and phase auto-covariance matrices, as reported in (8.5). As it can be noted, the matrix exhibits a block diagonal behavior, where each distinct point of a block refers to the correlation coefficient among the corresponding frequencies of the considered transmitting-receiving mode couple. For example, the blocks on the main diagonal refer to the frequency covariance matrix for the same transmitting-receiving mode pair. Hence, from the bottom-left to the top-right, the first three blocks correspond to the frequency correlation for the P-N⇒P, P-N⇒N and P-N⇒CM channels, while the last three blocks refer to the channels with the same

star-style receiving modes for the other Δ-style transmitting mode, namely P-E. Contrariwise, the out-of-diagonal blocks concern all the possible modes cross-combinations. Finally, differently from the imaginary part of $\dot{\mathcal{Q}}$ that, as seen, can be neglected, the real part depicted in Figure 8.2 assumes high and significant values almost everywhere.

However, the CFR behavior is influenced not only by the amplitude statistics and properties, but also by the phase ones, as clearly highlighted by the expression in (8.1). Thus, also the phase statistics has been assessed, observing as it is uniformly distributed in $[-\pi, \pi)$, for all the considered transmitter-receiver links and for any frequency sample. This is an expected result because, due to the 2π periodicity, the phase can assume any value for each frequency and regardless of the considered transmitting-receiving mode pairs. Furthermore, also the phase auto-covariance matrix has to be evaluated since, together with the amplitude auto-covariance matrix, it provides the real part of the channel covariance matrix displayed in Figure 8.2, according to the relation in (8.5). As happens for the amplitude part, also the phase matrix, reshaped according to (8.2), exhibits a certain degree of correlation. Indeed, the unwrapped phase of the in-home MIMO channels exhibits a linear decreasing profile along frequency, denoting a certain degree of correlation over frequency. This behavior is similar to that reported in Figure 3.6, obtained for the in-home SISO channels, as discussed in Section 3.2.3. The observed trend is almost the same for all the considered transmitting-receiving mode pairs that are available in the MIMO context. Obviously, besides the correlation between the frequency samples, there exists also a certain degree of phase correlation among the several possible transmitting and receiving mode combinations.

8.3 Synthetic Model Description

In this section, the procedure applied in order to generate a set of simulated channels, which are statistically equivalent to the actual measurements described in Section 8.2.1, is detailed. This is done in order to propose a practical implementation of the theoretical model discussed in Section 8.1. First of all, the generation of the amplitude part is discussed. Afterwards, the more complicated phase generation process is discussed. In order to aid the comprehension, the two generating procedures are separately considered in two distinct sections. Then, the results are validated assessing the performance distribution, in terms of maximum achievable rate, as well as computing the main average statistical metrics, for both simulated and experimental channels.

8.3.1 Amplitude Generation Process

As discussed in Section 8.2.2, the amplitude is log-normally distributed, hence, the dB version has a normal distribution. The generation of a set of correlated normal RVs

represents a quite easy process. Indeed, it is sufficient to generate a matrix of normally distributed RVs, namely $\mathbf{N} \sim \mathcal{N}(0,1)$, of dimensions $M \times N_M$, where M and N_M are the number of frequency samples and the number of desired simulated channels, respectively. Then, the equivalent set of correlated amplitudes, in dB scale, can be computed as

$$\mathbf{A}_{dB} = \mathcal{Q}_{A_{dB}}^{1/2}\mathbf{N} + \mathbf{m}_{A_{dB}}, \tag{8.6}$$

where $\{\cdot\}^{1/2}$ stands for the square root, while $\mathbf{m}_{A_{dB}} = E[\mathbf{H}_{dB}]$ identifies the vector of the mean values corresponding to the experimental measurement amplitudes, at each frequency sample. These values are depicted in Figure 8.1a for all the possible transmitting-receiving mode combinations. The mean value must be added since it has been subtracted in the calculation of the covariance matrix, which is computed as in (8.4). In order to limit the model parameters, a rougher representation of the mean values can be provided, e.g. approximating the experimental values depicted in Figure 8.1a through a linear fitting.

8.3.2 Phase Generation Process

The generation of an equivalent set of uniformly distributed RVs, with a given target normalized covariance matrix $\dot{\mathcal{Q}}_{\varphi}$, represents a more challenging problem. Indeed, the same procedure adopted for the amplitudes generation cannot be followed. This is because, in practice, the generation process involves the sum of a large number of independent variables, each one multiplied by the corresponding correlation coefficient. This, as known, leads to a set of variables that are correlated but, due to the central limit theorem (CLT), they tend to normality. Thus, if the same steps followed for the amplitude generation are adopted for the phase generation, the obtained result leads to correlated variables with the imposed correlation that, however, are no longer uniformly distributed. In order to solve this problem, the properties of a generic distribution function can be exploited as described in the following.

Given an uniformly distributed RV $u \sim \mathcal{U}(0,1)$ and a distribution function $F(\cdot)$, it is known as $x = F^{-1}(u)$ is distributed as $F(\cdot)$. This is since any distribution function express the probability that a given RV assume values that are less than, or equal to, a certain target value. Thus, $F(\cdot)$ ranges from 0 to 1, which is the co-domain of the function. Hence, when applying the distribution function $F(\cdot)$ to a variable that has a distribution $F(\cdot)$, the result is a RV uniformly distributed between 0 and 1. This way, if $F(\cdot)$ is the normal distribution function, a set of uniformly distributed RVs can be generated starting from a set of Gaussian distribute RVs that, as seen, are easy to correlate. However, the well-known Pearson, or linear, correlation is not invariant w.r.t. any transformation, such as that induced by a given distribution function. Hence, the uniform variables resulting from the above described generation procedure do not exhibit the same desired degree of correlation that has been imposed to the Gaussian RVs. To overcome this issue, the

relation among the Pearson, or linear, correlation and the Spearman, or rank, correlation can be exploited as discussed in [160].

Differently from the Pearson correlation, the Spearman correlation is invariant to any strictly increasing transformation, such as, for example, a distribution function. However, to follow the above mentioned procedure, a relationship among the Pearson (ρ_P) and the Spearman (ρ_S) correlation coefficients must be found and exploited. In particular, given two distributions, $F(\cdot)$ and $G(\cdot)$, and two RVs $\mathbf{x} \sim F$ and $\mathbf{y} \sim G$ distributed accordingly, the Spearman and Pearson correlations are related by the relationship

$$\rho_S(\mathbf{x}, \mathbf{y}) = \rho_P \left(F(\mathbf{x}), G(\mathbf{y}) \right). \tag{8.7}$$

For the normal distribution this relation is known and is given by [160]

$$\rho_P = 2 \sin \left(\frac{\pi}{6} \rho_S \right). \tag{8.8}$$

In conclusion, a vector of uniformly distributed RVs ($\mathbf{u}$), with normalized covariance matrix $\dot{\mathcal{Q}}_\varphi$, can be obtained from a vector of normal RVs ($\mathbf{n}$) correlated as $\mathcal{T}_\varphi = 2 \sin \left(\frac{\pi}{6} \dot{\mathcal{Q}}_\varphi \right)$ via the expression $\mathbf{u} = F(\mathbf{n})$. The correlation matrix imposed to the normally distributed RVs needs to be modified according to (8.8) so that, after the transformation via the normal distribution function, the uniformly distributed RVs exhibit the desired degree of correlation, namely $\dot{\mathcal{Q}}_\varphi$.

8.3.3 Numerical Results

In order to validate the proposed synthetic channel model as an effective tool, able to emulate a typical PLC network, the distribution of the achievable performance is assessed. In Figure 8.3 the C-CDF of the capacity, achieved by the 353 MIMO measurements and by an equivalent set of 2000 channel realizations, is depicted. It can be noted as, apart from some small differences, mainly focused in the middle part, the distribution of the performance is practically the same for both the experimental and the simulated channels. Indeed, the maximum discrepancy is in the order of 0.18 Gbps. The differences are mainly due to some inaccuracies in the generation process, as well as to some approximations, such as the independence of amplitude and phase.

Furthermore, also the average value of the most commonly used statistical metrics, namely the ACG, the RMS-DS and the channel capacity, has been computed for both the experimental and simulated channel sets. The computed quantities are listed in Table 8.1. It can be noted as similar ACG values are obtained and that the difference in terms of average capacity is approximately the 3 %, hence, a very low value. The only significant difference is related to the RMS-DS metric. Initially, we speculate that the underlying reason for such an high average dispersion, exhibited by the simulated channels, lies in the

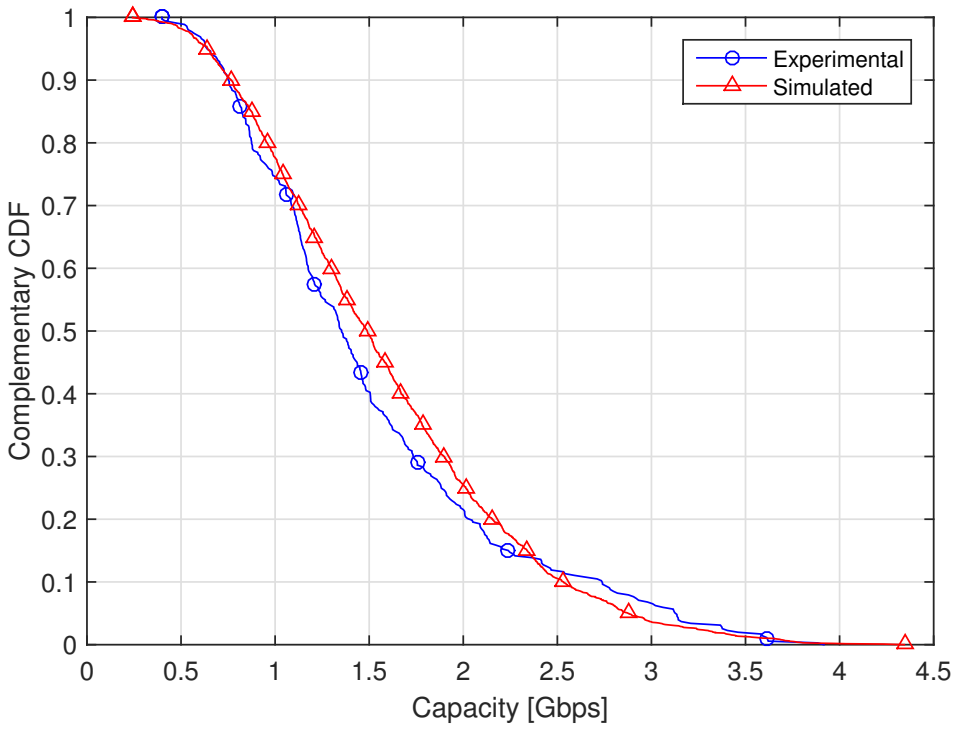

Figure 8.3: Capacity C-CDF comparison between experimental and simulated channels in the 1.8–100 MHz frequency band.

Table 8.1: Average value of the main statistical metrics for both the experimental and the simulated channels.

Type	Band (MHz)	$\overline{\mathcal{G}}$ (dB)	$\overline{\sigma}_\tau$ (μs)	$\overline{\mathcal{C}}$ (Gbps)
Experimental	1.8–100	−42.30	0.350	1.53
Simulated	1.8–100	−41.22	2.724	1.58

simplification introduced and discussed in Section 8.2.2, where A_{dB} and φ are assumed as independent RVs. However, performing an in depth analysis of the CFRs provided by the numerical model presented in this section, it has been observed as the phase of a specific generated realization assumes approximately random values regardless the considered frequency. Hence, since the phase jumps from one frequency to another are roughly random, this translates into a very steep unwrapped phase trend along frequency. This behavior completely differs from the smooth profile observed for the MIMO channel measurements, which, as stated in Section 8.2.2, is similar to that depicted in Figure 3.6 for the SISO case. It must be noted that, as discussed in Section 3.2.3 for the in-home SISO channels, the unwrapped phase slope affects the RMS-DS of the channel. In particular, referring to Figure 3.7a, it can be noted as the greater the phase slope the higher the RMS-DS value.

As highlighted by the great average RMS-DS value reported in Table 8.1 and by the aforementioned discussions, the proposed model, as it is, is unable to capture the corre-

lation of the phase along frequency. This happens because, through the phase generation process discussed in Section 8.3.2, an average degree of correlation is imposed. Hence, the adopted emulation strategy implies that the entire set of simulated channels exhibits a certain covariance matrix, which is equivalent to the measured one. However, when considering an individual channel realization, the linear relationship exhibited by the unwrapped phase along frequency, encountered in the channel measurements, may be lost due to the randomness of the generation process. In order to overcome this problem, a simple and effective solution, described in the following section, has been implemented.

8.4 Improved Model Version

As briefly recalled in Section 8.2.2 and thoroughly discussed in Section 3.2.3 for the in-home SISO case, the unwrapped phase exhibits a frequency dependent behavior. In particular, the unwrapped phase profile encountered within the MIMO scenario, for each one of the transmitting-receiving mode pairs, is very close to that reported in Figure 3.6 for the SISO channels. Hence, as it can be noted, the trend can be faithfully approximated through a linear fit. Thus, the unwrapped phase of each measurement is characterized by a specific slope and an y-intercept. As suggested by the experimental results assessed in Section 3.2.3, the RMS-DS depends on the unwrapped phase slope, as clearly depicted in Figure 3.7a. It is easy to understand that, in order to develop a fair model, able to provide not only a faithful capacity distribution and a good average ACG value, but that is also capable of emulate a proper level of channel energy dispersion, this dependence must be taken into account. This has been done according to the procedure described in the following.

8.4.1 Simplified Phase Generation Process

As previously mentioned, the basic idea to improve the synthetic channel model strategy proposed in Section 8.3 is to implement the unwrapped phase dependency along frequency. In order to meet this goal, the phase samples cannot be randomly and independently generated according to a uniform distribution and then correlated, as it has been described in Section 8.3.2. To keep the same frequency decreasing profile exhibited by the unwrapped phase of the channel measurements, the simulated phase samples are obtained from a linearly decreasing function that approximates the experimental unwrapped phase behavior. In practice, since all the measured profiles are roughly monotonically decreasing, with a starting value that by definition falls within the range $[-\pi, \pi)$, the y-intercept assumes small and similar values among the different measurements. Hence, it can be neglected and the only parameter considered for the phase generation is the slope of the experimental unwrapped phase.

The generation process works as follows. First, the robust regression fit for the unwrapped phase of all the available MIMO channels, considering each distinct transmitting-receiving mode, is evaluated. Afterwards, the distribution of the slope parameter is assessed exploiting the likelihood function discussed in Section 2.3.1. The distribution with the highest score is the one that is chosen for the generation process, since it represents the best fit for the slope statistics. For the in-home MIMO measurements presented in Section 8.2.1 and discussed in Chapter 4 the unwrapped phase slope exhibits a Nakagami-m distribution with shape parameter $m \simeq 1.39$ and a spread parameter $\Omega \simeq 2.32 \cdot 10^{-12}$. Then, a desired number of approximated unwrapped phase profiles, characterized by a simple linear slope along frequency, are generated so that the slope coefficients exhibit a distribution statistically equivalent to the experimental one, which is Nakagami-m in the considered case. From these simulated trends, the conventional phase in $[-\pi, \pi)$ is obtained by removing the corrections introduced in order to obtain the unwrapped phase. Thus, the simulated unwrapped phase values are limited in the range $[-\pi, \pi)$ by exploiting the phase periodicity. This confinement renders the phase uniform for each realization, hence, when all the corresponding frequency samples are considered together. Moreover, since the slope varies for each numerically generated realization, the phase extracted from the unwrapped phase profiles is uniformly distributed in $[-\pi, \pi)$ even for each frequency sample. This has also been validated through numerical results.

Obviously, the above detailed procedure provides a rougher approximation of the overall phase correlation w.r.t. the generation process described in Section 8.3.2. However, as it will be discussed in Section 8.4.2, this translates into great benefits in terms of RMS-DS, while maintaining unchanged the other statistical metrics.

8.4.2 Final Results

As it has been done for the first model implementation discussed in Section 8.3, the novel emulation strategy adopted for the phase generation described in Section 8.4.1, needs to be assessed. Similarly to the analysis carried out in Section 8.3.3, also in this case the model validity is assessed in terms of capacity distribution and through the average statistical metrics. In particular, when assessing the capacity C-CDF obtained with the improved modeling strategy detailed in Section 8.4, approximately the same results reported in Figure 8.3 are obtained. Thus, since the new phase generation approach does not influence the capacity distribution, the model is still suitable for the performance simulation of an experimental channel.

The only downside encountered with the generation procedure originally adopted in Section 8.3, is the great channel dispersion, i.e. the high average RMS-DS value reported in Table 8.1. Hence, it is of primary interest to compute the statistical metrics, namely ACG, RMS-DS, and CB, also for the new approach presented in Section 8.4. The results for the average metrics, averaged over 2000 realizations, are summarized in Table 8.2. It

Table 8.2: Average value of the main statistical metrics for both the experimental and the simulated channels, generated according to the simplified model version.

Type	Band (MHz)	$\overline{\mathcal{G}}$ (dB)	$\overline{\sigma}_\tau$ (μs)	$\overline{\mathcal{B}}_C^{(0.9)}$ (kHz)	$\overline{\mathcal{C}}$ (Gbps)
Experimental	1.8–100	−42.30	0.350	293.22	1.53
Simulated	1.8–100	−40.46	0.353	214.50	1.64

can be noted as, in this case, there is an almost perfect match among the metrics computed relying on the measurements and those calculated basing on the simulated channels, for all the considered quantities, including the RMS-DS. This results suggests as the phase properties greatly influence the channel dispersion. In particular, it is more convenient to take into account a punctual, i.e. realization by realization, phase dependency along frequency, as done with the simple procedure discussed in Section 8.4.1, rather than impose a faithful overall spatial and frequency correlation for all the ensemble of realizations, as done in Section 8.3.2. Furthermore, although the difference among the experimental and the simulated ACG and capacity average values for the novel model implementation, listed in Table 8.2, is slightly higher compared to that of the previous strategy reported in Table 8.1, they are still very close. Moreover, the set of computed capacity values exhibits a standard deviation that is equal to 0.74 and 0.73 Gbps for the experimental and the simulated channels, respectively, hence very similar.

It can be concluded that, the strength points of the simplified phase generation procedure detailed in Section 8.4.1 are the extreme simplicity and the ability to capture the frequency dependence of the unwrapped phase for each realization. A good emulation of this behavior is of primary importance since, as seen in Section 3.2.3, the unwrapped phase slope directly influences the RMS-DS. Indeed, this allows to simulate channels with a proper dispersion, as confirmed by the results in Table 8.2. Contrariwise, the procedure discussed in Section 8.3.2 better represents the overall phase correlation, especially among the different transmitting-receiving modes, but it is unable to obtain the correct frequency correlation for a single realization. This is proven by the high average RMS-DS value corresponding to the simulated channels obtained through the first implemented phase generation process that is listed in Table 8.1.

As a further model validation, the frequency behavior of the amplitude and the phase, exhibited by a typical experimental and simulated MIMO channels, are visually compared in Figure 8.4 and Figure 8.5, respectively. In particular, each figure reports the measurements profile (on top) and the simulated trend (on bottom) for all the three considered linearly independent star-style receiving modes, namely P, N and E, related to the Δ_1 transmitting mode P-N. A similar behavior has been noticed for the channels referred to the other Δ-style transmitting mode, i.e. P-E. Concerning the comparison in terms of PL profile, in dB scale, along frequency, depicted in Figure 8.4, the following can be noted.

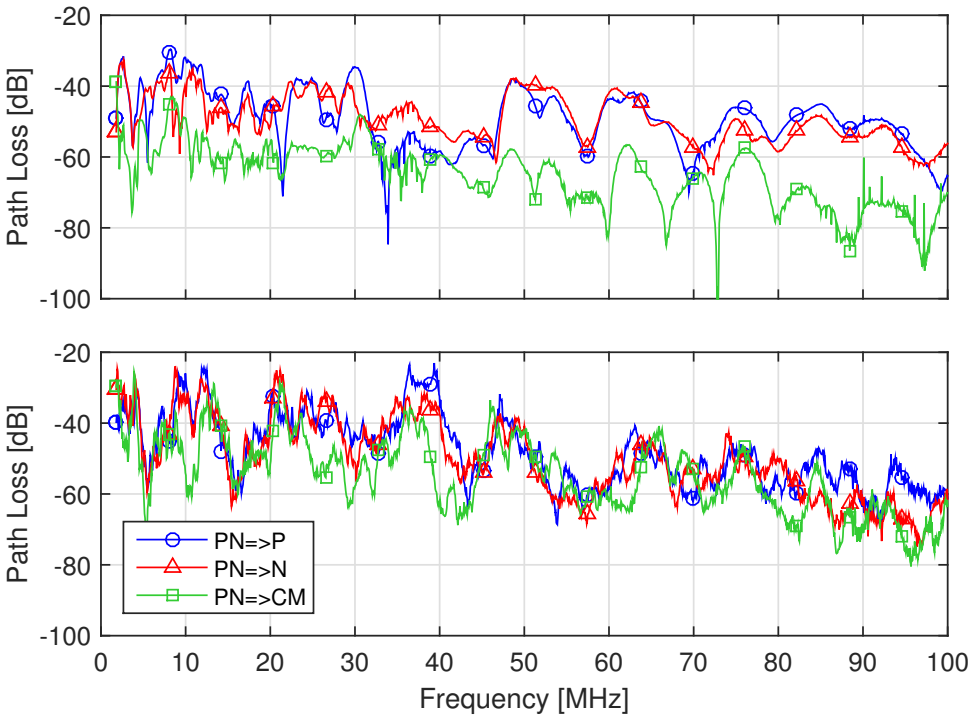

Figure 8.4: PL behavior exhibited by a typical experimental (a) and simulated (b) MIMO channel, along frequency.

First, both experimental and simulated channels show approximately the same decreasing trend, being characterized by a similar frequency selective behavior. Second, the PL assumes values that range within the same interval. The only marginal difference is the slightly noisier trend exhibited by the simulated channels. This is mainly related to the amplitude generation process, discussed in Section 8.3.1. In addition, also the unwrapped phase behavior along frequency is displayed in Figure 8.5. Even in this case there is a good match among experimental and simulated channels. In particular, the typical linearly decreasing profile exhibited by the channel measurements reported in Figure 8.5a, is faithfully reproduced by the simulated channels shown in Figure 8.5b, despite the rough linear approximation detailed in Section 8.4.1.

From the overall discussion carried out within this section, it has been proven as the proposed model is able to capture the global channel structure, the dependencies and the behavior of a real MIMO PLC scenario, representing a valuable solution for the channel emulation. Hence, it can be adopted as a simple development tool in order to numerically evaluate the effectiveness and the improvement given by the exploitation of new standards or devices.

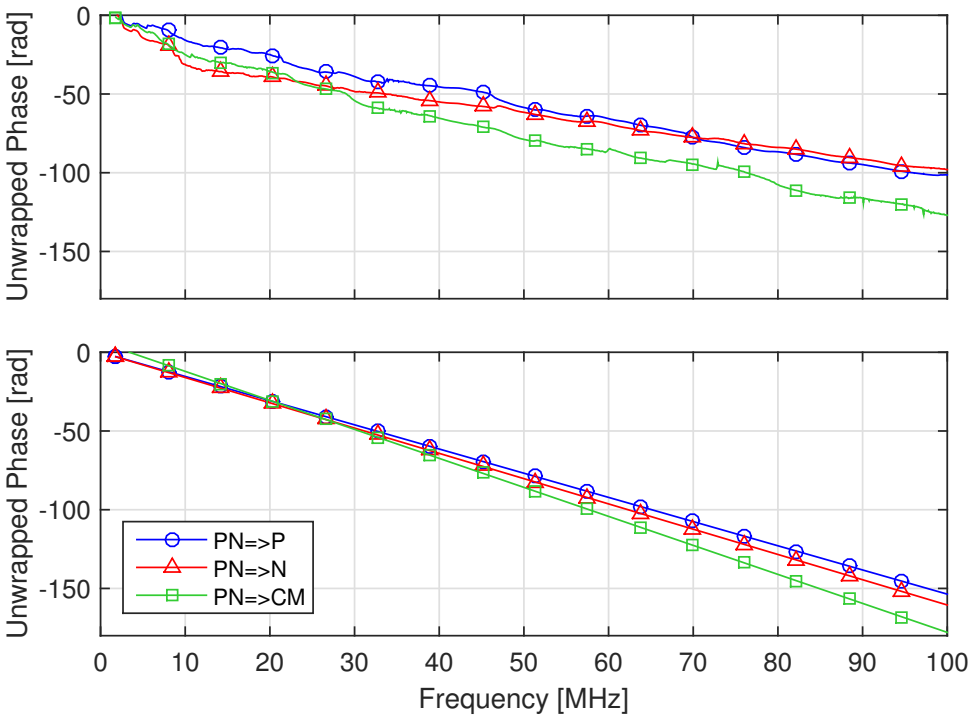

Figure 8.5: Unwrapped phase behavior exhibited by a typical experimental (a) and simulated (b) MIMO channel, along frequency.

8.5 Main Findings

Modeling has become a key issue, especially in recent times, since it allows to emulate a real application scenario, enabling costs and time saving. Thus, it is fundamental to provide updated and effective models that enable a simple and quick channel simulation. In this respect, a quick overview concerning the main modeling strategies and approaches has been given, highlighting the main findings reported in the literature. However, the focus of the scientific community is mainly on the SISO scheme, although MIMO communication has already been standardized and deployed.

This chapter proposes to provide an extremely synthetic top-down channel model for the MIMO PLC channel. The basic model idea and its theoretical basis have been discussed first. Then, the modeling procedure has been applied and tested on a specific in-home MIMO PLC scenario relying on experimental channels. By exploiting the intrinsic peculiarities exhibited by these measurements, some further simplifications have been introduced and exploited during the generation process. The proposed model has been evaluated comparing the main average statistical metrics and the performance, assessed in terms of capacity distribution. Since not all the simulated results fit the experimental metrics, the adopted generation procedure has been changed. In particular, taking advantage of the knowledge gained across the channel characterization, it has been possible to identify the relationships and the connections that cause the issues in the model im-

plementation and to find the correct strategy that must be adopted in order to overcome them. The final release of the proposed synthetic channel model, which is even more simple than the first one, has been validated via numerical results. Moreover, it has been shown as it achieves better results, despite the further simplifications.

The strengths of the proposed model are the simplicity, relying only on the amplitude and phase properties, the flexibility, being suitable for different application contexts, and the statistical representativeness, as the results show. An interesting further model development can be identified in the analysis of other communication scenarios. For example, one environment where the extension to the MIMO transmission scheme can be tested, while taking into account the spatial correlation, is represented by the in-ship PLC channels discussed in Chapter 5. This is of crucial importance in order to provide an overall and comprehensive PLC channel emulator, able to simulate several application contexts under different conditions.

Beyond Capacity: Security

9

In recent years, we have witnessed a fast and worldwide increase of data connectivity demand. This is due to the widespread use of social communication media and to the huge amount of exchanged multimedia contents. In order to satisfy this continuously growing amount of data transfer need, new wireless and wireline technologies, as well as improved standards, have been developed. Among the no-new-wires technologies, PLC has gained momentum and popularity due to its ability to offer high data rates exploiting the existing power delivery infrastructure. This leads to a considerable saving in costs and time for the infrastructure creation.

As it has been discussed, the PLC technology can be adopted for many application contexts, with devices that can be grouped into two categories, depending on the frequency spectrum they operate, i.e. NB and BB. Typically, NB-PLC devices are conceived for reliable low data rate applications, such as among sensors in a grid. Conversely, BB-PLC devices adopt multicarrier modulation in the form of OFDM at the PHY. These latter devices have been developed with the aim of offering multimedia services to domestic or small office environments. Thus, they can provide high data rates. A relevant example of commercial devices are those that comply with the HPAV2 specifications [39]. This standard exploits an OFDM scheme, together with MIMO transmission over multiple wires, and an extended band of 2–86 MHz, enabling data rates up to 2 Gbps via proper transmission techniques.

Similarly to the wireless communication scenario, the PLC networks are intrinsically broadcast, namely the channels are shared between the users who access it, so that a transmitted signal can reach each node belonging to the network. Therefore, especially in a MU network context, where confidential communications and private transactions are exchanged, data security is of crucial importance, aside from the maximum data rate that can be offered. Towards this end, security can be provided in two main ways, i.e. at high or low levels of the Open Systems Interconnection (ISO/OSI) stack model, which was issued by the International Organization for Standardization (ISO). The methods

that are implemented at high ISO/OSI levels concern a cryptographic approach based on algorithms, such as the Data Encryption Standard (DES) or the Rivest-Shamir-Adleman (RSA) cryptosystem. Instead, the second technique exploits the lowest ISO/OSI level, that considers the PHY. In particular, the physical medium, its time/frequency diversity and the differences between the users links can be exploited in order to provide security. This concept is known as PLS [161]. Although cryptographic mechanisms are generally used, the PLS can complement, extend and enhance the concept of security, implemented and provided by other layers.

9.1 Basic PLS Concepts and Purposes

There are essentially two schools of thought underlying the secrecy in a communication system, namely the complexity-based security and the information-theoretic security. The main differences are detailed below.

Complexity-based is the most common and deployed approach. It includes all the methods and the cryptographic techniques, such as the DES or the RSA. This cryptographic approach assumes the adversary to have limitations on the computational power and/or available resources. Thus, the computational resources required to extract and decrypt the original message (the plain-text) from the encrypted one (the cipher-text) render it practically unfeasible for the adversary, in a reasonable time. The difficulty to decipher the encrypted message determines the quality of a given security protocol.

Information-theoretic approach was first formulated by Shannon in 1949 [162], where the adversary is assumed to have unlimited computational resources and the objective is to ensure that absolutely no information is released to the adversary. This principle is widely accepted as the strictest notion of security and underlies the formulation of the PLS. In particular, the PLS exploits the physical medium time, frequency and spatial diversity in order to complement and enhance the security provided by other layers. Moreover, the optimal power allocation problem with secrecy constraints, from an information-theoretic viewpoint, resembles the general resource allocation problem in multicarrier systems [163].

Although PLS has been deeply investigated and analyzed for the wireless scenario, little effort has been spent for the PLC case. For example, the maximum achievable secrecy rate, i.e. the secrecy capacity, over a quasi-static Rayleigh fading channel (wireless case), is analyzed in [164] and in [165] in terms of outage probability. While, the secrecy capacity and the optimal power allocation, when transmission occurs over M orthogonal AWGN sub-channels or over a discrete-time memoryless fading channel, are derived in [166]. Furthermore, [167] provides an analytic formulation of the secrecy rate and derives the

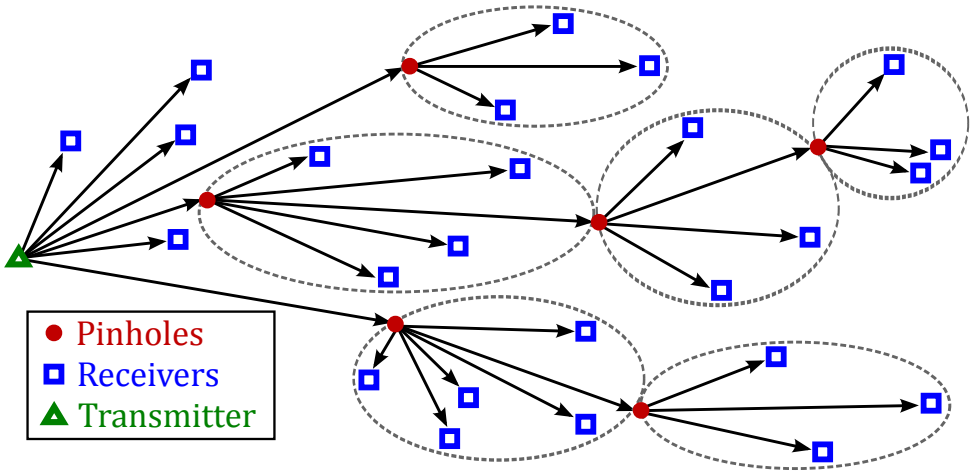

Figure 9.1: Generic scheme of a typical PLC network topology.

optimal power allocation for multicarrier, multi-antenna and MU scenarios. However, these studies focus on the wireless scenario, where the channel statistics is not the same as in PLC networks and the negative effects of spectral/spatial correlation, due to the network configuration, are less noticeable. The achievable rate in PLC networks, without secrecy constraints and for both experimental and statistical data, is investigated in [117] and [118]. Only in recent times more effort has been spent in the analysis of PLS in PLC networks. One of the most recent and comprehensive studies is addressed in [168], which discusses the PLS over MIMO PLC channels, in the 2–28 MHz frequency range and under AWGN.

As it will be clarified in the following description, the PLC environment significantly differs from the wireless scenario. Thus, in order to perform a thorough and fair analysis of PLS in PLC, it is important to first understand the properties of the PLC network and the channel characteristics, as done in the previous part of this thesis.

9.1.1 Wireless versus PLC

Even though wireless and PLC communication scenarios show some similarities, such as the broadcast nature, they significantly differ in channel statistics and properties, background noise and achievable performance. For example, the highly uncorrelated channel assumption, which usually holds in rich scattering wireless environments, is no longer valid for PLC networks. This is, since, wireless networks are essentially based on a star-style structure, while PLC ones deploy a tree topology, with multiple branches departing from the same node, as shown in Figure 9.1. In this configuration, the links to the end nodes share part of the wires up to a same node κ, named pinhole or keyhole, where branches depart. This network topology leads to what is known as keyhole effect [169–171], which typically affects PLC scenarios. For example, the keyhole effect in cooperative multi-hop PLC networks has been studied in [172].

Another prominent PLC channel characteristic is the frequency correlation between the sub-channels of a multicarrier transmission scheme, mainly due to cross-talks and coupling effects phenomena, as it has been discussed in Section 3.2.4. Furthermore, the PLC channels are also affected by fading, which exhibits different statistics from the wireless channels. Indeed, while wireless fading has a well-known Rayleigh amplitude distribution [142], the PLC scenario exhibits a log-normal fading statistics [73], as also demonstrated in Section 3.2.1. All these phenomena, together with the underlying PLC network topology, introduce high frequency and/or spatial correlation among the channel responses, as well as among the different users.

A final key feature that should be taken into account is the type of background noise. Unlike the wireless case, where AWGN is assumed, the PLC scenario is subject to colored Gaussian noise with an exponential decreasing profile, as discussed in Section 7.3. Consequently, all these channel and noise properties affect the performance achievable on PLC networks w.r.t. the wireless case, typically affected by uncorrelated Rayleigh fading under AWGN.

9.1.2 Main Contributions

The purpose of this chapter is to start with the investigation of the achievable secrecy rate in typical PLC channels and to highlight the differences with respect to the wireless communication case. In order to perform a statistical comparison among wireless and PLC networks, the well-known wireless theoretical results, concerning the PLS, have been exploited and applied to the PLC context. For simplicity a single carrier case is considered first. Although the achievable rate has been studied in PLC channels, both with experimental data and with the use of statistical simulators, e.g. in [117], [118], the PLS and the secrecy rate concepts are still poorly investigated within the PLC context. We show that PLS is possible in PLC. However, it will be shown that, since PLC channels are not characterized by Rayleigh fading, which is typical of wireless channels, lower secrecy rates can be achieved, compared to the wireless context. Furthermore, channel correlation, introduced by signals propagating in a shared tree structure network, can reduce further the secrecy rate.

Then, the PLS study is extended considering a multicarrier modulation, as well as a MU broadcast system. The effect of the channel statistics on the achievable secrecy rate is analyzed, highlighting fundamental and practically relevant questions related to many challenges arising from the secure physical layer communication in PLC scenarios. A comparison with the wireless scenario, in terms of secrecy capacity distribution, is also made. The results are computed using a statistical PLC channel model as a tool to infer the effect of certain phenomena, as the users/frequency correlation and the keyhole structure, and to explain the performance degradation obtained when considering a set of measured channels.

Finally, the MIMO transmission scenario in the extended frequency band 1.8–86 MHz is faced. The power allocation problem is assessed and solved by applying an AO algorithm. The considered MIMO transmission exploits not only the two differential transmitting modes over the three wires, but also the three star-style receiving modes, with the additional use of the CM. The reader is referred to Section 4.1.1 for details. The analysis relies on real channel and noise measurements and fulfills the HPAV2 standard specifications [39]. These assumptions allow to provide results of practical relevance.

The rest of the chapter is organized as follows. First, Section 9.2 offers an overview about the different channel configurations that have been considered in the PLS study framework. Then, Section 9.3 provides an information-theoretic formulation of the problem of secure communication over fading channels. Herein, the secrecy capacity is defined and the secrecy rate maximization problem is solved deriving the optimal power allocation for a NB channel. The differences between the wireless and the PLC scenarios, comparing the secrecy rate of a Rayleigh fading channel (wireless case) with that of a log-normal fading channel (typically exhibited by PLC networks), are also assessed.

Then, in Section 9.4 and Section 9.5, the secrecy rate optimization problem is discussed and solved, deriving the optimal power allocation for both multicarrier and MU scenarios, respectively. For both these cases, the SISO transmission scheme, in the 2–28 MHz frequency range and under AWGN, is considered, being compliant with the HPAV standard [29]. In particular, Section 9.4 assesses the influence of PLC channel statistics, frequency and MU correlation phenomena, as well as the keyhole effect, on the achievable secrecy rate via a numerical model. The simulated results are validated and compared to the performance achieved by PLC channel measurements, as well as to the secrecy rate obtained by typical wireless channels. Moreover, both the optimal and the uniform power allocation strategies are considered. Instead, Section 9.5 discusses the secrecy region for the MU broadcast system, obtained with an exhaustive search, and the average secrecy rate under a QoS constraint.

Finally, the 2×4 MIMO transmission scheme, in the extended band 1.8–86 MHz, is considered in Section 9.6 fulfilling the HPAV2 specifications. The non-convex optimization problem is solved via an AO algorithm and the results, in terms of achievable secrecy rate, are provided comparing a real colored and correlated background noise with an equivalent AWGN profile. A comparison with the channel capacity, without secrecy constraints, is also performed. A final overall comparison among the main provided results is summarized in Section 9.7.

9.2 The Wiretap Channel

The generic communication channel configuration depicted in Figure 9.2, where a transmitter Alice wishes to send a secret, or confidential message, to an intended, or legitimate,

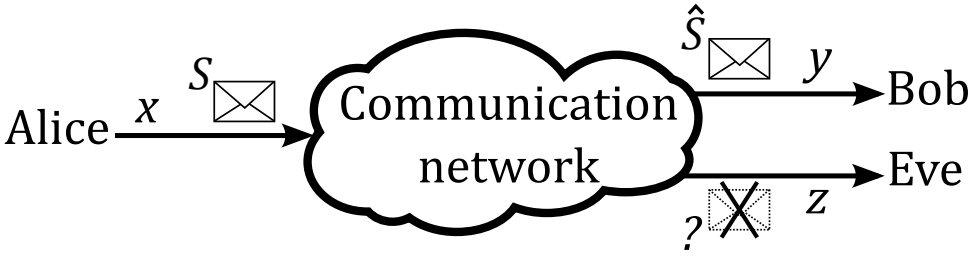

Figure 9.2: Generic wiretap channel transmission scheme.

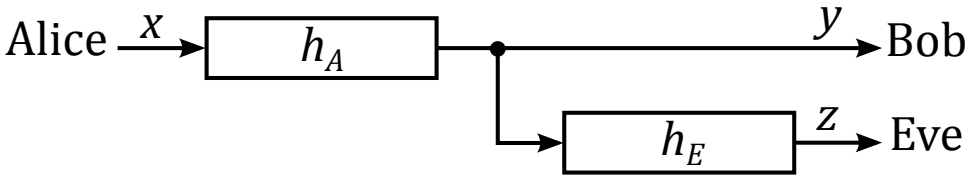

(a) Wyner configuration.

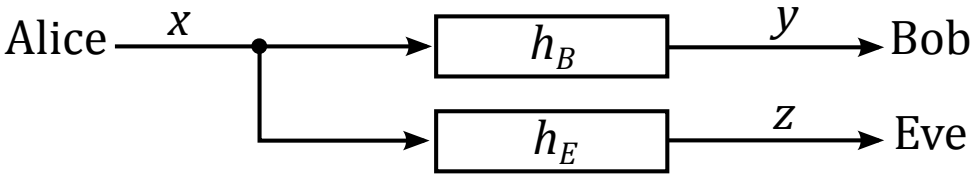

(b) Csiszár and Körner model.

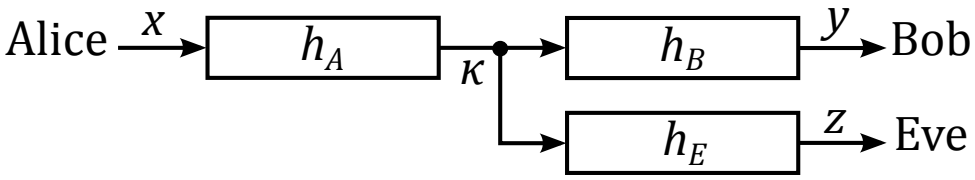

(c) Keyhole channel scheme.

Figure 9.3: Different wiretap channel models.

receiver Bob, so that absolutely no information can be inferred by an eavesdropper Eve, is known as wiretap channel. Eve represents the adversary, which tries to detect and disclose the message having an arbitrarily high amount of available computational resources, as the information-theoretic secrecy foresees.

There exist essentially three main types of channel configurations, modeling different possible communication scenario. Each configuration can be incorporated in a general representing scheme, as depicted in Figure 9.3. The three models and their features are listed below. The quantity h_A corresponds to the amplitude of the channel departing from the transmitter Alice, while h_B and h_E refer to the amplitudes of the channels connecting the receivers Bob and Eve, respectively. The knowledge of the quantities h_A, h_B or h_E means to have the CSI of the corresponding channel.

Wyner

The information-theoretic approach, which builds on Shannon's notion of perfect secrecy [162], was first studied by Wyner in [173]. In the classical wiretap channel proposed by Wyner [173], also referred to degraded wiretap channel, the two legitimate users communicate over a main channel (h_A) and an eavesdropper has access to a degraded versions of the channel outputs through the wiretapper channel (h_E), as depicted in Figure 9.3a. This is the simplest model since the channel to Bob is assumed ideal. This fact simplifies the analysis and the derivation of secrecy limits [174] because it assumes that Eve's received signal is always a degraded, or noisier, version of Bob's received signal. Furthermore, Wyner found that there is a trade-off between the transmission rate of the main user and the equivocation at the wiretapper.

Csiszár and Körner

Later, Csiszár and Körner [175] extended the Wyner's work to the general broadcast scenario, assuming the main and the eavesdropper channels as independent from each other, as depicted in Figure 9.3b. In this case, the transmitter channel, i.e. h_A, is assumed as ideal, whereas Bob's (h_B) and Eve's (h_E) channels are considered as independent from each other. This model, for example, is suitable for the representation of a star-style structure PLC topology, as well as of a typical wireless communication networks, where the rich scattering is such that the two channels, h_B and h_E, are affected by statistically independent fading.

Keyhole channel

The model depicted in Figure 9.3c is the most general one since it includes both the others by assuming h_B or h_A as ideal, as previously discussed. It can represent a tree or bus network configuration structure, which is very common in PLC networks. It is referred to as keyhole channel since the branch point κ is the keyhole, or pinhole, through which the signals to Bob and Eve need to pass through. Thus, the transmitted signal needs to cross the keyhole and travel an identical section, represented by h_A, before reaching the intended receiver or the eavesdropper through the corresponding channel. This propagation phenomenon introduces what has been defined as MU correlation in Section 2.1.5, as well as a rank-deficiency of the MIMO communication channel, limiting the achievable secrecy rate performance [169,170,172,176]. An example where the keyhole channel effect is deeply investigated over a MIMO transmission scheme was reported in [171], which, however, considers the wireless context.

9.2.1 Preliminaries

From an information-theoretic viewpoint, Alice's transmitted signal x and Bob's and Eve's received signals y and z, respectively, can be modeled as random variables (see Figure 9.3c). The corresponding channel input or output alphabets are written as $\mathcal{X}$, $\mathcal{Y}$ and $\mathcal{Z}$. In this communication system, Alice sends a secret message $\mathcal{S}$ to Bob, randomly chosen from the message set $\mathcal{S} = \{1, \ldots, \mathcal{M}\}$, with $\mathcal{M} = 2^{nR_S}$, that is transmitted in n channel uses. In this case, the secret has entropy $\mathcal{H}(\mathcal{S}) = nR_S$ bits and the secrecy communication rate is $R_S = H(\mathcal{S})/n$ bits per channel use. In this system, an $(\mathcal{M}, n)$-code consists of an encoder at the transmitter, which maps the secret message $\mathcal{S}$ into a codeword $\mathbf{x} = [x_1, \ldots, x_i, \ldots, x_n]$, and a decoding function at the legitimate receiver, which converts the received codeword $\mathbf{y} = [y_1, \ldots, y_i, \ldots, y_n]$ into the message $\hat{\mathcal{S}}$, with error probability $P_e = \Pr[\mathcal{S} \neq \hat{\mathcal{S}}]$. Afterwards, Eve overhears the output $\mathbf{z} = [z_1, \ldots, z_i, \ldots, z_n]$. Her residual uncertainty regarding $\mathcal{S}$ is given by the conditional entropy $H(\mathcal{S}|\mathbf{z})$, which is generally expressed by the equivocation rate $R_e = H(\mathcal{S}|\mathbf{z})/n$.

From the perspective of confidential and reliable communication, the system performance depends on both the communication rate R_S, between Alice and Bob, and the equivocation rate R_e, between Alice and Eve. The PLS problem turns out to be an optimization problem that aims to maximize the performance between the legitimate users, under a constraint of the maximum information obtainable from the unauthorized user. In particular, the secrecy rate R_S is said to be achievable, over the wiretap channel, if for any $\varepsilon \geq 0$, there exists an integer $n(\varepsilon)$ and a sequence of $(\mathcal{M}, n)$-codes of rate $R_S = \frac{1}{n} \log_2 \mathcal{M}$, such that, for all $n \geq n(\varepsilon)$, the average decoding error probability becomes arbitrarily small, i.e. $P_e \leq \varepsilon$ and the security constraint $R_e = H(\mathcal{S}|\mathbf{z})/n \geq R_S - \varepsilon$ is fulfilled [166, 167].

9.2.2 Secrecy Capacity

Perfect secrecy requires $R_e = R_S$, hence $\varepsilon = 0$. Thus, the secrecy capacity $\mathcal{C}_S$ is the maximum achievable secrecy rate R_S that guarantees the secrecy of the transmitted data, namely $\mathcal{C}_S = \max_{P_e \leq \varepsilon} R_S$, and such that the rate-equivocation pair $(R_S, R_e = R_S)$ is achievable. In practice, the secrecy capacity of a system represents the amount of information (e.g. bps) that can be reliably transmitted to the receiver. This means that the average decoding error probability approaches zero at the intended receiver, while the uncertainty at the eavesdropper, usually expressed by the equivocation rate, equals the secrecy rate. This way, no information is released to the eavesdropper, which cannot decode the messages from Alice at any positive rate, lower than the secrecy capacity [167].

For the degraded Gaussian wiretap channel in Figure 9.3a, which was introduced in [174], where the main channel has an higher information rate than the eavesdropper channel, the secrecy capacity is given by the maximum difference between two channel

mutual information, as

$$\mathcal{C}_S = \max_{f_x \in \mathcal{F}} [I(x;y) - I(x;z)], \tag{9.1}$$

where f_x is the pdf of the channel input x, whereas $\mathcal{F}$ is the set of all pdfs at the channel input, under a power constraint. While, $I(x;y)$ and $I(x;z)$ represent the mutual information terms among the signals x and y, and x and z, respectively. Instead, for the general Gaussian wiretap channel, as well as for the keyhole channel in Figure 9.3c, the secrecy capacity $\mathcal{C}_S$ has the same expression as in (9.1), but it is set to zero if Eve has a better channel realization than Bob. Thus, it is defined as [166]

$$\mathcal{C}_S = \max_{f_x \in \mathcal{F}} [I(x;y) - I(x;z)]^+, \tag{9.2}$$

where $[q]^+ = \max(q, 0)$. The mutual information terms $I(x;y)$ and $I(x;z)$ are convex in f_x so that a lower bound R_S, for the secrecy capacity in (9.2), can be formulated as [167]

$$\mathcal{C}_S \geq \left[\max_{f_x \in \mathcal{F}} [I(x;y)] - \max_{f_x \in \mathcal{F}} [I(x;z)] \right]^+ = R_S. \tag{9.3}$$

This lower bound R_S is often used for a simplified calculation of the achievable secrecy rate since it is known how to maximize the mutual information terms.

In the first part of this chapter, the SISO scheme is considered, but all the results can be extended to the MIMO communication scenario. In particular, the SISO channel coefficients h_A, h_B and h_E are described by matrices, while the signals x, y and z become vectors, in the MIMO case.

9.3 PLS on Narrowband Channels

A preliminary analysis of the PLS over PLC networks is addressed in this section starting with a simple SISO and single carrier wiretap channel. The secrecy rate maximization problem is solved, deriving the optimal power allocation strategy. Then, the main differences between the secrecy capacity and the well-known capacity, without secrecy constraints, as well as between wireless and PLC scenarios, are discussed.

9.3.1 Problem Formulation

Assuming the presence of additive noise and NB transmission, the model in Figure 9.3c can be mathematically written as

$$\begin{aligned} y &= h_M \cdot x + n_M, \\ z &= h_W \cdot x + n_W, \end{aligned} \tag{9.4}$$

where x is the channel input signal, while y and z are the channel outputs at the legitimate and the eavesdropper receiver, respectively. Furthermore, n_M and n_W represent the noise terms, assumed to be independent and identically distributed (i.i.d.) zero mean complex Gaussian in the following. Whereas, h_M and h_W are the channel gain coefficients, or amplitudes, for the main and the eavesdropper channels, respectively. This model is independently used n times to transmit the codeword $\mathbf{x} = [x_1, \ldots, x_i, \ldots, x_n]$, of length n, that is chosen for the message $\mathcal{S}$.

With reference to Figure 9.3c, h_M can be viewed as the product of the gains h_A and h_B. Similarly, h_W is obtained by the product of the gains h_A and h_E. Thus, the model in (9.4) can describe each one of the three different configurations represented in Figure 9.3.

9.3.2 Secrecy Capacity in Fading Channels

In order to model the effect of a fading channel, the gain coefficients h_M and h_W in (9.4) are assumed to be zero-mean proper complex random variables. The noise variables n_M and n_W are assumed zero-mean i.i.d. complex Gaussian, having variances σ_M^2 and σ_W^2, respectively. The input sequence $\mathbf{x}$ is subject to the average power constraint according to $\frac{1}{n}\sum_{i=1}^{n} E[x_i^2] \leq P_T$. Furthermore, the transmitter is assumed to have a perfect knowledge of the CSI for both the intended (Bob) and the eavesdropper (Eve) links. This resembles the situation when Eve is not an hostile node, but simply another user of the network, which is not the intended user.

According to the above mentioned system assumptions, it has been shown in [164] that the average secrecy capacity can be obtained from (9.2) as

$$\mathcal{C}_S = \max_{\mathcal{P} \text{ s.t. } \overline{P}_t \leq P_T} E_U \left[\log_2 \left(1 + \frac{P_t(\mathbf{h})|h_M|^2}{\sigma_M^2} \right) - \log_2 \left(1 + \frac{P_t(\mathbf{h})|h_W|^2}{\sigma_W^2} \right) \right], \tag{9.5}$$

where $U = \left\{ \mathbf{h} : \frac{|h_M|^2}{\sigma_M^2} > \frac{|h_W|^2}{\sigma_W^2} \right\}$, while $\mathbf{h} = (h_M, h_W)$ is a random vector having the same distribution as the marginal distribution of the process $\mathbf{h} = (h_M, h_W)$ at one time instant. Furthermore, $P_t(\mathbf{h})$ denotes the power allocation for a given realization of one channel pair $\mathbf{h}$, whereas $\mathcal{P} = \{P_t(\mathbf{h}) : \mathbf{h} \in U\}$ and $\overline{P}_t$ indicates the average power allocated for the set of realizations $\mathbf{h} \in U$. This formulation provides a solution in terms of average performance, thus, from a statistical viewpoint. It should be noted that, for arbitrarily large power $P_t(\mathbf{h})$, the capacity is upper bounded by

$$\lim_{P_t(\mathbf{h}) \to \infty} \mathcal{C}_S = E_U \left[\log_2 \left(\frac{|h_M|^2 \sigma_W^2}{\sigma_M^2 |h_W|^2} \right) \right], \tag{9.6}$$

which may assume small values. In the following it will be showed that higher secrecy rates are achievable by exploiting the additional degrees of freedom in a wideband multicarrier system or through the use of MIMO transmission techniques.

In order to find the optimal power allocation that maximizes (9.5) under a power constraint, we can exploit the fact that the argument in (9.5) is a concave function of $\mathcal{P}$. Therefore, the optimal power allocation $\hat{P}_t(\mathbf{h})$ that provides the secrecy capacity in (9.5), for a given channel realization pair (h_M, h_W), can be obtained via the Karush–Kuhn–Tucker (KKT) conditions as follows

$$\hat{P}_t(\mathbf{h}) = \begin{cases} \frac{1}{\lambda \ln 2} - \frac{\sigma_M^2}{|h_M|^2}, & \text{if } |h_W|^2 = 0, \lambda < \frac{1}{\ln 2}\frac{|h_M|^2}{\sigma_M^2}, \\ \frac{1}{2}\sqrt{\left(\frac{\sigma_W^2}{|h_W|^2} - \frac{\sigma_M^2}{|h_M|^2}\right)\left(\frac{4}{\lambda \ln 2} + \frac{\sigma_W^2}{|h_W|^2} - \frac{\sigma_M^2}{|h_M|^2}\right)} + \\ -\frac{1}{2}\left(\frac{\sigma_W^2}{|h_W|^2} + \frac{\sigma_M^2}{|h_M|^2}\right), & \text{if } |h_W|^2 > 0, \frac{|h_M|^2}{\sigma_M^2} > \frac{|h_W|^2}{\sigma_W^2}, \\ & \lambda < \frac{1}{\ln 2}\left(\frac{|h_M|^2}{\sigma_M^2} - \frac{|h_W|^2}{\sigma_W^2}\right), \\ 0, & \text{otherwise}, \end{cases} \tag{9.7}$$

where λ is chosen to satisfy the power constraint $\overline{P}_t(\mathbf{h}) = P_T$. It can be seen from (9.7) that the optimal power allocation is not the water filling solution. This is in contrast to what it is found for the capacity without the secrecy constraint. Furthermore, the solution in (9.7) will depend on the specific fading channel statistics exhibited by h_M and h_W, where stationary and ergodic conditions are assumed. The results in (9.5) and (9.7) are also derived in [164].

Considering the PLC context, the above detailed formulation, for the computation of the average secrecy rate, applies to three possible scenarios: (i) a scenario where a given triplet of nodes X (Alice), Y (Bob) and Z (Eve) is considered and the channels h_M and h_W are NB time variant, for instance because of a change in the loads; (ii) a scenario where a given intended transmission link is considered , i.e. a given pair (X, Y), and the eavesdropper Z changes with time; (iii) a scenario where we want to compute the average secrecy rate, under an average power constraint, over the ensemble of possible triplets (X, Y, Z) in a certain network.

9.3.3 Channel Statistics Effect on the PLS

As stated in Section 9.3.2, the solution in (9.7) applies to a general fading channel. Thus, in this section, two different types of wiretap channel are simulated, namely wireless and PLC. For the wireless case, a Rayleigh fading wiretap channel is considered, where h_M and h_W are zero mean proper complex Gaussian random variables with unit variances. Hence, $|h_M|^2$ and $|h_W|^2$ are exponentially distributed with parameter 1. Then, a log-normal fading is assumed for the PLC wiretap channel, where $|h_M|^2$ and $|h_W|^2$ have a log-normal distribution with parameters μ and σ^2, namely $h_M, h_W \in$ Log-$\mathcal{N}(\mu, \sigma^2)$.

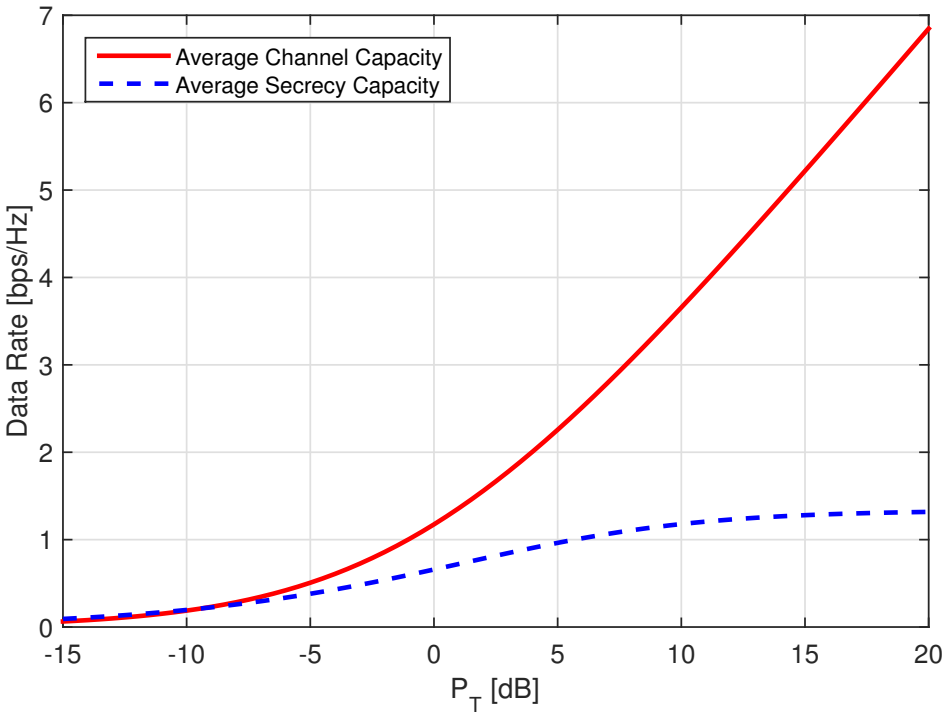

Figure 9.4: Comparison between the average channel capacity, without secrecy constraints, and the average achievable secrecy capacity, for transmission from Alice to Bob in a log-normal fading wiretap channel.

Indeed, it has been shown in [118] and in Section 3.2.1 that the log-normal distribution well fits the statistics of the channel gain, or amplitude, in the PLC scenario.

In order to perform a comparison between these two types of fading channels, i.e. Rayleigh and log-normal, we choose μ and σ^2 so that the log-normal fading shows the same mean and variance of the Rayleigh fading channel. Thus, knowing that the exponential distribution has mean λ^{-1} and variance λ^{-2}, and that the log-normal distribution has mean $e^{\mu+\sigma^2/2}$ and variance $(e^{\sigma^2}-1)e^{2\mu+\sigma^2}$, we obtain $\mu = -\ln(\lambda\sqrt{2})$ and $\sigma^2 = \ln(2)$. These equalities link and constrain the parameters in order to obtain the same statistical distribution for both the fading types. The AWGN is assumed to have unit variance.

Figure 9.4 shows the comparison between the average channel capacity, achieved without the secrecy constraints, and the average secrecy capacity, both in bps/Hz, w.r.t. the total power constraint P_T in dB and assuming log-normal fading. The average channel capacity exponentially increases with the increase of the total available power P_T, and thus, with the increase of the SNR. Conversely, the secrecy capacity is upper bounded by the constant value in (9.6), as pointed out in Section 9.3.2. Thus, the gap among these two quantities goes to infinity as the SNR increases.

A performance comparison, between the two types of aforementioned fading channels, and thus among the wireless and PLC environments, is depicted in Figure 9.5. The secrecy rate achieved by the optimal and uniform, i.e. allocating the same power for all channel states $\mathbf{h} \in U$, power allocation strategies, for both the Rayleigh and the log-normal

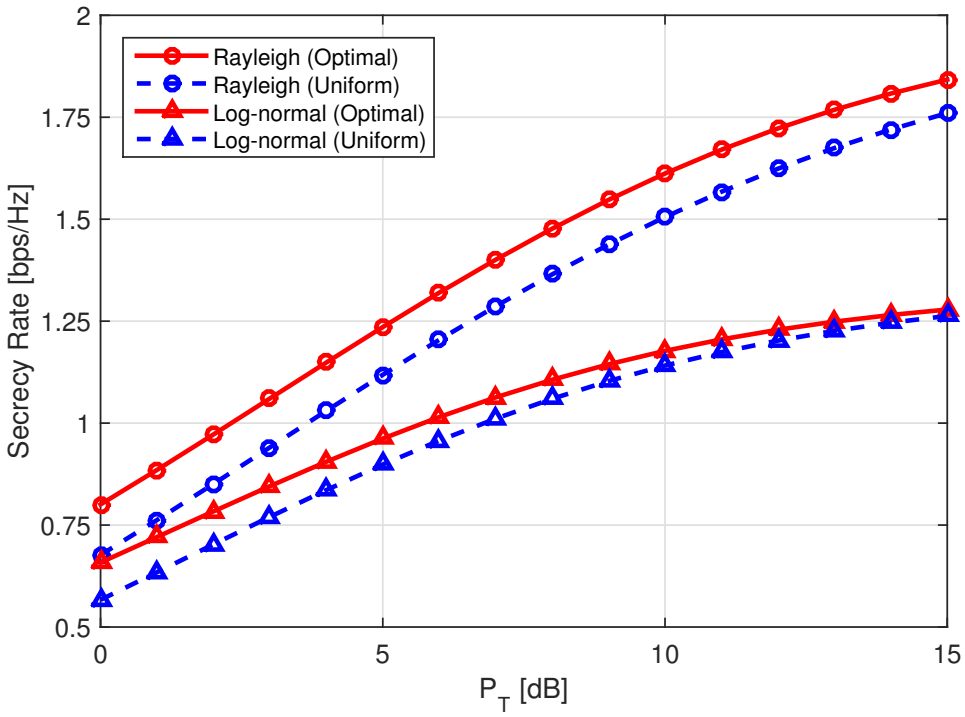

Figure 9.5: Comparison between the achievable secrecy rate for both optimal and uniform power allocation and for the two different types of analyzed fading channel statistics, i.e. Rayleigh and log-normal.

wiretap channels, is analyzed. It can be seen that the uniform power allocation provides worse performance than the optimal power allocation, for both fading statistics. However, for the SNR region of interest, the gap between these two power allocation strategies remains almost constant for the Rayleigh fading case. While, for the log-normal case, the gap decreases. Contrariwise to what depicted in Figure 9.5, the uniform power allocation can be close to optimum, even for moderate SNR levels, when the Rayleigh fading channel without the secrecy constraints is considered. Furthermore, the secrecy rate goes to zero as the available power decreases. Instead, for high power constraints, the secrecy rate is upper bounded by the value in (9.6) for both power allocations, i.e., optimal and uniform, as depicted in Figure 9.4. Finally and importantly, it should be noted that the secrecy rate for the log-normal fading channel is always lower than the secrecy rate for the Rayleigh fading channel. This behavior also applies to the secrecy rate bound, achieved for an high SNR. Therefore, this first result shows that the secrecy rate achievable on a typical PLC channel, characterized by a log-normal fading statistics, is lower than the one achievable on wireless channel, Rayleigh distributed. To validate this theoretical result and the proposed channel modeling strategy, the data acquired during an experimental channel measurement campaign are considered in the next section, comparing simulated and experimental results.

9.3.4 Model Validation

In order to validate the modeling strategy adopted in Section 9.3.3, used to compare wireless and PLC scenarios, the experimental measurements carried out on the cruse ship presented in [54] and discussed in Section 5.3 are herein considered. The aim is to compare the performance of the experimental channels to those of the simulated channels, generated so that they show the same statistical distribution, as previously done. Among all the possible databases, we chose the in-ship measurements since these channels are less affected by the typical PLC channel phenomena, such as attenuation and correlation, contrariwise, for example, to the in-home case. This is done in order to limit the secondary effects, which will be discussed in the following, focusing only on the channel statistical behavior and not on the relationships it exhibits.

As it has been discussed in Section 5.3, the in-ship network topology consists of a star and a bus structure. To avoid the influence of the keyhole and the correlation effects, only the star-style channels, from the SS to the DB, are considered. Thus, the model in Figure 9.3b applies. Since we are considering a NB scheme, the ACG is used as a representation of the channel. The considered frequency range for the ACG computation is 1.8–50 MHz. The analysis of the ACG reveals that it can be well fitted by a log-normal distribution with parameters $\mu \cong -5.7$ and $\sigma^2 \cong 2.1$. A comparison between the achievable secrecy rate, obtained by the log-normal fit and by the channel measurements, is shown in Figure 9.6. The figure shows a good match between theoretical and experimental results, validating the adopted modeling strategy. The slight discrepancy at low SNR values is amenable to the fact that the log-normal fit is an approximation of an ideal channel, while the experimental measures still exhibit some small correlation or non-ideality effects. These phenomena, as the channel correlation and the network topology, influence the secrecy capacity, as it will be discussed in the next section for the multicarrier modulation in the BB-FS.

9.4 Multicarrier SISO System

As thoroughly described in the first part of this thesis, PLC networks are subject to a variety of physical phenomena. In order to asses how these phenomena affect the PLS performance, different types of random channels are generated, through a numerical model, and compared. In particular, the impact of the channel statistics, the frequency and MU correlation, as well as the keyhole effect, are evaluated generating random channels responses with the appropriate statistics. As before, this approach allows a further PLC and wireless scenario comparison, relying on channel responses with different distributions. To facilitate the comprehension, the SISO channel is herein considered first. Moreover, to fairly compare wireless and PLC scenarios, the same background AWGN noise is assumed.

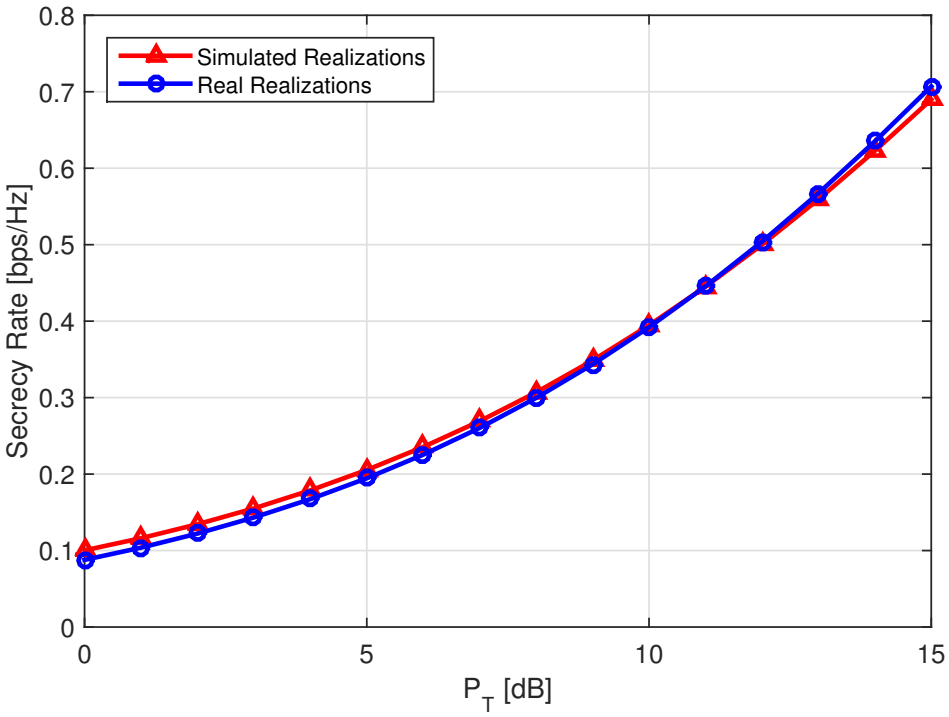

Figure 9.6: Comparison between the average secrecy rate achieved when considering the channel measurements versus that achieved by the simulated channel realizations, generated with the same channel statistical parameters.

The general model in Figure 9.3c can be straightforwardly extended to a multicarrier or to a MU scenario. In the following, the multicarrier scenario is investigated, defining the mathematical model, the optimization problem formulation and its optimal solution. Afterwards, a typical PLC application scenario is discussed, in which this optimal solution, deeply studied in the wireless case, can be applied.

9.4.1 System Model

Consider a multicarrier wiretap channel where Alice wants to send a confidential message to Bob, in a system with M parallel sub-channels (or carriers), keeping it secret from the eavesdropper Eve. This systems is equivalent to the scheme in Figure 9.3c used M times in parallel, which can be mathematically written, similarly to (9.4), as

$$\begin{aligned} y_m &= h_{M,m} \cdot x_m + n_{M,m}, \\ z_m &= h_{W,m} \cdot x_m + n_{W,m}, \end{aligned} \tag{9.8}$$

where $m = 1, \ldots, M$ is the sub-channel, or frequency sample, index. On each sub-channel Alice transmits the signal x_m, while Bob receives the signal y_m and Eve overhears the signal z_m. The channels coefficients are identified by $h_{M,m}$ and $h_{W,m}$, whereas the noise variables by $n_{M,m}$ and $n_{W,m}$, for the main and the eavesdropper link, respectively.

As already discussed in Section 9.3 in reference to Figure 9.3c, also in this case the

main and the wiretapper channels, i.e. $h_{M,m}$ and $h_{W,m}$, can be viewed as the product of the corresponding channel gains h_A, h_B and h_A, h_E. Thus, also the multicarrier model can describe each one of the three different models detailed in Section 9.2.

Assumptions

The variables $n_{M,m}$ and $n_{W,m}$ are circular symmetric i.i.d. and represent the effect of the complex Gaussian noise with zero mean and variance σ_n^2 at each frequency sample m. The transmitted signal x_m and the noise are assumed to be statistically independent from each other and for each sub-channel m. Moreover, as usually happens, the power at the transmitter is limited by a total power constraint $\sum_{m=1}^{M} |x_m|^2 \leq P_T$, where P_T is the total available power. Furthermore, we assume that Bob and Eve perfectly know their individual channel realization and that Alice has a full CSI knowledge. Thus, Alice has access to the channel gains of both the legitimate receiver (Bob) and the eavesdropper (Eve). The CSI knowledge is gained via the insertion of training symbols in the transmitted signal, which enable the receiver to evaluate the channel attenuation, or gain. Hence, the channel information is sent back to the transmitter. This resembles the situation where Eve is not an hostile node, but simply another user of the network, which is not the intended user. For the sake of simplicity, in this case we define

$$\beta_{M,m} = |h_{M,m}|^2 \quad \text{and} \quad \beta_{W,m} = |h_{W,m}|^2, \tag{9.9}$$

that are the channel power gains, or squared amplitudes, for the main and the eavesdropper channels, respectively.

9.4.2 Optimization Problem Formulation

For the system model described in Section 9.4.1, the secrecy rate can be computed according to (9.3) as [166]

$$R_S(\mathbf{P}_t) = B \sum_{m=1}^{M} \left[\log_2 \left(1 + \frac{\beta_{M,m} P_{t,m}}{\sigma^2} \right) - \log_2 \left(1 + \frac{\beta_{W,m} P_{t,m}}{\sigma^2} \right) \right]^+, \tag{9.10}$$

where B is the sub-channel bandwidth, whereas $P_{t,m}$ is the power allocated by Alice on the m-th sub-channel. The powers on the sub-channels are collected in a vector $\mathbf{P}_t = [P_{t,1}, \ldots, P_{t,M}]$, which denotes the power allocation strategy adopted at the transmitter, for a given channel realization. It can be noted that, for arbitrarily large powers $\mathbf{P}_t$, the secrecy rate is upper bounded by $\sum_{m=1}^{M} [\log_2(\beta_{M,m}/\beta_{W,m})]^+$, similarly to expression (9.6), which can be small if the channel does not provide enough diversity.

The secrecy rate optimization problem for the multicarrier system, under a total power

constraint, is given by

$$\max_{\mathbf{P}_t} R_S(\mathbf{P}_t) \text{ subject to } \begin{cases} \sum_{m=1}^{M} P_{t,m} \leq P_T, \\ P_{t,m} \geq 0. \end{cases} \tag{9.11}$$

This is a non-convex optimization problem with objective function R_S. It was shown in [177] that the optimal power allocation that solves (9.11) is to allocate zero power on the sub-channels where the main channel is worse than the wiretapper, i.e. $\beta_{M,m} \leq \beta_{W,m}$. The resulting problem is convex, hence, it can be easily solved via the KKT conditions [178]. Consequently, the optimal power allocation that solves (9.11) is given by [167]

$$P_{t,m} = \begin{cases} 0 & \text{if } \beta_{M,m} \leq \beta_{W,m}, \\ \left[\sqrt{\left(\frac{\sigma^2(\beta_{M,m}-\beta_{W,m})}{2\beta_{M,m}\beta_{W,m}} \right)^2 + \frac{1}{\lambda \ln 2} \frac{\sigma^2(\beta_{M,m}-\beta_{W,m})}{\beta_{M,m}\beta_{W,m}}} - \frac{\sigma^2(\beta_{M,m}+\beta_{W,m})}{2\beta_{M,m}\beta_{W,m}} \right]^+ & \\ & \text{otherwise.} \end{cases} \tag{9.12}$$

The parameter $\lambda > 0$ is chosen to satisfy the power constraint $\sum_{m=1}^{M} P_{t,m} \leq P_T$. As for the NB single carrier case in Section 9.3.2, in contrast to a generic optimization problem without secrecy constraints, the solution in (9.12) is not the water filling. In order to perform a fair analysis, the total power P_T equals the sum of the HPAV PSD constraint over the used sub-channels.

The computation of the secrecy rate formulated in (9.12) applies to a given channel realization. Thus, this result can be applied to any communication system and, in particular, to the PLC scenario. It is however of interest to investigate the performance considering a wide set of channels and, therefore, to carry out a statistical analysis of the secrecy rate. In a real PLC scenario, the solution in (9.12) can be averaged among the channel realizations, providing the average secrecy rate or, more in general, allows the computation of the cumulative distribution function.

9.4.3 PLC Channel Effects on Performance

The aim of this section is to evaluate the achievable secrecy rate in a multicarrier single-user PLC scenario and compare it with the wireless scenario. The purpose is to identify as the physical phenomena and the network topology affect the performance of real PLC networks. As detailed in Chapter 3 and pointed out in Section 9.1.1, PLC networks implement a tree topology, where part of the wires are shared among the communication links. This introduces frequency correlation, among the used sub-channels, as well as MU correlation, namely between the main and wiretapper channels. Furthermore, the sub-channels CFR in a multicarrier PLC system are affected by fading which does not have a Rayleigh

amplitude distribution, rather it is log-normal [73]. Consequently, the achievable secrecy rate may differ from that achieved in wireless channels, usually affected by uncorrelated Rayleigh fading, as it has been shown in Section 9.3.3 for the NB case. The impact of these effects is evaluated providing a channel model, which enables the generation of channel responses that are statistically equivalent to the channel measurements. To this end, the first step is to compute the statistical parameters and the relationships exhibited by the experimental measurements. Then, the simulated channels are generated accordingly, providing a comparison, in terms of secrecy rate, under different channel distributions and properties assumptions. The gains provided by the optimal power allocation w.r.t. uniform power allocation are also discussed.

System Assumptions

The evaluation is performed relying on the 1266 in-home experimental channel measures carried out in the measurement campaign presented in [129]. The considered frequency range is 2–28 MHz, which is compliant with the HPAV standard specifications [29]. Furthermore, it should be noted that, typically, PLC systems transmit with a uniform PSD of -50 dBm/Hz and are affected by a noise PSD with a floor of -130 dBm/Hz. Hence, a SNR of 80 dB has been assumed for the secrecy rate computation, without taking into account the channel attenuation. Moreover, PLC networks are often subjected to a composition of Gaussian and impulsive noise. Nevertheless, since we are interested in evaluating the effects introduced by the channel response only, AWGN is assumed in our analysis, as often done in PLC works. Obviously, multicarrier transmission is assumed, with optimal power allocation and under a total power constraint.

The secrecy rate achieved by the channel measurements is compared to that of the numerically simulated channel realizations, generated taking into account different channel effects, as follows.

1. *Independent channels*: the main and the wiretapper channels are independently generated with a log-normal distribution.

2. *Keyhole effect*: three independent log-normal channel realizations are generated for the Alice's, Bob's and Eve's channels, i.e. h_A, h_B and h_E, respectively (see Figure 9.3c). The parameters are imposed so that the mean and variance of the main and wiretapper channels, given by the cascade of the corresponding channels, turn out to be equivalent to those of the channel measurements. This is made possible by exploiting the properties of the product of log-normal variables.

3. *MU correlation*: in this case, the main and wiretapper channels are generated with a log-normal distribution, according to the measured correlation coefficient $|\psi_{tx}(f)|$ discussed in Section 3.4. This is done since h_M and h_W actually share the same

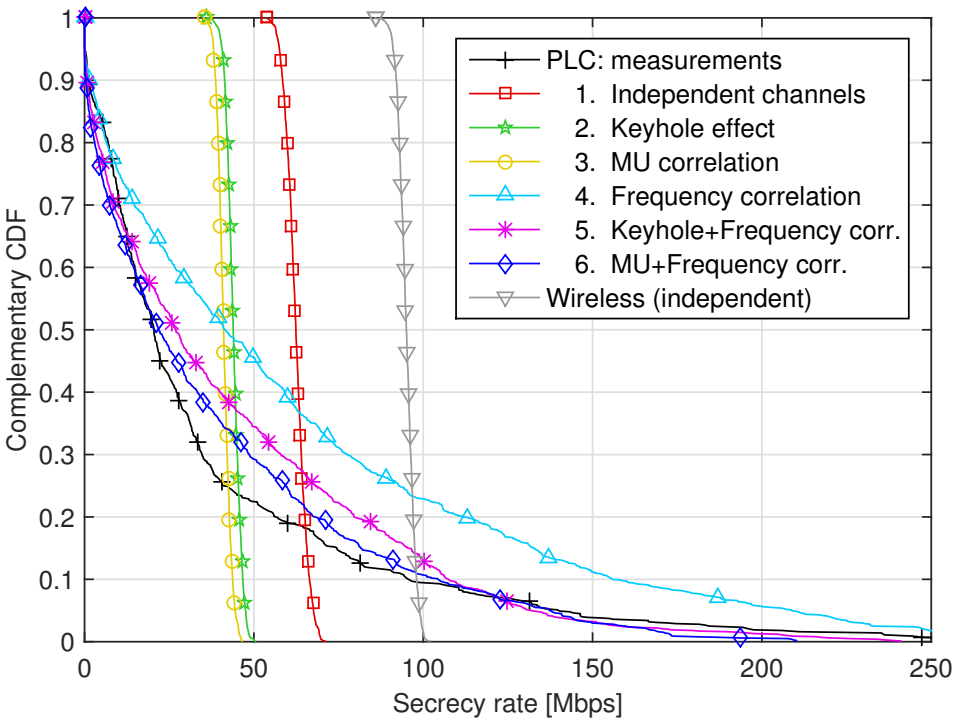

Figure 9.7: Secrecy rate C-CDF comparison among measurements and simulated realizations, assuming different phenomena. The secrecy rate for wireless independent channels is also depicted.

transmitter and belong to the same network. The frequency correlation is not considered.

4. *Frequency correlation*: the log-normally generated channels exhibit the same frequency correlation of the measured channels, analyzed in Section 3.2.4, but not considering the MU correlation among main and wiretapper channel.

5. *Keyhole effect and frequency correlation*: the same procedure as in step 2 is applied to the frequency correlated channels. Thus, the frequency correlation and the keyhole effect are jointly considered.

6. *MU and frequency correlation*: the generated channel realizations are affected by both frequency and MU correlation, between the main and the wiretapper channels, as actually happens in real PLC networks.

According to the power allocation solution provided in (9.12), the secrecy rate has been computed for all the above listed channel categories, as well as for the channel measurements. The comparison is depicted in Figure 9.7 in terms of C-CDF. It can be seen as the C-CDF for the measured channels completely differs from that of the independent log-normally distributed channels, in both trend and average secrecy rate, summarized in Table 9.1. Also when considering the keyhole effect (case 2) or the MU correlation (case 3) alone, the trend does not change, although there is an average secrecy

Table 9.1: Average secrecy rate for different simulated PLC channel phenomena.

Scenario	Channel type	R_S (Mbps)
Wireless	Independent	95.0
PLC	Independent	62.5
PLC	Keyhole effect	44.0
PLC	MU correlation	41.1
PLC	Frequency correlation	62.9
PLC	Keyhole & frequency corr.	43.7
PLC	MU & frequency corr.	38.9
PLC	Measurements	37.4

rate reduction. When frequency correlation is considered (case 4) the simulated C-CDF trend becomes more similar to the experimental one. Moreover, it closely approaches the measurements C-CDF when also the keyhole effect (case 5) or the MU correlation (case 6) are taken into account. The agreement can also be noted looking at the average secrecy rates, listed in Table 9.1, for all the above listed channels cases.

This analysis demonstrates that the channel statistics, together with the frequency and MU correlation, constrain and limit the PLC channel performance. Interestingly, it has been found that the secrecy rate C-CDF of the experimental channels, depicted in Figure 9.7, is well fitted by an exponential function given by $q = e^{-\delta x}$, where the average secrecy rate satisfies $E[R_S] = 1/\delta$, with $\delta = 0.0252$ $(\text{Mbps})^{-1}$. As a final remark, the results in Figure 9.7 validate the numerical model adopted for the channel generation.

Wireless versus PLC Performance

As done for the NB SISO system in Section 9.3.3, a comparison with the wireless case, within the multicarrier context, is also performed in terms of achievable secrecy rate. As known, differently from PLC channels, wireless links typically exhibit Rayleigh fading and are often independently faded. Thus, a Rayleigh fading channel is also considered, where $h_{M,m}$ and $h_{W,m}$ are assumed as zero mean proper complex Gaussian random variables. Hence, as before, the power gains $\beta_{M,m}$ and $\beta_{W,m}$ are exponentially distributed. In order to perform a fair comparison, the exponential distribution parameters are chosen so that the wireless channel gains show the same mean and variance of the independent PLC channel gains. Furthermore, as above specified, an equal SNR of 80 dB, without considering the channel attenuation, is assumed for both scenarios.

The secrecy rate achieved by the simulated wireless channels, generated so that they are statistically equivalent to the independent PLC channels, is also depicted in Figure 9.7. It can be noted as the log-normally distributed PLC channels always achieve a lower secrecy rate than the Rayleigh distributed wireless channels. If, in addition, the typical PLC channel phenomena are taken into account, such as the MU and frequency correlation, the secrecy rate diminishes further. The difference is noticeable looking at

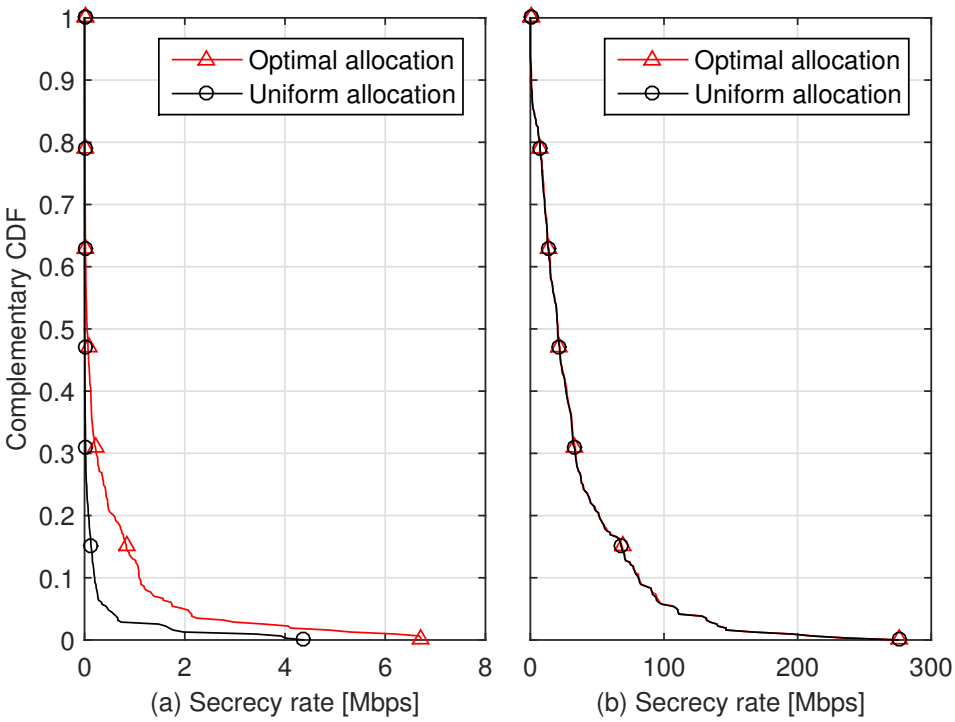

Figure 9.8: Comparison between optimal and uniform power allocation strategies, in terms of secrecy rate distribution, at a SNR equal to 0 dB (a) or 80 dB (b).

the measurements C-CDF trend in Figure 9.7 and also in terms of the average secrecy rate displayed in Table 9.1.

Optimal and Uniform Power Allocation

This final part of this section discusses the secrecy rate achieved in multicarrier BB-PLC channels comparing uniform and optimal power allocation strategies. Uniform power allocation involves the allocation of the same power across the used sub-channels, i.e., where the main channel gain is greater than the wiretapper gain, namely $\beta_{M,m} > \beta_{W,m}$. Uniform power allocation is what is done, for instance, in the HPAV specifications. In order to make a fair comparison, the total power constraint for the optimal power allocation, evaluated according to (9.12), equals the sum of the PSD values, i.e. -50 dBm/Hz for HPAV, over the set of used sub-channels.

A comparison between optimal and uniform power allocation strategies, in terms of secrecy rate C-CDF and for a SNR equal to 0 dB, is depicted in Figure 9.8a. An upwards shift can be observed for the secrecy rate C-CDF with optimal power allocation w.r.t. uniform power allocation. On the contrary, when the SNR equals 80 dB, as in Figure 9.8b, optimal and uniform power allocation strategies are almost equal, in terms of secrecy rate distribution. This is due to the fact that the SNR is so large that the differences among the channel gains are negligible, compared to the available power per sub-channel. It follows, that optimal power allocation can provide gains in bad channel environments.

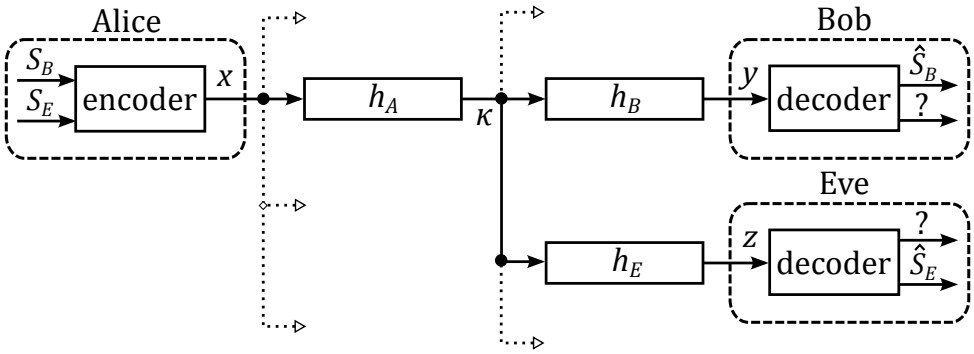

Figure 9.9: Broadcast channel basic model for two users.

9.5 MU Broadcast Scenario

The results provided in Section 9.4 can be extended to the MU down-link case. In particular, in a general broadcast channel, Alice wants to send N_U different confidential messages to N_U distinct receivers (users). As usual, the underlying network structure consists of a tree structured topology, as represented in Figure 9.1. For simplicity, a two users (receivers) system is considered, as depicted in Figure 9.9. In detail, Alice encodes the secret messages to Bob (S_B) and Eve (S_E) in a single transmitted signal x. Bob and Eve receive the signals y and z, respectively, and they are able to decode only their intended message. The dashed arrows in the scheme represent the possible presence of additional links in the considered network.

Assuming a multicarrier system with M parallel sub-channels, the system model is equivalent to the model in (9.8), but, in this case, Bob and Eve can eavesdrop each other. All the assumptions listed in Section 9.4.1 still hold, but the constraint on the total transmitted power translates into

$$\sum_{m=1}^{M} (P_{B,m} + P_{E,m}) \leq P_T, \tag{9.13}$$

where $P_{B,m}$ and $P_{E,m}$ are the powers allocated by Alice for the transmission to Bob and Eve on the m-th sub-channel, respectively.

9.5.1 Optimization Problem Formulation

In the system configuration above described, the achievable secrecy rate for the transmission to Bob and Eve is the sum of the secrecy rates over all the available sub-channels

and is given by

$$\begin{aligned} R_{S,B}(\mathbf{P}_B, \mathbf{P}_E) &= B \sum_{m=1}^{M} \left[\log_2 \left(1 + \frac{\beta_{M,m} P_{B,m}}{\sigma^2 + \beta_{M,m} P_{E,m}} \right) - \log_2 \left(1 + \frac{\beta_{W,m} P_{B,m}}{\sigma^2} \right) \right]^+, \\ R_{S,E}(\mathbf{P}_B, \mathbf{P}_E) &= B \sum_{m=1}^{M} \left[\log_2 \left(1 + \frac{\beta_{W,m} P_{E,m}}{\sigma^2 + \beta_{W,m} P_{B,m}} \right) - \log_2 \left(1 + \frac{\beta_{M,m} P_{E,m}}{\sigma^2} \right) \right]^+. \end{aligned} \tag{9.14}$$

This is a worst case assumption, in terms of secrecy, since we assume that the wiretapper, Eve or Bob, respectively, performs successive interference cancellation (SIC) [167]. Thus, the hostile user detects his own data, afterwards he subtracts it from the received signal and tries to decode the message intended to the other user.

In the following, the goal is to maximize the sum of the individual secrecy rates, named sum secrecy rate, which is given by

$$R_S^{sum}(\mathbf{P}_B, \mathbf{P}_E) = R_{S,B}(\mathbf{P}_B, \mathbf{P}_E) + R_{S,E}(\mathbf{P}_B, \mathbf{P}_E), \tag{9.15}$$

where $R_{S,B}$ and $R_{S,E}$ are the secrecy rates from Alice to Bob and from Alice to Eve, respectively. The powers allocated on the sub-channels to Bob and Eve are collected in the vectors $\mathbf{P}_B = [P_{B,1}, \ldots, P_{B,M}]$ and $\mathbf{P}_E = [P_{E,1}, \ldots, P_{E,M}]$, respectively. Since, in this case, there is more than one user, the secrecy rate becomes a secrecy rate region.

The corresponding optimization problem is given by

$$\max_{\mathbf{P}_B, \mathbf{P}_E} R_S^{sum}(\mathbf{P}_B, \mathbf{P}_E) \text{ subject to } \begin{cases} \sum\limits_{m=1}^{M} (P_{B,m} + P_{E,m}) \leq P_T, \\ P_{B,m} \geq 0, \\ P_{E,m} \geq 0. \end{cases} \tag{9.16}$$

It was shown in [177] that the optimal solution is to support only the best user per considered sub-channel. Thus, the sub-channel power allocation strategy $P_{t,m} = P_{B,m} + P_{E,m}$ becomes

$$P_{t,m} = \begin{cases} P_{B,m} & \text{if } \beta_{M,m} > \beta_{W,m}, \\ P_{E,m} & \text{if } \beta_{M,m} < \beta_{W,m}. \end{cases} \tag{9.17}$$

The case $\beta_{M,m} = \beta_{W,m}$ is neglected since we assume a continuous distribution for the channel power gain coefficients in fading scenarios, thus, $\Pr[\beta_{M,m} = \beta_{W,m}] = 0$. The optimal power allocation that solves the optimization problem in (9.16) can be derived from the formulation in (9.12) by replacing $(\beta_{M,m} - \beta_{W,m})$ with the quantity $(\max(\beta_{M,m}, \beta_{W,m}) - \min(\beta_{M,m}, \beta_{W,m}))$.

The optimization problem in (9.16) can be extended to the optimization of the weighted sum secrecy rate defined as [179]

$$R_S^{wgh}(\mathbf{P}_B, \mathbf{P}_E, \eta) = \eta R_{S,B}(\mathbf{P}_B, \mathbf{P}_E) + (1 - \eta) R_{S,E}(\mathbf{P}_B, \mathbf{P}_E), \tag{9.18}$$

where the variable $0 \leq \eta \leq 1$ can guarantee a certain QoS to the users. The optimal power allocation for this optimization problem reads as follows

$$P_{t,m} = \begin{cases} \left[\sqrt{\left(\frac{\sigma^2(\beta_{M,m}-\beta_{W,m})}{2\beta_{M,m}\beta_{W,m}} \right)^2 + \frac{\eta}{\lambda \ln 2} \frac{\sigma^2(\beta_{M,m}-\beta_{W,m})}{\beta_{M,m}\beta_{W,m}}} - \frac{\sigma^2(\beta_{M,m}+\beta_{W,m})}{2\beta_{M,m}\beta_{W,m}} \right]^+ \\ \qquad\qquad \text{if } \beta_{M,m} > \beta_{W,m}, \\ \left[\sqrt{\left(\frac{\sigma^2(\beta_{W,m}-\beta_{M,m})}{2\beta_{M,m}\beta_{W,m}} \right)^2 + \frac{1-\eta}{\lambda \ln 2} \frac{\sigma^2(\beta_{W,m}-\beta_{M,m})}{\beta_{M,m}\beta_{W,m}}} - \frac{\sigma^2(\beta_{M,m}+\beta_{W,m})}{2\beta_{M,m}\beta_{W,m}} \right]^+ \\ \qquad\qquad \text{if } \beta_{M,m} < \beta_{W,m}. \end{cases} \tag{9.19}$$

It can be noted that the optimal power allocation is basically the same computed in (9.12), but the power is assigned to a user or to another depending on the m-th sub-channel realization and on the QoS parameter η.

9.5.2 MU System Performance

In this section, the performance of the two users PLC system, described in Section 9.5, are assessed in terms of achievable secrecy rate region. The effects of frequency and MU correlation on the secrecy rate region, obtained with an exhaustive search, are depicted in Figure 9.10a, while the average secrecy rate under a QoS constraint is represented in Figure 9.10b. Optimal power allocation, under a total power constraint and a SNR equal to 80 dB, as defined in Section 9.4.3, are considered. The represented curves delimit the achievable region, obtained by interconnecting the outermost secrecy rate points jointly achieved by the pair of links from Alice to Bob and from Alice to Eve, evaluated as discussed in Section 9.5.1. Thus, the depicted lines represent an upper bound for the secrecy rate region.

When independent and log-normally distributed channels are assumed, the uncorrelated nature of the channels, from Alice to Bob and from Alice to Eve, is such that the rates are almost equal between the two links. Thus, the upper bound has a convex trend (curve with cross markers). Instead, the secrecy rate region for the experimental channels (curve with circles), as well as for the channels affected by correlation (curve with stars), is confined along the axes, with many rate pairs in the middle low rate region (among the axes). This property gives to the region bound a concave, or hyperbolic, trend. This behavior is due to the detrimental effects of the frequency and MU correlation. In fact, there is a good matching between these two secrecy region bounds (curves with circles and stars). The correlation implies that the Bob's and Eve's channels have nearly the same gain, thus a small secrecy rate is achieved. A high secrecy rate is achievable only when the channels are highly unbalanced. This is the reason why the large rate values are concentrated along the axes. The few points exceeding the independent channels re-

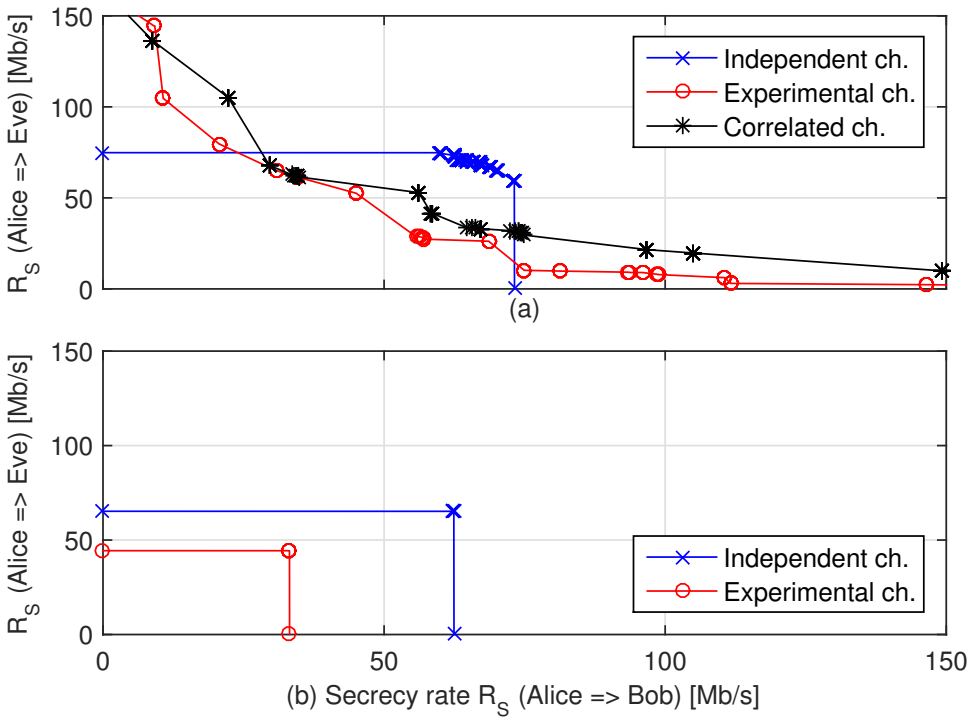

Figure 9.10: Secrecy rate region (a) and average secrecy rate under a QoS constraint (b) for the two users multicarrier broadcast channel. Experimental and independent channels are compared. The secrecy rate region for channels affected by MU and frequency correlation is also shown in (a).

gion bound (crosses) are due to the tails of the secrecy rate C-CDF (beyond 70 Mbps), depicted in Figure 9.7.

The average secrecy rate pair, averaged over the channel realizations, under a QoS constraint (for $0 \leq \eta \leq 1$), as discussed in Section 9.5.1, is depicted in Figure 9.10b. As expected, the independent channels outperform the experimental ones, affected by frequency and MU correlation. Such a high SNR, which equals 80 dB, involves the rate pairs to lay on a rectangle, due to the secrecy rate upper bound discussed in Section 9.4.2. Instead, low SNR values lead to rate pairs laying on a convex curved line.

9.6 MIMO Transmission Scheme

The limits on the secrecy rate, due to the PLC channel phenomena and to the underlying network structure before detailed, can be mitigated exploiting the spatial domain and extending the used bandwidth. The performance improvements provided by the MIMO transmission scheme with an additional receiving mode, namely the CM, by the bandwidth extension up to 86 MHz and by a novel AO approach, are herein assessed. It has already been proved in [168] that MIMO transmission can increase PLS performance on PLC networks. However, the work considers numerically generated channels, with two transmitting and receiving modes, in the 2–28 MHz frequency band and under AWGN.

In this section, the analysis is further extended relying on real channel and noise PSD measurements. As specified by the HPAV2 [39], the 2–86 MHz bandwidth is considered, and the maximum number of possible transmitting and receiving modes are exploited. As described in Section 4.1.1, two Δ-style modes can be exploited at the same time at the transmitter, while four star-style modes can be used at the receiver side. Thus, a 2×4 MIMO transmission scheme can be implemented between the transmitter and the receiver outlet. These assumptions provide actual performance results, that can be viewed as a target for future devices development.

9.6.1 Alternating Optimization Algorithm

The secrecy rate maximization belongs to the family of non-convex optimization problems, which are non-trivial and not easily solvable. This is because the secrecy capacity is obtained by the maximization of the difference of two convex terms, as shown in (9.2). The optimization problem becomes even more difficult when considering MIMO wiretap channels, with one or multiple eavesdroppers. Anyway, to provide a solution, an AO approach has been proposed in [180]. The secrecy capacity optimization problem has been reformulated with an equivalent expression, which can be brought back to two convex optimization problems, alternatively solved, as briefly described in the following.

For each used sub-channel m, the secrecy rate maximization in (9.11) can be reformulated for the MIMO transmission scheme as follows

$$\begin{aligned} \mathcal{C}_S = \max_{\mathbf{K}} \left[\log_2 \left| \mathbf{I} + \mathbf{H}_M^{\dagger} \mathbf{K} \mathbf{H}_M \right| - \log_2 \left| \mathbf{I} + \mathbf{H}_W^{\dagger} \mathbf{K} \mathbf{H}_W \right| \right], \\ \text{subject to } \ \mathrm{Tr}(\mathbf{K}) \leq P_{t,m}, \ \mathbf{K} \succeq 0, \end{aligned} \tag{9.20}$$

where $\mathbf{K}$ is the covariance matrix of the transmitted signal x, while $\mathbf{H}_M$ and $\mathbf{H}_W$ represent the main and wiretapper MIMO channel matrices, respectively. Furthermore, $P_{t,m}$ is the PSD constraint on the m-carrier, whereas $\mathbf{K} \succeq 0$ means that $\mathbf{K}$ must be positive semidefinite. The identity matrix is represented as $\mathbf{I}$. The optimization problem in (9.20) is properly reformulated exploiting the following lemma [181].

Lemma 1. *Let $\mathbf{E} \in \mathbb{C}$ be any $N \times N$ positive definite matrix ($\mathbf{E} \succ 0$). Consider the function $f(\mathbf{S}) = -\mathrm{Tr}(\mathbf{SE}) + \log_2 |\mathbf{S}| + \mathbf{N}$, then*

$$\log_2 |\mathbf{E}^{-1}| = \max_{\mathbf{S} \succeq 0} f(\mathbf{S}). \tag{9.21}$$

The optimal solution to the right-hand side of (9.21) is $\mathbf{S}^* = \mathbf{E}^{-1}$.

Hence, applying Lemma 1 via setting $\mathbf{E} = \mathbf{I} + \mathbf{H}_W^{\dagger} \mathbf{K} \mathbf{H}_W$, the problem in (9.20) can

be reformulated as

$$\max_{\mathbf{K},\mathbf{S}} \left[\log_2 |\mathbf{I} + \mathbf{H}_M^\dagger \mathbf{K} \mathbf{H}_M| - \mathrm{Tr}\left(\mathbf{S}(\mathbf{I} + \mathbf{H}_W^\dagger \mathbf{K} \mathbf{H}_W)\right) + \log_2 |\mathbf{S}|\right], \quad \text{subject to } \mathrm{Tr}(\mathbf{K}) \leq P_{t,m},\ \mathbf{K} \succeq 0,\ \mathbf{S} \succeq 0, \tag{9.22}$$

where $\mathbf{S}$ denotes a Hermitian positive semidefinite matrix. For simplicity, the constant $\mathbf{N}$ has been dropped. The problem in (9.22) is still non-convex w.r.t. both $\mathbf{K}$ and $\mathbf{S}$. However, it can be verified that the problem is convex w.r.t. either $\mathbf{K}$ or $\mathbf{S}$, fixing the other decision variable. This property motivated the use of an AO approach. Defined $\mathbf{K}^n$ and $\mathbf{S}^n$ as the solutions for the n-th iteration, the following two optimization problems are alternatively solved. In practice, they read as

$$\mathbf{S}^n = \arg\max_{\mathbf{S} \succeq \mathbf{0}} \left[\log_2 |\mathbf{S}| - \mathrm{Tr}\left(\mathbf{S}(\mathbf{I} + \mathbf{H}_W^\dagger \mathbf{K}^{n-1} \mathbf{H}_W)\right)\right], \tag{9.23}$$

$$\mathbf{W}^n = \arg\max_{\mathbf{W}} \left[\log_2 |\mathbf{I} + \mathbf{H}_M^\dagger \mathbf{K} \mathbf{H}_M| - \mathrm{Tr}(\mathbf{H}_W^\dagger \mathbf{S}^n \mathbf{H}_\mathbf{W} \mathbf{K})\right], \quad \text{subject to } \mathrm{Tr}(\mathbf{K}) \leq P_{t,m},\ \mathbf{K} \succeq 0. \tag{9.24}$$

As mentioned, both the problems (9.23) and (9.24) are convex and can be alternatively solved, as done by the AO algorithm. The solution is guaranteed to converge at a KKT point. For further details the reader is referred to [180]. However, the solution reported in [180] assumes AWGN. Herein, it is extended to the more complicated and realistic colored and correlated Gaussian noise scenario. A non-uniform power allocation solution is found. The results rely on real channel and noise assumptions.

9.6.2 Results for the MIMO Scenario

The focus is on the MIMO wiretap channel. The transmitter exploits the two Δ-style transmitting modes, while both Bob and Eve use all the four star-style receiving modes. The performance are evaluated exploiting the 353 MIMO channel measurements carried out through an experimental measurement campaign across Europe and collected by the ETSI STF-410 [78]. The considered frequency range is 2–86 MHz and the PSD constraint at the transmitter is -50 dBm/Hz in the 2–30 MHz, while -80 dBm/Hz in the 30–86 MHz, according to the latest HPAV2 standard [39]. Moreover, an AWGN and a colored and correlated Gaussian background noise profiles are considered. For the colored noise assumption, the exponential profile is taken from the STF-410 noise PSD measurements, while the spatial correlation is implemented between the modes as discussed in Section 4.2. The white noise, instead, has been generated so that it exhibits a total power equivalent to the colored one, in the considered bandwidth. The MIMO channel measurements are equally divided and assigned to the intended receiver and to eavesdropper, respectively.

Under the above system specifications, the secrecy rate achieved by the 2×4 MIMO

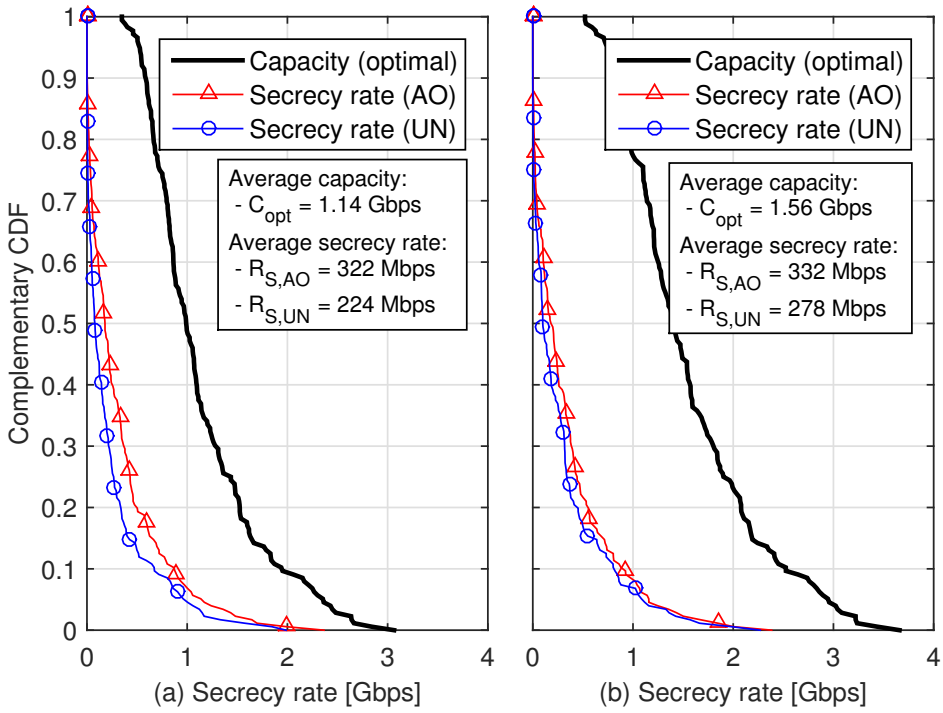

Figure 9.11: Secrecy rate C-CDF for uniform and AO approach power allocation strategies, under AWGN (a) or colored and correlated (b) Gaussian background noise. The channel capacity is also depicted.

wiretap channel is evaluated and depicted in Figure 9.11. As a term of comparison, two different noise models are taken into account, white and independent in Figure 9.11a, while colored and correlated in Figure 9.11b. Furthermore, the performance achieved with the allocation strategy provided by the AO algorithm are compared to those achieved under uniform power allocation, labeled AO and UN, respectively). The comparison is made in terms of secrecy rate C-CDF.

It can be noted as the AO algorithm translates into a performance improvement, for both the considered background noise models. This is even more evident looking at the average secrecy rate displayed in the boxes. In practice, an increase of about 30 % and 20 % has been noticed for the AWGN and the colored and correlated noise, respectively. When considering colored and correlated noise, the performance increases further. This happens, since, the noise correlation makes easier its cancellation at the receiver side. As a further term of comparison, the channel capacity, achieved without any secrecy constraint, is also computed and depicted in Figure 9.11. It can be noted as its average value is almost four times higher than the average secrecy rate. This consideration gives the idea on the cost in granting and providing secrecy and confidentiality, in terms of PLS performance.

Table 9.2: Average secrecy rate comparison for different transmission schemes, frequency ranges, power allocation strategies and background noise profiles. Two distinct databases are considered.

Scheme	Band (MHz)	Noise	Power allocation	Measurements database	R_S (Mbps)
SISO	2–28	AWGN	Optimal	In-home (Tx)	37.4
SISO	2–28	AWGN	Uniform	In-home	52.8
SISO	2–28	AWGN	Uniform	ETSI	62.9
MIMO	2–28	AWGN	Uniform	ETSI	90.4
MIMO	2–86	Measured	AO	ETSI	332

9.7 Overall Comparison

A comparison between the SISO and MIMO systems is reported in this section. The average secrecy rate, averaged over the channel realizations, for the two transmission schemes and for different frequency ranges and background noise models, is summarized in Table 9.2. As a term of comparison, both the in-home SISO channels discussed in Section 9.4.3 (identified by 'In-home'), and the ETSI MIMO measurements described in Section 9.6.2, are considered. Moreover, various power allocation strategies are assumed.

The results in Table 9.2 show that, when considering the 2–28 MHz frequency range and the keyhole effect, hence, when the main and the wiretapper channels share the same transmitting plug (listed as 'In-home (Tx)'), the average secrecy rate for the SISO scheme is not very high. This, even though the optimization problem is subject to a total power constraint, as detailed in Section 9.4.2. However, the SISO channel performance for the in-home scenario ('In-home') almost doubles when considering the entire measurements database, regardless of the transmitting plug. Indeed, with this choice, the channels used in the simulation are more uncorrelated. For comparison purposes, in this case, a uniform power constraint, equal to the HPAV PSD limit, is considered. However, this assumption does not significantly affect the achievable performance, as detailed in Section 9.4.3.

Then, the ETSI MIMO measurements are considered, under the same uniform power constraint and AWGN. Focusing on the reduced 2–28 MHz frequency range and converting the 2×4 Δ-style to star-style MIMO scheme into a Δ-style to Δ-style SISO channel, it can be seen as the average secrecy rate is only slightly higher, if compared to that achieved on the whole database of the in-home SISO measurement campaign ('In-home'), discussed in [129]. Thus, the two different scenarios can be compared. If the spatial dimension is exploited, through MIMO transmission, the performance increases further. Moreover, the bandwidth extension up to 86 MHz, the real background noise assumption, together with the AO algorithm, provide a drastic increase in the achievable secrecy rate. It can be concluded that the keyhole effect significantly limits the achievable secrecy rate. However, the performance improves through MIMO transmission, bandwidth extension,

real noise assumption and non uniform power allocation.

9.8 Main Findings

The PLS concept has been introduced within the wiretap channel scenario. All the analysis have been performed assuming a perfect CSI knowledge. Thus, the eavesdropper is seen as another non-intended user of the same network. Some results, obtained in the wireless communication context, have been presented and applied to the PLC context, starting from the NB single carrier channel. The upper bound on the secrecy capacity, due to its formulation, has been assessed and compared to the channel capacity, which can be obtained without any secrecy constraint. Then, the secrecy rate for both wireless and PLC scenarios has been computed, highlighting that, in PLC networks, the channel fading is not Rayleigh distributed, rather it is log-normal. As a consequence, it has been shown as the average secrecy rate for the PLC channel, under AWGN and with an average power constraint, is outperformed by that attainable on wireless channels. Furthermore, the proposed modeling strategy has been validated through experimental measurements.

Afterwards, the multicarrier SISO transmission scheme is considered, extending the results of the NB system. It has been shown that PLS over PLC is possible, although constrained by the channel properties, as well as by the network topology. Indeed, the typical tree-structured PLC network topology gives rise to what is known as keyhole effect, which causes MU correlation and rank deficiency. As it has been shown, these effects, together with the channel statistics, limit the PLS performance. The results confirm that PLC channels exhibit log-normal fading with frequency correlation, due to coupling, cross-talk and MU correlation, mainly caused by the underlying network structure. Depending on the prominence of these detrimental effects, the secrecy rate can diminish further. Also in this case, it has been shown as wireless outperforms PLC communication. Moreover, optimal and uniform power allocation strategies have been compared under a total power constraint. The results suggest that the optimal power allocation can lead to a performance improvement in low SNR scenarios.

Also the secrecy rate region, when considering a MU broadcast channel, has been studied. Simulation results have shown that the secrecy rate region bound has a shape that completely changes if independent channels (convex trend), or correlated channels (concave trend) agreeing with the experimental measures, are considered. The hyperbolic trend degenerates into two straight lines, corresponding to the axes, when strongly correlated channels and low SNR values are experienced. This shows that, in some situations, the PLC channels can be detrimental in terms of achievable secrecy rate.

Finally, although it has been demonstrated as the PLC channel represents a challenging communication scenario, the performance can be improved through the exploitation of the spatial dimension, via the use of MIMO transmission, extending the transmission

band 2–28 MHz to 2–86 MHz, and exploiting the power allocation provided by the AO algorithm. The performance improve further when colored and spatially correlated background noise is considered. The results have been obtained exploiting channel and noise PSD measurements. Therefore, they are of practical and scientific relevance, providing an indication of the maximum level of security that can be guaranteed, in terms of secrecy rate, when advanced physical layer mechanisms are considered.

10 Conclusions

In this thesis, the data transmission over the power delivery infrastructure, known as PLC, has been discussed. In particular, a thoroughly and comprehensive channel characterization has been performed. The collected results and the highlighted properties have been exploited in order to provide an effective and extremely synthetic channel model. Essentially, the work has been primarily divided into three main parts.

The initial and most important part deals with the PLC channel characterization, considering different environments. The well-known and widely investigated in-home SISO scenario has been considered first. The aim has been to provide a unique and worldwide valid procedure for the transmission medium analysis, thus, avoiding the crowd of different and hardly comparable solutions previously adopted in the literature. Then, the extended in-home MIMO transmission scheme has been considered, assessing both MIMO channel and noise properties. Not only the domestic environment, but also the vehicular communication scenario has been faced, focusing on the in-car and in-ship scenarios. Concerning the in-car PLC, two distinct application contexts have been considered, i.e. a compact electric car and a conventional fuel car. While, a large cruise ship has been accounted for the in-ship PLC context. Last, but not least, also the communication over the power distribution networks, namely the outdoor scenario, has been discussed, especially within the smart grid context. The study has compared both LV and MV lines in either the NB and BB spectra in order to highlight strengths and weaknesses, arguing which one is the more suitable solution for a worldwide PLC implementation. A final overall comparison among all the considered PLC context has been performed.

The second part of the work is based on the detailed channel characterization that has been carried out in the first part. In particular, the different propagation phenomena, the implicit relationships, as well as the dependencies on the underlying network structure, have been taken into account and exploited in order to the develop an extremely simple and effective channel model, better than the existing ones. The validity and the significance of the proposed modeling strategy has been proved through experimental

evidence.

Finally, the last part of the thesis extends the concept of reliable and high data rate communication, considering a further security constraint. The well-known PLS results within the wireless context have been applied and customized for the PLC scenario. The achievable performance, under the strict secrecy constraints, have been evaluated for a NB communication channel, a multicarrier SISO system, a MU broadcast scenario and a MIMO transmission scheme. In particular, it has been demonstrated as the more common channel capacity outperforms the secrecy capacity, highlighting how the typical PLC channel properties and propagation phenomena further affect and limit the achievable performance under secrecy constraints.

In the following, the main findings and the research activity results discussed within this thesis are recalled and separately reported for each corresponding chapter.

In-Home Scenario

A statistical characterization of the in-home PLC channel has been presented, bringing new insights on the channel behavior and confirming some prior results presented in the literature. The aim has been to allow a precise comparison between the results of this analysis and those from other measurement campaigns, providing common processing procedures and analytic formulations intended to be used for the analysis of the results of future measurement campaigns. Furthermore, a detailed statistical analysis of the PLC channel has been carried out in the 1.8–100 MHz band, showing that, typically, the CFR is log-normally distributed and affected by severe frequency selectivity. The log-normality applies also to the RMS-DS and ACG metrics. The most commonly used statistical metrics have also been compared, highlighting the corresponding relationships and providing the analytic parameters of the best fit of such relations. The coverage offered by PLC systems, similarly to the wireless scenario, and the performance improvements due to the bandwidth extension, have also been inferred in terms of capacity.

The correlation among channels that share, or not, the same transmitting or receiving plug within the same site, has been analyzed. It has been shown as, negligible correlation is exhibited by the overall ensemble of channels, while a pronounced level is experimented for the channels associated to the same transmitter or receiver. Even larger correlation has been found if the study is limited to the amplitude of the CFR, proving that the channel phase randomness can significantly reduces the MU correlation. Finally, the line impedance has been discussed, showing that it can assume a broad set of values and that high probability regions can be identified when it is related to the CFR.

MIMO Extension

A characterization of the MIMO PLC channel has been discussed, assessing the statistical properties and the degree of correlation exhibited by the MIMO channels, when consid-

ering all the possible star-style receiving mode pairs and the same transmitting mode. A detailed procedure for the MIMO noise covariance matrix computation, basing on noise measurements, has also been discussed.

The availability of both the MIMO channel measurements and the colored and correlated noise covariance matrix have enabled the capacity evaluation, providing significant results on the performance achievable on a real PLC scenario. In particular, two coding schemes have been discussed, considering both full or no CSI knowledge at the transmitter and providing the corresponding optimal allocation. The simulation results have shown that the CSI knowledge translates into a significant increase in performance only for bad channel realizations and low SNR values. For a high SNR, the uniform allocation strategy is optimal and no CSI feedback is required. Furthermore, the exploitation of all the possible transmit and receive ports, namely 2×4 in the considered case, outperforms any other SISO or SIMO coding scheme. In particular, the 2×4 MIMO experimental channels achieve a capacity that almost doubles that of a conventional SISO scheme.

In-Vehicle Scenario

The PLC channel and noise properties within the vehicular environment have been discussed. Two different contexts have been taken into account, namely the in-car scenario, with focus on the electric car, and the in-ship scenario. The measurements analysis has shown that, although the in-car network has a compact size, the PLC channel is affected by frequency selective fading and high attenuation. Moreover, the background noise of the EC has been deeply investigated, showing a prominent and severe influence at low frequencies, especially where NB-PLC operates, primarily due to the DC-DC converter switching activity and to the electric drives for the motors.

Contrariwise, the in-ship channels exhibit, on average, less attenuation thanks to fewer discontinuities and to better quality cables, despite the length. Furthermore, the measurements and the literature have shown that the in-ship scenario exhibits a noise PSD with a floor ranging from -95 to -145 dBm/Hz in the 1.8–50 MHz. Moreover, the presence of a three-phase distribution network allows the usage of MIMO transmission techniques that have the potentiality of almost doubling the channel capacity, as it has been shown.

It has been proven that, on an experimental basis, in both the assessed scenarios the PLC technique has the potentiality to offer high-speed data connectivity, despite the different nature of the underlying network structure and background noise properties. A comparison with the measurements concerning a conventional fuel car and with the most common in-home scenario has also been performed, highlighting differences and similarities.

Outdoor Scenario

The PLC technology implementation as a key strategy to deliver bi-directional connectivity in the power delivery network, enabling the use of several smart grid applications, has been assessed. The market offers a choice of engineered solutions that are compliant with the NB-FS (3–500 kHz) or the BB-FS (1.8–100 MHz) that have both been considered. Although these technologies are mature and ready for mass deployment, it is also true that these techniques have to evolve in order to be able to offer increased levels of performance w.r.t. what is achieved today. In particular, the aim has been to investigate strengths and weaknesses of both the NB and BB transmission solutions, as the right approach for the evolution of current PLC technology. It is often said that most smart grid applications require low data rates and, therefore, NB-PLC is the right choice. However, BB-PLC offer higher flexibility and a better trade-off between data rate, latency, robustness, coverage and energy efficiency. Thus, it has been argued that adaptive, scalable and flexible solutions, which can smartly use the spectrum and operate in both the NB-FS and BB-FS, are the right approach for the evolution towards the future PLC technology.

Basing on experimental measurements, as well as on some results reported in the literature, it has been shown that the low frequency bands show a low channel attenuation, but a high noise and low line impedance values, which hamper the signal injection. These effects challenge the realization of robust PLC modems and line drivers conceived for the NB-FS. Contrariwise, the transmission in the BB-FS enjoys lower noise, much higher line impedance values and it offers frequency diversity. However, transmission at high frequencies may be challenged by radiation limits, especially in overhead conductors and by coexistence problems. Complexity is also another point to consider, where the associated requirements can be defined depending on the application and on costs. Furthermore, the overall system performance depends on layer 1, but also on layer 2, or eventually on layer 3, when routing mechanisms are considered. All these techniques concur to improve the communication systems and its efficiency. Overall, it is of paramount importance to design light protocols that allow fast responses and network configuration, especially in smart grids, where the network recovery has to be immediate in the event of faults and blackouts.

Scenarios Comparison

As known, the PLC has become a mature technology, finding application in many different scenarios, from in-home automation and networking, to smart grid applications, as well as to in-vehicle communications. All these several application environments are highly heterogeneous, each one having its own features and particularities. The purpose it has been to summarize and compare the results obtained for all the previously discussed PLC scenarios. It has been shown as the PLC networks represent a challenging commu-

nication environment, mainly due to the channel characteristics and statistical behavior, but also because of the detrimental effect of the noise. In fact, the channel and noise properties depend on the specific application scenario, as it has been discussed. However, similar relations and behaviors have been identified for the PLC channel characteristics, such as severe frequency selectivity and high attenuation. Moreover, high levels of noise are experimented, which usually shows an exponentially decreasing PSD profile along frequency.

Despite the existence of recently standardized NB and BB PLC systems, there exists space for their further evolution. A challenging aspect is the design of reliable communication techniques that can cope with the nasty channel and the detrimental noise effect. Nevertheless, it has been inferred that the capacity, under the Gaussian noise assumption, is high and similar among all the considered environments. This, motivates the development of capacity approaching schemes. All the information and the relationships that have been collected and highlighted allowed the development of new and effective channel models, able to better emulate a real PLC scenario.

Channel Modeling

A quick overview, concerning the main modeling strategies and approaches provided in the literature has been given, highlighting the main findings. The aim has been to provide an extremely synthetic top-down channel model for the MIMO PLC channel, a technology that has been already standardized and deployed, but not thoroughly modeled yet. Initially, the basic model idea has been discussed and then the modeling procedure has been tested on a real in-home MIMO PLC scenario. By exploiting the intrinsic peculiarities of these channel measurements, some further simplifications have been introduced and exploited during the generation process. Finally, the proposed model has been validated assessing the average value of the most commonly used statistical metrics, as well as through a performance comparison in terms of capacity distribution. As it has been confirmed by the results, the model is proposed as a simple and statistical representative emulator of a real PLC network, exhibiting a high flexibility degree, being suitable for different application contexts. This is made possible by changing the corresponding parameters and relationships assumptions, which are considered within the numerical generation process, according to the measurements database.

Beyond Capacity: Security

The PLS concept has been introduced within the wiretap channel scenario. All the analysis have been performed assuming a perfect CSI knowledge. Thus, the eavesdropper is seen as another non-intended user of the same network. Some results, obtained in the wireless communication context, have been presented and applied to the PLC context, starting from the NB single carrier channel. The upper bound on the secrecy capacity,

due to its formulation, has been assessed and compared to the channel capacity, which can be obtained without any secrecy constraint. Then, the secrecy rate for both wireless and PLC scenarios has been computed, highlighting that, in PLC networks, the channel fading is not Rayleigh distributed, rather it is log-normal. As a consequence, it has been shown as the average secrecy rate of the wireless channel outperforms that attainable by the PLC channel.

Afterwards, the multicarrier SISO transmission scheme is considered, showing that PLS over PLC is possible, although constrained by the channel properties, as well as by the network topology. The results confirm that PLC channels exhibit log-normal fading with frequency correlation, due to coupling, cross-talk and MU correlation, mainly caused by the underlying network structure, which gives rise to what is known as keyhole effect. Optimal and uniform power allocation strategies have also been compared, under a total power constraint, showing that the optimal allocation can lead to a performance improvement in low SNR scenarios. Furthermore, the secrecy rate region, when considering a MU broadcast channel, has been studied. The simulation results have shown that the secrecy rate region bound has a shape that completely changes if independent (ideal) channels, or experimental (correlated) measures, are considered, proving that, in some situations, the PLC channels can be detrimental in terms of achievable secrecy rate.

Finally, it has been demonstrated that the performance can be improved through the exploitation of the spatial dimension, via the use of MIMO transmission, extending the transmission band 2–28 MHz to 2–86 MHz, and exploiting the power allocation provided by the AO algorithm. The performance improve further when colored and spatially correlated background noise is considered. The results have been obtained exploiting channel and noise PSD measurements. Therefore, they are of practical and scientific relevance, providing an indication of the maximum level of security, in terms of secrecy rate, that can be guaranteed.

10.1 Final Remarks

PLC technology has become a fruitful technique that can provide a means of communication for a wide range of applications in several environments. There have been numerous standardization and development efforts, in both the NB and BB spectra, over recent decades and a regulatory work, scheduled by the research community, has addressed different challenges, making great advances on the use of the PLC channel, which was not initially designed for data communication.

In this thesis, the main contributions and results reported in in the literature have been reviewed for all the considered PLC systems. In particular, some standardization considerations, a detailed channel characterization and a simple and effective modeling procedure, as well as some physical and higher layer techniques designed to provide se-

crecy, have been considered. Areas of further study have also been highlighted. Regarding the physical layer, it has been pointed out that future research directions may include channel coding and signal processing mechanisms in order to ensure coexistence among different PLC systems and among PLC and other communication technologies. Furthermore, the resource allocation in multicarrier and MIMO systems, as well as the bandwidth extension techniques have been assessed as a way to further extend coverage.

From the results and the discussions carried out along this thesis it can be concluded that PLC networks represents a challenging communication environment, exhibiting a great heterogeneity in terms of possible application contexts. Each scenario has its own peculiarities and exhibits different channel and network properties, as well as a different underlying network topology. However, typically, severe frequency selectivity and channel attenuation, as well as great deal of noise are experienced. Despite these detrimental effects, high and similar performance can be achieved in all the several PLC networks. Thus, due to the worldwide and widespread deployment of power lines, the implementation of the PLC technology is potentially ubiquitous, having the chance to become a major candidate for the future communication systems.

10.2 Future Perspectives

Based on the experience gathered during the research activity and on the results obtained by the detailed analysis performed relying on experimental measurements, some activities and key topics can be identified and proposed as a future development perspective. These insights can be followed by the research community with the aim of improving the overall knowledge within the PLC field. For example, a thorough characterization of the PLC channel needs to be performed for both the BB and the NB frequency spectra.

The investigation of the extended BB-FS, even beyond 100 MHz, is fundamental in order to guarantee further capacity improvements, being able to fulfill the future high data rate customers demand. Furthermore, the transmission at such high frequencies leads to non negligible radiation effects that may interfere with other devices in the neighborhoods, as well as with the network itself. In addition, also the effect of environmental radio signals and wireless communications, which couple to the PLC network, must be taken into greater consideration. The analysis of these issues should be further investigated in order to establish proper constraints and requirements for the PLC devices. Moreover, the exploitation of these radiated signals can be assessed as a further opportunity of transmission, discussing the feasibility of a hybrid PLC-wireless system, as already done by few early studies. This hybrid approach can provide some benefits, as, for example, a mobility degree within the PLC context.

Nevertheless, also the NB-FS must be deeply investigated since the scientific works that target the NB spectrum are limited, although there is a lot of interest in supporting

low data rate applications, e.g. among sensors. Within this field, a more comprehensive understanding of the NB-PLC systems influence on the other network equipment should be tackled in order to aid the definition of more general and widely accepted transmission PSD constraints. The establishment of such type of requirements is fundamental in order to ensure the coexistence between the various devices connected to the same network.

However, a thorough CFR characterization, alone, is not sufficient. Also other features, like the line impedance, requires an in depth investigation. As seen in this thesis, the impedance knowledge allows to develop proper PLC devices, able to overcome the signal injection issues due to the low impedance levels. Last, but not least, the thorough characterization of all the other channel properties, such as the frequency or spatial correlation, as well as the analysis of the most common statistical metrics, is beneficial in order to understand the implicit effects that affect the CFR behavior. A detailed analysis of such quantities, for all the possible environments in which the PLC technology can find application, would help to identify the major relationships between the network parameters and the causes underlying the main channel features. In addition, performing this study within the different scenarios enables to highlight the key differences that can discriminate one scenario from another.

When investigating the channel properties, such as the CFR or the line impedance, much more effort should be spent by the research community in assessing a further peculiarity, that has been recently detected also within the PLC context, i.e. the time-variance. Although some studies, characterizing this temporal changing behavior, have began to appear, this effect is still poorly investigated. The understanding of this phenomenon, and how it reflects on the channel performances and on the statistical metrics, would lead to a more accurate and fair characterization.

Besides the detailed channel properties evaluation, it would be very important to perform also noise measurements in order to identify its peculiarities and the effects on the performance. Moreover, the collected channel and noise measurements should be carried out together with the description of the underlying network structure existing between the measurement plugs. Possibly, this should be done providing the deployed electrical scheme, along with the wire lengths and interconnections position or, at least, providing the plugs location w.r.t. a reference point. This information aids to identify how the topology reflects on the network properties, as well as on the signal propagation phenomena of a certain configuration scheme.

A detailed analysis of the typical PLC channel and noise properties, as well as a thorough description of the relationships existing among their representing parameters, would allow to develop more fair and effective models, able to emulate the behavior and the features of a real communication scenario. Furthermore, establish a good general model, that can simulate several environments with different properties, would foster the research community in understanding of what effects and how they contribute to

the definition of the typical PLC phenomena. This would allow to collect new insights without the necessity of experimental measurements. Furthermore, such a model would represent an outstanding tool for the standardization organizations, as well as for the industries, in order to easily develop and provide new and updated PLC standards and devices, avoiding the on field tests.

When investigating the PLC context, besides the medium intrinsic properties, also the security aspects should be taken into great consideration, in order to ensure the confidentiality of the communication. Assess how the physical phenomena and the network topology affect the secrecy degree that can be guaranteed within the PLC environment is of fundamental importance, especially in an extremely interconnected world. Some interesting analysis have been performed for the wireless scenario, however the PLC context is still poorly investigated. All the collected information and the provided results would improve the overall scientific community knowledge, as well as the products and services provided to the final customers.

Bibliography

[1] S. Galli, A. Scaglione, and Z. Wang, "For the Grid and Through the Grid: The Role of Power Line Communications in the Smart Grid," *Proceedings of the IEEE*, vol. 99, no. 6, pp. 998–1027, June 2011.

[2] M. Schwartz, "Carrier-wave telephony over power lines: Early history [History of Communications]," *IEEE Communications Magazine*, vol. 47, no. 1, pp. 14–18, January 2009.

[3] H. C. Ferreira, L. Lampe, J. Newbury, and T. G. Swart, *Power Line Communications: Theory and Applications for Narrowband and Broadband Communications over Power Lines*. NY: Wiley & Sons, 2010.

[4] "802.11 Standard: Wireless LAN Medium Access Control and Physical Layer Specification," IEEE, 2012.

[5] A. Pinomaa, J. Ahola, A. Kosonen, and P. Nuutinen, "HomePlug Green PHY for the LVDC PLC Concept: Applicability Study," in *Proc. of IEEE International Symposium on Power Line Communications and its Applications (ISPLC)*, 2015.

[6] V. N. Papilaya, A. J. H. Vinck, K. Ouahadaz, A. Mengi, M. Weinand, and M. Koch, "Analysis of the Devolo's 500 kHz G3-PLC access technology based on smart grid field trials," in *Proc. of IEEE International Symposium on Power Line Communications and its Applications (ISPLC)*, March 2014, pp. 138–143.

[7] A. Pinomaa, J. Ahola, A. Kosonen, and P. Nuutinen, "Applicability of narrowband power line communication in an LVDC distribution network," in *Proc. of IEEE International Symposium on Power Line Communications and its Applications (ISPLC)*, 2014.

[8] A. Goedhart, R. Heymann, and H. Ferreira, "Adapting HomePlug C&C PLC for use in a low voltage smart grid," in *Proc. of IEEE International Symposium on Power Line Communications and its Applications (ISPLC)*, 2012.

[9] A. Pinomaa, J. Ahola, and A. Kosonen, "Power-line communication-based network architecture for LVDC distribution system," in *Proc. of IEEE International Symposium on Power Line Communications and its Applications (ISPLC)*, 2011.

[10] Y. He, N. Jenkins, J. Wu, and M. Eltayeb, "ICT infrastructure for smart distribution networks," in *Proc. of IEEE International Symposium on Power Line Communications and its Applications (ISPLC)*, 2010.

[11] J. Liu, B. Zhao, J. Wang, Y. Zhu, and J. Hu, "Application of power line communication in smart power consumption," in *Proc. of IEEE International Symposium on Power Line Communications and its Applications (ISPLC)*, 2010.

[12] P. Mlynek, M. Koutny, J. Misurec, and Z. Kolka, "Measurements and evaluation of PLC modem with G3 and PRIME standards for street lighting control," in *Proc. of IEEE International Symposium on Power Line Communications and its Applications (ISPLC)*, 2013.

[13] G. Dickmann, "DigitalSTROM®: A centralized PLC topology for home automation and energy management," in *Proc. of IEEE International Symposium on Power Line Communications and its Applications (ISPLC)*, 2011.

[14] L. R. Castor, R. Natale, J. Silva, M. E. Segatto *et al.*, "Experimental investigation of broadband power line communication modems for onshore oil & gas industry: A preliminary analysis," in *Proc. of IEEE International Symposium on Power Line Communications and its Applications (ISPLC)*, 2014.

[15] L. Lampe, A. M. Tonello, and T. G. Swart, *Power Line Communications: Principles, Standards and Applications from Multimedia to Smart Grid*, 2nd ed. Chichester, UK: John Wiley & Sons, 2015.

[16] O. Hersent, D. Boswarthick, and O. Elloumi, Eds., *The Internet of Things: Ket Applications and Protocols*, 2nd ed. Chichester, UK: John Wiley & Sons, 2012.

[17] D. Dzung, I. Berganza, and A. Sendin, "Evolution of powerline communications for smart distribution: From ripple control to OFDM," in *Proc. of IEEE International Symposium on Power Line Communications and its Applications (ISPLC)*, April 2011, pp. 474–478.

[18] L. Lampe, A. M. Tonello, and D. Shaver, "Power line communications for automation networks and smart grid [Guest Editorial]," *IEEE Communications Magazine*, vol. 49, no. 12, pp. 26–27, December 2011.

[19] S. Goel, S. F. Bush, and D. Bakken, Eds., *IEEE Vision for Smart Grid Communications: 2030 and Beyond*. IEEE Standard Association, 2013.

[20] European Committee for Electrotechnical Standardization (CENELEC), "Signalling on low-voltage electrical installations in the frequency range 3 kHz to 148,5 kHz – Part 1: General requirements, frequency bands and electromagnetic disturbances," IEC, Standard EN 50065-1, 1991, 2001, 2011,.

[21] Association of Radio Industries and Businesses (ARIB), "Power Line Communication Equipment (10kHz-450kHz)," November 2002, sTD-T84, Ver. 1.0, (in Japanese). [Online]. Available: http://www.arib.or.jp/english/html/overview/doc/1-STD-T84v1_0.pdf

[22] *Distribution automation using distribution line carrier systems – Part 5-1: Lower layer profiles – The spread frequency shift keying (S-FSK) profile (IEC 61334-5-1, ed. 2.0)*, IEC, May 2001.

[23] "Narrowband Orthogonal Frequency Division Multiplexing Power Line Communication Transceivers for PRIME Networks," Recommendation ITU-T G.9904, 2012.

[24] "Narrowband Orthogonal Frequency Division Multiplexing Power Line Communication Transceivers for G3-PLC Networks," Recommendation ITU-T G.9903, 2012.

[25] "Narrowband Orthogonal Frequency Division Multiplexing Power Line Communication Transceivers for ITU-T G.hnem networks," Recommendation ITU-T G.9902: Narrowband, ITU, October 2012.

[26] "IEEE Standard for Low-Frequency (less than 500 kHz) Narrowband Power Line Communications for Smart Grid Applications," IEEE 1901.2-2013, December 2013.

[27] H. A. Latchman and L. W. Yonge, "Power Line Local Area Networking," *IEEE Communications Magazine*, vol. 41, no. 4, pp. 32–33, April 2003.

[28] S. Galli, A. Scaglione, and K. Dostert, "Broadband is power: Internet access through the power line network," *IEEE Communications Magazine*, vol. 41, no. 5, pp. 82–83, May 2003.

[29] HomePlug Powerline Alliance, "HomePlug 1.0 Specification," 2001. [Online]. Available: http://www.homeplug.org/

[30] M. K. Lee, R. E. Newman, H. A. Latchman, S. Katar, and L. Yonge, "Homeplug 1.0 powerline communication lans – protocol description and performance results," *International Journal of Communication Systems*, vol. 16, no. 5, pp. 447–473, May 2003.

[31] S. Galli and O. Logvinov, "Recent Developments in the Standardization of Power Line Communications within the IEEE," *IEEE Communications Magazine*, vol. 46, no. 7, pp. 64–71, July 2008.

[32] V. Oksman and S. Galli, "G.hn: The new ITU-T home networking standard," *IEEE Communications Magazine*, vol. 47, no. 10, pp. 138–145, October 2009.

[33] "IEEE Standard for Broadband over Power Line Networks: Medium Access Control and Physical Layer Specifications," IEEE 1901-2010, September 2010.

[34] "Unified High-Speed Wireline-Based Home Networking Transceivers – System Architecture and Physical Layer Specification," Recommendation ITU-T G.9960, ITU, December 2010. [Online]. Available: https://www.itu.int/rec/T-REC-G.9960/en

[35] "Unified high-speed wireline-based home networking transceivers – data link layer specification."

[36] M. C. Sun and D. P. K. Lun, "Power-line communications using DWMT modulation," in *Proc. of IEEE International Symposium on Circuits and Systems (ISCAS)*, vol. 4, 2002, pp. IV–493–IV–496.

[37] "Coexistence mechanism for wireline home networking transceivers," ITU-T Recommendation G.9972, ITU, June 2010. [Online]. Available: http://www.itu.int/rec/T-REC-G.9972

[38] "Unified high-speed wireline-based home networking transceivers – Multiple input/multiple output specification," ITU-T Recommendation G.9963, ITU, September 2011. [Online]. Available: http://www.itu.int/rec/T-REC-G.9963

[39] L. Yonge, J. Abad, K. Afkhamie, L. Guerrieri, S. Katar, H. Lioe, P. Pagani, R. Riva, D. M. Schneider, and A. Schwager, "An Overview of the HomePlug AV2 Technology," *Journal of Electrical and Computer Engineering*, vol. 2013, pp. 1–20, 2013.

[40] HomePlug Powerline Alliance, "HomePlug Green PHY Specification, Release Version 1.0.0," June 2010. [Online]. Available: http://www.homeplug.org/tech-resources/green-phy-iot/

[41] W. Wu, B. Chen, and C. Li, "Experimental research on Triple Play via Power Line," in *Proc. of IEEE International Symposium on Power Line Communications and its Applications (ISPLC)*, 2012.

[42] A. Gnazzo, A. Bergaglio, M. Palma, F. Pittoni, M. Giunta, and F. Ballesio, "Powerline technology over coaxial cables for in-home multimedia applications: Performances and EMC issues," in *Proc. of IEEE International Symposium on Power Line Communications and its Applications (ISPLC)*, 2011.

[43] S.-C. Yeh, C.-K. Lin, and H. H. Chen, "Available bandwidth characteristics and estimation of in-home power line networks," in *Proc. of IEEE International Symposium on Power Line Communications and its Applications (ISPLC)*, 2008.

[44] C.-K. Lin, H.-W. Chu, S.-C. Yen, M.-T. Lu, J. Yao, and H. Chen, "Robust video streaming over power lines," in *Proc. of IEEE International Symposium on Power Line Communications and its Applications (ISPLC)*, 2006.

[45] P. Degauque, I. Stievano, S. Pignari, V. Degardin, F. Canavero, F. Grassi, and F. Canete, "Power-Line Communication: Channel Characterization and Modeling for Transportation Systems," *IEEE Vehicular Technology Magazine*, vol. 10, no. 2, 2015.

[46] M. Mohammadi, L. Lampe, M. Lok, S. Mirabbasi, M. Mirvakili, R. Rosales, and P. van Veen, "Measurement Study and Transmission for In-Vehicle Power Line Communication," in *Proc. of IEEE International Symposium on Power Line Communications and its Applications (ISPLC)*, March 2009, pp. 73–78.

[47] L. Guerrieri, P. Bisaglia, I. Stievano, and F. Canavero, "Statistical assessment of automotive PLC multipath channel models," in *Proc. of IEEE International Symposium on Power Line Communications and its Applications (ISPLC)*, March 2014, pp. 47–51.

[48] M. Lienard, M. Carrion, V. Degardin, and P. Degauque, "Modeling and Analysis of In-Vehicle Power Line Communication Channels," *IEEE Transactions on Vehicular Technology*, vol. 57, no. 2, pp. 670–679, March 2008.

[49] J. Cortés, M. Cerda, L. Díez, and F. Cañete, "Analysis of the periodic noise on in-vehicle broadband power line channels," in *Proc. of IEEE International Symposium on Power Line Communications and its Applications (ISPLC)*, March 2012, pp. 334–339.

[50] M. Antoniali, M. Girotto, and A. Tonello, "In-car power line communications: Advanced transmission techniques," *International Journal of Automotive Technology*, vol. 14, no. 4, pp. 625–632, August 2013. [Online]. Available: http://dx.doi.org/10.1007/s12239-013-0067-2

[51] P. Tanguy, F. Nouvel, and P. Maziearo, "Power Line Communication standards for in-vehicule networks," in *Proc. of International Conference on Intelligent Transport Systems Telecommunications (ITST).* IEEE, 2009, pp. 533–537.

[52] S. Barmada, M. Raugi, M. Tucci, and T. Zheng, "Power line communication in a full electric vehicle: Measurements, modelling and analysis," in *Proc. of IEEE International Symposium on Power Line Communications and its Applications (ISPLC)*, 2010.

[53] S. Barmada, L. Bellanti, M. Raugi, and M. Tucci, "Analysis of Power-Line Communication Channels in Ships," *IEEE Transactions on Vehicular Technology*, vol. 59, no. 7, pp. 3161–3170, September 2010.

[54] M. Antoniali, A. M. Tonello, M. Lenardon, and A. Qualizza, "Measurements and analysis of PLC channels in a cruise ship," in *Proc. of IEEE International Symposium on Power Line Communications and its Applications (ISPLC)*, 2011.

[55] V. Degardin, I. Junqua, M. Lienard, P. Degauque, and S. Bertuol, "Theoretical Approach to the Feasibility of Power-Line Communication in Aircrafts," *IEEE Transactions on Vehicular Technology*, vol. 62, no. 3, pp. 1362–1366, March 2013.

[56] V. Degardin, E. Simon, M. Morelle, M. Liénard, P. Degauque, I. Junqua, and S. Bertuol, "On the possibility of using PLC in aircraft," in *Proc. of IEEE International Symposium on Power Line Communications and its Applications (ISPLC)*, 2010.

[57] P. Karols, K. Dostert, G. Griepentrog, and S. Huettinger, "Mass transit power traction networks as communication channels," *IEEE Journal on Selected Areas in Communications*, vol. 24, no. 7, pp. 1339–1350, July 2006.

[58] S. Barmada, A. Gaggelli, A. Musolino, R. Rizzo, M. Raugi, and M. Tucci, "Design of a PLC system onboard trains: selection and analysis of the PLC channel," in *Proc. of IEEE International Symposium on Power Line Communications and its Applications (ISPLC)*, 2008.

[59] S. Galli, T. Banwell, and D. Waring, "Power line based LAN on board the NASA Space Shuttle," in *Proc. of IEEE Vehicular Technology Conference (VTC)*, vol. 2, May 2004, pp. 970–974 Vol.2.

[60] F. Minamiyama, H. Koga, K. Kobayashi, and M. Katayama, "Power supply overlaid communication and common clock delivery for cooperative motion control," in *Proc. of IEEE International Symposium on Power Line Communications and its Applications (ISPLC)*, 2011.

[61] A. T. Sherman, D. Phatak, B. Sonawane, and V. G. Relan, "Location authentication through Power Line Communication: Design, protocol, and analysis of a new out-of-band strategy," in *Proc. of IEEE International Symposium on Power Line Communications and its Applications (ISPLC)*, 2010.

[62] L. Zhang, X. Liu, and D. Xu, "A novel security monitoring system of coal mine based on power line communication dynamic routing technology," in *IEEE Industry Applications Society Annual Meeting*. IEEE, 2014, pp. 1–6.

[63] S. Tsuzuki and Y. Yamada, "Feasibility Study of Ubiquitous Sensor Networks by Inductively Coupled PLC Over PV Power Systems," in *Proc. of IEEE International Symposium on Power Line Communications and its Applications (ISPLC)*, 2015.

[64] A. de Beer, H. Ferreira, and A. Vinck, "Contactless power-line communications," in *Proc. of IEEE International Symposium on Power Line Communications and its Applications (ISPLC)*, 2014.

[65] S. Barmada, M. Raugi, and M. Tucci, "Power line communication integrated in a Wireless Power Transfer system: A feasibility study," in *Proc. of IEEE International Symposium on Power Line Communications and its Applications (ISPLC)*, 2014.

[66] M. Zimmermann and K. Dostert, "A Multipath Model for the Powerline Channel," *IEEE Transactions on Communications*, vol. 50, no. 4, pp. 553–559, April 2002.

[67] D. Liu, E. Flint, B. Gaucher, and Y. Kwark, "Wide Band AC Power Line Characterization," *IEEE Transactions on Consumer Electronics*, vol. 45, no. 4, pp. 1087–1097, November 1999.

[68] B. O'Mahony, "Field Testing of High Speed Power Line Communications in North American Homes," in *Proc. of IEEE International Symposium on Power Line Communications and its Applications (ISPLC)*, Orlando, USA, March 2006, pp. 155–159.

[69] "The impact of power line high data rate telecommunication systems on radiocommunication systems below 470 MHz," Recommendation ITU-R SM.1879-2, ITU, August 2013. [Online]. Available: https://www.itu.int/rec/R-REC-SM.1879/en

[70] M. Tlich, A. Zeddam, A. Moulin, and F. Gauthier, "Indoor Power-Line Communications Channel Characterization Up to 100 MHz – Part I: One-Parameter Deterministic Model," *IEEE Transactions on Power Delivery*, vol. 23, no. 3, pp. 1392–1401, July 2008.

[71] ——, "Indoor Power-Line Communications Channel Characterization up to 100 MHz – Part II: Time-Frequency Analysis," *IEEE Transactions on Power Delivery*, vol. 23, no. 3, pp. 1402–1409, July 2008.

[72] S. Galli, "A Simplified Model for the Indoor Power Line Channel," in *Proc. of IEEE International Symposium on Power Line Communications and its Applications (ISPLC)*, Dresden, Germany, April 2009, pp. 13–19.

[73] ——, "A Novel Approach to the Statistical Modeling of Wireline Channels," *IEEE Transactions on Communications*, vol. 59, no. 5, pp. 1332–1345, May 2011.

[74] J. A. Cortés, F. J. Cañete, L. Díez, and J. L. G. Moreno, "On the Statistical Properties of Indoor Power Line Channels: Measurements and Models," in *Proc. of IEEE International Symposium on Power Line Communications and its Applications (ISPLC)*, Udine, Italy, April 2011, pp. 271–276.

[75] M. Babic, M. Hagenau, K. Dostert, and J. Bausch, "D4: Theoretical Postulation of the PLC Channel Model OPERA," IST Integrated Project No. 507667 funded by EC, Tech. Rep., March 2005, OPERA Deliverable D4.

[76] P. Meier, M. Bittner, H. Widmer, J.-L. Bermudez, A. Vukicevic, M. Rubinstein, F. Rachidi, M. Babic, and J. S. Miravalles, "D5 Pathloss as a function of frequency, distance and network topology for various LV and MV European powerline networks." IST Integrated Project No. 507667, Tech. Rep., April 2005, OPERA Deliverable D5.

[77] M. Sigle, W. Liu, and K. Dostert, "On the Impedance of the Low-Voltage Distribution Grid At Frequencies Up to 500 kHz," in *Proc. of IEEE International Symposium on Power Line Communications and its Applications (ISPLC)*, 2012.

[78] ETSI TR 101 562-1 V 1.3.1, "PowerLine Telecommunications (PLT); MIMO PLT; Part 1: Measurement Methods of MIMO PLT," European Telecommunication Standardization Institute, Tech. Rep., 2012.

[79] L. Stadelmeier, D. Schill, A. Schwager, D. Schneider, and J. Speidel, "MIMO for Inhome Power Line Communications," in *Proc. of International ITG Conference on Source and Channel Coding (SCC)*, 2008, pp. 1–6.

[80] D. Schneider, J. Speidel, L. Stadelmeier, and D. Schill, "Precoded Spatial Multiplexing MIMO for Inhome Power Line Communications," in *Proc. of IEEE Global Telecommunications Conference (GLOBECOM)*, 2008, pp. 1–5.

[81] D. Schneider, A. Schwager, J. Speidel, and A. Dilly, "Implementation and Results of a MIMO PLC Feasibility Study," in *Proc. of IEEE International Symposium on Power Line Communications and its Applications (ISPLC)*, 2011, pp. 54–59.

[82] D. Schneider, A. Schwager, W. Baschlin, and P. Pagani, "European MIMO PLC Field Measurements: Channel Analysis," in *Proc. of IEEE International Symposium on Power Line Communications and its Applications (ISPLC)*, March 2012.

[83] R. Hashmat, P. Pagani, A. Zeddam, and T. Chonavel, "MIMO Communications for Inhome PLC Networks: Measurements and Results up to 100 MHz," in *Proc. of IEEE International Symposium on Power Line Communications and its Applications (ISPLC)*, 2010, pp. 120–124.

[84] A. Schwager, W. Baschlin, H. Hirsch, P. Pagani, N. Weling, J. Moreno, and H. Milleret, "European MIMO PLT field measurements: Overview of the ETSI STF410 campaign & EMI analysis," in *Proc. of IEEE International Symposium on Power Line Communications and its Applications (ISPLC)*, March 2012, pp. 298–303.

[85] ETSI TR 101 562-3 V 1.1.1, "PowerLine Telecommunications (PLT); MIMO PLT; Part 3: Setup and Statistical Results of MIMO PLT Channel and Noise Measurements," European Telecommunication Standardization Institute, Tech. Rep., 2012.

[86] D. Veronesi, R. Riva, P. Bisaglia, F. Osnato, K. Afkhamie, A. Nayagam, D. Rende, and L. Yonge, "Characterization of in-home MIMO power line channels," in *Proc. of IEEE International Symposium on Power Line Communications and its Applications (ISPLC)*, April 2011, pp. 42–47.

[87] A. Tomasoni, R. Riva, and S. Bellini, "Spatial correlation analysis and model for in-home MIMO power line channels," in *Proc. of IEEE International Symposium on Power Line Communications and its Applications (ISPLC)*, March 2012, pp. 286–291.

[88] L. T. Berger, A. Schwager, P. Pagani, and D. Schneider, *MIMO Power Line Communications: Narrow and Broadband Standards, EMC, and Advanced Processing*. Boca Raton, FL, USA: CRC Press, Inc., 2014.

[89] M. Antoniali, M. De Piante, and A. Tonello, "PLC noise and channel characterization in a compact electrical car," in *Proc. of IEEE International Symposium on Power Line Communications and its Applications (ISPLC)*, March 2013, pp. 29–34.

[90] S. Barmada, M. Raugi, R. Rizzo, and M. Tucci, "Channel evaluation for power line communication in plug - in electric vehicles," *IET Electrical Systems in Transportation*, vol. 2, no. 4, pp. 195–201, December 2012.

[91] J. Bausch, T. Kistner, M. Babic, and K. Dostert, "Characteristics of Indoor Power Line Channels in the Frequency Range 50 - 500 kHz," in *Proc. of IEEE International Symposium on Power Line Communications and its Applications (ISPLC)*, Orlando, Florida (US), March 2006, pp. 86–91.

[92] Draft Standard for PowerLine Intelligent Metering Evolution R1.3E. [Online]. Available: http://www.prime-alliance.org

[93] PLC G3 Physical Layer Specification. [Online]. Available: http://www.erdfdistribution.fr/

[94] M. L. V. Degardin, M. O. Carrion and P. Degauque, "In-vehicle power line communication: Impulsive noise characteristics," in *XXVIIIth General Assembly URSI*, New Delhi, India, October 2005.

[95] B. H. J. Yazdani, M. Scott, "Point to Point Multi-Media Transmission for Marine Application," in *Proc. of IEEE International Symposium on Power Line Communications and its Applications (ISPLC)*, Athens, Greece, March 2002, pp. 171–175.

[96] M. Zimmermann and K. Dostert, "Analysis and Modeling of Impulsive Noise in Broad-Band Powerline Communications," *IEEE Transactions on Electromagnetic Compatibility*, vol. 44, no. 1, pp. 249–258, February 2002.

[97] M. Gotz, M. Rapp, and K. Dostert, "Power line channel characteristics and their effect on communication system design," *IEEE Communications Magazine*, vol. 42, no. 4, pp. 78–86, April 2004.

[98] M. Antoniali, F. Versolato, and A. M. Tonello, "An Experimental Characterization of the PLC Noise at the Source," *to appear IEEE Transactions on Power Delivery*, 2015.

[99] M. H. L. Chan and R. W. Donaldson, "Amplitude, Width, and Interarrival Distributions for Noise Impulses on Intrabuilding Power Line Communication Networks," *IEEE Transactions on Electromagnetic Compatibility*, vol. 31, no. 3, pp. 320–323, August 1989.

[100] F. Gianaroli, F. Pancaldi, E. Sironi, M. Vigilante, G. M. Vitetta, and A. Barbieri, "Statistical Modeling of Periodic Impulsive Noise in Indoor Power-Line Channels," *IEEE Transactions on Power Delivery*, vol. 27, no. 3, pp. 1276–1283, July 2012.

[101] D. Middleton, "Statistical-Physical Models of Electromagnetic Interference," *IEEE Transactions on Electromagnetic Compatibility*, vol. 19, no. 3, pp. 106–127, August 1977.

[102] H. Meng, Y. L. Guan, and S. Chen, "Modeling and Analysis of Noise Effects on Broadband Power-Line Communications," *IEEE Transactions on Power Delivery*, vol. 20, no. 2, pp. 630–637, April 2005.

[103] M. Katayama, T. Yamazato, and H. Okada, "A Mathematical Model of Noise in Narrowband Power Line Communication Systems," *IEEE Journal on Selected Areas in Communications*, vol. 24, no. 7, pp. 1267–1276, July 2006.

[104] J. A. Cortés, L. Díez, F. J. Cañete, and J. J. Sánchez-Martínez, "Analysis of the Indoor Broadband Power-Line Noise Scenario," *IEEE Transactions on Electromagnetic Compatibility*, vol. 52, no. 4, pp. 849–858, November 2010.

[105] L. di Bert, P. Caldera, D. Schwingshackl, and A. M. Tonello, "On Noise Modeling for Power Line Communications," in *Proc. of IEEE International Symposium on Power Line Communications and its Applications (ISPLC)*, Udine, Italy, April 2011, pp. 283–288.

[106] T. Esmailian, F. R. Kschischang, and P. Glenn Gulak, "In-Building Power Lines as High-Speed Communication Channels: Channel Characterization and a Test Channel Ensemble," *International Journal of Communication Systems*, vol. 16, no. 5, pp. 381–400, June 2003.

[107] M. Tlich, H. Chaouche, A. Zeddam, and P. Pagani, "Novel Approach for PLC Impulsive Noise Modelling," in *Proc. of IEEE International Symposium on Power Line Communications and its Applications (ISPLC)*, Dresden, Germany, March 2009, pp. 20–25.

[108] D. Rende, A. Nayagam, K. Afkhamie, L. Yonge, R. Riva, D. Veronesi, F. Osnato, and P. Bisaglia, "Noise Correlation and Its Effect on Capacity of In-home MIMO Power Line Channels," in *Proc. of IEEE International Symposium on Power Line Communications and its Applications (ISPLC)*, April 2011, pp. 60–65.

[109] A. Pittolo, A. M. Tonello, and F. Versolatto, "Performance of MIMO PLC in measured channels affected by correlated noise," in *Proc. of IEEE International Symposium on Power Line Communications and its Applications (ISPLC)*, March 2014, pp. 261–265.

[110] J. S. Barnes, "A Physical Multi-Path Model for Power Distribution Network Propagation," in *Proc. of IEEE International Symposium on Power Line Communications and its Applications (ISPLC)*, Tokyo, Japan, March 1998, pp. 76–89.

[111] O. G. Hooijen, "On The Relation Between Network-Topology and Power Line Signal Attenuation," in *Proc. of IEEE International Symposium on Power Line Communications and its Applications (ISPLC)*, March 1998, pp. 45–56.

[112] I. C. Papaleonidopoulos, C. G. Karagiannopoulos, I. E. Anagnostopoulos, and N. J. Theodorou, "An HF multipath-propagation analysing method for power delay profile estimations of indoor single phase low voltage PLC channels," in *Proc. of IEEE International Symposium on Power Line Communications and its Applications (ISPLC)*, Kyoto, Japan, March 2003, pp. 154–159.

[113] H. Meng, Y. L. Guan, C. L. Law, P. L. So, E. Gunawan, and T. Lie, "Modeling of Transfer Characteristics for the Broadband Power Line Communication Channel," *IEEE Transactions on Power Delivery*, vol. 19, no. 3, pp. 1057–1064, July 2004.

[114] S. Galli and T. C. Banwell, "A deterministic frequency-domain model for the indoor power line transfer function," *IEEE Journal on Selected Areas in Communications*, vol. 24, no. 7, pp. 1304–1316, July 2006.

[115] J. Anatory, N. Theethayi, and R. Thottappillil, "Power-Line Communication Channel Model for Interconnected Networks – Part I: Two-Conductor System," *IEEE Transactions on Power Delivery*, vol. 24, no. 1, pp. 118–123, January 2009.

[116] F. Cañete, J. Cortés, L. Díez, and J. Entrambasaguas, "A Channel Model Proposal for Indoor Power Line Communications," *IEEE Communications Magazine*, vol. 49, no. 12, pp. 166–174, 2011.

[117] A. M. Tonello and F. Versolatto, "Bottom-Up Statistical PLC Channel Modeling – Part I: Random Topology Model and Efficient Transfer Function Computation," *IEEE Transactions on Power Delivery*, vol. 26, no. 2, pp. 891–898, April 2011.

[118] A. Tonello and F. Versolatto, "Bottom-Up Statistical PLC Channel Modeling – Part II: Inferring the Statistics," *IEEE Transactions on Power Delivery*, vol. 25, no. 4, pp. 2356–2363, 2010.

[119] F. Versolatto and A. Tonello, "An MTL Theory Approach for the Simulation of MIMO Power-Line Communication Channels," *IEEE Transactions on Power Delivery*, vol. 26, no. 3, pp. 1710–1717, July 2011.

[120] ——, "A MIMO PLC random channel generator and capacity analysis," in *Proc. of IEEE International Symposium on Power Line Communications and its Applications (ISPLC)*, April 2011, pp. 66–71.

[121] J. Anatory, N. Theethayi, and R. Thottappillil, "Power-Line Communication Channel Model for Interconnected Networks – Part II: Multiconductor System," *IEEE Transactions on Power Delivery*, vol. 24, no. 1, pp. 124–128, January 2009.

[122] O. G. Hooijen, "A Channel Model for the Residential Power Circuit Used as a Digital Communications Medium," *IEEE Transactions on Electromagnetic Compatibility*, vol. 40, no. 4, pp. 331–336, November 1998.

[123] H. Phillips, "Modelling of Powerline Communication Channels," in *Proc. of IEEE International Symposium on Power Line Communications and its Applications (ISPLC)*, Lancaster, U.K., March 1999, pp. 14–21.

[124] A. M. Tonello, "Wideband Impulse Modulation and Receiver Algorithms for Multiuser Power Line Communications," *EURASIP Journal on Advances in Signal Processing*, vol. 2007, pp. 1–14, 2007.

[125] A. M. Tonello, F. Versolatto, B. Béjar, and S. Zazo, "A Fitting Algorithm for Random Modeling the PLC Channel," *IEEE Transactions on Power Delivery*, vol. 27, no. 3, pp. 1477–1484, June 2012.

[126] A. Canova, N. Benvenuto, and P. Bisaglia, "Receivers for MIMO-PLC Channels: Throughput Comparison," in *Proc. of IEEE International Symposium on Power Line Communications and its Applications (ISPLC)*, March 2010, pp. 114–119.

[127] R. Hashmat, P. Pagani, A. Zeddam, and T. Chonave, "A Channel Model for Multiple Input Multiple Output in-home Power Line Networks," in *Proc. of IEEE International Symposium on Power Line Communications and its Applications (ISPLC)*, April 2011, pp. 35–41.

[128] S. Galli, "A Simple Two-Tap Statistical Model for the Power Line Channel," in *Proc. of IEEE International Symposium on Power Line Communications and its Applications (ISPLC)*, Rio de Janeiro, Brazil, March 2010, pp. 242–248.

[129] F. Versolatto and A. M. Tonello, "PLC Channel Characterization up to 300 MHz: Frequency Response and Line Impedance," in *Proc. of IEEE Global Telecommunications Conference (GLOBECOM)*, December 2012, pp. 3525–3530.

[130] A. M. Tonello, F. Versolatto, and C. Tornelli, "Analysis of impulsive UWB modulation on a real MV test network," in *Proc. of IEEE International Symposium on Power Line Communications and its Applications (ISPLC)*, April 2011, pp. 18–23.

[131] F. Versolatto, A. M. Tonello, C. Tornelli, and D. D. Giustina, "Statistical Analysis of Broadband Underground Medium Voltage Channels for PLC Applications," in *Proc. of IEEE International Conference on Smart Grid Communications (SmartGridComm)*, November 2014, pp. 493–498.

[132] F. J. Harris, "On the use of windows for harmonic analysis with the discrete fourier transform," *Proceedings of the IEEE*, vol. 66, no. 1, pp. 51–83, January 1978.

[133] J. G. Proakis, *Digital Communications*, ser. McGraw-Hill series in electrical and computer engineering: communications and signal processing. McGraw-Hill, 2007.

[134] P. J. Bickel and K. A. Doksum, *Mathematical Statistics, Basic Ideas and Selected Topics*. Prentice Hall, 2001, vol. 1.

[135] F. Versolatto and A. M. Tonello, "On the Relation Between Geometrical Distance and Channel Statistics in In-Home PLC Networks," in *Proc. of IEEE International Symposium on Power Line Communications and its Applications (ISPLC)*, Beijing, China, March 2012, pp. 280–285.

[136] From the PLC Channel Measurements to the Statistics: A Matlab Script. [Online]. Available: www.diegm.uniud.it/tonello

[137] F. J. C. Corripio, J. A. C. Arrabal, L. D. del Rio, and J. T. E. Munoz, "Analysis of the Cyclic Short-Term Variation of Indoor Power Line Channels," *IEEE Journal on Selected Areas in Communications*, vol. 24, no. 7, pp. 1327–1338, July 2006.

[138] F. J. Cañete, J. A. Cortés, L. Díez, J. T. Entrambasaguas, and J. L. Carmona, "Fundamentals of the cyclic short-time variation of indoor power-line channels," in *Proc. of IEEE International Symposium on Power Line Communications and its Applications (ISPLC)*, April 2005, pp. 157–161.

[139] J. A. Cortés, F. J. Cañete, L. Díez, and J. T. Entrambasaguas, "Characterization of the cyclic short-time variation of indoor power-line channels response," in *Power Line Communications and Its Applications, 2005 International Symposium on*, April 2005, pp. 326–330.

[140] F. Gianaroli, F. Pancaldi, and G. M. Vitetta, "Broadband System Models Based on Zadeh's Representation for Indoor Powerline Channels: An Experimental Validation," in *Proc. of IEEE International Conference on Communications (ICC)*, June 2013, pp. 2897–2902.

[141] M. Antoniali, "Experimental Activity And Analysis of PLC Technology in Various Scenarios," Ph.D. dissertation, University of Udine, 2012.

[142] G. L. Stüber, *Principles of Mobile Communication*. Norwell, MA, USA: Kluwer Academic Publishers, 2001. [Online]. Available: http://books.google.it/books?id=65fF83bja0C

[143] B. Praho, M. Tlich, P. Pagani, A. Zeddam, and F. Nouvel, "Cognitive Detection Method of Radio Frequencies on Power Line Networks," in *Proc. of IEEE International Symposium on Power Line Communications and its Applications (ISPLC)*, Rio de Janeiro, Brazil, April 2010, pp. 225–230.

[144] M. Antoniali, A. M. Tonello, and F. Versolatto, "A Study on the Optimal Receiver Impedance for SNR Maximization in Broadband PLC," *Journal of Electrical and Computer Engineering*, vol. 2013, p. 11, 2013.

[145] B. Holter, "On the Capacity of the MIMO Channel: A Tutorial Introduction," in *Proc. of IEEE Norwegian Symposium on Signal Processing*, Trondheim, Norway, 18-20 October 2001, pp. 167–172.

[146] A. Schwager, D. Schneider, W. Baschlin, A. Dilly, and J. Speidel, "MIMO PLC: Theory, Measurements and System Setup," in *Proc. of IEEE International Symposium on Power Line Communications and its Applications (ISPLC)*, April 2011, pp. 48–53.

[147] D. P. Palomar, J. M. Cioffi, and M. A. Lagunas, "Joint Tx-Rx Beamforming Design for Multicarrier MIMO Channels: A Unified Framework for Convex Optimization," *IEEE Transactions on Signal Processing*, vol. 51, no. 9, pp. 2381–2401, September 2003.

[148] A. Sendin, J. Simon, I. Urrutia, and I. Berganza, "PLC deployment and architecture for Smart Grid applications in Iberdrola," in *Proc. of IEEE International Symposium on Power Line Communications and its Applications (ISPLC)*, March 2014, pp. 173–178.

[149] R. Pighi and R. Raheli, "On multicarrier signal transmission for high-voltage power lines," in *Proc. of IEEE International Symposium on Power Line Communications and its Applications (ISPLC)*, April 2005, pp. 32–36.

[150] N. Strandberg and N. Sadan, "HV-BPL Phase 2 Field Test Report," U.S. Department of Energy, Tech. Rep. DOE/NETL-2009/1388, November 2009.

[151] R. Aquilue, I. Gutierrez, J. Pijoan, and G. Sanchez, "High-Voltage Multicarrier Spread-Spectrum System Field Test," *IEEE Transactions on Power Delivery*, vol. 24, no. 3, pp. 1112–1121, July 2009.

[152] S. Galli, A. Scaglione, and Z. Wang, "Power Line Communications and the Smart Grid," in *Proc. of IEEE International Conference on Smart Grid Communications (SmartGridComm)*, October 2010, pp. 303–308.

[153] F. Issa, M. Goldberg, and E. Marthe, "Power Line Communications using low and medium voltage networks," in *Proc. of General Assembly of the International Union of Radio Science (URSI)*, 2005.

[154] G. Chu, J. Li, and W. Liu, "Narrow Band Power Line Channel Characteristics for Low Voltage Access Network in China," in *Proc. of IEEE International Symposium on Power Line Communications and its Applications (ISPLC)*, March 2013, pp. 297–302.

[155] T. A. Papadopoulos, A. I. Chrysochos, and G. K. Papagiannis, "Narrowband power line communication: Medium voltage cable modeling and laboratory experimental results," *Electric Power Systems Research*, vol. 102, no. 0, pp. 50–60, 2013.

[156] L. D. Bert, S. D'Alessandro, and A. M. Tonello, "Enhancements of G3-PLC Technology for Smart-Home/Building Applications," *Journal of Electrical and Computer Engineering*, vol. 2013, p. 11, 2013.

[157] M. Antoniali and A. M. Tonello, "Measurement and Characterization of Load Impedances in Home Power Line Grids," *IEEE Transactions on Instrumentation and Measurements*, vol. 63, no. 3, pp. 548–556, March 2014.

[158] M. Nassar, J. Lin, Y. Mortazavi, A. Dabak, Il Han Kim, and B. L. Evans, "Local Utility Power Line Communications in the 3–500 kHz Band: Channel impairments, noise, and standards," *IEEE Signal Processing Magazine*, vol. 29, no. 5, pp. 116–127, September 2012.

[159] J. A. Cortés, A. Sanz, P. Estopiñán, and J. I. García, "Analysis of narrowband power line communication channels for advanced metering infrastructure," *EURASIP Journal on Advances in Signal Processing*, vol. 2015, no. 1, pp. 1–13, 2015.

[160] M. Gili, D. Maringer, and E. Schumann, *Numerical Methods and Optimization in Finance*. Access Online via Elsevier, 2011, ch. 7: Modeling dependencies, pp. 165–173.

[161] Y.-S. Shiu, S. Y. Chang, H.-C. Wu, S. C.-H. Huang, and H.-H. Chen, "Physical Layer Security in Wireless Networks: A Tutorial," *IEEE Wireless Communications Magazine*, vol. 18, no. 2, pp. 66–74, April 2011.

[162] C. E. Shannon, "Communication Theory of Secrecy Systems," *The Bell System Technical Journal*, vol. 28, no. 4, pp. 656–715, October 1949.

[163] I. Kalet, "The Multitone Channel," *IEEE Transactions on Communications*, vol. 37, no. 2, pp. 119–124, February 1989.

[164] Y. Liang, H. Poor, and S. Shamai, "Secure Communication Over Fading Channels," *IEEE Transactions on Information Theory*, vol. 54, no. 6, pp. 2470–2492, June 2008.

[165] J. Barros and M. Rodrigues, "Secrecy Capacity of Wireless Channels," in *Proc. of IEEE International Symposium on Information Theory (ISIT)*, July 2006, pp. 356–360.

[166] Z. Li, R. Yates, and W. Trappe, *Securing Wireless Communications at the Physical Layer*. Springer US, 2010, ch. 1: Secrecy Capacity of Independent Parallel Channels, pp. 1–18. [Online]. Available: http://dx.doi.org/10.1007/978-1-4419-1385-2_1

[167] E. A. Jorswieck, A. Wolf, and S. Gerbracht, *Trends in Telecommunications Technologies*. InTech, March 2010, ch. 20: Secrecy on

the Physical Layer in Wireless Networks, pp. 413–435. [Online]. Available: http://sciyo.com/articles/show/title/secrecy-on-the-physical-layer-in-wireless-networks

[168] Y. Zhuang and L. Lampe, "Physical layer security in MIMO power line communication networks," in *Proc. of IEEE International Symposium on Power Line Communications and its Applications (ISPLC)*, March 2014, pp. 272–277.

[169] D. Chizhik, G. Foschini, and R. Valenzuela, "Capacities of multi-element transmit and receive antennas: Correlations and keyholes," *IET Electronics Letters*, vol. 36, no. 13, pp. 1099–1100, June 2000.

[170] P. Almers, F. Tufvesson, and A. Molisch, "Keyhole Effect in MIMO Wireless Channels: Measurements and Theory," *IEEE Transactions on Wireless Communications*, vol. 5, no. 12, pp. 3596–3604, December 2006.

[171] D. Chizhik, G. Foschini, M. Gans, and R. Valenzuela, "Keyholes, correlations, and capacities of multielement transmit and receive antennas," *IEEE Transactions on Wireless Communications*, vol. 1, no. 2, pp. 361–368, April 2002.

[172] L. Lampe and A. Vinck, "Cooperative multihop power line communications," in *Proc. of IEEE International Symposium on Power Line Communications and its Applications (ISPLC)*, March 2012, pp. 1–6.

[173] A. Wyner, "The wire-tap channel," *The Bell System Technical Journal*, vol. 54, no. 8, pp. 1355–1387, October 1975.

[174] S. Leung-Yan-Cheong and M. Hellman, "The Gaussian wire-tap channel," *IEEE Transactions on Information Theory*, vol. 24, no. 4, pp. 451–456, July 1978.

[175] I. Csiszár and J. Körner, "Broadcast channels with confidential messages," *IEEE Transactions on Information Theory*, vol. 24, no. 3, pp. 339–348, May 1978.

[176] D. Gesbert, H. Bölcskei, D. A. Gore, and A. J. Paulraj, "Outdoor MIMO wireless channels: models and performance prediction," *IEEE Transactions on Communications*, vol. 50, no. 12, pp. 1926–1934, December 2002.

[177] E. Jorswieck and A. Wolf, "Resource allocation for the wire-tap multi-carrier broadcast channel," in *Proc. of International Conference on Telecommunications (ICT)*, June 2008, pp. 1–6.

[178] S. Boyd and L. Vandenberghe, *Convex Optimization*. New York, USA: Cambridge University Press, 2004. [Online]. Available: https://web.stanford.edu/~boyd/cvxbook/bv_cvxbook.pdf

[179] E. A. Jorswieck and S. Gerbracht, "Secrecy Rate Region of Downlink OFDM Systems: Efficient Resource Allocation," in *Proc. of International OFDM Workshop (InOWo)*, Hamburg, Germany, 2009.

[180] Q. Li, M. Hong, H.-T. Wai, Y.-F. Liu, W.-K. Ma, and Z.-Q. Luo, "Transmit Solutions for MIMO Wiretap Channels using Alternating Optimization," *IEEE Journal on Selected Areas in Communications*, vol. 31, no. 9, pp. 1714–1727, September 2013.

[181] J. Jose, N. Prasad, M. Khojastepour, and S. Rangarajan, "On Robust Weighted-Sum Rate Maximization in MIMO Interference Networks," in *Proc. of IEEE International Conference on Communications (ICC)*, June 2011, pp. 1–6.